2003

Flow-induced vibration of elastically supported rectangular cylinders

Jeffrey L. Garrett
Iowa State University

Flow-induced vibration of elastically supported rectangular cylinders

by

Jeffrey L. Garrett

A dissertation submitted to the graduate faculty

in partial fulfillment of the requirements for the degree of

DOCTOR OF PHILOSOPHY

Major: Civil Engineering (Structural Engineering)

Program of Study Committee:
Lowell F. Greimann, Co-major Professor
Partha P. Sarkar, Co-major Professor
Fouad S. Fanous
Terry J. Wipf
Loren W. Zachary

Iowa State University

Ames, Iowa

2003

Graduate College
Iowa State University

This is to certify that the doctoral dissertation of

Jeffrey L. Garrett

has met the dissertation requirements of Iowa State University

Signature was redacted for privacy.

Committee Member

Signature was redacted for privacy.

Committee Member

Signature was redacted for privacy.

Committee Member

Signature was redacted for privacy.

Co-major Professor

Signature was redacted for privacy.

Co-major Professor

Signature was redacted for privacy.

For the Major Program

DEDICATION

I wish to dedicate the entire academic endeavor summarized in this dissertation to my Dad, Ross B., and to the memory of my Mother, Evelyn. Because the two of them understood the value of education, I spent my entire childhood knowing that I would attend college and I have spent my entire adult life, thus far, benefiting from their wisdom and foresight. Their love, support, encouragement and, sometimes forceful but necessary, insistence have made my life possible.

TABLE OF CONTENTS

LIST OF FIGURES

LIST OF TABLES

ACKNOWLEDGEMENTS

In the Summer of 1975, I was waiting for my graduate school placement exam results. When my advisor started to speak, his manner and choice of words told me I had not done well. In fact, as a recent architecture grad turned structural engineer wantabe, I soon learned my scores were so poor my admission was in doubt. He asked if this was what I really wanted to do. Not knowing if it were, I said yes. He then asked if I was willing to commit the extra time and effort. Unaware of just how big that commitment would be, I said yes. He asked if, given the opportunity, I promised to do my best in graduate school. Without knowing if my best would be good enough, I said yes. Only then did he offer to take a chance and admit me to the graduate program in Structural Engineering at Iowa State University.

For his willingness to take that chance, I would like to acknowledge and thank Professor Lowell Greimann. His confidence, trust, guidance, and support helped me successfully complete a Master's program, pursue a career in structural engineering, and now earn a Ph.D. in Structural Engineering at Iowa State University, a dream of mine since 1977.

I would like to acknowledge Professor Partha Sarkar for providing the guidance, support, and requisite prodding to thoroughly explore the experimental portion of my research and for scheduling time for my project in the Bill James Wind Tunnel. I would especially like to thank him for freely giving of his time, knowledge and wisdom in the fields of wind engineering, vibrations and dynamics, and experimental methods.

I would like to thank my friend and rocket scientist, Christopher White, Ph.D. His enthusiasm and extraordinary level of understanding rekindled my interest in the subject of dynamics and kept me energized throughout this endeavor. The breadth and depth of his knowledge of dynamics has been, and continues to be, an incentive and an inspiration to learn more.

I would like to thank my former co-workers, Elizabeth Webster, Ph.D., Dennis McCann, Ph.D., and especially Steven Smith, Ph.D. for quietly enduring the cynical old guy and for freely sharing their knowledge at the white board. I was very fortunate to have had the opportunity to work with, and learn from, these bright young persons, as their academic achievements were a source of inspiration.

I would like to thank Ms. Josephine O'Brien and Mr. Paul Kreski for helping me with the production logistics and graphics. Their assistance was invaluable and timely when both had no time to spare.

A special thanks and acknowledgement is extended to Mr. Peter Nussbaum, P.E., for his much-appreciated editorial review and constructive critique. He gave up precious bicycle-riding time to read, what had to have been, a very boring paper. However, he was kind enough to offer to perform this valuable task, so I took him up on his offer. Herr Nussbaum, du hast es dir selbst zuzuschreiben.

Finally, I would like to thank my wife, Linda, and son, Michael. They are the ones who put up with my books and papers strewn about the house and the time I spent on schoolwork and not with them. They are the ones who have supported and encouraged me through it all. They are the ones who sacrificed so that I could work on my research. I love you both.

CHAPTER 1

INTRODUCTION

1.1. Background

Large advertising signs are a common sight at the intersections of most major U.S. highways. The signs are typically supported by tall, steel pipe structures that generally consist of two or three sections of pipe. The sections of pipe decrease in diameter from bottom to top and are joined by welded connections to facilitate field erection and low maintenance. These monopole structures typically support an illuminated sign constructed of translucent plastic and sheet metal with an internal steel frame. The height of these signs sometimes exceeds 100 *feet*. .

During the Fall of 1990, three such advertising signs failed within a five-week period, all three signs located in the upper Midwest (Figure 1.1). The three signs had been in service for less than 6 months. All were located along major interstate highways in rural locations surrounded by flat, open terrain. Wind histories for the three sites were obtained from recording stations at nearby airports. In each case, the peak wind velocity recorded during the life of the structure was less than half of the design wind velocity.

Metallurgical examination of the fracture surfaces indicated that the three collapses resulted from a fatigue initiated crack that resulted in the fracture of the steel pipe at the toe of a transverse fillet weld between two pipe sections (Figure 1.2). In each of the three cases, fatigue cracks formed on opposite sides of the pipe. The locations of crack initiation coincided with the wide faces of the sign (Figure

1.3). Over time, the two cracks propagated around the circumference of the pipe until approximately 90% of the pipe cross-section had fractured. Final collapse of each structure occurred when the two remaining portions of the pipe section suffered a ductile failure during moderate wind loading, much less than the design wind load.

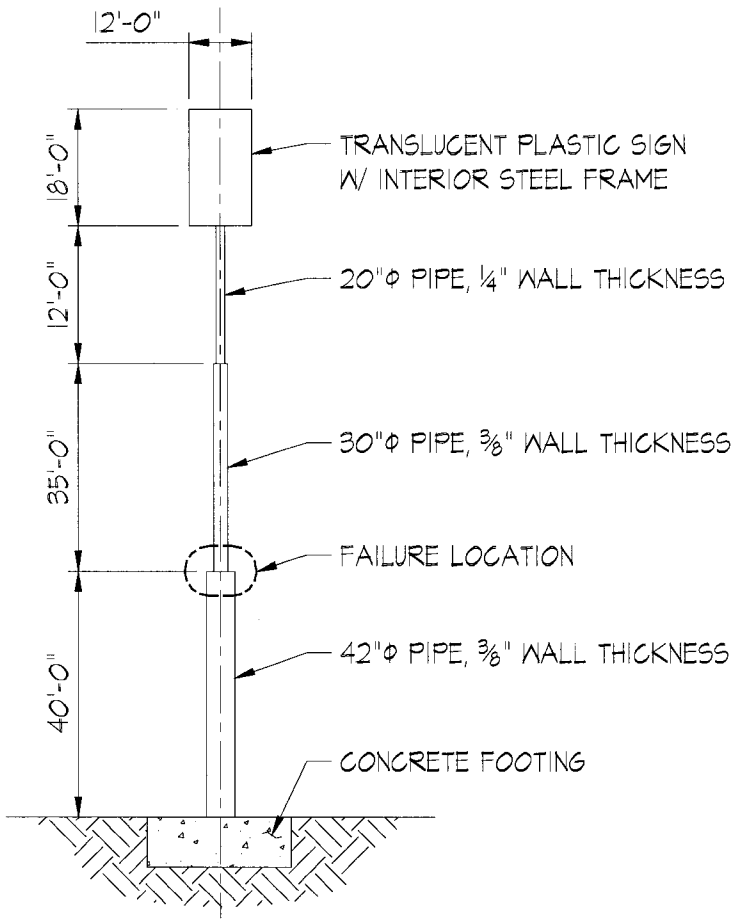

Figure 1.1. Advertising sign elevation.

Based on sign geometry, wind records, and the observed mode of structural failure, the investigation of the collapse determined the failure resulted from a high-cycle fatigue fracture that initiated at the welded joint. However, because of the regular appearance of the fracture surfaces, the investigation determined the fatigue failure was not caused by wind buffeting against the wide face of the sign; but, rather by wind-induced vortex shedding from the trailing edges. Based on the location of crack initiation and the direction of propagation, the investigation concluded that vortex shedding occurred with the wind flowing parallel to the wide face of the signs.

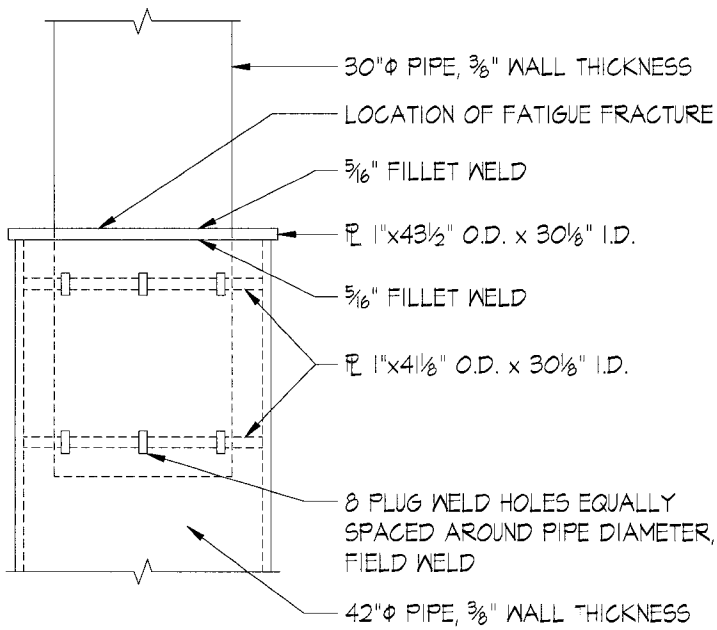

Figure 1.2. Detail of failed connection.

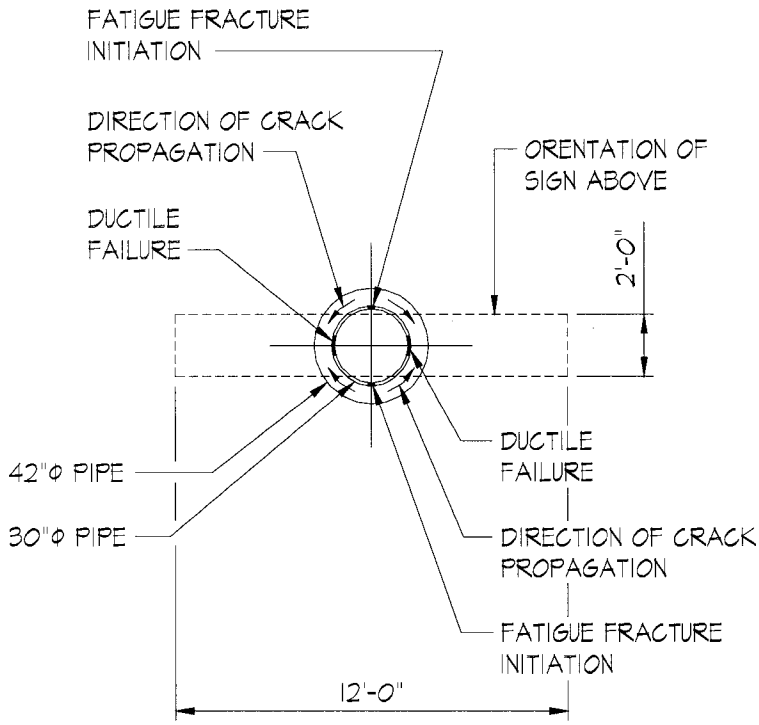

Figure 1.3. Detail of failed connection.

At the time of the investigation, a literature search of pertinent engineering publications was conducted by the investigating engineers. They discovered that vortex-induced vibrations of circular cylinders had been the subject of much research and that a large body of information has been published on the subject. Only limited references were found regarding the study of stationary rectangular cylinders subjected to vortex-induced vibrations. However, very little information was found regarding vortex-induced vibration of elastically supported rectangular cylinders.

As evidenced by the failure of the advertising signs, civil engineering structures are becoming more susceptible to wind-induced vibrations, and possibly failure, as the structures become taller, lighter and more flexible. This is due, in part, to the availability of stronger but lighter materials, advanced computer-based analysis techniques, and more efficient designs. However, this is also due to adverse aerodynamic effects, such as vortex shedding, flutter and galloping, which result in loads not normally considered during the design process.

The engineers discovered during the failed sign investigations that very little published literature pertaining to the vortex-induced vibration of elastically supported rectangular cylinders is available to guide an engineer during the design of such structures. Therefore, the motivation for this research project was to advance the level of understanding of the subject through the study of the vortex-induced dynamic response of elastically supported rectangular cylinders of various aspect ratios. In particular, the end result of this research is to determine and report dynamic parameters such as the Strouhal numbers, maximum amplitude of vibrations, and range of velocities when vibrations, transverse to the air flow, occur.

1.2. Objective

The objective of this research is to study the dynamic behavior of elastically supported rectangular cylinders suspended in laminar airflow and constrained to only cross-flow response, experimentally determine the aerodynamic parameters of the cylinders, and report the findings, conclusions and opinions resulting from the research.

1.3. Approach

To meet the research objectives, rectangular cylinders with eight aspect ratios, the ratio of along-flow dimension to across-flow dimension, were tested. For each of the eight aspect ratios, five specimen of different mass were tested. Each specimen of rectangular cylinder was positioned with an angle of attack of zero degrees. Plates were attached to both ends of each specimen to maintain a two-dimensional flow field and minimize three-dimensional flow effects at the ends. Finally, the rectangular cylinders were constrained to allow only cross-flow motion in the vertical direction; torsion and along-flow degrees of freedom were not considered.

Results of primary importance are the Strouhal number of elastically supported rectangular cylinders, their amplitude of vibration, the critical range of wind velocities that produce vibrations, and the effect of the mass-damping parameter on the amplitude of vibration.

The vibration amplitude and mass-damping data are utilized to derive equations that predict the reduced amplitude given the mass-damping parameter, the Scruton number.

1.4. Scope of Work

For the current research project, the following tasks were completed:

1. A search of pertinent technical literature regarding vortex shedding from circular and rectangular cylinders. Of primary interest were publications dealing with the response of elastically supported rectangular cylinders

subject to steady-state fluid flow, including the dynamic response characteristics, maximum vibration amplitude, range of fluid flow velocities that produce lock-in, the effect the system mass and damping have on the vibration amplitude, and the Strouhal number of the elastically supported system.

2. Experiments were designed to study the flow-induced vibration of elastically supported rectangular cylinders. The experiments were conducted in the Bill James Wind Tunnel that is located in the Wind Simulation and Testing (WiST) Laboratory, Department of Aerospace Engineering, Iowa State University. Rectangular cylinders with eight different aspect ratios that varied from two to seven were tested. Each model was tested five times, each time by adding a different amount of mass to the test apparatus. In total, forty specimens were tested. The models were suspended in the wind tunnel on a force-balance apparatus and the natural frequency, structural stiffness, mass, damping, and Scruton number were determined experimentally. The force-balance apparatus was designed to limit the degrees of freedom to only vertical cross-flow motion. Each model was tested in a smooth airflow at zero degree incidence and the time history of vibration response was observed and recorded. During each test, the range of air velocity bracketed the velocity where vortex shedding was predicted by the Strouhal relationship for stationary rectangular cylinders.
3. The vibration response of each model was observed and recorded. From the experimental data, the Strouhal number, the maximum vibration amplitude at

each increment of fan speed, and the critical range of wind velocities that produced vibrations, were determined for each specimen.

4. The results of the experiments, along with a discussion of the results, were reported in written form.

CHAPTER 2

LITERATURE REVIEW: BLUFF BODY AERODYNAMICS

2.1. Introduction

The vortex shedding phenomena, while unexplained until the last 100 years, has been observed for centuries. The ancient Greeks knew the strings on their wind harps, known as Aeolian harps, would elicit tones when subjected to winds of certain speeds (Dowell, et al, 1995; Blevins, 1994). According to rabbinic records, King David hung his Kinnor, a 10-string harp or lyre, over his bed where it sounded the arrival of the midnight breeze (Blevins, 1994). Later, in the fifteenth century, Leonardo da Vinci sketched a row of vortices in the wake of a pile in a stream.

In 1878, a Czechoslovakian scientist, Vincenz Strouhal, produced the first quantitative measurements of Aeolian tones. He used a hand-operated apparatus to rotate various diameter wires stretched between two radial supports. Strouhal established that the frequency of the Aeolian tone was proportional to the ratio of air velocity to wire diameter when the velocity exceeded a certain minimum. He found that the proportional constant, now known as the Strouhal number, varied between 0.156 and 0.205, depending on the diameter of the wire.

Strouhal observed that the amplitude of sound was greatly increased when the Aeolian tone coincided with the natural tone of the wire; that is, at the natural frequency of the wire. He erroneously concluded, however, that the tones were caused by friction generated between the wind and the wire. He also concluded,

again erroneously, that this friction produced wire motion parallel to the flow of the wind.

At about the same time, Lord Rayleigh established that a violin string stretched across a chimney and immersed in the upward flow of the draft vibrated primarily in a cross-flow direction. He also discovered that the Strouhal number for circular cylinders is a function of Reynolds number.

Later, Bénard, in 1908, and von Kármán, in 1912, independently observed the staggered vortex street and established that the periodicity in the wake was associated with the vortex formation. This led to the discovery by Rayleigh in 1915 that the across-flow vibrations of circular objects were caused by the periodic vortex shedding (Blevins, 1994).

Finally, von Kármán established the stability of the staggered vortex street with his closed-form expression for the velocity potential (Blevins, 1994). Because of his work, the vortices shed from the trailing edge of bluff bodies are known as von Kármán vortices.

Since that time, vortex-induced vibration of bluff bodies has been the subject of a great deal of research. For the most part, the focus of this research topic has been the vortex-induced vibration of circular cylinders. This is due, in large part, to three issues: (1) The simple geometric shape easily lends itself to nondimensional analysis; (2) Circular cylinders are only susceptible to cross-flow response; that is, these cylinders are not susceptible to galloping or flutter; and (3) The dependency of the wake vortex characteristics on the upstream fluid velocity. At the same time, the subject of vortex-induced vibration of rectangular cylinders has not been researched

nearly as much. This may be due to the response characteristics that differ depending on the aspect ratio of the cylinder; that is, the ratio of the along-flow to cross-flow dimensions. In addition, rectangular cylinders may be susceptible to more than one mode of flow-excited motion depending on the aspect ratio, the number of degrees of freedom available to the body, and the characteristics of the oncoming flow.

Therefore, the subject of vortex-induced vibration of circular cylinders will be reviewed here because that body of work has served as the foundation of the current research of rectangular cylinders. Thus, the balance of this chapter includes information regarding vortex-induced vibration of bluff bodies in general and particularly circular cylinders and rectangular cylinders.

2.2. Vortex Induced Vibration

2.2.1. Bluff bodies defined. Simply put, a bluff body is the antithesis of an aerodynamic body. Aerodynamic bodies are typically streamlined in design; where the design goal is to reduce flow separations and reduce drag. Bluff bodies, which include most civil engineering structures, are designed to meet non-aerodynamic objectives. Typically, these structures are not streamlined in design and flow-induced loads are usually of secondary importance. Since civil engineering structures are generally subjected to natural wind within the lower planetary boundary layer, their aerodynamic response characteristics are limited to low-speed, incompressible flow phenomena.

In general, when a bluff body is placed in a smooth fluid flow, the flow will separate from the body surface at a point where the flow reversal occurs. An unstable shear layer forms along the side of the body and time dependent lift and drag forces are produced. The separated flow initiates a fluid-structure interaction phenomenon that controls the characteristics of the wake. When the body is elastically supported, the fluid-structure interaction initiates flow-induced motion. If the flow velocity is within or beyond a certain range, the motion could result in aeroelastic instability such as vortex-induced vibration, galloping or flutter.

2.2.2. Characteristics of bluff body flow. As a volume of fluid approaches the leading edge of a bluff body, the fluid pressure increases from the free stream pressure and approaches the stagnation pressure. The pressure increase causes the fluid to decelerate and forces the flow around the body as a boundary layer forms along the surface of the body (Blevins, 1994).

Within the boundary layer, viscous effects retard the fluid velocity. A no-slip condition exists at the interface of the fluid and body surface where the fluid velocity is zero (Anderson, 2001). Away from this interface, the velocity increases with distance from the surface until, at the edge of the boundary layer, the velocity equals the free stream velocity. The boundary layer thickness is typically very small relative to the body dimensions. Thus, the velocity gradient and the resulting fluid shear stress within the boundary layer are usually very large.

The flow accelerates after the fluid passes the leading edge, resulting in a favorable pressure gradient in the boundary layer (Figure 2.1). A laminar boundary layer develops under the favorable pressure gradient; until, at a sufficient distance

from the stagnation point, the boundary layer becomes turbulent (Blevins, 1992). As the viscous flow develops across the boundary layer, an adverse pressure gradient causes the flow to decelerate until the velocity is reversed near the body surface (Anderson, 2001).

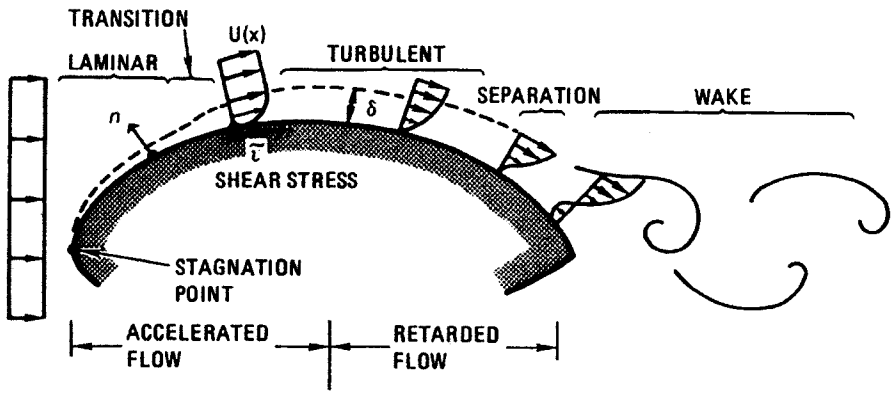

Figure 2.1. Flow around a bluff body (Blevins, 1992).

At the point where the flow reverses, the turbulent boundary layer separates from the surface to form a free shear layer. Because of the reversed flow, the fluid rolls over itself and form vortices in the shear layer that travel to the rear of the body at a velocity less than the free stream velocity. At the rear of the body, the shear layers from each side of the body interact and alternating vortices are formed in the near wake. The vortices are fed by fluid and additional vorticity from their respective shear layers until they are strong enough to draw the opposing shear layer across the near wake.

Eventually, the growing vortex is cut off from the adjacent shear layer by entrainment from the counter-rotating vortex developing on the opposite side of the body (Naudascher and Rockwell, 1994). With the fluid supply no longer available, the vortex is shed and travels into the wake at a velocity that is less than the free-stream velocity. The sequence is repeated on the opposite side of the body and the alternating vortices typically form the classic von Kármán vortex street.

The formation and shedding of these vortex pairs produces alternating pressures on each side of the body (Dowell, et al, 1995). The pressures, and resultant forces, act normal to the body surface with a frequency equal to that of the vortex shedding from one side of the cylinder. The alternating forces are coupled to the wake structure through a complex fluid-structure interaction. This feedback control organizes the wake structure and results in higher lateral body forces. If the body is elastically supported, cross-flow vibrations commence at the vortex shedding frequency defined by vortices from both sides of the cylinder.

The vortex formation described here assumes two-dimensional flow. However, stationary bodies that are long relative to their cross-flow dimension do not shed perfect two-dimensional vortices. Not all vortices form and produce forces that are in phase with each other along the length of the body. Consequently, there is limited correlation of vortex-induced load acting on the body and the net exciting force is smaller per unit length than the force resulting from the perfect two-dimensional vortex shedding sequence (King, 1977). However, significant increases of the correlation length and exciting force occur with increasing amplitude of cylinder vibration.

For any unique bluff body, the flow pattern along its length is unique to that body and is dependent, in part, on body shape, after-body length, body motion, fluid viscosity, flow velocity, and flow turbulence. Despite the differences in local flow patterns; however, the vortex street that forms in the trailing wake organizes into a recognizable structure that is similar for most bluff bodies. In fact, within certain flow velocity ranges, the von Kármán vortex street can be seen to be deterministic in character (Blevins, 1994).

In the case of a rectangular cylinder with sharp leading and trailing edges, the flow is characterized by a separation of the boundary layer at the leading edge. The separated shear layers may reattach to the after-body surface depending, primarily, on the flow velocity and the length of the after-body. The shear layers that flow toward the rear of the body are not fully stabilized and vortices form within these layers. The vortices subsequently roll to the rear of the body where they are shed from the trailing edge (Holmes, 2001). Once the vortices are shed they coalesce into the distinguishable structure of the von Kármán vortex street.

2.2.3. Vortex-induced vibrations.

Strouhal number. Within a certain range of flow velocities, a stationary bluff body sheds alternating vortices into the trailing wake at regular frequencies according to the nondimensional Strouhal relation,

$$St = \frac{f_s D}{U} \quad \text{..... (Equation 2.1)}$$

where St = the Strouhal number,

f_s = the vortex-shedding, or Strouhal, frequency,

D = a representative cross-flow body dimension, and,

U = the free stream flow velocity.

The reduced velocity, V_r, is equal to the inverse of the Strouhal number with the natural frequency of the body, f_n, substituted for the Strouhal frequency, f_s,

$$V_r = \frac{U}{f_n D} \quad \text{(Equation 2.2)}$$

where f_n = the natural frequency of the body.

Reynolds number. For bluff bodies with square or nearly square corners, the boundary layer will separate from the body at the leading edge under most fluid flow velocities. For these types of bluff bodies, the Strouhal number is predominately dependent only on body geometry. If the bluff body has rounded corners and edges, the Strouhal number depends on body geometry and the Reynolds number of the fluid flow.

The Reynolds number is defined as the ratio of inertial forces to viscous forces. When the ratio of these two forces is large, inertial forces control the fluid force balance; when the ratio is small, the viscous forces control. Therefore, the ratio is an index of the type of flow characteristics or phenomena that may be expected to occur. The Reynolds number, Re, is expressed as a nondimensional parameter,

$$Re = \frac{\rho UD}{\mu} = \frac{UD}{\nu} \quad \text{(Equation 2.3)}$$

where ρ = the fluid density,

μ = the coefficient of fluid viscosity,

D = a representative cross-flow body dimension,

U = the upstream uniform flow velocity, and

v = the coefficient of kinematic fluid viscosity.

Concurrent with the vortices shedding from alternating sides of the body, oscillating fluid pressures are generated on the body. If the body is elastically supported, the alternating pressure and the fluid-structure interaction result in, predominately, cross-flow vibrations. The vortex shedding may also excite along-flow motions as well as torsion, galloping and flutter, depending on the degrees of freedom available to the body (Dowell, et al, 1995), the shape of the body, the Reynolds number associated with the flow, and the ratio of the Strouhal frequency to the natural body frequency (Naudascher and Rockwell, 1994).

If the Strouhal frequency is sufficiently different, either smaller or greater, than the natural body frequency, there is little interaction between the near-wake dynamics and structural motion (Goswami, et al, 1993). The oscillating fluid pressures only weakly excite the bluff body and the resulting vibration amplitudes are quite small. In this state, the frequency of the shed vortices agrees with the Strouhal relationship; and the structural response contains two distinct frequencies, the Strouhal frequency, f_s, and the natural body frequency, f_n.

Lock-in. For a circular cylinder, the amplitude of the body motion increases significantly when the Strouhal frequency nearly equals the natural body frequency. A marked increase in the feedback control from the near-wake to the body coincides with the increase in vibration amplitude (Naudascher and Rockwell, 1994). When the ratio of the two frequencies, f_s/f_n, is nearly one, the vortex-shedding phenomenon is controlled by the body motion at the natural frequency of the body. This control

occurs even when a small change in flow velocity moves the Strouhal frequency away from the body frequency (Simiu and Scanlan, 1996).

The control of the vortex shedding by the bluff body motion is known as lock-in. During lock-in, body response resembles that of a mechanical system at resonance. However, the oscillation amplitude is self-limiting and usually less than one-half the cross-flow body dimension. Self-limiting behavior is present regardless of the level of structural damping. In this respect, vortex-induced vibrations are distinctly dissimilar to unbounded instabilities such as galloping and flutter. According to Dowell, et al (1995), the self-limiting oscillation phenomenon results from amplitude-dependent fluid damping.

The effect of lock-in upon the vortex shedding frequency is represented in Figure 2.2. In the lock-in region, the vortex-shedding frequency is constant and nearly equal to the natural frequency of the body, rather than a linear function of the wind velocity as suggested by the Strouhal relation. This phenomenon was first reported by Feng in 1968 (Blevins, 1994).

Flow characteristics. During lock-in, vortices are shed when the vibration is near its maximum displacement. However, as the shedding frequency passes through the natural body frequency, there is a 180-degree phase shift between shedding and cylinder motion. For vibration frequencies below the shedding frequency, the vortex is shed from the side opposite the side experiencing maximum displacement. Conversely, for vibration frequencies above the shedding frequency, the vortex is shed from the same side as the maximum displacement (Zdravkovich, 1982). The phase shift contributes to a hysteresis effect whereby the range of lock-

in depends to a degree on whether the shedding frequency is being approached from above or below.

Vortex shedding is strongly affected by three-dimensional end effects, where the fluid flows around the ends of the body rather than across the body. Vortices, with axes parallel to the flow, form at the free end of a body (King, 1977). These secondary vortices disrupt the shedding of von Kármán vortices and weaken the cross-flow excitation. King (1977) reported that, for circular cylinders, a length to diameter ratio of approximately 45 must be achieved before end effects become negligible and that cylinders of finite length were excited at lower flow velocities than those of infinite length; that is, with end plates.

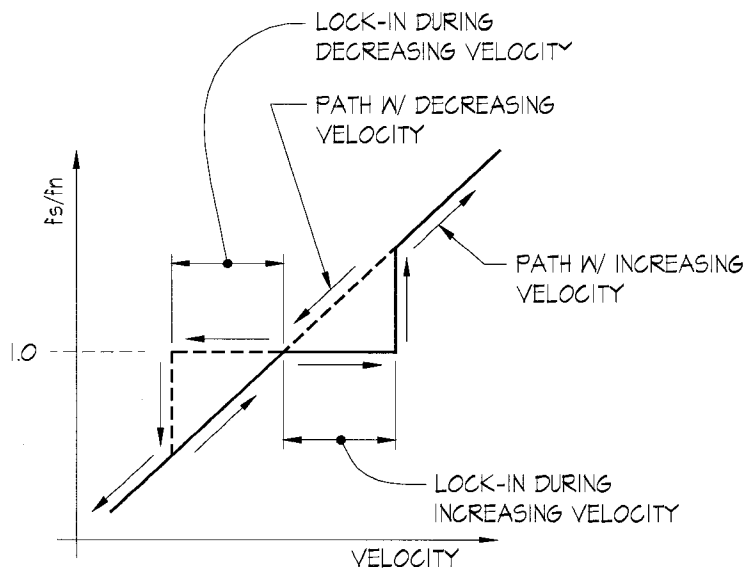

Figure 2.2. Lock-in region.

2.3. Circular Cylinders

2.3.1. Stationary circular cylinders. For a stationary circular cylinder, the aerodynamic behavior of the wake, including the flow characteristics, Strouhal number, and correlation of vortex shedding along the length, are sensitive to a large number of influences; primarily Reynolds number, surface roughness, and the turbulence scale and intensity.

Flow characteristics. At very low Reynolds numbers, $Re < 5$, the fluid flow follows the cylinder contours without separation (Figure 2.3). In the range $5 < Re < 45$, the flow separates from the rear of the cylinder and forms a symmetric pair of vortices in the near wake. The along-flow length of the vortices increases linearly with Reynolds number and reaches a length of approximately three cylinder diameters at $Re \approx 45$ (Blevins, 1994). In the range, $150 < Re < 300$, the wake becomes unstable and transitions from laminar to turbulent. Alternating vortices break away from the body into the near wake. The vortices trail down stream and form a periodic wake of alternating vortices.

In the *subcritical range*, $300 < Re < 1.5\text{x}10^5$, the vortex shedding is strong and periodic. The laminar boundary layer separates from the body surface at about 80 degrees aft of the nose of the cylinder and transitions into a turbulent separated layer where vortices form. The vortices trail into the near wake and form the von Kármán vortex street.

In the *transitional range*, $1.5\text{x}10^5 < Re < 3.5\text{x}10^6$, the laminar boundary layer separates from the body at about 80 to 100 degrees aft of the nose. Separation bubbles randomly form; and, when they do, the separated layer reattaches. Because

of the unstable boundary layer, a second, turbulent separation occurs at about 140 degrees aft of the nose. The irregular formation of the laminar separation bubbles, and subsequent three-dimensional effects, disrupts the regular shedding process and broadens the spectrum of shedding frequencies (Basu, 1985).

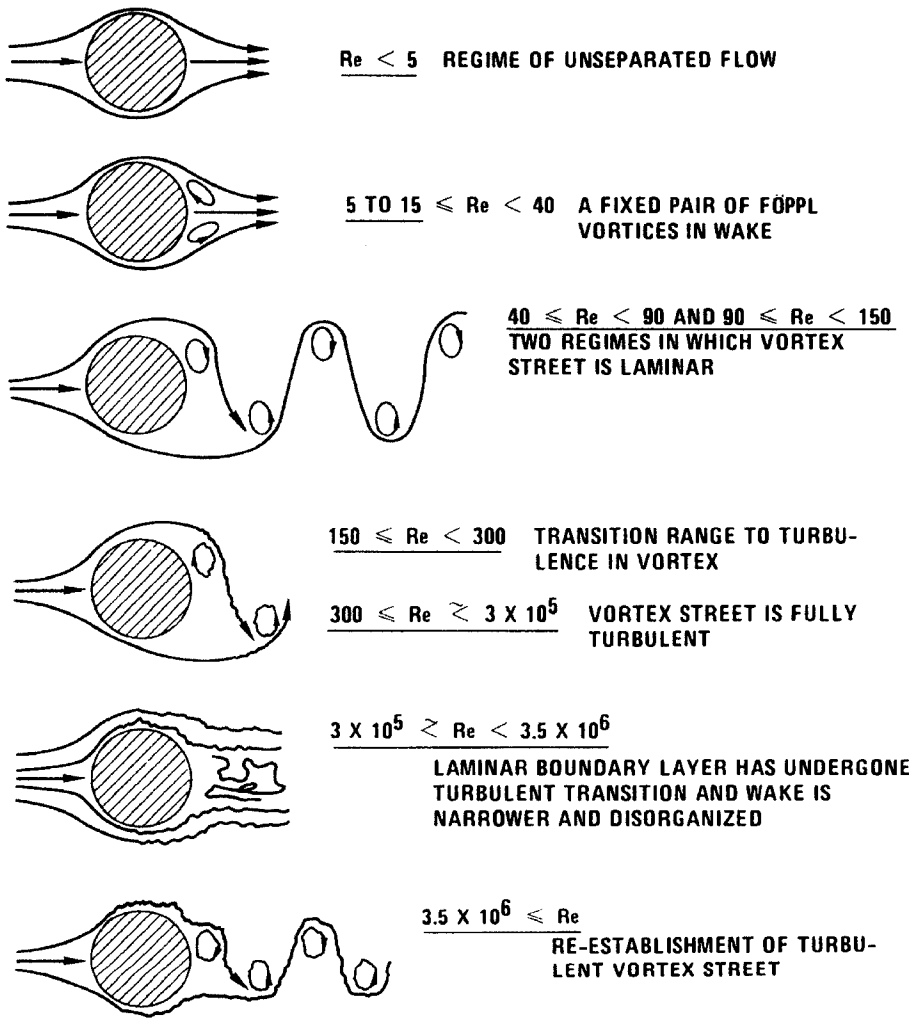

Figure 2.3. Vortex shedding regimes (Blevins, 1992).

In the *supercritical range*, $Re > 3.5x10^6$, regular vortex shedding is re-established with a turbulent boundary layer. The separation bubbles of the *transitional range* no longer form and the turbulent boundary layer separation occurs at 100 degrees aft of the nose of the cylinder (Basu, 1985).

Strouhal number. The Strouhal number of a stationary circular cylinder is a function of Reynolds number and, to a lesser extent, surface roughness and free stream turbulence (Figure 2.4). Throughout the *subcritical range* where the vortex shedding is strongest, $300 < Re < 1.5x10^5$, the Strouhal number varies only slightly and is approximately $St \approx 0.21$. At the upper end of the *subcritical range*, near the critical Reynolds number of $Re \approx 2.0x10^5$, an abrupt shift of the separation point and a sudden decrease in the drag coefficient occur (Liu, 1991). Beyond this point and into the *transitional range*, the flow around smooth cylinders results in the irregular

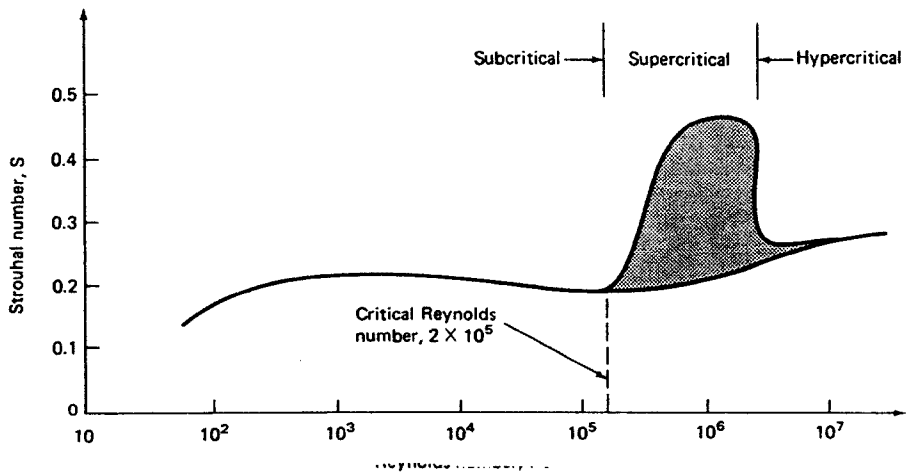

Figure 2.4. Strouhal number for circular cylinder (Liu, 1991).

formation of separation bubbles that generate a chaotic, disorganized, high-frequency wake and Strouhal numbers as high as $St \approx 0.46$ (Bearman, 1969). In this same range, however, rough surface cylinders produce organized, periodic wakes with Strouhal numbers of approximately $St \approx 0.25$. Note that, in the *transitional range*, elastically supported circular cylinders produce vortex shedding at $St \approx 0.2$ rather than the higher Strouhal number exhibited by stationary cylinders (Blevins, 1994). For Reynolds number greater than $Re \approx 3.5$ to 4×10^6; that is, in the *supercritical range*, the wake behind stationary cylinders becomes more regular and periodic and the vortex shedding occurs at approximately $St \approx 0.2$.

Three-dimensional effects. The three-dimensional effects of vortex shedding can be characterized by a span-wise correlation length. Typical values for stationary cylinders range from 100 or more diameters for laminar vortex streets at $Re \approx 60$, 20 diameters at $Re \approx 100$, and 5 diameters for $Re \approx 10 \times 10^3$ (Blevins, 1994). Typical correlation lengths for stationary cylinders within the *subcritical range*, $300 < Re < 1 \times 10^5$, range from 3 cylinders diameters at $Re \approx 10^4$ to about 6 diameters at $Re \approx 10^5$. Beyond $Re \approx 10^5$, the correlation lengths drop to less than one diameter (Basu, 1986).

2.3.2. Elastically supported circular cylinders. Similar to a stationary circular cylinder, the aerodynamic characteristics of the wake trailing an elastically supported circular cylinder are dependent, primarily, on Reynolds number. When the shedding frequency is sufficiently far from the natural frequency of the cylinder, there is very little fluid-structure interaction. Consequently, the wake behaves as if the cylinder were stationary. However, as the shedding frequency approaches the

natural body frequency, the elastically supported cylinder is free to respond to the alternating pressures produced by the shedding vortices.

Lock-in. Cross-flow cylinder vibration near the shedding frequency organizes the wake through an increase in feedback control. Consequentially, the strength of the vortices and alternating body pressures are significantly larger. The larger pressures and resultant forces, in turn, cause the amplitude of the vibrations to increase until, when the two frequencies are equal, the shedding frequency locks in to the natural frequency of the body.

For a circular cylinder of adequate length, lock-in begins when the ratio of shedding frequency, f_s, to natural body frequency, f_n, is nearly 1.0 and ends when the ratio is approximately 1.40 (Sarpkaya, 1979). The maximum amplitude occurs near the middle of this range. For tests conducted in air lock-in was found to occur at a reduced velocity in the range $4.75 < V_r < 8$ while the maximum amplitudes occur in the range $5.5 < V_r < 6.5$. However, the range of reduced velocity over which lock-in occurs increases with oscillation amplitude.

At the end of the lock-in range, the vortex-shedding frequency suddenly jumps to the frequency governed by the Strouhal equation, but the cylinder continues to oscillate at its natural frequency, albeit at a greatly reduced amplitude. The lock-in and jump phenomena occur whether the shedding frequency approaches the natural body frequency from below or above.

In free-vibration tests, the vibration amplitudes are self-limiting and rarely exceed one-half diameter. During forced-vibration tests, the pattern of regular vortices begins to break up if the amplitude is increased beyond one-half diameter.

This breakup implies that the fluid forces imposed on the cylinder by the vortex shedding are a function of the cylinder amplitude and may be self-limiting at large vibration amplitudes (Blevins, 1994). At an amplitude of one diameter, three vortices are formed per cycle of vibration instead of the stable pattern of two per cycle that occur naturally at lower amplitudes.

While the largest amplitudes of cross-flow vibrations are generated during lock-in, excitation to a lesser degree can also involve superharmonic and subharmonic resonance. This occurs when the ratio of the two frequencies, f_s/f_n, approaches 3 and 1/3, respectively (Naudascher and Rockwell, 1994). The higher and lower modes occurs at frequency ratios of 3 and 1/3, rather than 2 and 1/2, due to compatibility between the vortex- and movement-induced forces on the cylinder related to the velocity of the fluid flow past the side of the body.

The correlation of vortex shedding along the cylinder length increases rapidly with amplitude (Sarpkaya, 1979). This increase has been found to be much larger in smooth flow than in turbulent flow and is especially true if the cylinder oscillates with an amplitude greater than the threshold amplitude, estimated to be approximately 10% of the cylinder diameter (King, 1977). In smooth flow the correlation length is estimated to increase from about 3.5 diameters to 40 diameters for $Re \approx 1.9\text{x}10^4$ with the ratio of amplitude to body diameter in the range $0.05 < A/D < 0.1$.

Strouhal number. The Strouhal number for elastically supported circular cylinders remains approximately ≈ 0.21 over the tested Reynolds number range, $300 \leq Re \leq 5\text{x}10^7$ (Liu, 1991). The sudden jump in the Strouhal number that occurs for

stationary circular cylinders when the critical Reynolds number is Re $\approx 2x10^5$ does not occur for elastically supported circular cylinders. Blevins (1994) speculates that the cylinder motion organizes the wake and disrupts the disorganized shedding.

Damping and the Scruton number. King (1977) showed that by increasing the structural damping, lock-in and the associated large amplitude vibrations could be avoided. Conversely, he showed that for extremely small ratios of structural damping the range velocity that produces lock-in increases significantly with increased amplitude. Naudascher and Rockwell (1994) reported that, with an increase in damping ratio, the maximum amplitude and width of lock-in range are severely reduced.

According to Khalak and Williamson (1999), the development of the mass-damping parameter is as follows. The equation of motion of the vortex-induced vibration of a circular cylinder is generally taken to be,

$$m\ddot{y} + c\dot{y} + ky = F(t) \quad \text{.....(Equation 2.4)}$$

where m =the total oscillating structural mass,

c = the structural damping,

k = the spring constant, and

$F(t)$ = the fluid force in the cross-flow direction.

At lock-in, a good first approximation of the force and response is given by,

$$F(t) = F_0 \sin(\omega_s t + \phi), \quad \text{.....(Equation 2.5)}$$

$$y(t) = y_0 \sin(\omega_s t) \quad \text{.....(Equation 2.6)}$$

where $\omega_s = 2\pi f_s = 2\pi f$,

y_0 = the self-limiting amplitude,

f = the actual body oscillation frequency $\approx f_n$, and.

φ = the phase angle.

The response amplitude and frequency may be derived in a straightforward manner from Equation 2.4 through 2.6. After manipulation, the response amplitude and frequency can be formulated using nondimensional parameters (Khalak and Williamson, 1999),

$$A_r = \frac{1}{4\pi^3}\frac{C_Y \sin\phi}{(m^*+C_A)\zeta}\left(\frac{V_r}{f^*}\right)^2 f^* \quad \text{..... (Equation 2.7)}$$

$$f^* = \sqrt{\frac{m^*+C_A}{m^*+C_{EA}}} \quad \text{..... (Equation 2.8)}$$

where m^* = the mass ratio = $\frac{m}{\rho(\pi D^2(l/4))}$,

ζ = the critical damping ratio = $\frac{c}{2\sqrt{km}}$,

V_r = the reduced velocity ratio = $\frac{U}{f_n D}$,

A_r = the reduced amplitude ratio = $\frac{y_0}{D}$,

f^* = the frequency ratio = $\frac{f}{f_n}$,

C_Y = the transverse force coefficient = $2\frac{F_y(t)}{\rho U^2 Dl}$,

C_A = the added mass coefficient $\approx$1.0, and

C_E = the potential added mass coefficient = $\frac{1}{2\pi^3}\frac{C_Y \cos\phi}{A_r}\left(\frac{V_r}{f^*}\right)^2$.

For large mass ratios as expected in air; that is, $m^* >> 1$, the actual cylinder oscillation frequency, f, at lock-in will be very close to the vortex-shedding frequency of the static cylinder, f_s, and also very close to the system natural frequency, f_n; that is, $f \approx f_s \approx f_n$, and $f^* \approx 1.0$. This can be seen in Equation 2.8 with very large m^*. Then at lock-in, the reduced velocity ratio, V_r, is equal to $U/fD \approx U/f_sD = 1/St$; the inverse of the Strouhal number for a stationary cylinder. Given that $St \approx 0.20$, the expected cylinder response at lock-in over a wide range of Reynolds numbers will occur at a reduced velocity of $V_r \approx 5$. Based on this, the assumption is often made that both the reduced velocity, V_r, and the frequency ratio, f^*, are constants at lock-in, giving,

$$A_{r,\max} \propto \frac{C_Y \sin\phi}{(m^* + C_A)\zeta} \quad \text{..... (Equation 2.9)}$$

Finally, under these assumptions, $A_{r,\,max}$ is a function (inversely proportional) of the product of the mass ratio and the damping ratio; that is, $(m^*)(\zeta)$.

According to Khalak and Williamson (1999), Scruton used such a parameter to describe his experiments with elastically supported circular cylinders. The parameter is commonly referred to as the Scruton number, Sc,

$$Sc = \frac{\pi}{4}(m^*)(\zeta) = \frac{m_e\zeta}{\rho D^2} \quad \text{..... (Equation 2.10)}$$

where ζ = the structural damping ratio,

m_e = the system mass per unit length,

ρ = the fluid density, and

D = the cross-flow body dimension.

The time varying force, $F(t)$, in Equation 2.4, can be expressed as (Skop and Griffin, 1975),

$$F(t) = \frac{1}{2}\rho U^2 D l C_Y \quad \text{(Equation 2.11)}$$

Substituting this expression into Equation 2.4 and dividing through by m and D gives,

$$\frac{\ddot{y}}{D} + \frac{2\zeta\omega_n}{D}\dot{y} + \frac{\omega_n^2}{D}y = \frac{\rho U^2 l}{2m}C_Y = \mu\omega_s^2 C_Y \quad \text{(Equation 2.12)}$$

where $\mu = \dfrac{\rho D^2 l}{8\pi^2 St^2 m}$, and

$\omega_s = \dfrac{2\pi StU}{D}$, from the Strouhal relation, Equation 2.1.

The first term, μ, is proportional to,

$$\mu \propto \frac{1}{8\pi^2 St^2 Sc} \quad \text{(Equation 2.13)}$$

As reported in Simiu and Scanlan (1996), Griffin, Skop, and Ramberg used this term in an empirical formula they developed to predict the maximum amplitude for a circular cylinder,

$$\frac{y_o}{D} = \frac{1.29}{\left[1 + 0.43\left(8\pi^2 St^2 Sc\right)\right]^{3.35}} \quad \text{(Equation 2.14)}$$

where y_o = the maximum amplitude,

D = the cross-flow body dimension, and

St = the Strouhal number.

This equation is plotted in Figure 2.5, along with experimental results of tests conducted by Goswami, et al (1993) using elastically supported circular cylinders. From Equation 2.14, the maximum self-limiting reduced amplitude, as $Sc \rightarrow 0$, is seen to be 1.29. However, the maximum observed reduced amplitude for a circular cylinder is approximately $A_r \approx 0.5$.

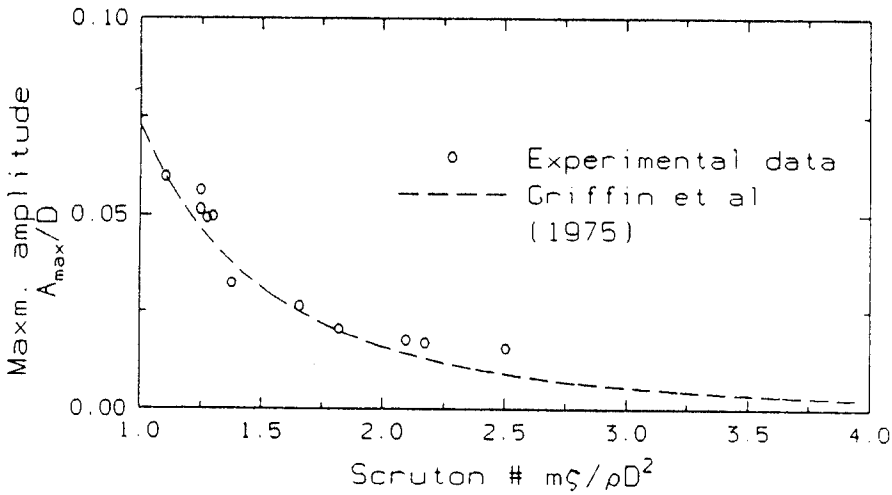

Figure 2.5. Plot of Equation 2.14 (Goswami, et al, 1993).

2.4. Stationary Rectangular Cylinders

2.4.1. Introduction. Because of the presence of the sharp corners, the flow separation points are fixed at the corners of a rectangular cylinder and do not move fore and aft on the body as with circular cylinders. Similar to circular cylinders, however, the flow characteristics round rectangular cylinders change dramatically at specific Reynolds numbers and produce abrupt jumps, and possibly double values, in the Strouhal number for certain aspect ratio.

2.4.2. Flow characteristics. The characteristics of the flow around a stationary rectangular cylinder suspended in a smooth flow are dependent on the Reynolds number and the length of the after-body; that is, the portion of the body behind the leading edges. In general, the flow characteristics include a flow separation at the leading edge, the growth of a separation bubble immediately behind the leading edge, and the formation of the von Kármán vortex street in some form (Laneville and Yong, 1983).

At extremely low Reynolds number, the flow separates at the trailing edges rather than the leading edges where the separated flow immediately reattaches. With an increase in Reynolds number, the boundary layer separates from the body at the leading edges where part of the separated flow is absorbed by a growing separation bubble of fluid. The unabsorbed part of the fluid continues into the shear layer in a proportion controlled by the cylinder after-body length. According to the time of the cycle, the fluid and the vorticity contained in the shear layer feed either the adjacent vortex or the vortex on the opposite body surface while they are forming.

As the adjacent wake vortex is forming, the separation bubble assumes different sizes and can be considered as a buffer; filling itself with fluid and vorticity then releasing them when the vortex is shed (Laneville and Yong, 1983). Depending on the length of the after-body, the bubble releases its fluid and vorticity either into the forming wake vortex that is about to be shed, for $L/D < 3$, or into patches of vorticity along the cylinder side surfaces, for $L/D > 3$. Immediately after the adjacent vortex has been shed, the separation bubble shrinks to its minimum size.

For relatively short after-bodies ($L/D < 2$ to 3), the flow separates at the leading edge and forms a wide von Kármán vortex street in the near wake of the body. This has been termed leading edge vortex shedding. The bubble of fluid forms in the separated flow immediately behind the leading edge; but, the side wall is not long enough to trap the bubble. As a result, the bubble releases its fluid and vorticity directly into the vortex forming in the near wake.

As the vortex is forming in the near wake, it draws fluid from the adjacent separated shear layer as well as from the wake further downstream and from the opposite shear layer. When the bubble releases its fluid, the vortex reaches its final size and is strong enough to draw part of the opposite shear layer across the wake. This entrains the flow from the adjacent shear layer and cuts it off from the forming vortex. The vortex is shed into the wake and develops into the von Kármán street further downstream. Immediately preceding the shedding of the adjacent vortex, the opposite vortex starts to form and the process repeats itself.

For medium length after-bodies (2 to $3 < L/D < 5$ to 7), the increase in after-body length results in flow separation at the leading edge and impingement of the leading edge vortices along the side surfaces of the body. This has been termed impinging leading edge vortex shedding. According to Laneville and Yong (1983), the separation bubble that forms behind the leading edge is trapped and cannot release directly into the wake vortex because of the extended after-body length. As with the shorter body, $L/D < 3$, the separation bubble grows during the periodic cycle until it reaches its maximum size and then releases its fluid and vorticity. However, in this case ($L/D > 3$), the vortices travel along the body side surface. These vortices form

a secondary region of flow that is entrained against the body side surfaces by the external flow. At the rear of the body, the vortices are shed and coalesce into a von Kármán vortex street that is wider than the cross-flow dimension of the body but not as wide as the wake shed from short cylinders.

For longer after-bodies (L/D > 5 to 7), the separated flow from the leading edge reattaches along the side surfaces of the body. However, the velocity of the reattached fluid is only approximately 63% that of the free-stream velocity (Nakamura, et al, 1991). The reattached fluid is stable and forms a laminar flow that is shed from the trailing edge of the body. A narrow von Kármán vortex street, approximately equal in width to the cross-flow dimension of the body, is formed in the wake. This has been termed trailing edge vortex shedding. The velocity of the von Kármán vortex street is approximately 86% of the free-stream velocity (Nakamura, et al, 1991).

For even longer after-bodies (L/D > 8 to 10), it is believed that the reattached, laminar flow along the body side surface becomes turbulent after traveling a critical distance from the leading edge, is shed into the wake, and forms a von Kármán vortex street that is wider than the body cross-flow dimension.

2.4.3. Strouhal number. For stationary rectangular cylinders, the Strouhal number appears to be independent of the Reynolds number when the Reynolds number, defined as $Re = UD/v$, is greater than approximately 1.22×10^3. Above this Reynolds number, the Strouhal number is dependent only on the aspect ratio, L/D. When the Reynolds number is less than 1.22×10^3, the Strouhal number is dependent

on the Reynolds number, the aspect ratio of the cylinder and on subtle changes in the flow pattern around the cylinder.

Rectangular cylinders, $1 \leq L/D \leq 4$. Okajima (1982) tested stationary rectangular cylinders with aspect ratios that varied from $1 \leq L/D \leq 4$, at Reynolds numbers that varied from 200 to $2\text{x}10^4$. He reported discontinuities in the Strouhal numbers that are dependent on the Reynolds number, but that the range of Reynolds number where the discontinuity occurs is dependent on the aspect ratio, L/D, of the rectangular cylinders.

For a square cylinder ($L/D = 1.0$), the Strouhal number was found to vary only slightly from 0.15 to 0.13 for $Re \leq 2\text{x}10^4$. The flow separates from the leading edges at all Reynolds numbers and creates a wide wake where vortices form the von Kármán street with a regular frequency near the Strouhal frequency established for stationary cylinders.

For an aspect ratio of $L/D = 2$, the Strouhal number increased with Reynolds number up to $Re \approx 500$, where it reached a value of $St \approx 0.18$. Between $500 \leq Re \leq 600$, Okajima reported a sharp drop in the Strouhal number to $St \approx 0.07$. Above $Re \approx 600$, the Strouhal number varied only slightly from 0.07 to a maximum of $St \approx 0.09$ when $Re > 5\text{x}10^3$. He attributed the sudden shift in Strouhal number to an abrupt change in the flow pattern along the sides of the cylinder. At $Re < 500$, the flow that has separated at the leading edges reattaches to the sides of the body to be shed in a narrow wake from the trailing edges. At $Re > 500$, the reattachment no longer occurs and the separated flow from the leading edges forms a much wider wake.

The increase of the Reynolds number and the sudden widening of the wake results in an abrupt decrease in the Strouhal number.

For cylinders with an aspect ratio of $L/D = 3$, the Strouhal number is approximately equal to $St \approx 0.16$ at $Re \leq 10^3$. However, when $Re \approx 1.22\text{x}10^3$, Okajima found that the wake alternated between two wave patterns that produced three distinct Strouhal numbers. Mode I, with small amplitude and high frequency, resulted in $St \approx 0.16$. Mode II, with irregular shape and frequency, resolved into two kinds of response with Strouhal numbers of 0.06 and 0.12, respectively. Therefore, three distinct Strouhal numbers occur simultaneously in this region. With an increase in Reynolds number, the Strouhal number of Mode I disappears and the Strouhal number of the lower component of Mode II decays. As the Reynolds number is increased further, the higher component of Mode II produces a Strouhal number that increases from 0.12 and approaches 0.16. Okajima attributes the shift in the Strouhal number at $Re \approx 1.22\text{x}10^3$ to changes in the flow pattern similar to those described for the aspect ratio of 2.

He notes that the shift occurs for an aspect ratio of 3 at $Re \approx 1.22\text{x}10^3$ while the shift occurs for an aspect ratio of 2 at $Re \approx 5\text{x}10^2$; that is, the larger aspect ratio of 3 results in a higher critical value of Reynolds number where the sudden shift in Strouhal number occurs. Thus, for a longer after-body, the flow must be faster for the separated flow from the leading edges to no longer reattach to the sides. The longer after-body of the cylinder tends to prevent the separated flows from expanding and keeps them attached to the side surfaces.

Finally, for a rectangular cylinder with an aspect ratio of $L/D = 4$, the Strouhal number is independent of the Reynolds number. For all ranges of Reynolds number, Okajima found that $St \approx 0.14$. He reported that there is no sudden shift in the Strouhal number for an aspect ratio of four, as the separated flow from the leading edges reattaches to the sides at all Reynolds numbers.

Rectangular cylinders, $1 \leq L/D \leq 25$. Knisely (1990) tested stationary rectangular cylinders with aspect ratios that varied from 0.04 to 1; and, because each cylinder was rotated 90 degrees, the tests also included cylinders with aspect ratios from 1 to 25. The water channel experiments were conducted at Reynolds between 7.2×10^2 and 3.1×10^4. The wind tunnel tests were conducted at Reynolds numbers between 8.8×10^3 and 8.1×10^4. The results of the tests involving cylinders $L/D \geq 1.0$ are plotted in Figure 2.6.

Knisely confirms the data reported by Okajima for the rectangular cylinder with L/D of 1; that is, $St \approx 0.15$. However, he did not find the abrupt jump in Strouhal number for a cylinder with $L/D = 2$ that Okajima observed; as the Reynolds number in the tests conduced by Knisely were not as low as the Reynolds numbers in the tests conducted by Okajima.

For a rectangular cylinder with an aspect ratio $L/D = 2.5$, Knisely reported that the Strouhal number was approximately 0.06. For this aspect ratio, the Reynolds number used in the tests ranged from 7.5×10^3 to 2.2×10^4. If Okajima's conclusion was correct, that a critical Reynolds number exists where the abrupt shift in Strouhal number occurs for aspect ratios less than about 4, then Knisely's tests were conducted at a Reynolds number too large to capture the double Strouhal numbers.

Knisely did report an abrupt jump in Strouhal number between aspect ratios of 2.5 and 3.33. For a cylinder with L/D = 3.33, the Strouhal number was determined to be approximately 0.14. This aspect ratio was tested at Reynolds numbers that ranged from 5.6×10^3 to 2.2×10^4. Once again, if Okajima was correct, then Knisely reported the Strouhal number produced by a Reynolds number that is too low to capture the double Strouhal numbers.

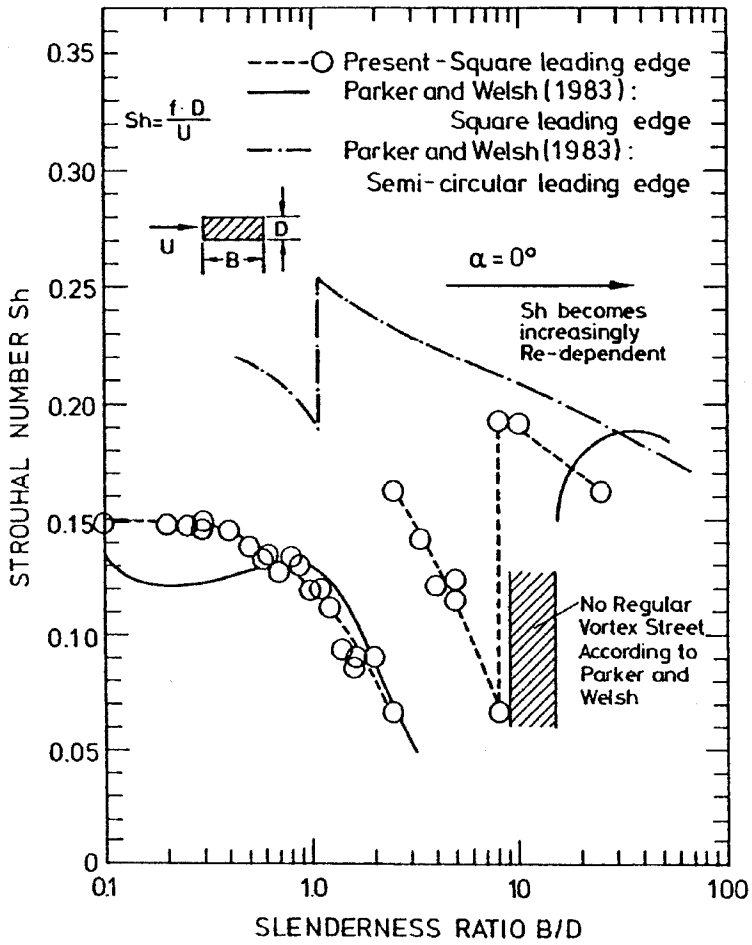

Figure 2.6. Strouhal numbers for rectangular cylinders (Knisely, 1990).

For cylinders with an aspect ratio $L/D = 4.0$, Knisely confirmed the single Strouhal number reported by Okajima, i.e.; St $\approx$ 0.13. For cylinders with aspect ratios between 3.33 to about 8, he found an almost linear decrease in the Strouhal number from approximately 0.17 to 0.07. Finally, for an aspect ratio of 10, Knisely reports a Strouhal number of approximately 0.20, indicating that another abrupt jump must have occurred in the Strouhal number in the range of $8 < L/D < 10$.

Knisely did report an abrupt jump in the Strouhal number when the aspect ratio is $2.5 < L/D < 3.33$ and implies that another jump occurs when the aspect ratio is between $5 < L/D < 10$. Parkinson (1989) confirms the abrupt changes in Strouhal number in the range $2.0 < L/D < 3.0$, and attributes the jump to the reattachment of the shear layers on the after-body sides, with final separation occurring at the downstream corners. Deniz and Staubli (1997) attribute the double Strouhal numbers, occurring at aspect ratios of $L/D \approx 2$ to 3 and $L/D \approx 4$ to 7, to the transition from leading edge vortex shedding to impinging edge vortex shedding and from impinging edge vortex shedding to trailing edge vortex shedding, respectively.

2.4.3. New look at the Strouhal number. Nakamura, et al (1991) reported on tests of stationary rectangular cylinders that varied in aspect ratio from 3 to 16. Their experiments were conducted in a low-speed wind tunnel at Reynolds number ranging from 10^3 to $3x10^3$.

They found at least one dominant frequency in the shedding spectra from the wake of all rectangular cylinders up to an aspect ratio of 15. At $L/D = 16$, the frequency spectrum of the trailing wake was broad banded with no dominant frequency. In general, the value of the dominant frequency gradually decreased with

increasing *L/D* and then jumped to a higher value at a certain value of *L/D*. The decrease and jump in frequency repeated with increasing *L/D* and two dominant frequencies appeared at each jump. However, Nakamura, et al, cautioned that the signal did not contain two dominant frequency components simultaneously. Rather, the signal exhibited only one dominant frequency at a time during a random-length time interval.

They found that the Strouhal number, when based on the length of the after-body, *L*, is nearly constant and equal to 0.6 for *L/D* = 3 to 5. However, they also found that, with an increase in *L/D*, the Strouhal number increases stepwise to values that are approximately equal to integer multiples of 0.6 and that the steps occurred at *L/D* ≈ 6, 9, and 12 (Figure 2.7).

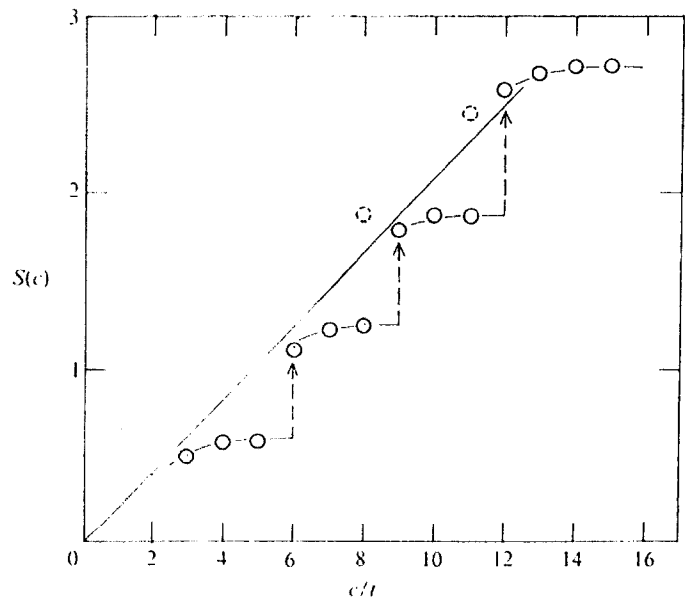

Figure 2.7. Strouhal number based on body length, *L* (Nakamura, et al, 1991).

Based on the results of their research, if defined in terms of the after-body length, L, the Strouhal number relationship becomes,

$$St = \frac{f_s L}{U} = 0.6n \quad \text{..... (Equation 2.15)}$$

where $n = \text{integer}\left(\frac{L}{3}\right)$ for $L/D \geq 3$.

They reasoned that there is a relation between the wavelength of the velocity fluctuation and the length of the plate; that is, the wavelength is just equal (n = 1 and 2) or approximately equal (n = 3 and 4) to fractions of the plate's length. In other words, the integer, n, represents the number of vortices that are formed on the plate's surface.

Thus, it is clear that vortex shedding from flat plates with square leading and trailing edges and aspect ratios up to L/D = 15, is characterized by the instability of the impinging shear layer along the sides of the rectangular cylinder. The impinging shear layer instability initiates at about $L/D \approx 3$ where the wavelength of vortex shedding is just equal to the after-body length. As L/D is increased, the wavelength is locked-on to the plate's length through a nonlinear flow process until a certain limit is reached. At the limit, transition of the mode of vortex shedding from n = 1 to n = 2 occurs. With a further increase in L/D, the same cycle of events repeats.

2.5. Elastically Supported Rectangular Cylinders

2.5.1. Introduction. Vortex-induced vibrations can occur for any elastically supported bluff cylinder where the cross-section includes an appreciable after-body.

Semi-circular bodies, when placed in a flow with their blunt edge facing the flow exhibit vortex-induced vibrations; but, when reversed in the flow with their blunt edge facing down stream, the same bodies exhibit no motion. For vortex-induced excitation to occur, the alternating pressure loading must occur principally on the after-body surface. Therefore, the most important physical parameter of a two-dimensional body subjected to vortex-induced or galloping oscillation is the size and shape of its after-body (Bearman, et al, 1987).

2.5.2. Flow characteristics. Similar to elastically supported circular cylinders, the amplitudes of vortex-induced vibration of elastically supported rectangular cylinders are limited to less than one half the cross-flow dimension and the vibrations occur only in discrete ranges of wind speed (Corless and Parkinson, 1988). Unlike circular cylinders, however, vibrations do not typically occur when the ratio of the vortex shedding, or Strouhal, frequency, f_s, to the natural body frequency, f_n, approaches one. Bluff bodies typically vibrate at a frequency ratio, f_s/f_n, less than one. Furthermore, some aspect ratios exhibit vibration in two ranges of Reynolds number flow.

In the ranges of wind speed that produce vibrations, the frequencies measured in the wake do not contain the expected Strouhal frequency; but rather a single frequency very close to the natural frequency of the body as was found with the circular cylinder. This is representative of the familiar lock-in phenomenon.

As with stationary rectangular cylinders, three distinct classes of vortex formation can be observed when the angle of attack is held to zero: leading-edge

vortex shedding, impinging leading-edge vortices, and trailing-edge vortex shedding (Deniz and Staubli, 1997).

Leading-edge vortex shedding. With short rectangles ($L/D < 2$ to 3), the flow separates from the leading edge and strong vortices shed into the wake forming a von Kármán vortex street. The oscillating wake is several times wider than the cross-flow body dimension and includes the whole section of the body (Nguyen and Naudascher, 1991). Body vibration is mainly excited by von Kármán vortices, and a typical response diagram shows a sharp peak near vortex resonance, $V_r = 1/St$. When V_r increases beyond $1/St$, the response ceases. However, with further increase in V_r, the body will eventually become self-excited and start to gallop.

Impinging leading-edge vortices. With an increase in aspect ratio (2 to 3 $< L/D <$ 4 to 7), the vortices that form in the shear layer behind the leading edge impinge on the side surfaces and establish a feedback-controlled source of excitation of their own. For this range of aspect ratios, the von Kármán vortex excitation is weak due to the narrow, irregular wake. The impinging vortex excitation mechanism becomes particularly enhanced if the body starts to vibrate. Through feedback, the transverse body motion induces stronger leading-edge vortices that, in turn, strengthen the impinging vortex excitation.

Within a certain range of wind velocities, the leading-edge vortices coalesce with the vortices that are formed in the shear layers. Consequently, the combined vortices increase in strength and induce oscillating pressures along the sides of the cylinder that, in turn, amplify and sustain the body motion.

Trailing-edge vortex shedding. With long rectangular profiles ($L/D \geq 4$ to 7), the flow remains attached to the side surfaces and separates from the trailing edges. In contrast to leading edge vortex shedding, the wake and von Kármán vortex street is much narrower. Thus, the Strouhal number is higher, and resonant vibrations start at lower values of free stream velocity, U. The occurrence of oscillations in this group depends not only on the trailing edge geometry but also on the leading-edge geometry. Sharp leading edges may suppress the periodicity of the vortex shedding by introducing large-scale turbulence into the shear layers (Naudascher and Rockwell, 1994). Therefore, rectangular cylinders in this L/D range appear to be less susceptible to vortex-induced vibration than streamlined profiles.

2.5.3. Strouhal number. As discussed below, elastically supported rectangular cylinders with aspect ratios greater than one do not vibrate with appreciable amplitude at the velocity predicted by the Strouhal number based on stationary tests.

Rectangular cylinders, $1 \leq L/D \leq 4$. Washizu, et al (1978) conducted experiments on stationary rectangular cylinders, $1 < L/D < 4$, and reported that two Strouhal numbers were observed for cylinders of $2.0 \leq L/D \leq 2.8$. Subsequently, they conducted experiments on elastically supported rectangular cylinders, $1 < L/D < 4$, with the intent of verifying the existence of lock-in at the Strouhal frequencies produced by the stationary cylinders. Their experiments were conducted in a wind tunnel where the speed of the flow was increased incrementally while all specimen parameters were held constant. Prior to initiating the flow, each model was stopped and held stationary. At each increment of speed, the model was manually given an initial cross-flow displacement and then allowed to vibrate freely in the flow.

The results of the work by Washizu et al are shown in Figures 2.8 and 2.9 for L/D = 2 and L/D= 4, respectively. In these figures, the ordinate is the reduced amplitude, the abscissa is the reduced velocity, and ♦ indicates the assumed lock-in speed; that is, the flow speed where the stationary Strouhal shedding frequency coincides with the natural frequency of the model. The Scruton number is referred to with the symbol, μ_h, in the two figures.

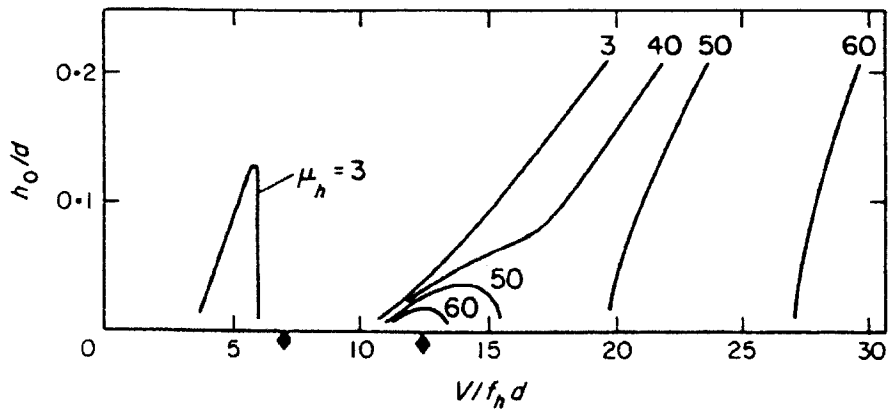

Figure 2.8. Cross-flow vibrations, L/D = 2.0 (Washizu, et al, 1978).

For L/D = 2 (Figure 2.8), they found that two regions of instability existed when the Scruton number was sufficiently small. One is in the vicinity of the lower lock-in speed, while the other commences at a speed near the upper lock-in speed. For the latter, the oscillation with large amplitude persists far beyond the upper lock-in speed. They reported that, as the Scruton number increases, the former diminishes and disappears finally, while the latter splits into two unstable regions. The first region is a small range of instability in the vicinity of the upper lock-in speed. The

second commences at a critical speed that is higher than the upper lock-in speed and is dependent on the magnitude of the Scruton number. They attribute the instability regions in the vicinity of the upper and lower lock-in speeds to vortex-excited oscillations and the instability observed beyond the critical speed to transverse galloping.

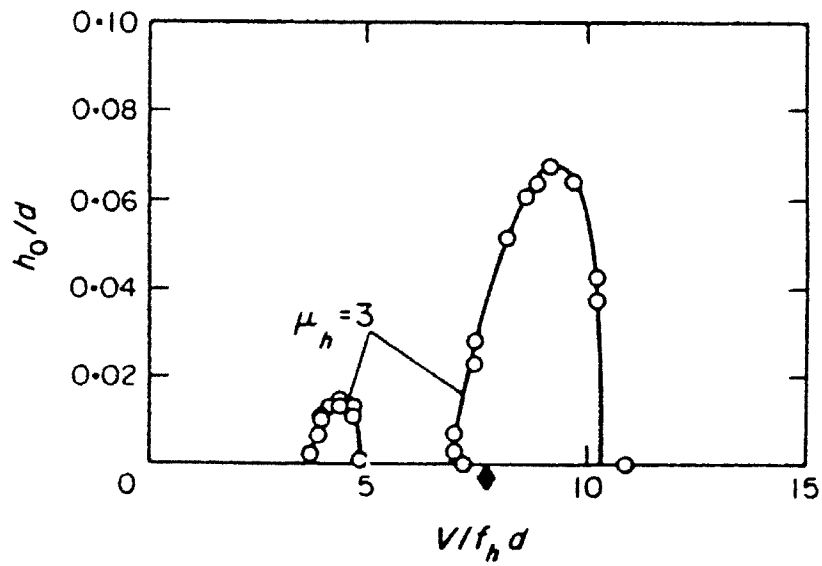

Figure 2.9. Cross-flow vibrations, L/D = 4.0 (Washizu, et al, 1978).

For the cylinder with aspect ratio L/D = 4 (Figure 2.9), they reported that the response was quite different from the response of the cylinder with L/D = 2. When the Scruton number is sufficiently small, two regions of instability were found. Only one of the regions is in the vicinity of the lock-in speed determined from stationary cylinder tests. When the Scruton number was increased, the two unstable regions diminish and finally disappear, suggesting that the two unstable regions may

be attributed to vortex-excited oscillation and that no transverse galloping exists for this model.

Rectangular cylinders, $2 < L/D < 5$. Komatsu and Kobayashi (1980), conducted wind tunnel experiments with elastically supported rectangular cylinders with aspect ratios that ranged from $2 \leq L/D \leq 5$. The cylinders were suspended in a smooth air-flow at zero angle of attack and constrained to only cross-flow motion. The air speed was increased incrementally.

At each increment of speed, the cylinder was manually set into motion with a sufficiently large amplitude, then allowed to oscillate freely in the flow. Depending on the range of air speed, it was observed that the model either settled down to a harmonic-oscillating state with constant amplitude or returned to the rest state. For velocities of flow where sustained harmonic oscillation resulted, the cylinder was initially held in the rest position and then released in order to determine whether it remained in a stationary state or began to oscillate because of wind excitation. For specific velocities dependent on the aspect ratio, they found that, while no spontaneous oscillation occurs if the cylinder is initially at rest, an initial amplitude could trigger sustained oscillation.

For rectangular bodies with separation points at their leading edges, vortex-induced oscillation occurs within two different ranges of wind velocity. One of these ranges includes the response they attributed to excitation by von Kármán vortex-shedding. The second range of responses is attributed to a motion-induced vortex that appears at the leading edge, and then synchronizes with the motion of the cylinder. The vortex travels along the side of the body surface because of the

dragging action of the mean flow along the cylinder during the half-cycle of the oscillation. As the vortex travels along the side, it produces a reduction of pressure on the surface of the cylinder. They found that the frequency of this type of oscillation does not change at all in the unstable region and coincides with the natural frequency of the cylinder.

The response curves for their tests are shown in Figure 2.10. The velocity ranges during which self-sustaining oscillation occurred only when the cylinders had been initially set in motion by hand (even though they remained stationary when initially at rest) are indicated by the dashed curves. They found that the models with L/D = 2, 4, and 5 exhibited vibrations in two distinct ranges of air speed, as seen in Figure 2.10.

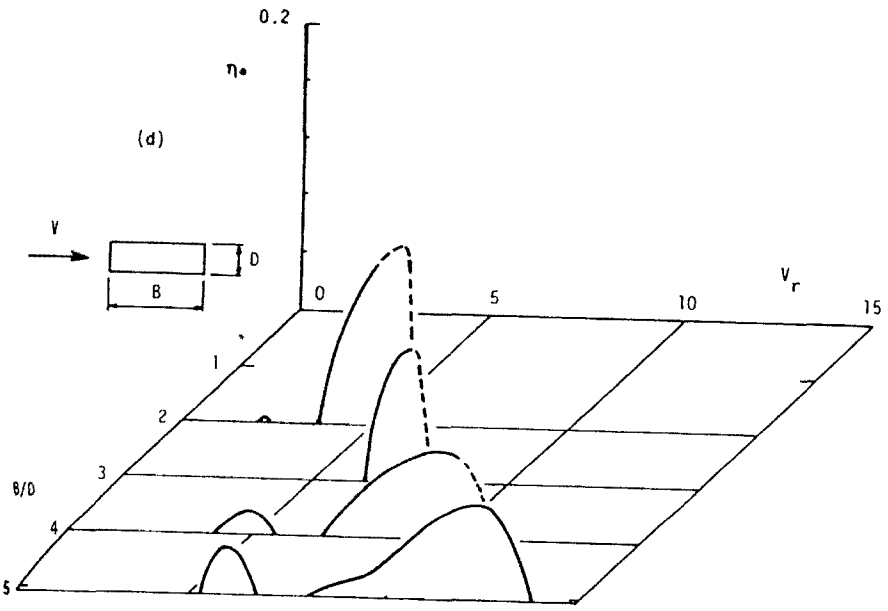

Figure 2.10. Response curves, $2 \leq L/D \leq 5$ (Komatsu and Kobayashi, 1980).

Komatsu and Kobayashi reported that all aspect ratios oscillated at the critical reduced velocity, $V_{r,cr}$. This velocity is calculated from the reciprocal of the Strouhal number for stationary rectangular cylinders, $V_{r,cr} = 1/St$. However, they reported that $V_{r,cr}$ did not coincide with the velocity producing the maximum amplitudes of oscillation.

The velocity at which peak amplitudes of vortex-induced oscillation are attained are compared with $V_{r,cr}$ in Figure 2.11. As shown, the peak amplitudes for the elastically supported rectangular cylinders tend to two common straight lines, whereas the $V_{r,cr}$ curve exhibits the variation of Strouhal number, derived for stationary cylinders, relative to each aspect ratio.

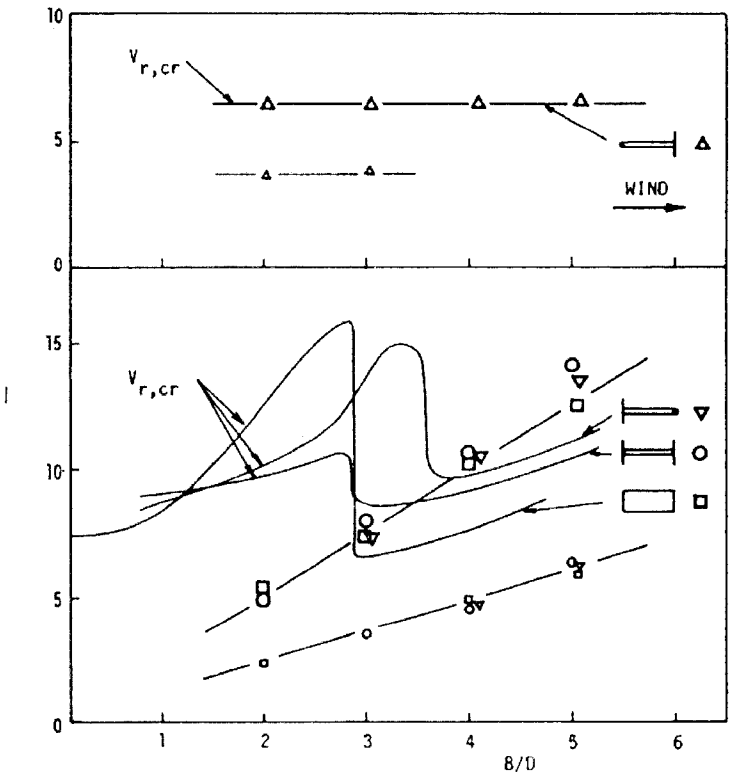

Figure 2.11. Reduced velocity at peak amplitudes (Komatsu and Kobayashi, 1980).

They considered the total work done by the oscillating system and developed formulae to predict the critical wind velocities at which the vortex-induced oscillations of rectangular cylinders having various *L/D* ratios occur with maximum amplitude,

$$V_r = 2.4\frac{L}{D} + 0.5 \quad \text{..... (Equation 2.16)}$$

$$V_r = 1.2\frac{L}{D} + 0.5 \quad \text{..... (Equation 2.17)}$$

They also developed a formula that gives the velocity range within which no vortex-induced oscillation due to motion-induced vortices occurs but within which, for relatively small *L/D* ratios, galloping occurs,

$$V_r = 4.8\frac{L}{D} + 0.5 \quad \text{..... (Equation 2.18)}$$

These formulas are plotted in Figure 2.12.

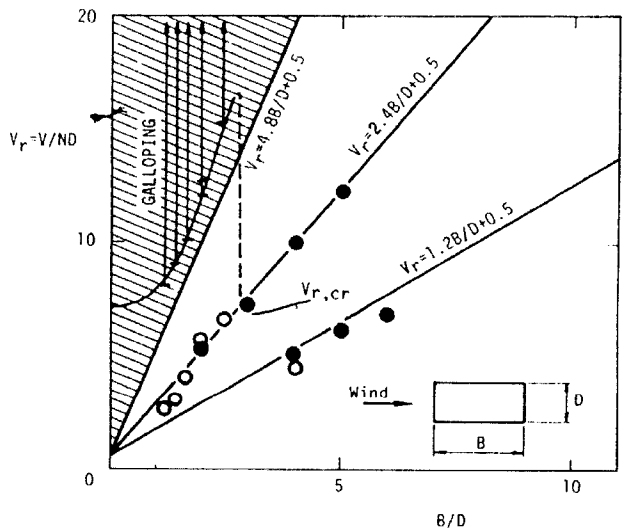

Figure 2.12. Critical reduced velocities (Komatsu and Kobayashi, 1980).

Rectangular cylinders, $2 < L/D < 5$. Nakamura and Nakashima (1986) also conducted wind tunnel experiments with elastically supported rectangular cylinders with aspect ratios in the range $2 \leq L/D \leq 5$. Similar to the discussion above regarding the experiments conducted by Komatsu and Kobayashi, the cylinders were suspended in a smooth airflow at zero angle of attack and constrained to only cross-flow motion.

Like Komatsu and Kobayashi, they attributed the observed cylinder motion to the impinging-shear layer rather than to von Kármán vortices in the trailing wake. Based on their observations, the separated shear layer from the upstream corner became unstable, rolled-up into discrete vortices that traveled along the body side surface, and was shed from the downstream corner. The impinging-shear layer instability occurs over a range of $L/D = 3$ to 6 for rectangular cylinders. For that range of cylinders, they found that the Strouhal number was approximately equal to 0.6 when based on the body length.

Rectangular cylinders, $1 < L/D < 10$. Nguyen and Naudascher (1991) conducted water channel experiments with elastically supported rectangular cylinders with aspect ratios in the range $1 \leq L/D \leq 10$. The cylinders were suspended in a water channel flow at zero angle of attack. The results of their work are shown in Figure 2.13.

They attribute the lateral response of the square cylinder ($L/D = 1$) to leading edge vortex shedding, cylinders with $L/D = 2$ through 6 to impinging leading edge vortices, and cylinders with $L/D > 6$ to trailing-edge vortex shedding. They found that the square cylinder produced the most periodic von Karman vortex-induced

excitation. However, they reported that, at comparable values of total effective damping, cylinders with L/D = 2, 3, and 4 vibrated with larger amplitudes in the lower range of reduced velocities. According to their results, this is proof that the leading-edge vortex shedding may lead to a stronger excitation than the von Kármán vortices.

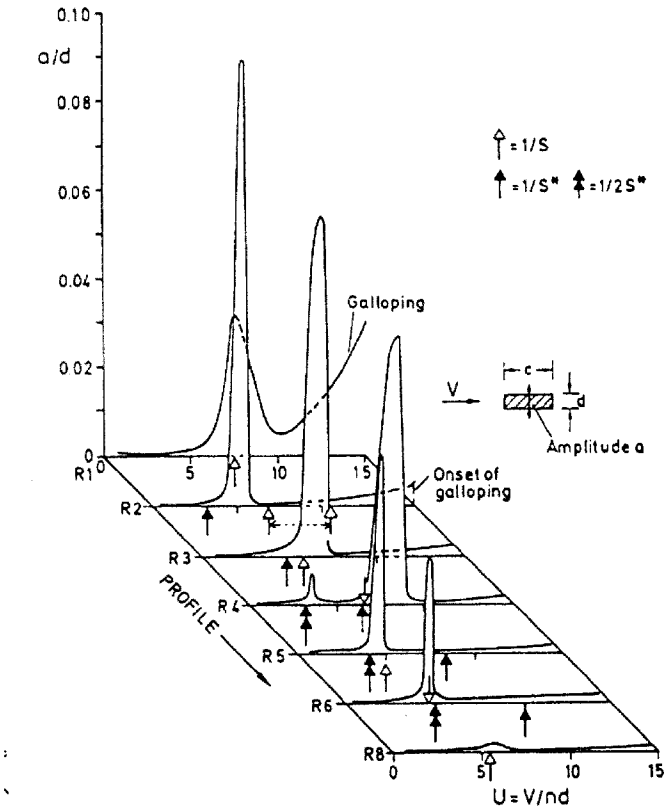

Figure 2.13. Cross-flow response, $1 \leq L/D \leq 8$ (Nguyen and Naudascher, 1991).

They introduced a modified Strouhal number based on the length of the after-body and average velocity of the fluid along the side surface of the cylinder. Given the average convection velocity of the leading-edge vortices of approximately 0.6

times the approach velocity, U, and the length of the side surface, L, the frequency of the vortex-induced excitation is,

$$f_s = \frac{0.6U}{L} \quad \text{(Equation 2.19)}$$

2.5.4. Modified Strouhal number. Clearly, a complicating factor in the analysis of flow-induced vibrations of elastically supported rectangular cylinders is the different mechanisms that can excite vibrations. Based on the literature, there are three regimes where a different mechanism in each regime provides the excitation (reference Figure 2.6).

Regime 1 is associated with leading edge vortex shedding, $0 \leq L/D \leq 3$, for smooth flow. Regime 2 is associated with impinging leading edge vortices and extends from $3 \leq L/D \leq 6$. In an extension of Regime 2, $6 \leq L/D \leq 16$, very little regular vortex shedding occurs for a stationary cylinder (Naudascher and Wang, 1993), and in regime 3, $L/D \geq 16$, boundary layers develop past reattachment and combine to form a stable vortex street a short distance downstream of the trailing edge.

For Regime 2, the vortex formation is controlled by a flow instability instigated by the impinging shear layers; vortices that form in the unstable free shear layers on the two sides of the cylinder are transported with a convection velocity equal to approximately 60% of the free-steam fluid velocity toward the trailing edges. Here they generate pressure pulsations that are fed back upstream and trigger the development of new vortices. With a vibration frequency, f, close to the natural

cylinder frequency in still fluid, f_n, impinging leading-edge vortex excited vibrations are likely to set in if the reduced velocity is (Naudascher and Wang, 1993),

$$V_r = \frac{U}{f_n D} = \frac{1}{St_n} \quad \text{..... (Equation 2.20)}$$

From Equation 2.19, if $f_s \approx f_n$, then,

$$V_r = \frac{L}{0.6D} = \frac{1}{St_n} \quad \text{..... (Equation 2.21)}$$

Thus, the modified Strouhal number, St_n, for impinging leading edge vortex shedding is defined as,

$$St_n = n\left(0.6\frac{D}{L}\right) \quad \text{..... (Equation 2.22)}$$

where n = 1, 2, 3, ...

The ranges where flow-induced vibration for lightly damped, rectangular cylinders may occur is shown in Figure 2.14. Naudascher and Wang (1993) note that the value of the mass-damping parameter, i.e.; the Scruton number, determines what harmonic of the impinging leading edge vortex frequency develops.

Flow visualization tests have shown that there is both vortex generation and vortex convection along the body side surface towards the trailing edge (Matsumoto, 1999). Furthermore, secondary vortices have been seen in the near wake at the trailing edge, induced by body motion. He reports that the average convection velocity of the vortex, from the leading edge to the trailing edge, has been measured to be approximately 60% of the free stream velocity.

For rectangular cylinders in cross-flow vibrations, Matsumoto reports that the vortex generated at the leading edge reaches the trailing edge where it coalesces

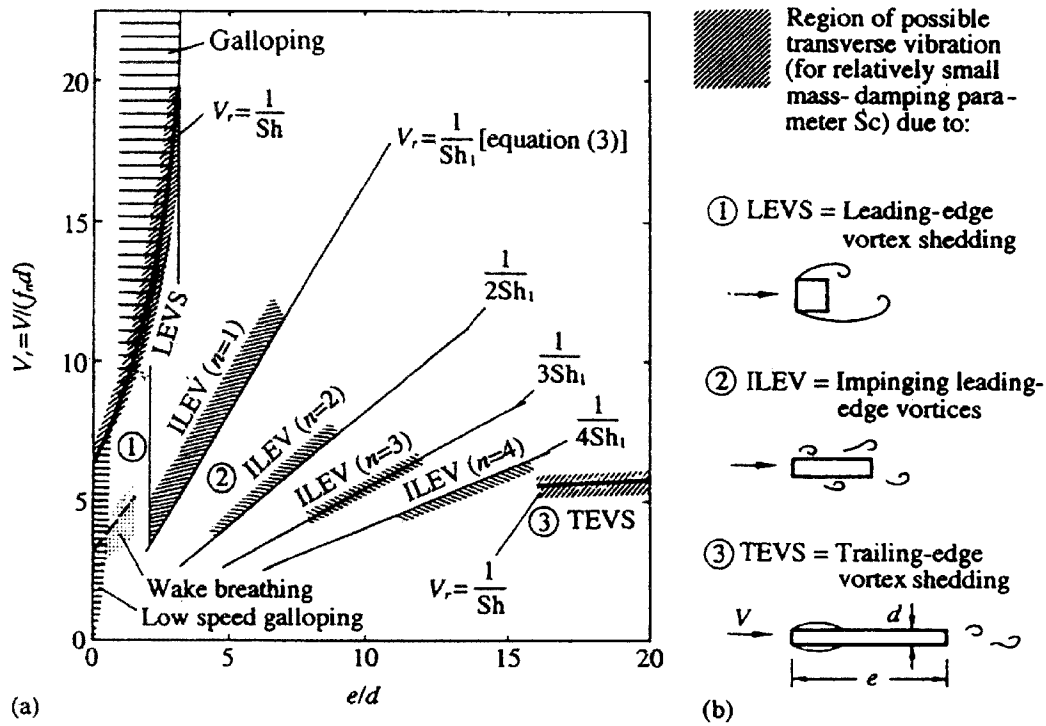

Figure 2.14. Cross-flow response (Naudascher and Wang, 1993).

with the secondary trailing edge vortex. Thus, an intensive vortex can be shed in one cycle motion at the particular reduced velocity where the vortex-induced vibrations occur. This coalescence condition is formulated as follows,

$$L = 0.6nUT_0 \quad \text{(Equation 2.23)}$$

where L = the body length parallel to the flow

n = the number of cycles, n = 1, 2, ...,

U = the free stream flow velocity, and

T_0 = the natural period of the cross-flow motion.

Rearranging this equation gives,

$$V_{r,cr} = \frac{1}{0.6n}\frac{L}{D} \quad \text{(Equation 2.24)}$$

where $V_{r,cr}$ = the critical reduced velocity $= \frac{U}{f_n D}$, and

D = the cross-flow body dimension.

Reduced velocities, V_r, versus the aspect ratio, L/D, are shown in Figure 2.15 for $n = 1, 2$. This formula agrees with the modified Strouhal number formula proposed by Nakamura and Nakashima (1986), and Equation 2.21, above. Thus, for $n = 1$, the modified Strouhal number becomes,

$$St_1 = \frac{f_n L}{U} = 0.6 \quad \text{(Equation 2.25)}$$

This modified Strouhal number accurately predicts the free stream wind velocity at which cross-flow vibrations occur for fundamental structural bluff bodies (Matsumoto, 1999).

2.6. Summary

Based on the vast amount of literature regarding circular cylinders, the wind-induced vibrations result from the classic von Kármán vortex shedding. However, the source of the excitation for rectangular cylinders is dependent on the length of the after-body; that is, the length of cylinder behind the leading edges.

Except in extremely slow wind speeds, short rectangular cylinders, $L/D \leq 2.8$, are excited by the classic von Kármán vortex shedding similar to circular cylinders. In these cases, the flow separates at the leading edges and creates a wide wake that

coalesces into the von Kármán vortex street. The body response is very similar to the response of a circular cylinder and the stationary Strouhal number accurately predicts the wind speed where lock-in occurs.

Longer rectangular cylinders, $3 \leq L/D \leq 15$, do not behave as the circular cylinders because of the presence of the after-body. The flow separates at the leading edges but the separated flow reattaches in an unstable shear layer where vortices form. The vortices travel to the trailing edge of the cylinder where a secondary vortex street forms.

However, the trailing edge vortex street is not the principal form of excitation. The main form of excitation is the formation of the vortices along the side surfaces of the cylinder and the resulting alternating pressures on the body side surfaces. Thus, for rectangular cylinders where $L/D \geq 2.8$, the stationary Strouhal number cannot be used to predict the wind velocity where lock-in will occur. The modified Strouhal number that is dependent on the length of the body accurately predicts where lock-in will occur.

While several researchers (Washizu, et al, 1978; Komatsu and Koyashi, 1980; Nguyen and Naudascher, 1991) have reported amplitudes of wind-induced vibrations for rectangular cylinders, none have attempted to develop equations to predict the expected amplitude of these vibrations.

Therefore, the focus of this research will be the range, or ranges, of air speed where wind-induced vibrations occur for rectangular cylinders; the determination of the modified Strouhal number where the vibrations occur, the amplitude of the

vibrations; and the development of a mathematical equation to predict the wind speeds when lock-in, and thus the maximum amplitude, occurs.

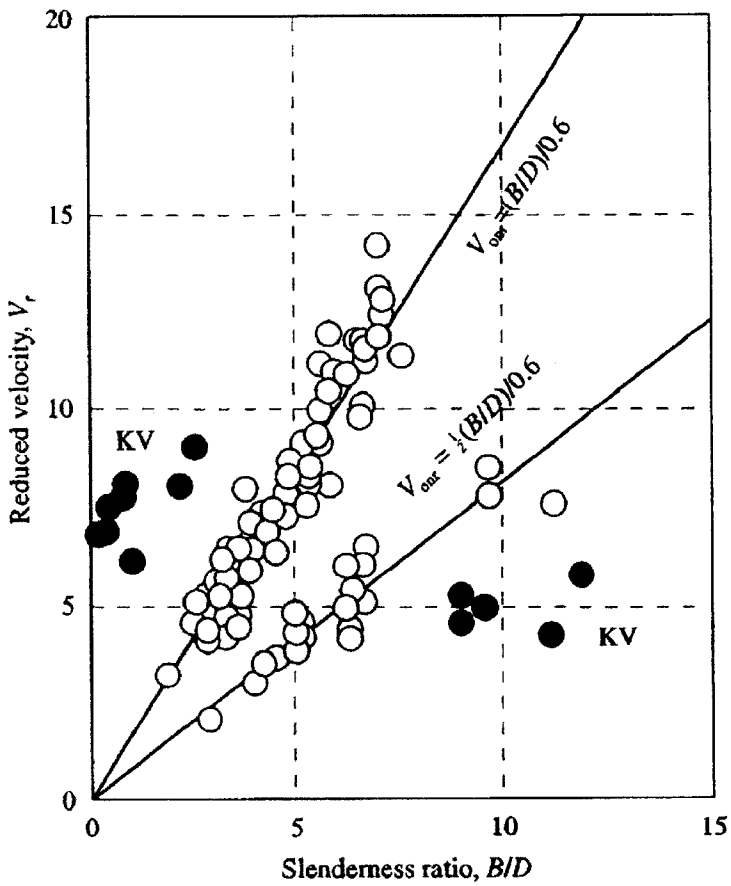

Figure 2.15. Cross-flow response (Matsumoto, 1999).

CHAPTER 3

LITERATURE REVIEW: WIND ENGINEERING

3.1. Introduction

As civil engineering structures become thinner, taller, and lighter, they become more susceptible to wind-induced vibrations and, subsequently, the detrimental effects of fatigue. The initiation and magnitude of wind-induced vibrations are functions of the wind flow characteristics and the dynamic characteristics of the structure. Therefore, it falls to the structural engineer to use suitable analysis and design methods to produce safe, dependable designs.

3.2. Wind Engineering

3.2.1. Atmospheric boundary layer. The air mass that envelops the earth forms an atmospheric boundary layer near the surface of the earth similar to the boundary layer of a body submerged in a fluid flow. The air velocity is zero at the earth's surface due to viscous effects. At the top of the boundary layer, the air velocity is equal to the free stream velocity, known as the geostrophic wind velocity. The thickness of the boundary layer and the variation of the wind velocity within the boundary layer are functions of the surface roughness.

For heights up to 30% of the atmospheric boundary layer, the Logarithmic Law is used to compute the mean velocity, U, at height, z, above the ground,

$$U(z) = \frac{1}{k}(u*)\ln\frac{z}{z_0} \quad \text{(Equation 3.1)}$$

where $k \approx 0.4$,

z = the height above the surface,

z_0 = the roughness length,

$U(z)$ = the mean wind speed, and

u^* = the shear velocity of the flow.

If the mean wind speed at height, z_1, at a particular site is known, the Logarithmic Law can be used to calculate the mean wind speed at height, z_2,

$$\frac{U(z_2)}{U(z_1)} = \frac{\ln(z_2) - \ln(z_0)}{\ln(z_1) - \ln(z_0)} \quad \text{(Equation 3.2)}$$

From the definition of the mean, the value of the mean wind speed depends upon the averaging time; as the length of the averaging interval decreases, the maximum mean speed increases (Simiu and Scanlan, 1996). The ratio of probable maximum speed averaged over the period, t, to that averaged over one hour, equal to 3,600 seconds, is given in Figure 3.1, known as the Durst chart.

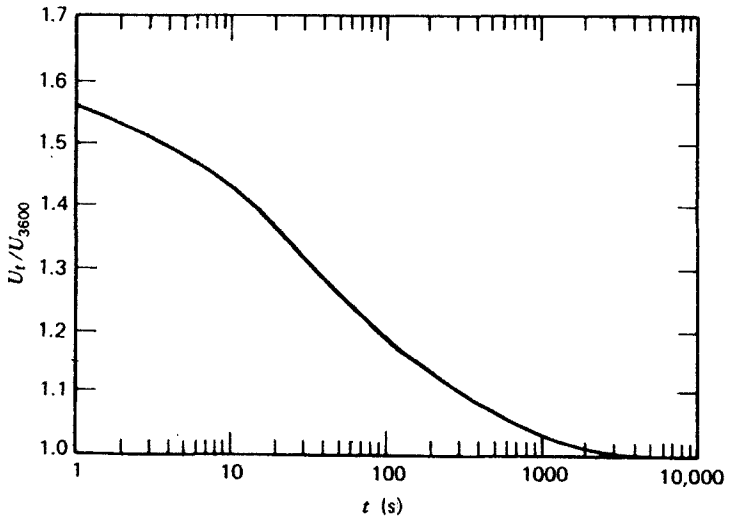

Figure 3.1. Durst chart (Simiu and Scanlan, 1996).

3.2.2. Statistical description of the wind. The natural wind in the atmospheric boundary layer is inherently turbulent and cannot be described in deterministic terms. However, the instantaneous wind velocity can be decomposed into two velocity components: a mean velocity and a turbulent velocity that varies with time. Because of its random nature, the turbulent component must be described in statistical terms.

The distribution of wind velocities is typically displayed on a histogram, or frequency diagram, and statistically described by a probability density function. Relative to the design of civil structures, the wind velocity distribution is usually fitted to a Weibull type probability density function (Holmes, 2001),

$$f_U(u) = \frac{k u^{k-1}}{u_0^k} \exp\left[-\left(\frac{u}{u_0} \right)^k \right] \quad \text{..... (Equation 3.3)}$$

The probability that a wind speed, U, exceeds a particular wind speed, u, is then calculated from the cumulative distribution function:

$$P(U \geq u) = 1 - F_U(u) = 1 - \int_u^\infty f_U(u) du = \exp\left[-\left(\frac{u}{u_0} \right)^k \right] \quad \text{..... (Equation 3.4)}$$

The function parameters include the scale factor, u_0, which is the modal wind velocity taken to be 1.13 $\bar{U}_A$, where $\bar{U}_A$ is the annual, or yearly mean wind velocity (Ruscheweyh, 1994). The value of $\bar{U}_A$ depends on site-specific conditions and typically ranges from 10 to 33 *ft/s*. The dimensionless shape factor, k, falls in the range $1.3 \leq k \leq 2.0$, and is usually taken as 2.0 (Holmes, 2001). When $k = 2.0$, the distribution is known as the Rayleigh distribution.

The probability density function of Equation 3.3 describes the distribution of wind velocity, but does not describe how quickly the wind changes; that is, the turbulence. Turbulence may be considered to be the superposition of conceptual eddies, with frequencies, f, transported by the mean wind (Simiu and Scanlan, 1996). The turbulence, or more accurately the frequency content of the turbulence, is described by a one-sided power spectral density function, or spectrum.

The spectrum is defined such that the contribution to the variance of the turbulence, σ_u^2, in the range of frequencies from f to $f + df$, is given by $S_u(f)df$, where $S_u(f)$ is the value of the spectral density function at frequency f (Holmes, 2001). Then, the variance of the turbulence is found by integrating the spectrum over all positive frequencies,

$$\sigma_u^2 = \int_0^\infty S_u(f)df \quad \text{(Equation 3.5)}$$

A number of mathematical forms for $S_u(f)$ have been developed for use in wind engineering and are available in the literature (c.f. Holmes, 2001; Simiu and Scanlan, 1994). The most common of these, the von Kármán-Harris spectrum, describes the longitudinal turbulent velocity component (Figure 3.2). This spectrum is written in non-dimensional form as:

$$\frac{fS_u(f)}{\sigma_u^2} = \frac{4\left(\frac{fL_u^x}{\overline{U}}\right)}{\left[1+70.8\left(\frac{fL_u^x}{\overline{U}}\right)^2\right]^{5.6}} \quad \text{(Equation 3.6)}$$

where L_u^x = the longitudinal turbulence length scale.

The value of $fL_u^X/\bar{U}$ where the peak of the $fS_u(f)/\sigma_u^2$ versus $fL_u^X/\bar{U}$ curve occurs is known as the peak wavelength. This wavelength represents the most predominant frequency in the turbulence.

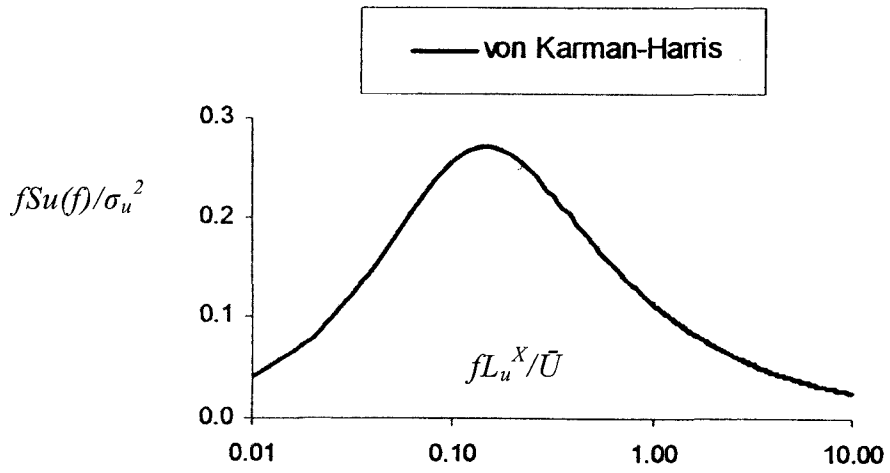

Figure 3.2. von Kármán-Harris wind spectrum (Holmes, 2001)

The turbulence length scale, L_u^X, is a measure of the average size of the conceptual eddies in the flow (Dyrbye and Hansen, 1997). Full-scale measurements are used to estimate turbulence length scales. However, results show extensive scatter due to the variability of the length of the wind records (Simiu and Scanlan, 1996). The turbulence length scale is site specific and depends on the height, z, above ground and on the terrain roughness, z_0. It has been documented that the wind velocity may also influence the integral length scales at a site (Dyrbye and Hansen, 1997). The following empirical expression for the longitudinal turbulence length scale is valid for heights between 10 to 240 *meters* (Simiu and Scanlan, 1996),

$$L_u^x = cz^m \quad \text{..... (Equation 3.7)}$$

where z = the height above the surface, and

c and m depend on roughness length z_0.

The values of c and m are obtained from Figure 3.3. Simiu and Scanlan (1996) report that the equation returns values for $L_u{}^X$ that are almost twice as high as field measured values.

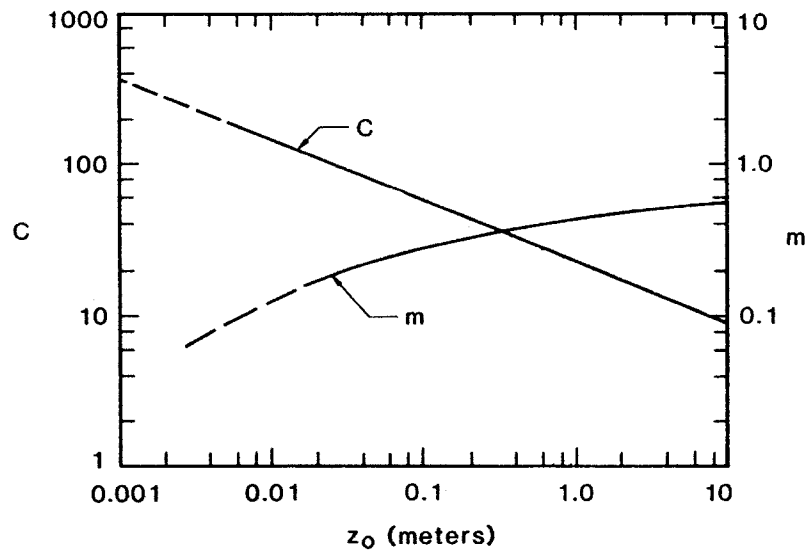

Figure 3.3. Turbulence parameters (Simiu and Scanlan, 1996).

For design applications where the height, z, is in the range of 10 to 200 *meters*, the following equation for the turbulence length scale has been proposed (Dyrbye and Hansen, 1997),

$$L_u^x = L_{10}\left(\frac{z}{z_{10}}\right)^{0.3} \quad \text{..... (Equation 3.8)}$$

where L_u^x is expressed in meters,

L_{10} is taken to be a constant at 100 m, and

z_{10} is taken to be a constant at 10 m.

3.3. Metal Fatigue

Metal fatigue is a phenomenon that takes place in metallic structures subjected to repetitive or fluctuating stress. Fatigue manifests itself in the deterioration of the material's ability to carry load (Sobczyk and Spencer, 1992). When subjected to cyclic stress, the structure will fail at a stress much lower than that required to cause failure during a single, near-static application of load.

In general, fatigue is divided into two major categories: high-cycle and low-cycle fatigue. High-cycle fatigue is usually associated with cyclic loads that produce relatively low strains that are confined to the elastic range and where the number of cycles to failure is high. Low-cycle fatigue is usually associated with cyclic loads that produce significant amounts of plastic strain occur during each cycle and where the number of cycles to failure is low. The transition from low-cycle to high-cycle fatigue behavior is typically in the range of 10^4 to 10^5 cycles (Collins, 1993). Wind-induced vortex shedding usually results in high-cycle fatigue.

Fatigue cracks nucleate, or form, on the free surface of a body at locations of high stress concentration such as surface imperfections, welds or abrupt changes of body geometry. Fatigue distress originates with the atomic yielding of the material. Microscopic cracks form, grow, and join together to form macroscopic cracks that

continue to grow as the cyclic load is applied. From experimental testing generally limited to constant amplitude fatigue loading, it is recognized that crack growth is affected by (Rolfe and Barsom, 1997, Fuchs and Stephens, 1980) stress range, stress ratio, stress complexity, mechanical properties of the material, metallurgical factors, environmental factors, and specimen geometry.

Fatigue damage, and the subsequent crack nucleation and growth, is mainly due to the stress reversals induced during the variable loading process. Accordingly, crack growth equations for deterministic stress conditions include the stress range and the maximum stress values. For random loading, however, it is important to characterize the extreme values of stress (Sobczyk and Spencer, 1992).

S–N curves plot the stress level, *S*, versus the number of cycles to failure, *N*, for a given material subjected to constant amplitude, high-cycle fatigue (Figure 3.4) (Dieter, 1986). The mathematical model used to describe the fatigue life of a component or structure under constant-amplitude fatigue loading is given by:

$$NS^m = K \quad \text{..... (Equation 3.9)}$$

where N = the number of cycles to failure

S = the constant amplitude stress, and

K and m are constants depending on the material.

K and m are typically taken as constants but, in fact, are random variables. Constant amplitude fatigue test results provide estimates of m and K for a given material. As a rule, conservative values of m and K are used in a model that produces a safe estimate of fatigue life N. For a more realistic prediction, expected values need to

be used, together with an analysis of the influence of the uncertainty in their parameters (Melchers, 1999).

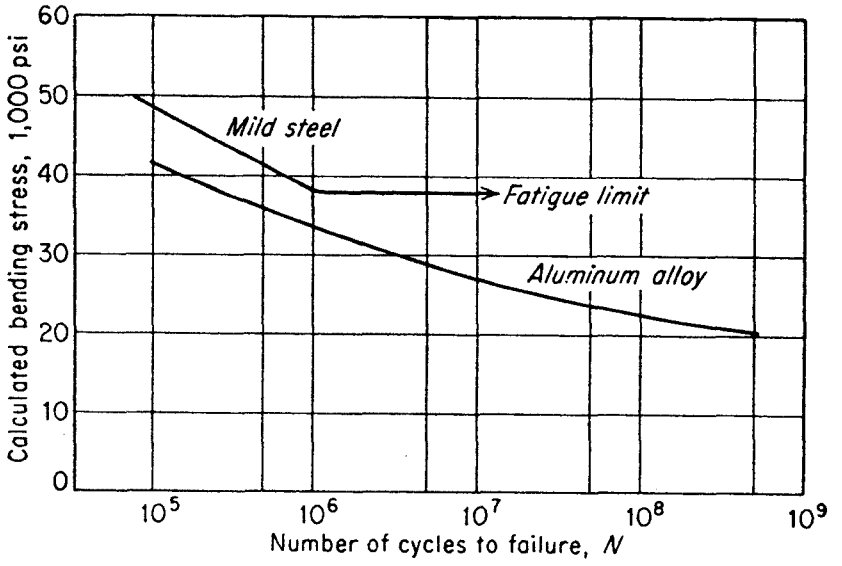

Figure 3.4. Typical S-N curves for mild steel and aluminum (Dieter, 1986).

Subjected to random load, the structure experiences variable amplitude, time-dependent fatigue stresses. Under this condition, the direct use of a standard S–N curve is not recommended as the curve is based on constant amplitude stress. To estimate fatigue life for variable amplitude loading, Palmgren and Miner theorized that fatigue fracture resulted from a linear accumulation of partial fatigue damage (Sobczyk and Spencer, 1992). The Palmgren and Miner rule states that the damage fraction, Δ_i, at any stress level, S_i, is linearly proportional to the ratio of the number

of cycles at this stress amplitude, n_i, to the total number of cycles that would cause failure at that stress level, N_i,

$$\Delta_i = \frac{n_i}{N_i},\ n_i \leq N_i \quad \text{(Equation 3.10)}$$

For each stress level, the appropriate N_i is found from the *S-N* curve and a new partial damage is calculated for the number of cycles at that particular stress level. The total accumulated damage is then given by,

$$D = \sum \frac{n_i}{N_i} \leq 1.0 \quad \text{(Equation 3.11)}$$

The life to failure is estimated by summing the percentage of fatigue life expended at each stress level. Accordingly, it is assumed that failure occurs when the total accumulated damage reaches 100%, that is when $D \geq 1.0$. However, due to the variability inherent in fatigue testing, typical experimental values of D at failure range from 0.5 to 2.0 (Sobczyk and Spencer, 1992).

3.4. Dynamic Response of Linear SDOF Systems

From elementary vibration theory, the response, $y(t)$, of a linear, single degree of freedom (SDOF) system, excited by sinusoidal function, $x(t) = x_0 \sin\omega t$, will itself be a sine wave,

$$y(t) = y_0 \sin(\omega t - \varphi) \quad \text{(Equation 3.12)}$$

where y_0 = amplitude,

ω = frequency, and

φ = phase shift between excitation and response.

The amplitude ratio, y_0/x_0, and the phase angle, φ, define the complex frequency response function, $H(\omega)$, of the system at frequency ω. This transfer function is defined such that its magnitude is equal to the amplitude ratio and the ratio of its imaginary part to its real part is equal to the tangent of the phase angle,

$$H(\omega) = A(\omega) - iB(\omega) \quad \text{(Equation 3.13)}$$

where $A(\omega)$ and $B(\omega)$ are real functions of ω. Then,

$$|H(\omega)| = \sqrt{(A^2 + B^2)} = \frac{y_0}{x_0} \quad \text{(Equation 3.14)}$$

$$\frac{\text{Im}}{\text{Re}} = \frac{B}{A} = \tan\phi \quad \text{(Equation 3.15)}$$

Therefore, if a linear system is excited by a harmonic input function, such as,

$$x(t) = x_0 e^{i\omega t} \quad \text{(Equation 3.16)}$$

the corresponding output, $y(t)$, will be,

$$y(t) = H(\omega) x_0 e^{i\omega t} \quad \text{(Equation 3.17)}$$

For a linear SDOF system, the complex frequency response function, $H(\omega)$, is given by,

$$H(\omega) = \frac{1}{-m\omega^2 + ic\omega + k} \quad \text{(Equation 3.18)}$$

From random vibration theory, it can be shown that the response spectrum, $S_y(\omega)$, and the input spectrum, $S_x(\omega)$, are related by the magnitude of the frequency response function (Newland, 1993),

$$S_y(\omega) = |H(\omega)|^2 S_x(\omega) \quad \text{(Equation 3.19)}$$

When a SDOF is subjected to a random excitation, and, if the input spectrum of the excitation is known, the mean square of the response can be calculated directly from the definition of the autocorrelation function, evaluated at $\tau = 0$,

$$R_y(\tau = 0) = E[y(t)y(t+\tau)] = E[y^2] = \int_0^\infty S_y(\omega)d\omega \quad \text{(Equation 3.20)}$$

$$E[y^2] = \sigma_y^2 = \int_0^\infty S_y(\omega)d\omega \quad \text{(Equation 3.21)}$$

$$\sigma_y^2 = \int_0^\infty |H(\omega)|S_x(\omega)d\omega \quad \text{(Equation 3.22)}$$

3.5. Statistics of Linear Systems

3.5.1. Crossing analysis. For a narrow band process, the number of times the process crosses the level, $y = a$, during a set time interval is calculated as follows (Sólnes, 1997, Newland, 1993, Melchers, 1999). If $n_a^+(T)$ denotes the number of positive slope crossings of $y = a$ in time T for a typical sample, then the expected value, or mean, for all the samples is defined as $N_a^+(T)$, where:

$$N_a^+(T) = E[n_a^+(T)] \quad \text{(Equation 3.23)}$$

Since the process is stationary, if a second interval of duration T immediately following the first is taken, it is assumed that the same result will be obtained, and for the two intervals together (total time equal to $2T$) the mean value will be equal to:

$$N_a^+(2T) = 2N_a^+(T) \quad \text{(Equation 3.24)}$$

Then for a stationary process the average number of crossings is proportional to the time interval T,

$$N_a^+(T) \propto T \quad \text{(Equation 3.25)}$$

or,

$$N_a^+(T) = \nu_a^+ T \quad \text{(Equation 3.26)}$$

where ν_a^+ = the average frequency of positive slope crossing of the level $y = a$.

Since only the positive crossings of the level $y = a$ are of interest, the velocity, $\dot{y}$, must be positive; that is, the displacement has a positive slope. Thus, the probability of the crossing of level $y = a$ while the velocity is positive must be determined,

$$\text{Probability(y = a and + } \dot{y}\text{)} = \iint p(y, \dot{y}) dy d\dot{y} \quad \text{(Equation 3.27)}$$

Or,

$$p(y, \dot{y}) = p(y = a, \dot{y}) \quad \text{(Equation 3.28)}$$

It can be shown that,

$$\text{Probability(y = a and + } \dot{y}\text{)} = dt \int_0^\infty p(a, \dot{y}) \dot{y} d\dot{y} \quad \text{(Equation 3.29)}$$

For the case where dt is sufficiently small and the process, $y(t)$, is smooth so that there can only be one crossing of $y = a$ in time dt, then,

$$\nu_a^+ dt = dt \int_0^\infty p(a, \dot{y}) \dot{y} d\dot{y} \quad \text{(Equation 3.30)}$$

Simplifying this expression gives the following result for the frequency parameter ν_a^+ in terms of the joint probability density function $p(y\,\dot{y})$:

$$v_a^+ = \int_0^\infty p(a,\dot{y})\dot{y}d\dot{y} \quad \text{(Equation 3.31)}$$

This is a general result that applies to any probability distribution. However, for the special case of a Gaussian process, it is known that y and its derivative, $\dot{y}$, are uncorrelated for any stationary random process, $y(t)$ (Newland, 1993). Therefore, the normalized covariance, $\rho_{y\dot{y}}$, is always zero. It follows that,

$$p(y,\dot{y}) = p(y)p(\dot{y}) \quad \text{(Equation 3.32)}$$

Therefore,

$$p(a,\dot{y}) = \frac{1}{\sqrt{2\pi}\sigma_y}\exp\left[\frac{-a^2}{2\sigma_y^{\,2}}\right]\frac{1}{\sqrt{2\pi}\sigma_{\dot{y}}}\exp\left[\frac{-\dot{y}^2}{2\sigma_{\dot{y}}^{\,2}}\right] \quad \text{(Equation 3.33)}$$

If this result is substituted into Equation 3.31, the number of positive crossings is given by:

$$v_a^+ = \frac{1}{\sqrt{2\pi}\sigma_y}\exp\left[\frac{-a^2}{2\sigma_y^{\,2}}\right]\int_0^\infty \frac{1}{\sqrt{2\pi}\sigma_{\dot{y}}}\exp\left[\frac{-\dot{y}^2}{2\sigma_{\dot{y}}^{\,2}}\right]\dot{y}d\dot{y} \quad \text{(Equation 3.34)}$$

The integral is a standard result in Gaussian statistics (Newland, 1993),

$$\int_0^\infty \frac{1}{\sqrt{2\pi}\sigma_{\dot{y}}}\exp\left[\frac{-\dot{y}^2}{2\sigma_{\dot{y}}^{\,2}}\right]\dot{y}d\dot{y} = \frac{\sigma_{\dot{y}}}{\sqrt{2\pi}} \quad \text{(Equation 3.35)}$$

Therefore, for a Gaussian process, the number of positive crossings of level, $y = a$ is,

$$v_a^+ = \frac{1}{2\pi}\frac{\sigma_{\dot{y}}}{\sigma_y}\exp\left[\frac{-a^2}{2\sigma_y^{\,2}}\right] \quad \text{(Equation 3.36)}$$

3.5.2. Distribution of peaks. Once the frequency of crossings of the output $y = a$, has been obtained, it is possible to determine the probability of the distribution of peaks. If $p_p(a)da$ is the probability that the magnitude of a peak, chosen at random, lies in the range of $y = a$ to $a + da$, then the probability that any peak is greater than a is,

$$\text{Probability(Peak value exceeds y = a)} = \int_a^{\infty} p_p(a)da \quad \text{..... (Equation 3.37)}$$

It is known that, on average, in time T there will be v_0^+T cycles, since one positive crossing of $y = 0$ occurs for each full cycle of the narrow band process. In that same time, only v_a^+T will have peak values exceeding $y = a$. The proportion of cycles whose peak value exceeds $y = a$ is,

$$\frac{v_a^+}{v_0^+}.$$

Therefore, this is the probability that any peak value, chosen at random, exceeds $y = a$. Hence the probability that the peak value exceeds $y = a$, is given as,

$$\int p(a)da = \frac{v_a^+}{v_0^+} \quad \text{..... (Equation 3.38)}$$

Differentiating with respect to a results in,

$$-p_p(a) = \frac{1}{v_0^+}\frac{d}{da}\left(v_a^+\right) \quad \text{..... (Equation 3.39)}$$

This is the probability density function for the occurrence of peaks and applies for any narrow band process provided that it is a smooth process with each cycle crossing the mean level $y = 0$, so that all the maximums occur above $y = 0$ and all

the minimums occur below $y = 0$. This probability density function applies for any probability distribution, but if $y(t)$ is Gaussian then there is a simple and important result for $p_p(a)$. Substituting the expression for the number of positive crossings into this function,

$$-p_p(a) = \frac{d}{da}\left(e^{-a^2/2\sigma_y^2}\right) = -\frac{a}{\sigma_y^2}\left(e^{-a^2/2\sigma_y^2}\right) \quad \text{(Equation 3.40)}$$

$$p_p(a) = \frac{a}{\sigma_y^2}\left(e^{-a^2/2\sigma_y^2}\right) \text{ for } 0 \le a \le \infty \quad \text{(Equation 3.41)}$$

This is the Rayleigh probability density function of the probability for the occurrence of peaks. The function $p_p(a)$ has its maximum value at $a = \sigma_y$, the standard deviation of the output process, and it can be shown that the majority of peaks have a magnitude close to this value. The probability of finding very small or very large peaks is small and the probability that any peak, chosen at random, exceeds a is,

$$\text{Probability(Peak value exceeds a)} = e^{-a^2/2\sigma_y^2} \quad \text{(Equation 3.42)}$$

3.6. Wind-Induced Fatigue.

3.6.1. Narrow band fatigue loading. The response to a narrow band random excitation is composed of response frequency contributions over a narrow range of frequencies concentrated near the fundamental resonant frequency of the structure. In the case of a narrow band wind-induced response, the resulting deflections and subsequent stress variations are taken to be sinusoidal with a fixed frequency and randomly varying amplitudes.

To determine the total expected fractional damage resulting from a narrow-band random stress, $S(t)$, the proportion of cycles with amplitudes in the range from S to $S+dS$ is determined from $f_p(S)dS$, where $f_p(S)$ is the probability density function of the peaks. Because the stress variations are taken to be sinusoidal with a fixed frequency, the total number of cycles in a time period, T, is v_o^+T, where v_o^+ is the rate of crossing of the mean stress. For a narrow band response with a frequency close to the resonant frequency of the structure, v_o^+ is taken to be equal to the natural frequency of vibration of the structure.

Then the total number of cycles with amplitudes in the range s to δs, is taken to be:

$$n(S) = v_o^+ T f_p(S) dS \quad \text{..... (Equation 3.43)}$$

If $N(S)$ is the number of cycles at stress amplitude, S, that causes failure, $N(S)=KS^{-m}$ as in Equation 3.9, then the fractional damage at this stress level can be found from:

$$\Delta_S = \frac{n(S)}{N(S)} = \frac{v_o^+ T f_p(S) S^m dS}{K} \quad \text{..... (Equation 3.44)}$$

The total expected fractional damage over all stress amplitudes according to Miner's rule, is found from the following,

$$D = \sum_0^\infty \frac{n(S)}{N(S)} = \frac{v_o^+ T \int_0^\infty f_p(S) S^m dS}{K} \quad \text{..... (Equation 3.45)}$$

Because wind-induced narrow-band vibration can be taken to have a normal or Gaussian probability distribution, the resulting stress peaks or amplitudes, S, have a Rayleigh distribution (Holmes, 2001):

$$f_p(S) = \frac{S}{\sigma^2}\exp\left(-\frac{S^2}{2\sigma^2}\right) \quad \text{(Equation 3.46)}$$

where σ^2 = the standard deviation of the entire stress history.

By substituting the expression of the stress peak distribution, Equation 3.46, into the equation for the total expected fractional damage, Equation 3.45, the total expected fractional damage can be calculated from:

$$D = \frac{v_o^+ T}{K\sigma^2}\int_0^\infty S^{m+1}\exp\left(-\frac{S^2}{2\sigma^2}\right)dS = \frac{v_o^+ T}{K}\left(\sqrt{2}\sigma\right)^m \Gamma\left(\frac{m}{2}+1\right) \quad \text{(Equation 3.47)}$$

where the following mathematical result has been used (Holmes, 2001),

$$\frac{1}{\sigma^2}\int_0^\infty S^{m+1}\exp\left(-\frac{S^2}{2\sigma^2}\right)dS = \left(\sqrt{2}\sigma\right)^m \Gamma\left(\frac{m}{2}+1\right) \quad \text{(Equation 3.48)}$$

defining $\Gamma(x)$ as the Gamma Function (Ang and Tang, 1975):

$$\Gamma(x) = \int_0^\infty k^{x-1}e^{-k}dx = (x-1)\Gamma(x-1) \quad \text{(Equation 3.49)}$$

This expression for the total expected fractional damage is a closed-form solution that is restricted by two assumptions. First, it is assumed that the structure is subjected to high-cycle fatigue behavior in which steel strain remains in the elastic range such that an S-N curve is valid. Second, it is assumed that the resulting dynamic response is a narrow band response at a single resonant mode, typically assumed to be the resonant mode of the structure.

In wind-induced vibration problems, Equation 3.47 is a good model of the behavior for vortex-shedding induced vibrations in low turbulence conditions (Holmes, 2001).

3.6.2. Wide band fatigue loading. A wide band random vibration response includes response contributions over a broad range of frequencies, with a large peak near the resonant frequency of the structure. To determine the total expected fractional damage due to this type of loading, the number of cycles of the wide band stress variations has to be counted. An empirical counting method is proposed (Wirsching, et al, 1995) where the total expected fractional fatigue damage under a wind-induced random stress process is related to an equivalent narrow-band vibration process:

$$D = \lambda . D_{nb} \quad \text{(Equation 3.50)}$$

where D_{nb} is the damage calculated for narrow-band vibration with the same standard deviation, σ^2, and λ is an empirically determined parameter.

Wirsching, et at (1995) determined λ by simulating wide-band processes with spectral densities of various shapes and bandwidths and utilizing the rain flow counting technique to determine the number of fatigue cycles. As a result, they proposed the following formula to estimate the value of λ:

$$\lambda = a + (1-a)(1-\varepsilon)^b \quad \text{(Equation 3.51)}$$

where a and b are functions of m, the exponent from Equations 3.9 and 3.47, obtained by least-squares fitting from the following,

$$a \cong 0.926 - 0.033m \quad \text{(Equation 3.52)}$$

$$b \cong 1.587m - 2.323 \quad \text{(Equation 3.53)}$$

and ε is a spectral bandwidth parameter found from,

$$\varepsilon = 1 - \frac{\mu_2^{\,2}}{\mu_0 \mu_4} \quad \text{(Equation 3.54)}$$

Here, μ_k is the k^{th} moment of the spectral density defined by:

$$\mu_k = \int_0^\infty n^k S(n) dn \quad \text{(Equation 3.55)}$$

For narrow band vibration, it was found that ε tends to zero and that the value for λ approaches 1.0. Therefore, it can be seen that, as ε tends to its maximum possible value of 1.0, λ approaches a. With these ranges of values for λ and ε, the upper and lower limits on the total expected fractional damage, D, can be determined.

3.6.3. Effect of varying wind speed. Equation 3.47 applies to a standard deviation of stress, σ^2, that is related to the mean wind speed, $\bar{U}$ through the spectral density function. This relationship can be written in the form (Holmes, 2001),

$$\sigma = A\overline{U}^{\,n} \quad \text{(Equation 3.56)}$$

where A and n are constants.

As the mean wind speed, $\bar{U}$, is a random variable, its probability distribution can be represented by a Weibull distribution,

$$f_U(\overline{U}) = \frac{k\overline{U}^{\,k-1}}{u_0^k} \exp\left[-\left(\frac{\overline{U}}{u_0}\right)^k\right] \quad \text{(Equation 3.57)}$$

The total damage from narrow-band vibration for all possible mean wind speeds can be obtained by combining equations 3.47, 3.56 and 3.57 and integrating. Since the fraction of the time T during which the mean wind speed falls between U and $U + dU$ is $f_U(U)*dU$, the amount of damage generated while this range of wind speed occurs is:

$$D_U = \frac{v_0^+ T f_U(U) dU}{K} \left(\sqrt{2} A U^n\right)^m \Gamma\left(\frac{m}{2}+1\right) \quad \text{..... (Equation 3.58)}$$

The total expected fractional damage in time T during all mean wind speeds between 0 and ∞ can then be found from:

$$D = \frac{v_0^+ T\left(\sqrt{2} A\right)^m}{K} \Gamma\left(\frac{m}{2}+1\right) \int_0^\infty U^{mn} f_U(U) dU \quad \text{..... (Equation 3.59)}$$

By substituting the Weibull probability density function from Equation 3.57 into Equation 3.59, the total expected fractional damage is determined from:

$$D = \frac{v_0^+ T\left(\sqrt{2} A\right)^m}{K} \Gamma\left(\frac{m}{2}+1\right) \int_0^\infty U^{mn+k-1} \left(\frac{k}{c^k}\right) \exp\left[-\left(\frac{U}{c}\right)^k\right] dU \quad \text{.. (Equation 3.60)}$$

This expression can be integrated numerically for general values of k. Since k is usually around 2, the total expected fractional damage is found to be, after substituting 2 for the value of k into Equation 3.60:

$$D = \frac{2 v_0^+ T\left(\sqrt{2} A\right)^m}{K c^2} \Gamma\left(\frac{m}{2}+1\right) \int_0^\infty U^{mn+1} \exp\left[-\left(\frac{U}{c}\right)^2\right] dU \quad \text{..... (Equation 3.61)}$$

The integral in this equation can be determined as:

$$D = \frac{2 v_0^+ T\left(\sqrt{2} A\right)^m}{K c^2} \Gamma\left(\frac{m}{2}+1\right) \frac{c^{mn+2}}{2} \Gamma\left(\frac{mn+2}{2}\right) \quad \text{..... (Equation 3.62)}$$

By combining terms and simplifying, Equation 3.62 becomes:

$$D = \frac{v_0^+ T\left(\sqrt{2} A\right)^m c^{mn}}{K} \Gamma\left(\frac{m}{2}+1\right) \Gamma\left(\frac{mn+2}{2}\right) \quad \text{..... (Equation 3.63)}$$

This expression is a closed form solution for the fatigue damage over a lifetime of wind speeds, assuming narrow band vibration.

The total expected fractional damage of wide band vibrations can be determined by multiplying Equation 3.63 by the factor, λ, where λ is determined above in Equation 3.51:

$$D = \frac{\lambda v_0^{+} T\left(\sqrt{2}A\right)^m c^{mn}}{K}\Gamma\left(\frac{m}{2}+1\right)\Gamma\left(\frac{mn+2}{2}\right) \quad \text{..... (Equation 3.64)}$$

If, in Equations 3.63 and 3.64, D is set equal to 1.0; that is, the total expected fractional damage has resulted in failure, and the equations rearranged to solve for the fatigue life, T, the lower and upper limits of the fatigue life can be found from (Holmes, 2001):

$$T_{lower} = \frac{K}{v_0^{+}\left(\sqrt{2}A\right)^m c^{mn}\Gamma\left(\frac{m}{2}+1\right)\Gamma\left(\frac{mn+2}{2}\right)} \quad \text{..... (Equation 3.65)}$$

$$T_{upper} = \frac{K}{\lambda v_0^{+}\left(\sqrt{2}A\right)^m c^{mn}\Gamma\left(\frac{m}{2}+1\right)\Gamma\left(\frac{mn+2}{2}\right)} \quad \text{..... (Equation 3.66)}$$

CHAPTER 4

EXPERIMENTAL SETUP AND PROCEDURES

4.1. Objectives

The wind tunnel experiments that were conducted as part of this work were performed to study the wind-induced vibration of elastically supported rectangular cylinders and document their response behavior. To meet these research objectives, rectangular cylinders with eight aspect ratios were tested in the wind tunnel. The models were suspended in a laminar airflow and constrained to cross-flow response by the spring force-balance system. Results of primary importance include the Strouhal number of elastically supported rectangular cylinders, the amplitude of the vibration response, the range of wind velocities producing vibrations, and the effect of the mass-damping parameter, the Scruton number, on the amplitude of vibration.

Because of the complexity associated with the study of flow-induced vibrations of rectangular cylinders, a degree of simplification is required in order to reduce the number of parameters influencing the results. In this study, the following simplifications were employed.

- The oncoming air flow was uniform and free of turbulence.
- The geometry used for the models was a regular, prismatic body with constant cross-section; that is, a rectangular cylinder with fixed across-flow thickness and width and various along-flow lengths.
- The models were constructed with sharp corners and smooth body surfaces.

- The models were constrained to a single degree of freedom allowing only motion transverse to the flow of air.
- To maximize the vibration amplitude, no external structural damping of the system was utilized.
- To minimize three-dimensional flow effects and enhance two dimensional flow effects, side plates were attached to each model.
- The model surface area exposed to the air flow, relative to the cross-sectional area of the wind tunnel, was limited so that blockage effects could be ignored.

4.2. Test Models

The eight test models were constructed using commercially available, blue polystyrene foam board produced by Dow Chemicals. The polystyrene foam board material was selected to minimize the mass of each model. Because vibration amplitude is inversely proportional to the body mass, the light weight foam board material was used to produce the maximum cross-wind vibration amplitudes.

The area of the model face exposed to the air stream was arbitrarily set to limit blockage of the wind tunnel to around 5%. Thus the area was selected to be 60 in^2. This area resulted in approximately 5.5% blockage of the wind tunnel. Thus blockage effects were ignored.

The thickness of the models was selected to be 4 *inches*. This thickness was selected to maximize vibration amplitudes since the amplitude is proportional to the cross-wind dimension of the body parallel to the direction of the flow-induced

vibrations. The width of the models was set as 15 *inches* to maintain the desired area of the model face exposed to the air stream. The 15-inch width also left space on either side of the model to allow room to clamp extra mass to the support tube as described below.

Eight models were tested with different aspect ratios, the ratio of the along-wind length to the across-wind thickness, which varied from $2 \leq L/D \leq 7$. Thus the models ranged in length from 8 *inches* to 28 *inches*. This range of aspect ratio was selected as it included the aspect ratios of 3 and 6 where the stationary Strouhal number was expected to abruptly jump. Furthermore, the range included the aspect ratio of the failed advertising signs, $L/D = 6$. The physical dimensions of each model are listed in Table 4.1.

Table 4.1. Model dimensions

Model designation	Width *inch*	Thickness *inch*	Length *inch*	Aspect Ratio *L/D*
20.X*	15	4	8	2.0
30.X	15	4	12	3.0
40.X	15	4	16	4.0
50.X	15	4	20	5.0
55.X	15	4	22	5.5
60.X	15	4	24	6.0
65.X	15	4	26	6.5
70.X	15	4	28	7.0

* X designates the number of clamps added to the model

The models were constructed using 2-inch thick polystyrene foam boards that were cut to size then laminated together with a commercially available adhesive to form the 4-inch thick models. Care was taken to avoid damaging the sharp edges of the models. Each model was lightly sanded with extra fine grit sand paper to obtain a smooth finish to the polystyrene and to remove any excess adhesive used to laminate the two thicknesses of foam board. A 4-inch square and 3/8-inch thick plywood block was set into each side of every model and glued into place. The face of the plywood block was set flush with the side face of every model.

Set-screw collars were screwed into the plywood blocks and clamped the model to a hollow aluminum alloy tube. The tube spanned horizontally across the wind tunnel where each end of the tube was connected to the force balance system. The 5/8 *inch* diameter aluminum alloy tube was installed by sliding the tube through a 3/4 *inch* diameter hole in the center of each plywood block and the center of the foam board model. The set-screw collars were slid over each end of the tube, screwed into the plywood blocks, and tightened to clamp the model to the tube.

The end plates were installed to minimize the three-dimensional end effects of the flow and maintain the two-dimension flow characteristics on the model. The size of the end plates, relative to the size of each model, is shown in Figure 4.1. The end plates were cut from sheets of thin corrugated cardboard and attached to each side of the model. The end plates were held in place by small brass washers and nuts threaded onto two, 3/32-*inch* diameter threaded brass rods. The rods penetrated each model parallel to the across-flow length near the leading and trailing edges. Over-sized circular holes at the center of the end plates provided clearance for the

aluminum tube and set-screw collars. Immediately adjacent to the over-sized holes, two small screws were installed through the end plates and into the plywood blocks to secure the end plates to the mid-section of the model.

To test multiple specimens of different mass at each aspect ratio, pairs of commercially available C clamps were clamped to the aluminum tube to add mass to the model. The C clamps weighed approximately 1/2 *lb* each. A total of four pairs of clamps were used to produce five different specimens at each aspect ratio. The clamps were attached to the aluminum rod in alternating directions to avoid introducing torsion into the tube. Each clamp thumb screw bar was secured in place to minimize the introduction of extraneous signals into the recorded data.

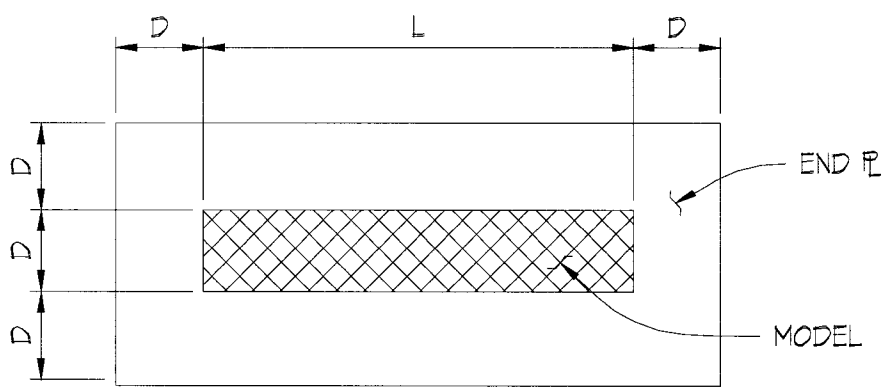

Figure 4.1. Cross-section through model.

4.3. Wind Tunnel

The wind tunnel used to conduct this research is the Bill James Open Circuit Wind Tunnel located in the Wind Simulation and Testing Laboratory (WiST Lab), Department of Aerospace Engineering, Iowa State University, Ames. The suction-type tunnel has a 22:1 contraction ratio following the turbulence-reducing mesh screens.

The wind tunnel has two test sections, the size of each being 3 *ft* x 2.5 *ft*. The total length of the two test sections extends for a length of 8 *ft* beyond the contraction exit where the flow is least turbulent. Each section has an acrylic viewing window adjacent to the wind tunnel control station and an access door on the opposite wall (Figure 4.2). Both test sections can be equipped with the necessary instrumentation to record aeroelastic and aerodynamic forces. Each test section can be positioned in the wind tunnel and removed when not required. The experiments were conducted in the first of the two test sections dedicated to section-model testing; that is, the upstream test section.

The fan, located down-stream from the two test sections, is powered by a 100 *hp*, 3-*phase*, 440-*volt* motor. An analog remote control knob located at the wind tunnel control station and connected to the variable frequency drive of the fan, provides continuous control of the fan speed. The fan speed can be changed stepwise, in increments of approximately 0.51 *ft/s*, using this remote control. The fan can generate a maximum wind velocity of 180 *mph* or 264 *ft/sec*.

Depending on the aspect ratio of the model, the experiments were conducted with a velocity that ranged from 6.2 *ft/sec* to 59.5 *ft/sec*. This represents a range in

Reynolds number of $9.9\text{x}10^3 \leq Re \leq 1.3\text{x}10^5$, when the Reynolds number is calculated using the across-flow thickness as the representative body length.

Figure 4.2. Control station, Bill James Wind Tunnel.

4.4. Force-balance System

The spring suspension system was attached to a frame that was fixed to the test section floor and ceiling immediately adjacent to the side walls. The load cell frame was constructed from small structural steel channels and two 3/4 *inch* diameter

threaded steel rods, one on each side of the test section, which spanned vertically from floor to ceiling.

The suspension system was designed to only allow a single degree of freedom; that is, the test models were free to only vibration transverse to the cross-flow in the vertical direction. Figure 4.3 is a schematic showing the general suspension system along with the location of the load cells. Figure 4.4 is a photograph of the suspension system, with a model in place, inside the wind tunnel test section.

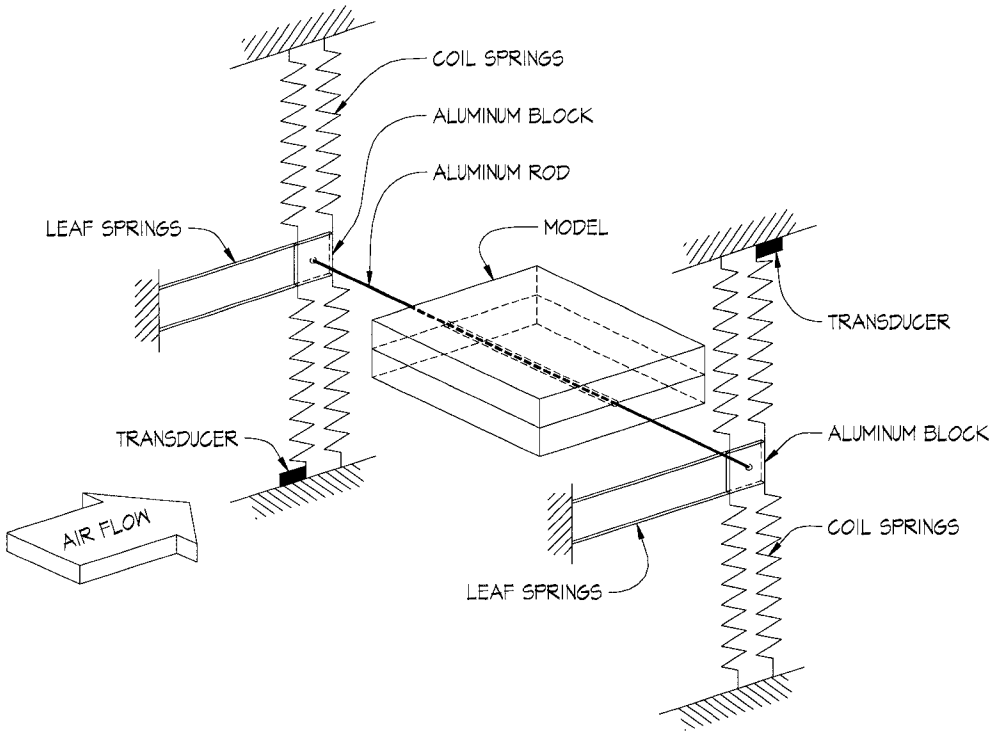

Figure 4.3. Schematic diagram of test set-up.

Each model was clamped to a circular aluminum alloy tube that penetrated through its center. The model was attached to the tube by two set-screw collars that were fixed to the model, one on each side. The tube spanned horizontally across the width of the test section and was clamped into an aluminum alloy block on each side of the test section. The clamp arrangement allowed for angular tilt adjustment of the model. The two aluminum blocks were attached to a set of extension type coil springs and leaf springs, which were anchored to the load cell frame.

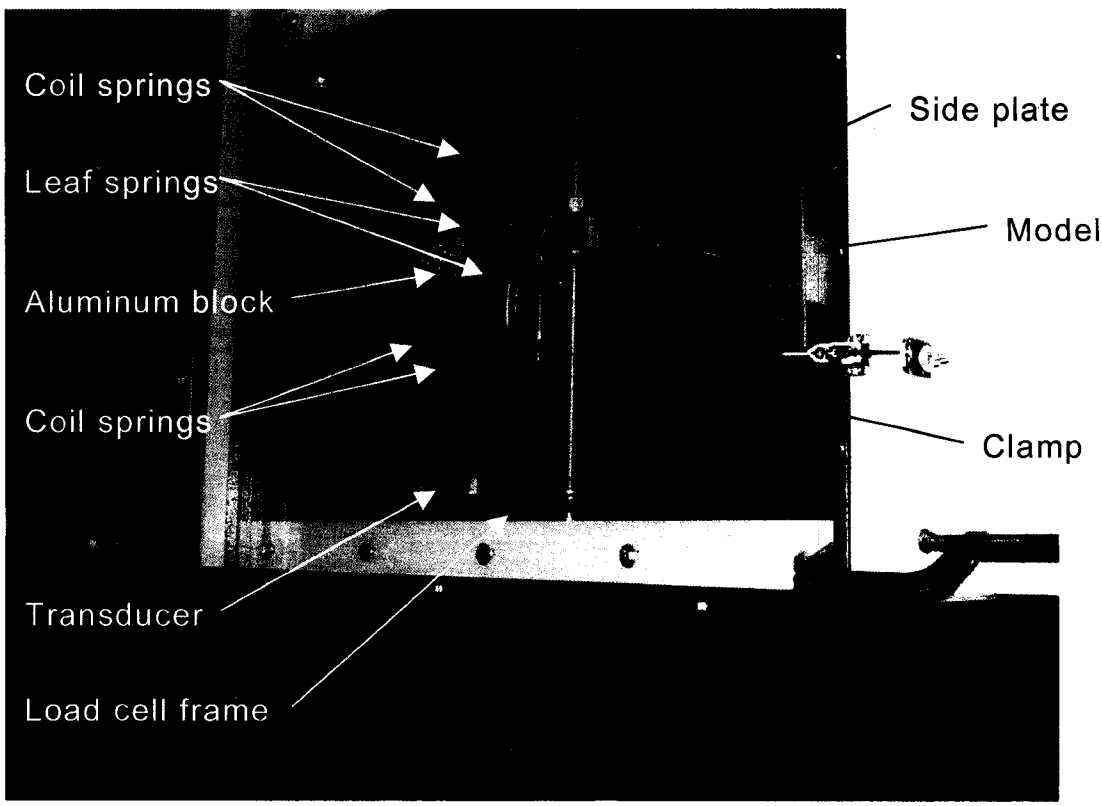

Figure 4.4. Force-balance system with model in place.

Each model was suspended by a set of eight linear coil springs, four on each side of the model. The stiffness of an individual coil spring was rated at 4.1 *lb/inch*, as listed in the manufacturer' literature. The combined stiffness of the eight springs was calculated to be 393.6 *lb/ft*. Two leaf springs on each side of the test section restrained the model in the along-flow direction. The leaf springs were 1.25 *inches* wide, 0.010 *inch* thick, and approximately 9 *inches* long. Each end of the leaf springs was clamped in place and assumed to be a fixed boundary condition that can be used for the calculation of the spring stiffness. The up-wind ends of the leaf springs were clamped to a short section of hollow steel rectangular tube. A hole had been drilled through the tube to allow the tube to be fixed to the steel rod that spanned from the floor to ceiling of the test section. The stiffness of an individual leaf spring was calculated to be 0.07 lb/inch. The combined stiffness of the 4 leaf springs was calculated to be 3.47 lb/ft. The total static stiffness of the system, including the eight coil springs and four leaf springs, was calculated as 397.1 *lb/ft*.

No external damping was designed as part of the system. The damping present was inherent internal damping and consisted of the material damping of the coil and leaf springs.

4.5. Electronic Data Acquisition

The elastic spring force generated as a result of linear vertical motion was measured to obtain the displacement time histories. These force measurements were accomplished with strain gage force transducers (Transducer Techniques, Model MLP-XX, where XX is the capacity in pounds). For these experiments, miniature

low-profile load cells with 25 *lb* capacities were used as force transducers. The transducers were rated at 1.50 *V* per 22 *lb* of force. The gain used during the experiments was 500 *mV* and the excitation signal was set at 10. This produced an output voltage to force ratio of 340.91 *mV* per *lb*. With the stiffness of the coil spring attached to the transducer rated at 4.1 *lb/in*, the voltage to displacement ratio was calculated as approximately 1.40 *V* per *inch*.

Two transducers were used in these experiments. The transducers were located on diagonally opposite corners of the test frame, one on each side of the test section. The transducer adjacent to the viewing window was located near the test section floor (Figure 4.4). The transducer adjacent to the back wall was located near the test section ceiling. As described below, the signal from the two transducers was added then halved to record the average vertical motion of the test model. This arrangement of transducers and resulting signals that were combined helped to eliminate noise from any spurious pitching or heaving modes of vibrations.

A dual channel signal analyzer Model 2032, produced by Brüel and Kjær Instruments, Inc., was used for the on-line processing of signals. The signal analyzer has an array of built-in frequency response functions and input/output analysis functions. The frequency range of the signal analyzer is 0 to 25.6 kHz. A maximum sampling frequency of 66 kHz is available with a 12-bit analog to digital conversion. The analyzer has several time averaging and weighting functions and has options of instantaneous time and spectrum displays.

The commercially available software package *Lab-View*, developed and marketed by National Instruments, was used for the acquisition of the transducer force data

from the wind tunnel experiments. The data acquisition program recorded the model displacement from two channels of data from the transducers. The features of the *Lab-View* software enabled the development of a program in C-Language that would simultaneously record data from multiple channels. The program contained a control panel showing the recorded data (voltage) plotted against time and a block diagram showing the data acquisition and processing circuit. The signals from the two transducers were added, then divided by two to obtain the average model vibration amplitude. To test the authenticity of the program, a known sine wave was fed to the program by a signal generator and faithfully recorded and displaced by the program. After the authenticity had been established, the program was utilized to record all data from the experiments using two force transducers to generate the recorded signals. A Pentium IV PC with Windows NT operating system was used to power the data acquisition software.

4.6. Experimental Procedure

The experimental work was carried out during the period between September 2002 and February 2003. The following steps describe the experimental procedure in general.

- Calibration of fan speed vs. air speed.
- Installation of each model into the force balance system.
- Determination of system mass, stiffness, and frequency for each model.
- Determination of system damping for each model.
- Calculation of the Scruton number for each model.

- Test each model over a range of air speeds, increased incrementally, that would produce wind-induced vibrations.
- Record maximum displacement displaced on the signal analyzer at each increment of wind speed that produced vibrations.
- Record time histories of displacement for the different models over the range of wind speeds that produced vibrations with appropriate sampling rates and durations.
- Plot the reduced amplitude as a function of reduced velocity to explore large-amplitude motions in different regimes of flow.

4.6.1. Calibration of fan speed vs. air speed. The fan speed vs. wind speed calibration was completed by installing a pitot tube through the floor of the wind tunnel in the section immediately ahead of the test section. The pitot tube was connected to a hand-held anemometer with digital read-out. The fan speed was varied from 1.50 *Hz* to 15.0 *Hz*. At each increment of fan speed, wind speeds recorded by the anemometer were tabulated. Because of a slight wandering of the values displayed by the anemometer, two and sometimes three closely spaced wind speeds were recorded at each fan speed. These data are tabulated in Appendix A. A linear regression of the data was performed (Figure 4.5) using the commercially available *Excel* software package. The regression produced a linear relationship between the fan speed in *Hz* and the wind tunnel air speed in feet per second, *ft/s*.

4.6.2. Installation of model into force balance system. Prior to testing each model, the aluminum rod was inserted through the model as described above. Each end of the rod was inserted into an aluminum block that was supported by the

spring-balance system on either side of the wind tunnel. The horizontal pitch of the model was checked with an electronic level with digital read-out. If required, adjustments in the model pitch were made until the electronic level indicated that the pitch was level to within 0.1 degree. During the adjustments, care was taken not to induce a rotation of the aluminum blocks that would load or unload respective pairs of coil springs. After the model was level, the rods were clamped in place in the aluminum blocks.

The levelness of the leaf springs was then checked with the electronic level. If required, the height of the steel block attached to the threaded rod was adjusted until the leaf springs were level to within 0.1 degree. The leaf springs were then clamped in place to the steel block. Care was taken not to kink the leaf springs as this would increase the system damping and dynamic stiffness resulting in a reduced vibration amplitude.

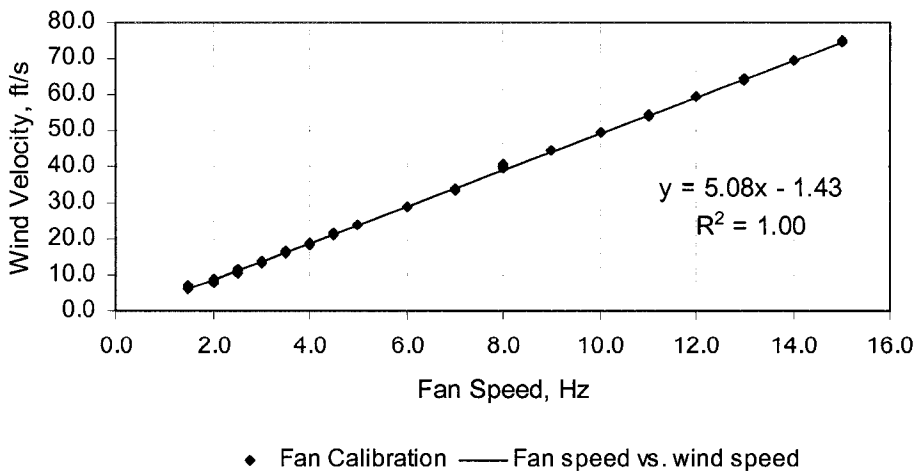

Figure 4.5. Fan speed vs. wind speed calibration.

4.6.3. Determination of model mass, stiffness, and frequency. The dynamic mass, stiffness and natural frequency for each model were determined experimentally using the added mass method described in Appendix B. The dynamic characteristics for each model are listed in Tables 4.2 through 4.9.

4.6.4. Determination of system damping. The system damping for each model was determined experimentally using the logarithmic declination method described in Appendix C. The damping for each model, expressed as a percentage of critical damping, is listed in Tables 4.2 through 4.9. The calculated damping varied from approximately 0.11% to 0.35% of critical damping. Sources of system damping included internal material damping of the coil and leaf springs and slight misalignment of the leaf springs.

4.6.5. Calculation of the Scruton number. Two Scruton numbers for each model were calculated using the methods described in Appendix D. These Scruton numbers are listed in Tables 4.2 through 4.9.

4.6.6. Experimentation. Each model was tested over a range of wind speeds that would produce wind-induced vibrations. The wind speeds were increased in increments of 0.1 *Hz* of fan speed. Each increment of fan speed represented an approximately 0.51 *ft/s* increase in the wind speed.

The models were held stationary in still air. The fan speed was set to a speed that would not produce vibrations and the fan was switched on. After a sufficient amount of time to allow vibrations to develop, if no vibrations occurred the fan speed was increased by 0.1 *Hz*, or approximately 0.51 *ft/s* wind speed. This process was repeated until cross-wind vibrations occurred. At each increment of wind speed

where vibrations were observed, the fan speed and the maximum amplitude vibration from the signal analyzer were recorded by hand and the time history of the vibration was recorded electronically with appropriate sampling rates and durations. The fan speed was increased several increments after cross-wind vibration ceased to observe the behavior of the model.

Originally the intent was to select the range of fan speeds that bracketed the speed where the stationary Strouhal number predicted lock-in would occur. However, as reported in the literature, rectangular cylinders are not excited by trailing edge vortex shedding but rather impinging leading edge vortices along the cylinder side surfaces. Therefore, the range of fan speeds was developed, on a model by model basis, to include the range of wind speeds where vibrations were observed during preliminary tests.

The data read from the signal analyzer is tabulated in Appendix E. Data included in the tables is the fan speed in *Hz*, the air speed in *ft/s*, the Reynolds number, the amplitude in *mV*, the amplitude in *inches*, the reduced velocity and the reduced amplitude. The table of electronic files, available on CD ROM, is located in Appendix F. The sampling rate and length of time history is listed in the table. The data recorded on the electronic files includes an integer counter representing time and the amplitude in *mV*.

Table 4.2. Model properties, $L/D = 2.0$

Model Designation	D *inch*	L *inch*	Aspect Ratio *L/D*	Mass *slugs*	Stiffness *lb/ft*	Frequency *Hz*	Damping *% critical*	Scruton # *D*D*	Scruton # *D*L*
20.0	4	8	2.0	0.090	332.42	9.68	0.18	0.4893	0.2446
20.2	4	8	2.0	0.138	337.70	7.88	0.13	0.5413	0.2707
20.4	4	8	2.0	0.169	322.48	6.95	0.17	0.8710	0.4355
20.6	4	8	2.0	0.213	330.31	6.27	0.17	1.0940	0.5470
20.8	4	8	2.0	0.244	321.48	5.77	0.16	1.1821	0.5911

Table 4.3. Model properties, $L/D = 3.0$

Model Designation	D *inch*	L *inch*	Aspect Ratio *L/D*	Mass *slugs*	Stiffness *lb/ft*	Frequency *Hz*	Damping *% critical*	Scruton # *D*D*	Scruton # *D*L*
30.0	4	12	3.0	0.102	331.89	9.12	0.16	0.4941	0.1647
30.2	4	12	3.0	0.144	333.17	7.65	0.17	0.7415	0.2472
30.4	4	12	3.0	0.186	328.47	6.69	0.17	0.9563	0.3188
30.6	4	12	3.0	0.237	342.50	6.09	0.14	1.0021	0.3340
30.8	4	12	3.0	0.250	308.88	5.60	0.14	1.0585	0.3528

Table 4.4. Model properties, $L/D = 4.0$

Model Designation	D *inch*	L *inch*	Aspect Ratio *L/D*	Mass *slugs*	Stiffness *lb/ft*	Frequency *Hz*	Damping *% critical*	Scruton # *D*D*	Scruton # *D*L*
40.0	4	16	4.0	0.112	334.21	8.69	0.11	0.3731	0.0933
40.2	4	16	4.0	0.153	333.80	7.44	0.15	0.6929	0.1732
40.4	4	16	4.0	0.193	328.41	6.56	0.19	1.1104	0.2776
40.6	4	16	4.0	0.217	310.07	6.02	0.15	0.9846	0.2461
40.8	4	16	4.0	0.254	307.47	5.54	0.15	1.1514	0.2879

Table 4.5. Model properties, $L/D = 5.0$

Model Designation	D *inch*	L *inch*	Aspect Ratio *L/D*	Mass *slugs*	Stiffness *lb/ft*	Frequency *Hz*	Damping *% critical*	Scruton # *D*D*	Scruton # *D*L*
50.0	4	20	5.0	0.126	337.25	8.25	0.22	0.8350	0.1670
50.2	4	20	5.0	0.170	333.86	7.06	0.22	1.1289	0.2258
50.4	4	20	5.0	0.219	347.60	6.35	0.20	1.3227	0.2645
50.6	4	20	5.0	0.251	339.50	5.85	0.27	2.0513	0.4103
50.8	4	20	5.0	0.302	345.13	5.38	0.18	1.6458	0.3292

Table 4.6. Model properties, $L/D = 5.5$

Model Designation	D *inch*	L *inch*	Aspect Ratio *L/D*	Mass *slugs*	Stiffness *lb/ft*	Frequency *Hz*	Damping *% critical*	Scruton # *D*D*	Scruton # *D*L*
55.0	4	22	5.5	0.137	344.12	7.99	0.24	0.9910	0.1802
55.2	4	22	5.5	0.178	343.34	7.00	0.24	1.2900	0.2345
55.4	4	22	5.5	0.213	330.31	6.27	0.21	1.3515	0.2457
55.6	4	22	5.5	0.258	333.13	5.72	0.19	1.4834	0.2697
55.8	4	22	5.5	0.298	338.52	5.36	0.22	1.9862	0.3611

Table 4.7. Model properties, $L/D = 6.0$

Model Designation	D *inch*	L *inch*	Aspect Ratio *L/D*	Mass *slugs*	Stiffness *lb/ft*	Frequency *Hz*	Damping *% critical*	Scruton # *D*D*	Scruton # *D*L*
60.0	4	24	6.0	0.137	344.12	7.99	0.24	0.9910	0.1652
60.2	4	24	6.0	0.194	362.34	6.87	0.28	1.6466	0.2744
60.4	4	24	6.0	0.213	330.31	6.27	0.28	1.8020	0.3003
60.6	4	24	6.0	0.243	315.30	5.73	0.29	2.1349	0.3558
60.8	4	24	6.0	0.351	380.96	5.24	0.33	3.5076	0.5846

Table 4.8. Model properties, $L/D = 6.5$

Model Designation	D *inch*	L *inch*	Aspect Ratio *L/D*	Mass *slugs*	Stiffness *lb/ft*	Frequency *Hz*	Damping *% critical*	Scruton # *D*D*	Scruton # *D*L*
65.0	4	26	6.5	0.142	336.51	7.74	0.28	1.2042	0.1853
65.2	4	26	6.5	0.181	331.69	6.81	0.25	1.3710	0.2109
65.4	4	26	6.5	0.236	350.00	6.13	0.27	1.9287	0.2967
65.6	4	26	6.5	0.262	331.87	5.66	0.25	1.9824	0.3050
65.8	4	26	6.5	0.314	340.60	5.25	0.23	2.1821	0.3357

Table 4.9. Model properties, $L/D = 7.0$

Model Designation	D *inch*	L *inch*	Aspect Ratio *L/D*	Mass *slugs*	Stiffness *lb/ft*	Frequency *Hz*	Damping *% critical*	Scruton # *D*D*	Scruton # *D*L*
70.0	4	28	7.0	0.151	346.53	7.63	0.32	1.4607	0.2087
70.2	4	28	7.0	0.186	339.52	6.81	0.28	1.5717	0.2245
70.4	4	28	7.0	0.217	317.05	6.09	0.20	1.3100	0.1871
70.6	4	28	7.0	0.278	345.23	5.61	0.21	1.7675	0.2525
70.8	4	28	7.0	0.314	340.60	5.25	0.21	1.9924	0.2846

CHAPTER 5

RESULTS AND DISCUSSION

5.1. Introduction

The experiments described in Chapter 4 were conducted in the Wind Simulation and Testing (WiST) Laboratory, Iowa State University, Ames between September, 2002 and February, 2003. Elastically supported models with eight aspect ratios that varied from $2 \leq L/D \leq 7$ were tested in the wind tunnel. The eight models were tested five times, each time with a different mass for a total of 40 test cases (Table 4.2 through 4.9). The experiments were conducted according to the procedure discussed in Section 4.6. Following the calibration of the wind tunnel fan speed described in Section 4.6.1 and Appendix A, each model was suspended in the force balance system as described in Section 4.6.2. The dynamic parameters of each model was determined and recorded as discussed in Sections 4.6.3 and 4.6.4 and Appendices B and C. The fan speed was increased incrementally and the wind speed and maximum vibration amplitude at each wind speed, where vibrations were observed, were recorded for each of the forty models.

Based on the experimental data, modified Strouhal numbers were determined and compared to published data. A mass/damping/geometry parameter analogous to the Scruton number was derived for rectangular cylinders. Finally, based on the data obtained from the tests of the forty models, an equation was developed that predicts the maximum reduced amplitude response given the Scruton number derived for rectangular cylinders.

5.2. Wind-Induced Vibrations

The range of Reynolds numbers over which each model was tested are listed in Appendix E, Tables E.1 through E.40, and summarized in Table 5.1. All models exhibited wind-induced vertical vibrations transverse to the direction of the air flow during at least one Reynolds number range. Five test cases exhibited transverse vibrations during two ranges of Reynolds numbers.

Table 5.1. Range of Reynolds numbers

Aspect ratio *L/D*	Reynolds number	
	Minimum	Maximum
2.0	1.31×10^4	1.26×10^5
3.0	1.21×10^4	5.62×10^4
4.0	1.21×10^4	7.24×10^4
5.0	9.90×10^3	4.01×10^4
5.5	9.90×10^3	3.79×10^4
6.0	9.90×10^3	3.90×10^4
6.5	1.10×10^4	3.68×10^4
7.0	9.90×10^3	2.93×10^4

In general, the Reynolds number of the fluid flow where vibrations were first observed decreased as the mass of the model increased. Likewise, the Reynolds number at the maximum vibration amplitude decreased as the mass of the model

increased. However, at a given Reynolds number the vibration amplitude increased as the model mass increased.

Each test began with the model at rest. The initial fan speed was selected such that the first several increments of wind speed would not excite the model. However, the signal analyzer indicated the presence of very small amplitude random vibrations with amplitudes of less than 1 mV at almost every increment of wind speed. The signals are believed to have been caused by noise inherent in the system when the fan was operating. As the wind speed was increased stepwise, and immediately prior to the initiation of vortex-induced vibrations, all models exhibited small-amplitude motion characterized by long period beating. The maximum amplitude of the beating was generally less than 10 mV, or approximately 0.007 *inch* and the beating period was approximately eight to ten seconds.

When the critical wind speed where vibration first occurred was approached, the beating was replaced by what appeared to be a slight rocking motion with virtually no vertical cross-wind motion. The amplitude of angular motion was limited by the rotational restraint provided by the force balance system. The rotational mode was evident, however, in the alternating buckling and straightening of the pair of leaf springs on each side of the force balance system. The rocking motion was observed during at least one increment of wind speed before the wind-induced transverse vibrations commenced. This type of rocking motion is assumed to provide the necessary perturbation for vortex-induced vibration to commence in some cases.

In all tests the magnitude of the vortex-induced transverse vibrations quickly grew to near maximum amplitude once the transverse vibrations commenced. The

initiation of vortex-induced vibration was taken to be the beginning of lock-in. The lock-in vibrations were observed for a maximum of 20 increments of fan speed, or over a range of less than approximately 10 *ft/s*. Near the end of lock-in, defined to be where vortex-induced vibrations cease, the amplitude decreased rapidly and decayed into the rocking motion observed at the beginning of lock-in. Typically, the rocking motion continued for at least one and sometimes two increments of wind speed. With further increase of wind speed, the motion transitioned into the very low amplitude beating. The beating response that was observed following lock-in was similar to the beating response observed prior to lock-in.

5.2.1. Aspect ratio, *L/D* = 2.0. The five models exhibited vortex-induced vibrations transverse to the air flow. The wind speed at the initiation of vortex-induced vibration, taken as the beginning of lock-in, varied from approximately 8 to 20 *ft/s* depending on the model mass (Figures 5.1 and 5.2). The maximum amplitude of vibration, y_0, varied from approximately 0.40 *inch* to 0.48 *inch* depending on model mass and system damping.

When reduced to the nondimensional form of reduced amplitude vs. reduced velocity, the vortex-induced responses are seen to be nearly coincidental for the five models (Figure 5.10). The reduced velocity at the beginning and end of lock-in was approximately 3.5 and 6.4, respectively. The maximum reduced amplitude varied from approximately 0.10 to 0.12. The maximum reduced amplitudes of all five models occurred at a reduced velocity of nearly 6.0.

Taking the inverse of the reduced velocity to be the traditional Strouhal number, lock-in occurred at a Strouhal number of approximately 0.3. The maximum amplitude occurred at a Strouhal number of approximately 0.2.

All five models began to gallop when the wind speed was increased beyond the lock-in range of velocities (Figure 5.1). As expected, the amplitude of the galloping increased without bound as the wind speed was increased for each of the five models. Similar to the initiation of lock-in, the wind speed at the initiation of galloping decreased as the mass of the model increased. Furthermore, Figure 5.1 indicates that, at a given wind speed, the amplitude of galloping increased as the mass of the model increased. All five tests were stopped when the galloping amplitudes became excessive to avoid causing damage to the force balance system.

5.2.2. Aspect ratios, *L/D* = 3.0 and 4.0. Similar to the models with $L/D = 2.0$, all models with aspect ratios of $L/D = 3.0$ and 4.0 exhibited vortex-induced vibrations transverse to the direction of the wind flow. However, these models did not exhibit any galloping instabilities. The vibration responses in terms of amplitude vs. wind speed are plotted in Figures 5.3 and 5.4 for $L/D = 3.0$ and 4.0, respectively. The vibration responses in terms of reduced amplitude vs. reduced velocity are plotted in Figures 5.11 and 5.12 for $L/D = 3.0$ and 4.0, respectively. Both models exhibited vortex-induced vibrations at two distinct ranges of wind speed. The range of reduced velocities where the vibrations occurred varied with the aspect ratio.

For $L/D = 3.0$, lock-in occurred when the reduced velocity was between 2.5 and 3.5 and between 5.5 and 7.5, respectively (Figure 5.11). Maximum amplitude

vibrations occurred when the reduced velocity was approximately equal to 3 and 6.5 for the first and second reduced velocity range, respectively. The maximum amplitude observed during the first reduced velocity range was less than 1/8 the maximum amplitude of the second reduced velocity range.

For L/D = 4.0, vibrations occurred when the reduced velocity was between 3.5 and 5 and between 6.5 and 11 (Figure 5.12). Maximum amplitude vibrations occurred when the reduced velocity was approximately equal to 4.5 and 7.5. The maximum amplitude of the first range was approximately half that of the maximum amplitude of the second reduced velocity range.

For L/D = 3.0, lock-in commenced at the traditional Strouhal numbers of approximately 0.4 and 0.18 for the two ranges of wind speeds. Maximum amplitude vibrations occurred at Strouhal numbers of approximately 0.33 and 0.15. For L/D = 4.0, lock-in began at the traditional Strouhal numbers of approximately 0.3 and 0.15, while maximum amplitude vibrations occurred at Strouhal numbers of approximately 0.22 and 0.13.

As seen in Figure 5.11, the maximum reduced amplitudes for Models 30.0, 30.2, 30.4, and 30.6 gradually decrease from approximately 0.073 for Model 30.0 to 0.068 for Model 30.6. However, a sharp decrease in reduced amplitude occurs between the responses of Model 30.6 and 30.8 from 0.068 to 0.058. Likewise, as seen in Figure 5.12, the maximum reduced amplitudes for Models 40.0, 40.2, and 40.4 vary from approximately 0.045 for Model 40.0 to 0.041 for Model 40.4. An abrupt decrease occurs between the responses for Model 40.4 and Models 40.6 and 40.8. The

maximum reduced amplitudes for Models 40.6 and 40.8 were observed to be approximately 0.033 and 0.030, respectively.

5.2.3. Aspect ratios, $5.0 \leq L/D \leq 6.0$. As seen in Figures 5.5 through 5.7 and Figures 5.13 through 5.15, the response of the three models in this range of aspect ratios included vibrations in two ranges of velocities. For L/D = 5.0 and 5.5, the ranges are distinct and occur between the reduced velocities of approximately 2.7 and 3.7 at the lower range and between 4.5 and 5.5 at the upper range. For L/D = 6.0, however, the ranges overlap and are not distinct as seen in Figure 5.15. Vibration amplitudes produced in the first velocity range were smaller than the vibration amplitudes produced in the second velocity range, similar to the case with models of smaller aspect ratios.

Lock-in first occurred at the traditional Strouhal numbers of approximately 0.38, 0.31, and 0.30 for L/D = 5.0, 5.5 and 6.0, respectively. Lock-in occurred a second time at Strouhal numbers of approximately 0.23, 0.22, and 0.21 for L/D = 5.0, 5.5 and 6.0, respectively. For each of the three models the maximum amplitude vibration that occurred during the second range of velocity occurred at a traditional Strouhal number of 0.20.

As seen in Figures 5.5 through 5.7, there is a jump in the relative magnitude of the vibration amplitudes of the two models in each aspect ratio with the least mass and the amplitudes of the three models in each aspect ratio with the most mass. As an example, the maximum reduced amplitude for Models 50.0 and 50.2 is approximately 0.033; however, the maximum reduced amplitude for Models 50.4, 50.6, and 50.8 is approximately equal to 0.030.

5.2.4. Aspect ratio, *L/D* = 6.5. All models with an aspect ratio of *L/D* = 6.5 exhibited only one range of velocities where vortex-induced vibrations occur (Figure 5.8 and 5.16). However, the velocity range included two reduced velocities where peaks of the vibration amplitudes occurred (c.f., Figure 5.16). Unlike previous models, the larger of the two maximum amplitudes occurred at a lower velocity rather than the higher velocity.

The range of reduced velocity where vibrations were observed is between 3.6 and approximately 5.8, with the exception of Model 65.0. Model 65.0 exhibited beating with a reduced amplitude of approximately 0.002 at reduced velocities between 5.8 and 6.5 (Figure 5.16). If the beating amplitude for this model was removed from the plot, all five models at this aspect ratio would cease vibration at a reduced velocity of 5.8. The maximum reduced amplitudes are less than 0.009 and occur in the reduced velocity range of approximately 3.8 to 4.2. Lock-in occurs at a traditional Strouhal number of 0.28 while maximum amplitudes occur at a traditional Strouhal number of approximately 0.24.

5.2.5. Aspect ratio, *L/D* = 7.0. Vortex-induced vibrations were observed during only one range of wind velocities (Figures 5.9 and 5.17). The range of reduced velocities where vibrations were observed was between 3.8 and approximately 5.3. The maximum reduced amplitudes were generally less than 0.014 and occur at a reduced velocity of 4.4 to 4.6. Note that the vibrations amplitudes for models with *L/D* = 7.0 are approximately 50% greater than the amplitudes for modes with *L/D* = 6.5.

Lock-in occurred at a traditional Strouhal number of 0.26. Maximum amplitude vibration occurred at a traditional Strouhal number of approximately 0.22.

5.2.6. Summary. The experimental data presented in Figures 5.10 through 5.17, and discussed above, closely agree with the data presented in Figure 2.13 and discussed in Nguyen and Naudascher (1991). The range of reduced velocities when lock-in was observed to begin and end is summarized for each aspect ratio in Table 5.2. The maximum reduced amplitude, the reduced velocity at maximum reduced amplitude, and the Reynolds number at maximum reduced amplitude are summarized for each aspect ratio in Table 5.3.

All models exhibited vertical vortex-induced vibrations transverse to the wind flow direction during at least one range of wind speeds. Five models exhibited vortex-induced vibrations in two ranges of wind speeds. Based on observed behavior of the models, the models were excited by impinging leading edge vortices along the sides of the rectangles rather than by vortex shedding from the trailing edge of the rectangles.

In general, the velocity where vibrations were first observed decreased with an increase in model mass. Likewise, the maximum vibration amplitude decreased with an increase in model mass and damping. Finally, at a given wind velocity, the vibration amplitude increased with an increase in model mass.

Traditional Strouhal numbers determined for stationary rectangular cylinders (Knisely, 1990) do not predict the critical reduced velocity were vibrations first occur for elastically supported rectangular cylinders. Furthermore, the modified Strouhal numbers established for stationary rectangular cylinders and based on the

length of the cylinder (Nakamura et al, 1991) do not predict the critical reduced velocity where vibrations first occur. However, the modified Strouhal numbers based on the aspect ratio (Naudascher and Wang, 1993; Matsumoto, 1999) accurately predict the critical reduced velocity where lock-in occurs.

Table 5.2. Range of V_r during lock-in

Aspect ratio *L/D*	V_r at onset and end of lock-in					
	Wind regime, *n*					
	n = 1		*n* = 2		*n* = 3	
	Onset	End	Onset	End	Onset	End
2.0	3.5	6.0	-	-	-	-
3.0	5.5	7.5	2.5	3.5	-	-
4.0	6.5	11.0	3.5	5.0	-	-
5.0	-	-	4.5	5.5	2.7	3.7
5.5	-	-	4.5	5.5	2.7	3.7
6.0	-	-	4.2	5.8	3.3	4.2
6.5	-	-	-	-	3.6	5.8
7.0	-	-	-	-	3.8	5.3

Table 5.3. Maximum reduced amplitudes

Aspect ratio L/D	Maximum reduced amplitude, Wind regime, n			Reduced velocity at max. reduced amplitude	Reynolds number at max. reduced amplitude
	$n = 1$	$n = 2$	$n = 3$		
2.0	0.12	-	-	6.0	4.03×10^4
3.0	0.074	0.012	-	6.8	4.46×10^4
4.0	0.044	0.024	-	9.5	5.94×10^4
5.0	-	0.033	0.005	5.0	2.97×10^4
5.5	-	0.025	0.005	5.0	2.97×10^4
6.0	-	0.015	0.006	5.0	2.76×10^4
6.5	-	-	0.010	4.2	2.34×10^4
7.0	-	-	0.015	4.5	2.12×10^4

5.3. Modified Strouhal Numbers

5.3.1. Modified Strouhal numbers. The reduced velocity where vortex-induced vibration was first observed is taken as the onset of lock-in. From the discussion in Section 2.5.4, the reduced velocities, V_r, and modified Strouhal numbers, St_n, at the onset of lock-in were calculated from data presented in Section 5.2. The calculated modified Strouhal numbers, along with the modified Strouhal numbers predicted by Equation 2.22, are presented in Table 5.4 and plotted in Figure 5.18 for each wind regime. The modified Strouhal numbers obtained from the current data and presented in the table and figure closely agree with Naudascher and Wang (1993).

Table 5.4. Modified Strouhal numbers

Aspect ratio *L/D*	Modified Strouhal number. Current data			Modified Strouhal number Equation 2.22		
	Wind regime, *n*			Wind regime, *n*		
	$n = 1$	$n = 2$	$n = 3$	$n = 1$	$n = 2$	$n = 3$
2.0	0.26 to 0.29	(1)	(1)	0.30	0.60	0.90
3.0	0.19 to 0.21	0.38 to 0.42	(1)	0.20	0.40	0.60
4.0	0.15 to 0.16	0.29 to 0.31	(1)	0.15	0.30	0.45
5.0	(1)	0.22 to 0.24	0.36 to 0.38	0.12	0.24	0.36
5.5	(1)	0.22 to 0.23	0.31 to 0.33	0.11	0.22	0.33
6.0	(1)	0.21 to 0.22	0.29 to 0.31	0.10	0.20	0.30
6.5	(1)	(1)	0.27 to 0.28	0.09	0.19	0.28
7.0	(1)	(1)	0.26 to 0.28	0.09	0.17	0.26

Note 1. No vibrations observed.

5.3.2. Flow regimes. The reduced velocities, V_r, calculated from the current data, are presented in Figure 5.19 as a function of aspect ratio, *L/D*. Referring to the figure, models with aspect ratio $L/D = 2.0$ exhibited lock-in vibrations at a reduced velocity in the first wind velocity regime; that is, by the modified Strouhal number with $n = 1$.

Models with aspect ratios $L/D = 3.0$ and 4.0 exhibited lock-in vibrations at reduced velocities in both the first and second wind velocity regimes; that is, by the

modified Strouhal number with n = 1, 2. However, for these two aspect ratios the maximum amplitude occurred only in the first regime.

The three models, L/D = 5.0, 5.5, and 6.0, exhibited lock-in vibrations at reduced wind velocities in both the second and third wind velocity regimes; that is, the modified Strouhal number with n = 2, 3. However, for these three aspect ratios, the maximum amplitude occurred only in the second regime.

Finally, for aspect ratios, L/D = 6.5 and 7.0, the models exhibited lock-in vibrations in the third wind velocity regime only; that is, by the modified Strouhal number when n = 3.

The straight-line plots of the three regimes of reduced velocity, V_r, as defined by Equation 2.21 with n = 1, 2, and 3 are also plotted in Figure 5.19. The current data closely agrees with Equation 2.21 and with the data presented in Figure 2.14 (Naudascher and Wang, 1993) and Figure 2.15 (Matsumoto, 1999).

5.3.3. Reduced amplitude vs. L/D and St_n. To study the relation between the reduced amplitude, V_r, and the aspect ratio, L/D, the reduced amplitude was plotted against the aspect ratio in Figure 5.20. Likewise, to study the relation between reduced amplitude and the modified Strouhal number, St_n, the reduced velocity was also plotted against the modified Strouhal number in Figure 5.20. From the figure, the maximum reduced amplitude has almost no dependency on the modified Strouhal number. In particular, the reduced amplitude is not sensitive to the particular flow regime where the lock-in vibrations occur.

A best-fit curve was derived for the reduced amplitude vs. aspect ratio data and was determined to be,

$$\frac{y_o}{D} = \frac{2.1}{\left[1+\left(\frac{L}{D}\right)\right]^{2.47}} \quad \text{..... (Equation 5.1)}$$

with a correlation coefficient, $R^2 = 0.93$. Therefore, in consideration of the high value of the correlation coefficient returned from Equation 5.1 and the observations made from Figure 5.20, the reduced amplitude is dependent on the aspect ratio or some function of the aspect ratio.

5.3.4. Summary. In the current experiments, three rectangular models were observed to vibrate at lock-in during at least one regime of reduced velocity. Five rectangular models were observed to vibrate at lock-in during at least two regimes of reduced velocity. These observations are in agreement with published data. In all test cases the modified Strouhal number determined from the current experiments agrees with the value returned from Equation 2.22 (Figure 5.18). Furthermore, in all test cases the critical reduced velocity at the onset of lock-in in each wind regime agrees with the value returned from Equation 2.21 (Figure 5.19). However, for those aspect ratios where lock-in was observed during two regimes, the maximum amplitude of vibration occurred only during the regime with the smaller value of n.

Based on the data presented in Figure 5.20 and Equation 5.1, the value of the maximum reduced amplitude for each of the eight aspect ratios is seen to be related to the aspect ratio, L/D. However, as seen in Figure 5.20, the maximum reduced amplitude is not related to the modified Strouhal number, St_n.

As a comparison, the equation developed to predict the vortex-induced response of circular cylinders (Equation 2.14) includes the Strouhal number raised to a power

in the denominator. The traditional Strouhal number for all circular cylinders is approximately equal to 0.20 over a broad range of Reynolds number and, therefore, can be taken as a constant in Equation 2.14. Consequently, the vortex-induced response of circular cylinders is not a function of the traditional Strouhal number. Analogously, the vortex-induced response of rectangular cylinders is not a function of the modified Strouhal number.

5.4. Scruton Numbers

5.4.1. Scruton numbers, *Sc1* and *Sc2*. Naudascher and Wang (1993) note that the reduced velocity and therefore the wind regime at which vibrations first occur is a function of the product of the mass and damping parameter; that is, the Scruton number. As discussed in Section 4.6.5, two Scruton numbers were calculated for each model (Tables 4.2 through 4.9). The first Scruton number, identified as *Sc1*, was based on the across-wind thickness, D^2; the second Scruton number, identified as *Sc2*, was based on the product of the across-wind thickness and the along-wind length, *DL*.

The reduced amplitude was plotted against the two Scruton numbers of the forty models in Figures 5.20 and 5.21. The values of the Scruton numbers, *Sc1*, were used in Figure 5.20; the values of the Scruton numbers, *Sc2*, were used to plot Figure 5.21.

5.4.2. Response equation form. A curve equation similar in form to Equation 2.14 was selected to describe the relation between the reduced amplitude and the Scruton number. This form of equation was selected based on the following criteria.

First, the equation returns a reduced amplitude that is asymptotic to the x-axis as the Scruton number increases; that is, the reduced amplitude approaches zero as the Scruton number becomes large. Second, due of the form of the denominator, the equation returns finite valued reduced amplitudes as the Scruton number becomes small and approaches zero. Last, in the theoretical limit where the Scruton number equals zero, the equation returns the value of the maximum, self-limiting reduced amplitude.

For the reasons stated above, an equation similar in form to Equation 2.14 was used to describe the vortex-induced vibration response of rectangular cylinders in nondimensional terms. For convenience, Equation 2.14 is repeated here,

$$\frac{y_o}{D} = \frac{1.29}{\left[1 + 0.43\left(8\pi^2 St^2 Sc\right)\right]^{3.35}} \quad \text{..... (Equation 2.14)}$$

Taking the Strouhal number for circular cylinders to be a constant, the equation can be rewritten in the form,

$$\frac{y_o}{D} = \frac{1.29}{\left[1 + 33.95 St^2 Sc\right]^{3.35}} \quad \text{..... (Equation 5.2)}$$

From an inspection of the data plotted in Figures 5.20, 5.21 and 5.22, the vortex-induced response of rectangular cylinders can be predicted by an equation similar to Equation 5.2. Based on the discussion in Section 5.3, the reduced amplitude is not a function of the modified Strouhal number, St_n. However, from the same discussion, the reduced amplitude is a function of the aspect ratio, L/D. Therefore, the response equation for rectangular cylinders takes the following form,

$$\frac{y_0}{D} = \frac{C1}{\left[1 + C2\left(\frac{L}{D}\right)^x Scn\right]^{C3}} \quad \text{..... (Equation 5.3)}$$

where *C1*, *C2*, and *C3* are constants to be determined,

y_0/D = the reduced amplitude,

$(L/D)^x$ = the aspect ratio raised to the power x,

x = an exponential to be determined, and

Scn = the Scruton number, *Sc1* or *Sc2*.

The values of the constants, *C1*, *C2*, and *C3*, and the exponential, x, are dependent on the form of Scruton number that is used; that is, *Sc1* or *Sc2*. The following procedure was developed to determine the constants for Equation 5.3 using the current experimental data.

5.4.3. Best-fit curve using *Excel*. Taking the base 10 logarithm of both sides of Equation 5.3, results in,

$$\log\left(\frac{y_0}{D}\right) = \log(C1) - C3\log\left[1 + C2\left(\frac{L}{D}\right)^x (Scn)\right] \quad \text{..... (Equation 5.4)}$$

This is the equation of a straight line with a negative slope,

$$y = b - mx \quad \text{..... (Equation 5.5)}$$

where $y = \log\left(\frac{y_0}{D}\right)$,

$b = \log(C1)$,

$m = C3$, and

$$x = \log\left[1 + C2\left(\frac{L}{D}\right)^{x}(Scn)\right].$$

The constants, *C1*, *C2*, and *C3*, and the exponential, x, were determined by fitting a straight line to the log form of the nondimensional data set for each aspect ratio when the data is plotted in Cartesian coordinates. That is, the log of the reduced amplitude was plotted against the log of the sum of one plus the product of the Scruton number, the aspect ratio raised to a power, x, and a constant. Using the least squares method, a straight line was fitted to the log/log data with the *Excel* software package, commercially available from Microsoft Corporation. The slope of the line, the y-intercept, and the coefficient of correlation, were determined by the software regression subroutine.

To reduce the number of unknowns to be determined by the software, the value of the exponential, x, was arbitrarily set equal to 1.0 for each of the two Scruton numbers, *Sc1* and *Sc2*. The constants *C1* and *C3* were calculated from the output of the linear regression by inputting trial values of the constant *C2* and maximizing the coefficient of correlation. This procedure produced eight curves for each Scruton number; one curve for each aspect ratio (Figures 5.23 and 5.24). The correlation coefficients, R^2, varied from 0.45 to 0.93. Due to the small range of Scruton numbers within the data set of each aspect ratio, the procedure returned correlation coefficients that were insensitive to small changes in the value of *C2*; even though the small changes in *C2* resulted in relatively large variations in the value of *C3*.

In an attempt to validate the method of determining the equation constants, the experimental data obtained from Figure 2.5 (Goswami et al, 1993) was fitted to a

power curve equation similar to Equation 2.14 using the iterative method described above. The procedure returned coefficients *C1*, *C2*, and *C3* that were approximately equal to the coefficients of Equation 2.14 and a correlation coefficient equal to 0.94. However, as was found when fitting curves to the current data, small variations in the value of *C2* resulted in large variations in the value of *C3* while the correlation coefficient remained equal to 0.94. Therefore, this method of determining equation constants was abandoned due to the infinite number of solutions with nearly equal correlation coefficients.

5.4.4. Best-fit curve using *TableCurve 2D*. The commercially available software package *TableCurve 2D*, produced and marketed by Jandel Scientific Software, was then utilized to determine one equation based on the set of forty data points. The software evaluates the applicability of up to approximately 9,000 equation forms from the software's built-in equation library. The software then determines the constants and correlation coefficient for each suitable equation and ranks the equations in descending order based on the correlation coefficient values.

Operating on the 40 sets of current data, the program identified 29 possible equation forms. Of the 29 equations, eight were decay type equations that exhibited asymptotic behavior relative to the x-axis and that returned finite values of y when the value of x approached zero. Of the eight decay type equations, the following equation was selected for use in the current study,

$$y = \left[a^{1-c} + bx(c-1)\right]^{\frac{1}{1-c}} \quad \text{(Equation 5.6)}$$

This equation meets the criteria discussed above pertaining to the x- and y-axes. Furthermore, the equation can be rewritten into the form of Equation 2.14 and Equation 5.3. Constants a, b, and c and the correlation coefficient, R^2, were determined by the *TableCurve 2D* software. Coefficients *C1*, *C2*, and *C3* were subsequently determined by calculation using the output from the software.

To validate the use of Equation 5.6, the data from Figure 2.5 (Goswami et al, 1993) was evaluated using the *TableCurve 2D* software. Based on the data from Figure 2.5 and the output from the *TableCurve 2D* software, the vortex-induced response equation for circular cylinders was determined to be,

$$\frac{y_o}{D} = \frac{1.09}{\left[1 + 33.0St^2(Sc)\right]^{3.15}} \quad \text{..... (Equation 5.7)}$$

The software returned a coefficient of correlation, R^2, equal to 0.94 for the trial data. The reduced amplitudes determined from Equations 5.2 and 5.7, along with the data published by Goswami et al (1993) are plotted in Figure 5.25.

The *TableCurve 2D* software was then utilized to determine the constants for Equation 5.6 using the response data set from the 40 test cases. This was done in lieu of evaluating the five data sets from each of the eight aspect ratios as was attempted earlier with the *Excel* software. However, as noted, the values of the constants and exponential depend on the form of Scruton number.

5.4.5. Value of exponentials. The 40 data sets were read into the curve-fit software and evaluated for each of the Scruton numbers, *Sc1* and *Sc2*. The nondimensional input data included the reduced amplitude, y_0/D, and the product of the Scruton number and the aspect ratio raised to an exponential x, $(Scn)(L/D)^x$.

For *Sc1*, the value of the exponential, x, was arbitrarily selected to vary from 1.0 to 3.0 in half-integer increments; that is, x = 1.0, 1.5, 2.0, 2.5, 3.0. For *Sc2*, the value of the exponential was selected to vary from 1.0 to 4.0 in half-integer increments. In all, twelve data sets were evaluated.

The results obtained from the curve-fit software based on the twelve sets of data indicated that the best-fit curve for *Sc1* was obtained when x = 2 and for *Sc2* when x = 3. In both cases the value of the correlation coefficient was equal to R^2 = 0.94. For both forms of Scruton number, the software returned higher values of the correlation coefficient as the value of the exponential, x, was increased. However, when the value of the exponential was increased, the software returned response equation constants that resulted in smaller values of the maximum reduced amplitude.

After analyzing the twelve sets of data, the value of the exponential, x, was determined according to the following procedure. The maximum reduced amplitudes predicted from each of the two derived equations were plotted against the value of the exponential (Figures 5.26 and 5.27). Furthermore, the weighted maximum reduced amplitudes; that is, the product of the maximum reduced amplitudes and correlation coefficients, were plotted against the value of the exponentials (Figure 5.26 and 5.27). Second order polynomials were fitted to the sets of points as shown in the two figures. The first derivative of each polynomial was calculated and set equal to zero to locate the maximum reduced amplitude. The value of the exponential at the point of maximum reduced amplitude was taken as the value of the exponential in the response equation, Equation 5.6.

For *Sc1*, the maximum reduced amplitudes from the two curves were found when the value of the exponential, x, is equal to 1.92 and 2.19, respectively. From Figure 5.26, the two values of the exponential are seen to bracket the exponential value of 2.0. Thus, when the Scruton number is defined as *Sc1* the value of the exponential was taken to be 2.0.

Likewise for *Sc2*, the maximum reduced amplitudes from the two curves were found when the value of the exponential is equal to 2.88 and 3.17, respectively. From Figure 5.27, the two values of the exponential are seen to bracket the exponential value of 3.0. Thus the value of the exponential was taken to be 3.0 when the Scruton number is defined as *Sc2*.

The curve-fit software output, including the equation constants and correlation coefficients, and the calculated equation constants from Equation 5.6 are presented in Table 5.5 for the two sets of Scruton numbers, *Sc1* and *Sc2*, with the value of the exponential equal to 2 for *Sc1* and equal to 3 for *Sc3*.

Table 5.5. Response equation constants

	Results from *TableCurve 2D* software				Calculated equation constants		
Scruton number	*a*	*b*	*c*	R^2	*C1*	*C2*	*C3*
Sc1	0.176	1.93	2.18	0.94	0.176	0.293	0.85
Sc2	0.176	1.88	2.17	0.94	0.176	0.287	0.85

5.4.6. Rectangular Scruton number. Using the constants from Table 5.5, the two response equations take the form,

$$\frac{y_o}{D} = \frac{0.176}{\left[1 + 0.29\left(\frac{L}{D}\right)^{x}(Scn)\right]^{0.85}} \quad \text{(Equation 5.8)}$$

where n is equal to 1 or 2, depending on which Scruton number is used and the value of the exponential, x, is equal to 2 when $Sc1$ is used and equal to 3 when $Sc2$ is used.

Evaluating the product inside the bracket, and ignoring the constant 0.29, it can be shown that for $Sc1$,

$$Sc1\left(\frac{L}{D}\right)^{2} = \frac{m_e\zeta}{\rho D^2}\left(\frac{L^2}{D^2}\right) = \frac{m_e\zeta}{\rho}\frac{L^2}{D^4} \quad \text{(Equation 5.9)}$$

and for $Sc2$,

$$Sc2\left(\frac{L}{D}\right)^{3} = \frac{m_e\zeta}{\rho DL}\left(\frac{L^3}{D^3}\right) = \frac{m_e\zeta}{\rho}\frac{L^2}{D^4} \quad \text{(Equation 5.10)}$$

Therefore, by substituting 2 for the value of the exponential in Equation 5.9; and 3 for the value of the exponential in Equation 5.10, the two equations are equivalent. Consequently, the Scruton number for rectangular members, $Sc(r)$, is defined as the product of the mass ratio, the system damping, and a geometric function that is dependent on the along-wind length, L, and the across-wind thickness, D,

$$Sc(r) = \frac{m_e\zeta}{\rho}\frac{L^2}{D^4} \quad \text{(Equation 5.11)}$$

When the rectangular Scruton number is defined by Equation 5.11, the amplitude response equation (Equation 5.8) is seen to be independent of the modified Strouhal number, just as the response equation developed for circular cylinders is

independent of the traditional Strouhal number. The reduced amplitudes from the current study are plotted against the rectangular Scruton number, *Sc(r)*, in Figure 5.28.

5.4.7. Single response equation. With the rectangular Scruton number defined as *Sc(r)* in Equation 5.11, a single equation is derived from Equation 5.8 that returns the reduced amplitude response due to vortex-induced vibration of rectangular cylinders given the rectangular Scruton number. The response equation is written as,

$$\frac{y_o}{D} = \frac{0.176}{\left[1 + 0.29Sc(r)\right]^{0.85}} \quad \text{(Equation 5.12)}$$

This equation is plotted in Figure 5.29 along with the experimental data of each aspect ratio in terms of the rectangular Scruton number, *Sc(r)*. As seen in the figure, the equation accurately describes the response behavior of the forty models when *Sc(r)* is plotted along the horizontal axis. Furthermore, Equation 5.12 is seen to satisfy the asymptotic requirement when the Scruton number becomes large and the maximum, self-limiting reduced amplitude requirement as the Scruton number becomes small.

5.4.8. Summary. Circular cylinders are excited by trailing edge vortices and the vortex-induced response is a function of the Scruton number that is independent of the traditional Strouhal number. Therefore, a single response equation, Equation 5.2, describes the maximum reduced amplitude of the vortex-induced response for all circular cylinders. For the rectangular models tested during the current study, the vortex-induced vibrations were excited primarily by impinging leading edge

vortices rather than trailing edge vortices due to the flow separation at the leading edge. Consequently, the vortex-induced response of rectangular bodies is not a function of the traditional Strouhal number.

Due to the exciting forces that act along the length of the rectangular cylinders, the response is a function of the mass/damping parameter and of the aspect ratio, *L/D*. Analogous to the Scruton number, the rectangular Scruton number, *Sc(r)* was defined in Equation 5.11. A summary of the rectangular Scruton numbers calculated for the experimental data from the current study is tabulated in Tables 5.6 through 5.13.

With the rectangular Scruton number, *Sc(r)*, from Equation 5.11, the vortex-induced vibration response of rectangular cylinders with aspect ratio from $2 \leq L/D \leq 7$ can be predicted by a single equation, Equation 5.12. As seen in Figure 5.29, when Equation 5.12 is plotted and compared to the data from the current study, the response curve accurately predicts the maximum reduced amplitude due to vortex-induced vibration at lock-in given the rectangular Scruton number, *Sc(r)*, for the system.

Table 5.6. Rectangular Scruton number, *Sc(r)*, *L/D* = 2.0

Model Designation	D *inch*	L *inch*	Mass *slugs*	Damping *% critical*	Scruton number *Sc(r)*
20.0	4	8	0.090	0.18	1.96
20.2	4	8	0.138	0.13	2.17
20.4	4	8	0.169	0.17	3.48
20.6	4	8	0.213	0.17	4.38
20.8	4	8	0.244	0.16	4.73

Table 5.7. Rectangular Scruton number, *Sc(r)*, *L/D* = 3.0

Model Designation	D *inch*	L *inch*	Mass *slugs*	Damping *% critical*	Scruton number *Sc(r)*
30.0	4	12	0.102	0.16	4.45
30.2	4	12	0.144	0.17	6.67
30.4	4	12	0.186	0.17	8.61
30.6	4	12	0.237	0.14	9.02
30.8	4	12	0.250	0.14	9.53

Table 5.8. Rectangular Scruton number, *Sc(r)*, *L/D* = 4.0

Model Designation	D *inch*	L *inch*	Mass *slugs*	Damping *% critical*	Scruton number *Sc(r)*
40.0	4	16	0.112	0.11	5.97
40.2	4	16	0.153	0.15	11.09
40.4	4	16	0.193	0.19	17.77
40.6	4	16	0.217	0.15	15.75
40.8	4	16	0.254	0.15	18.42

Table 5.9. Rectangular Scruton number, *Sc(r)*, *L/D* = 5.0

Model Designation	D *inch*	L *inch*	Mass *slugs*	Damping *% critical*	Scruton number *Sc(r)*
50.0	4	20	0.126	0.22	20.88
50.2	4	20	0.170	0.22	28.22
50.4	4	20	0.219	0.20	33.07
50.6	4	20	0.251	0.27	51.28
50.8	4	20	0.302	0.18	41.15

Table 5.10. Rectangular Scruton number, *Sc(r)*, *L/D* = 5.5

Model Designation	D *inch*	L *inch*	Mass *slugs*	Damping *% critical*	Scruton number *Sc(r)*
55.0	4	22	0.137	0.24	29.98
55.2	4	22	0.178	0.24	39.02
55.4	4	22	0.213	0.21	40.88
55.6	4	22	0.258	0.19	44.87
55.8	4	22	0.298	0.22	60.08

Table 5.11. Rectangular Scruton number, *Sc(r)*, *L/D* = 6.0

Model Designation	D *inch*	L *inch*	Mass *slugs*	Damping *% critical*	Scruton number *Sc(r)*
60.0	4	24	0.137	0.24	35.68
60.2	4	24	0.194	0.28	59.28
60.4	4	24	0.213	0.28	64.87
60.6	4	24	0.243	0.29	76.86
60.8	4	24	0.351	0.33	126.27

Table 5.12. Rectangular Scruton number, *Sc(r)*, *L/D* = 6.5

Model Designation	D *inch*	L *inch*	Mass *slugs*	Damping *% critical*	Scruton number *Sc(r)*
65.0	4	26	0.142	0.28	50.88
65.2	4	26	0.181	0.25	57.92
65.4	4	26	0.236	0.27	81.49
65.6	4	26	0.262	0.25	83.76
65.8	4	26	0.314	0.23	92.19

Table 5.13. Rectangular Scruton number, *Sc(r)*, *L/D* = 7.0

Model Designation	D *inch*	L *inch*	Mass *slugs*	Damping *% critical*	Scruton number *Sc(r)*
70.0	4	28	0.151	0.32	71.57
70.2	4	28	0.186	0.28	77.01
70.4	4	28	0.217	0.20	64.19
70.6	4	28	0.278	0.21	86.61
70.8	4	28	0.314	0.21	97.63

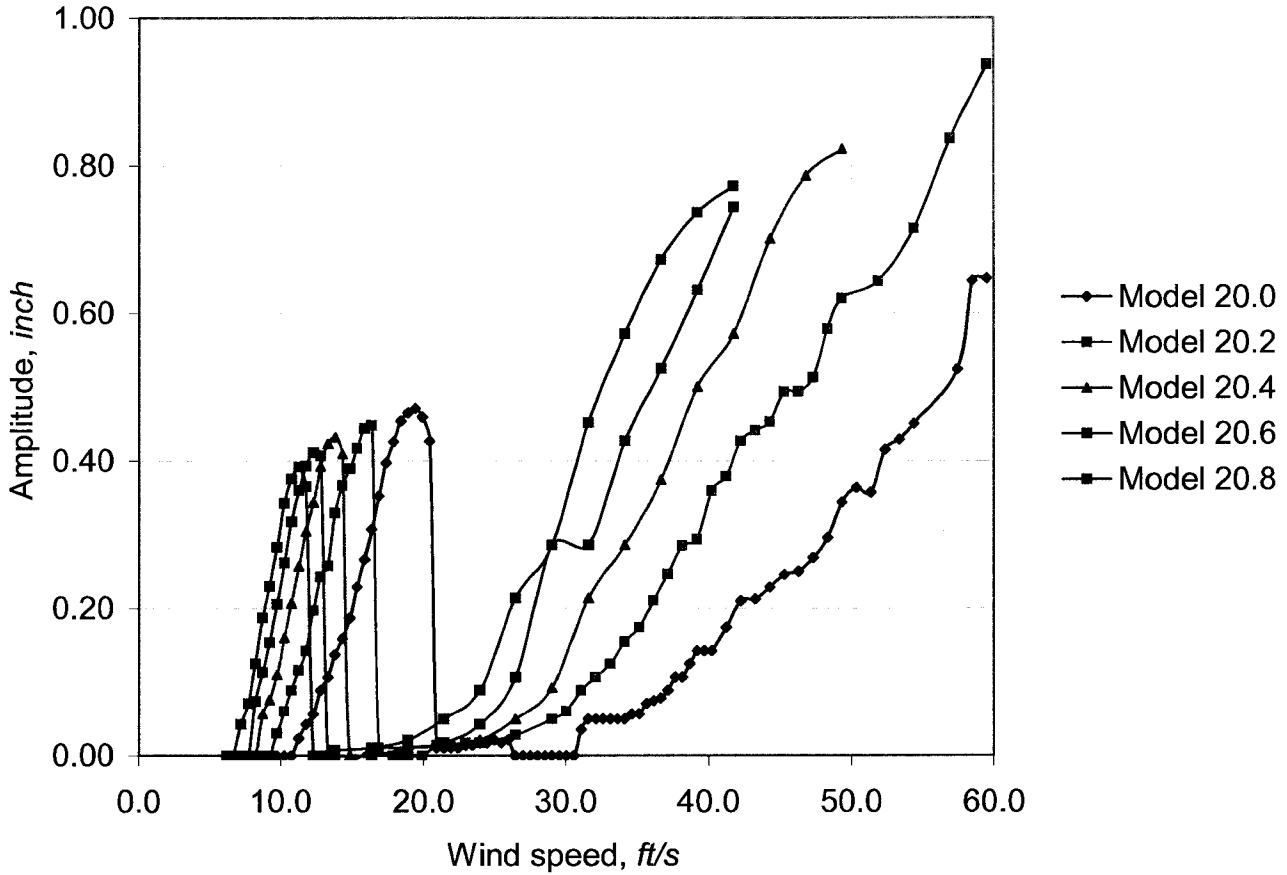

Figure 5.1. Amplitude vs. wind speed, $L/D = 2.0$

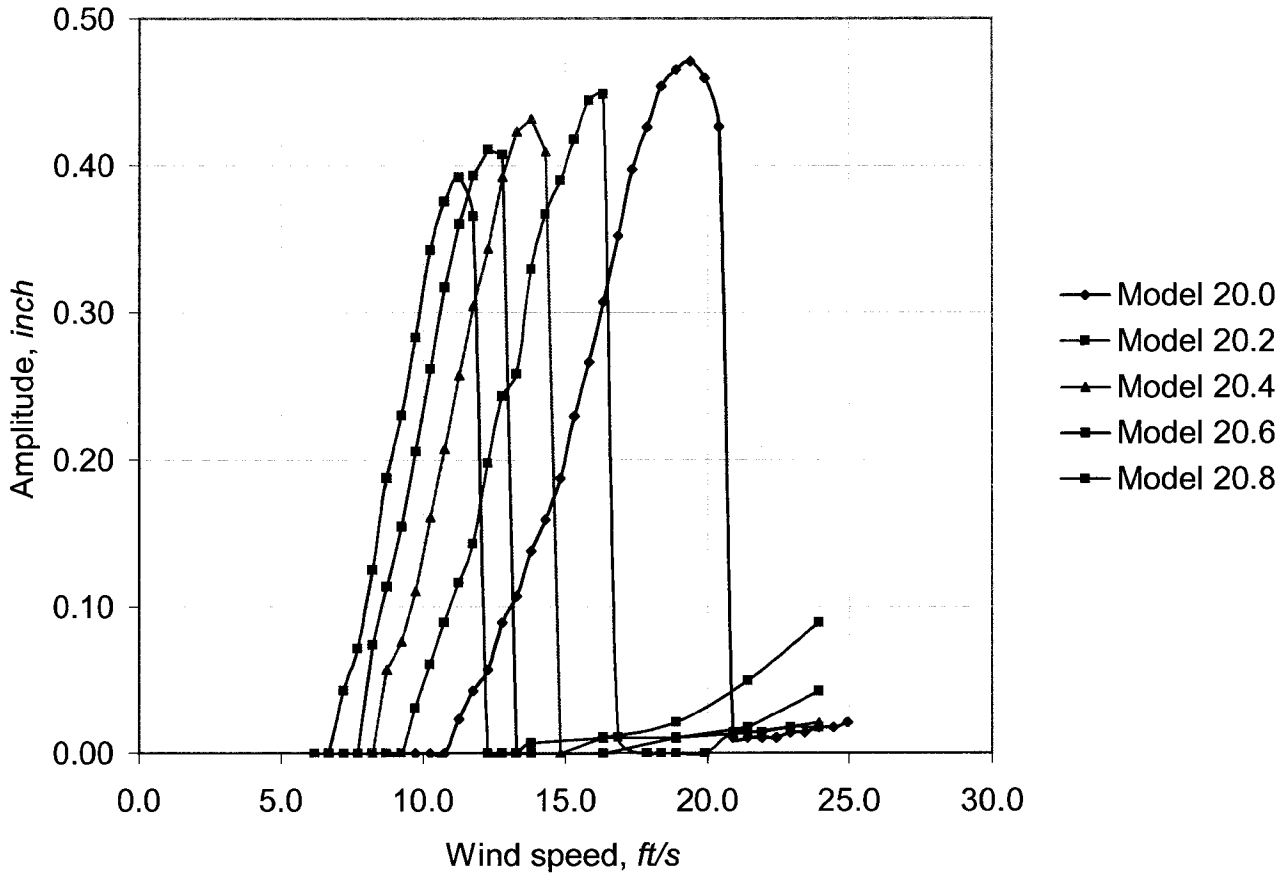

Figure 5.2. Amplitude vs. wind speed, $L/D = 2.0$

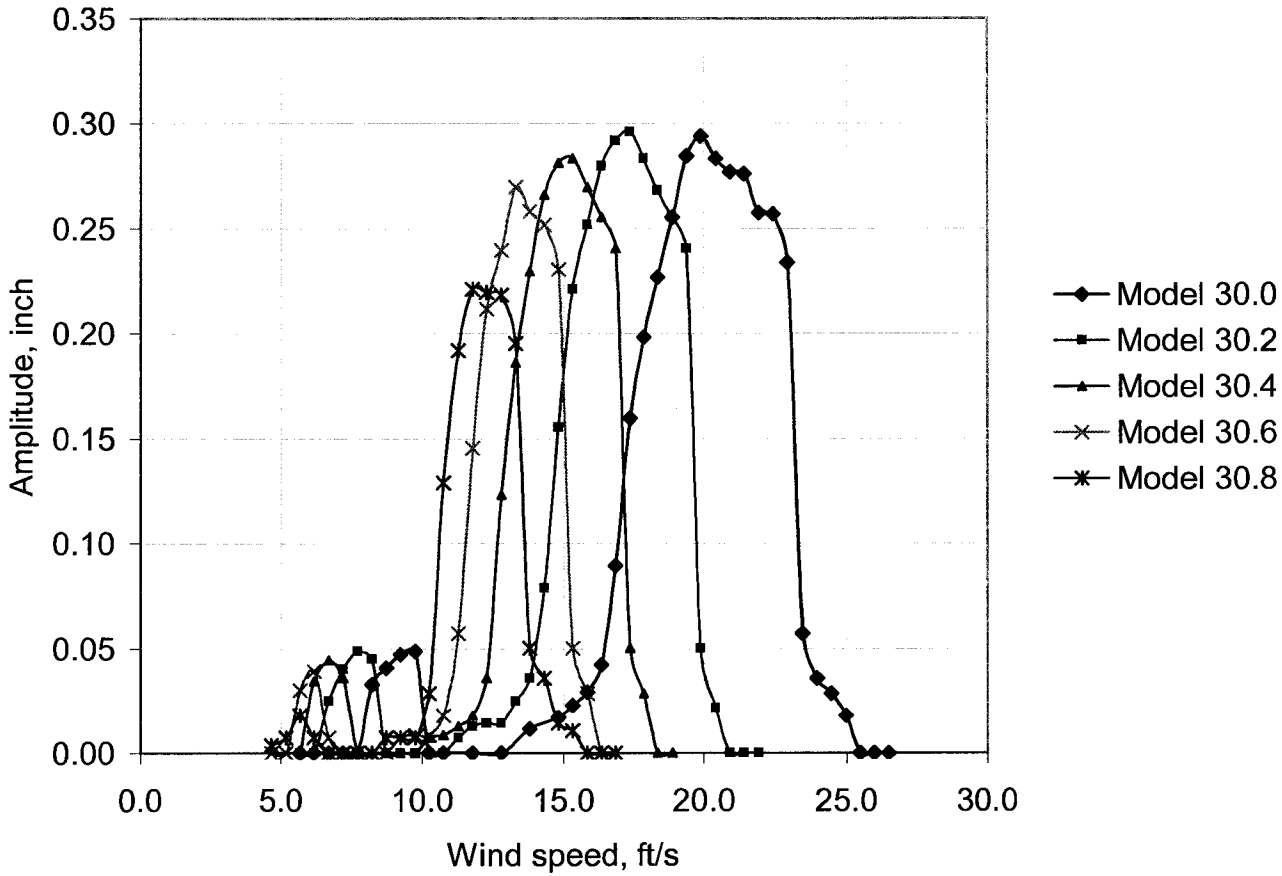

Figure 5.3. Amplitude vs. wind speed, $L/D = 3.0$

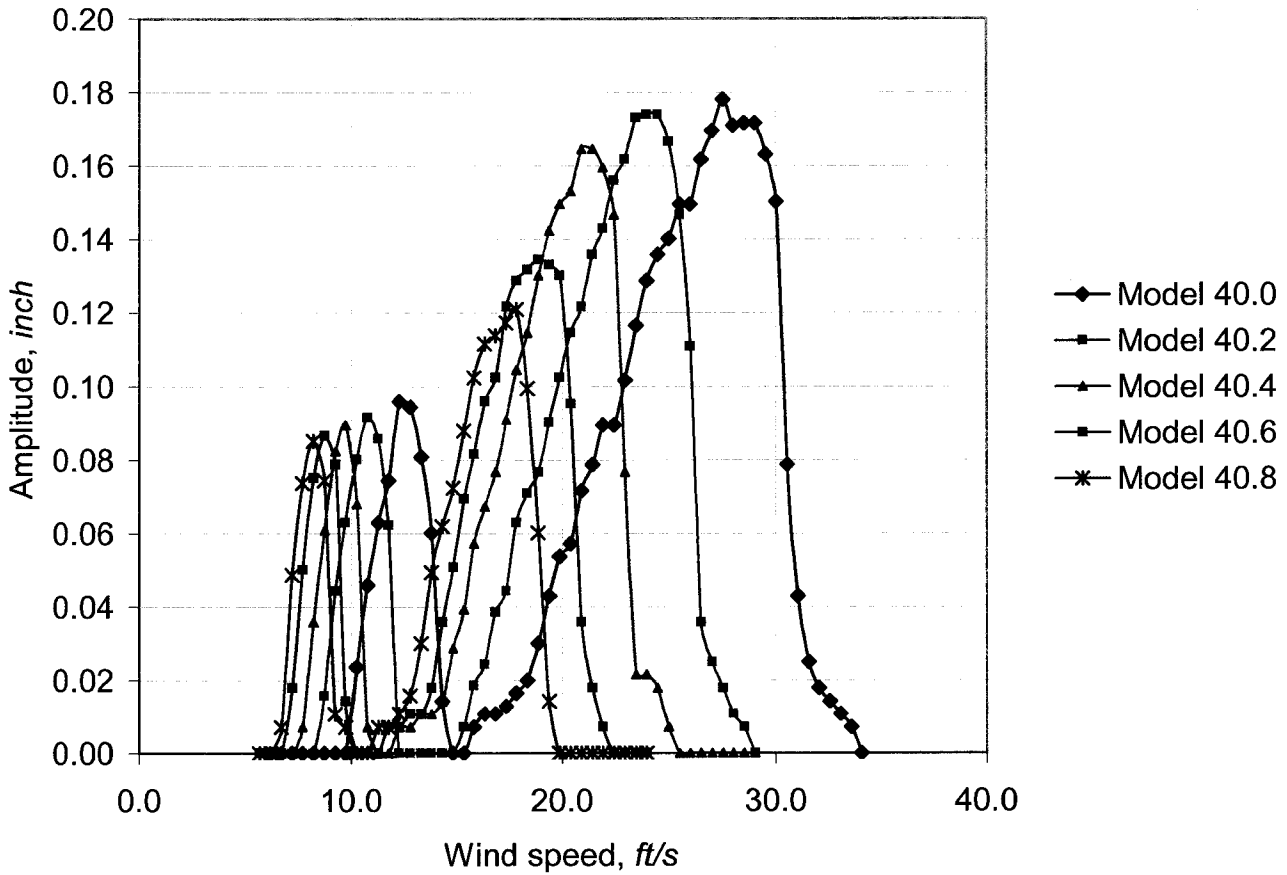

Figure 5.4. Amplitude vs. wind speed, $L/D = 4.0$

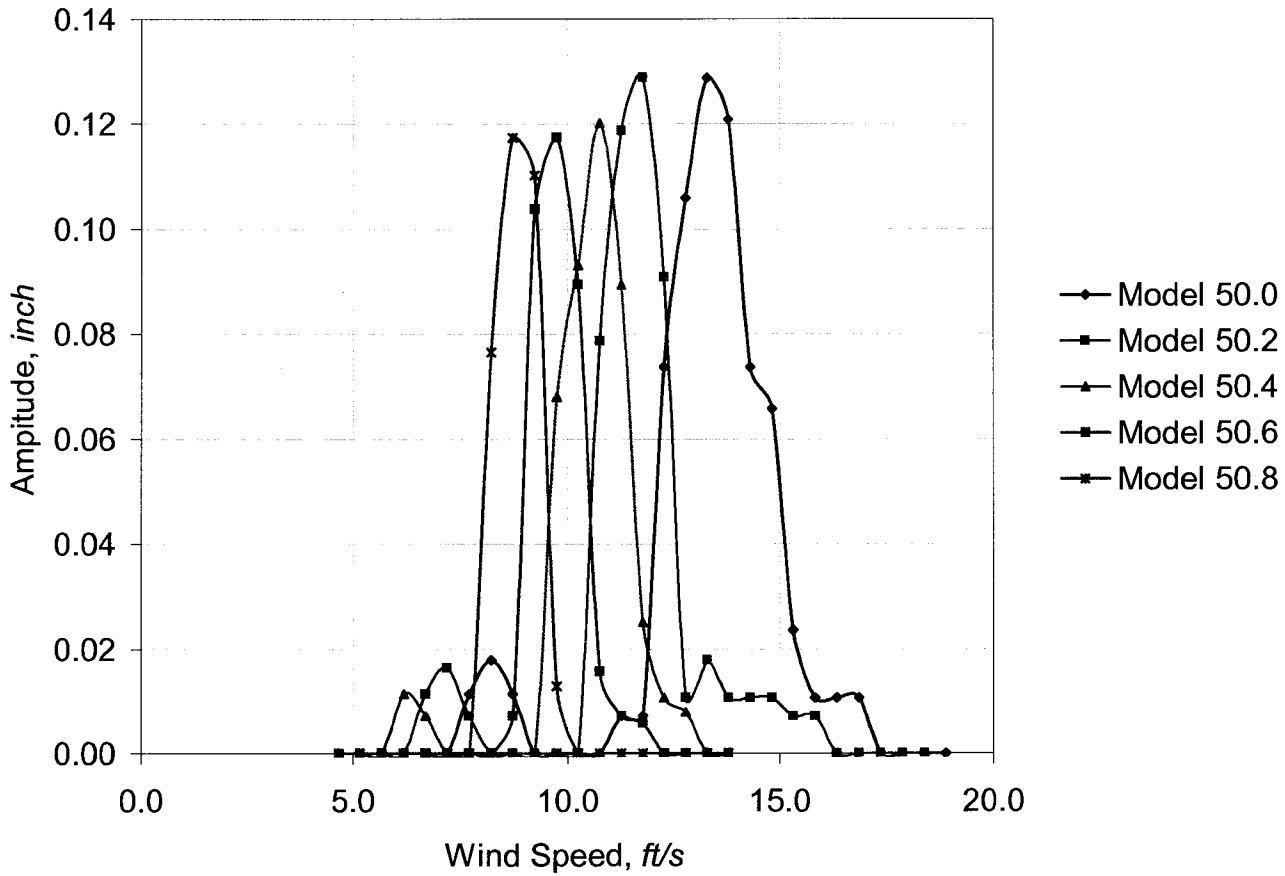

Figure 5.5. Amplitude vs. wind speed, $L/D = 5.0$

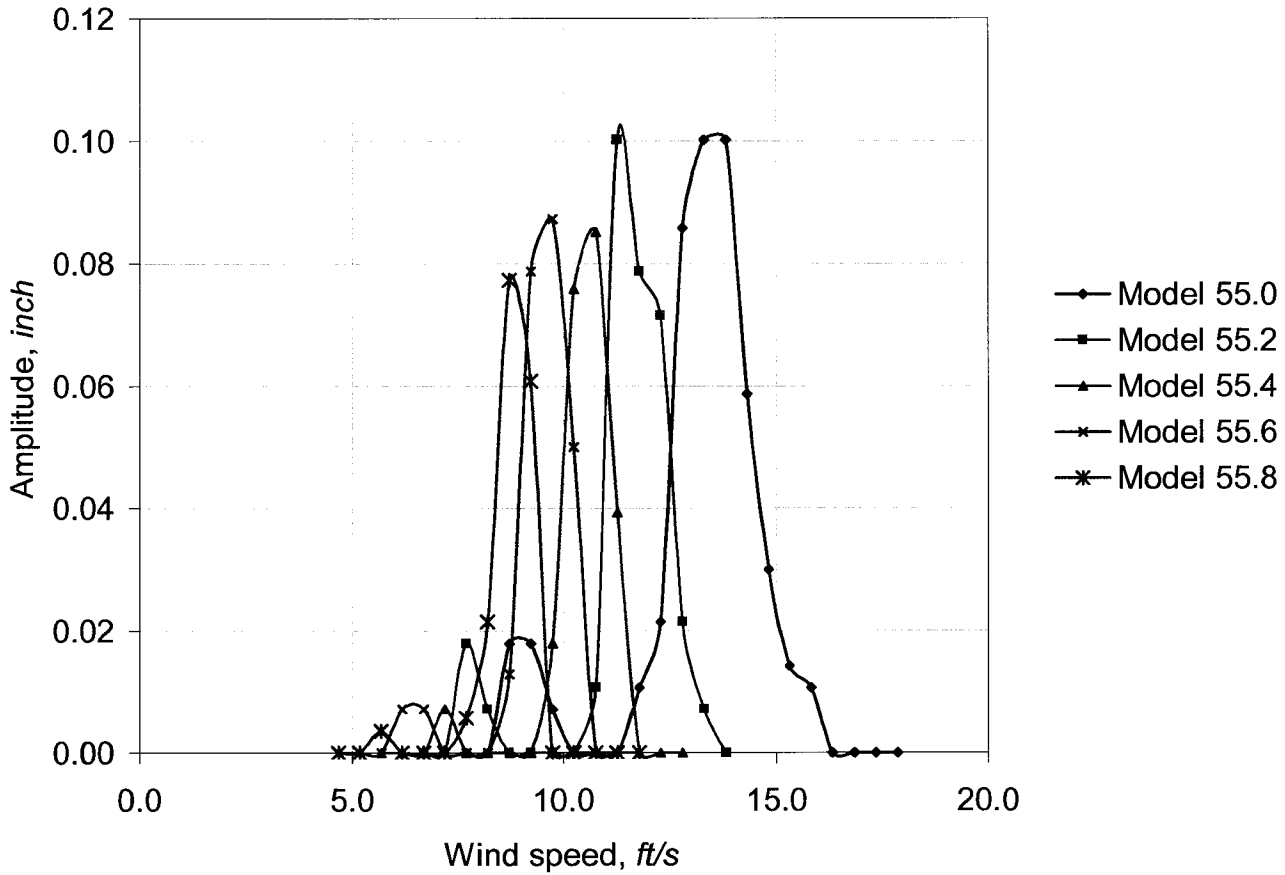

Figure 5.6. Amplitude vs. wind speed, $L/D = 5.5$

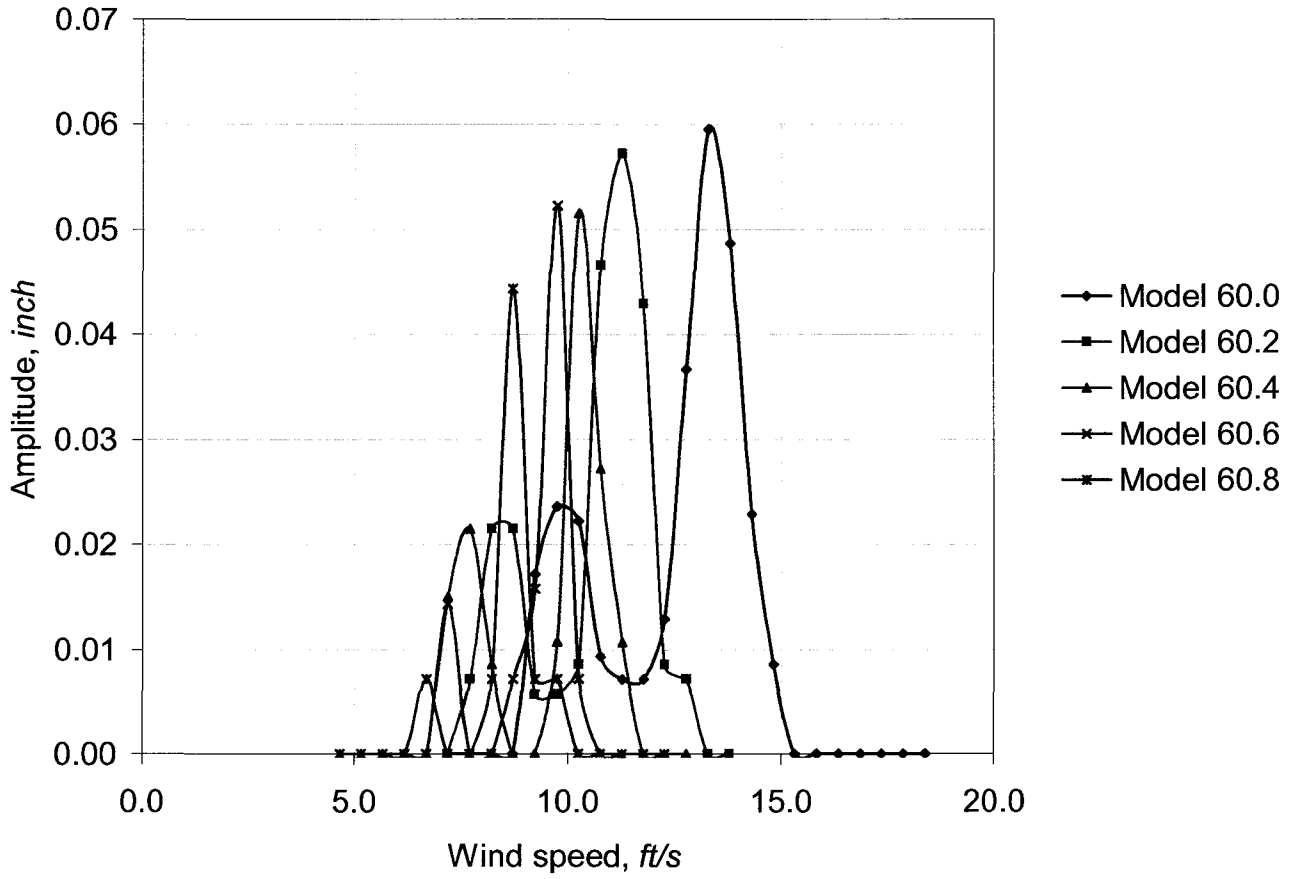

Figure 5.7. Amplitude vs. wind speed, $L/D = 6.0$

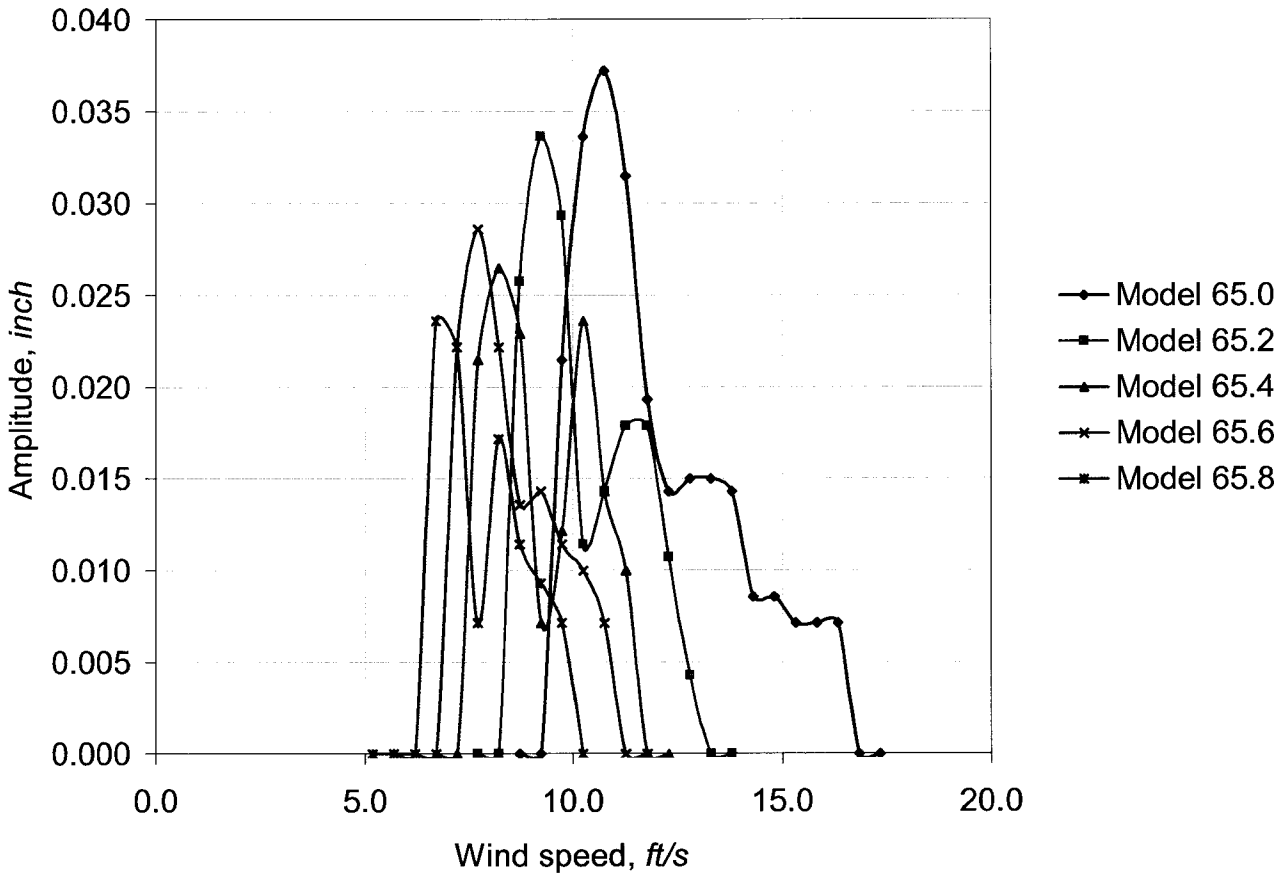

Figure 5.8. Amplitude vs. wind speed, $L/D = 6.5$

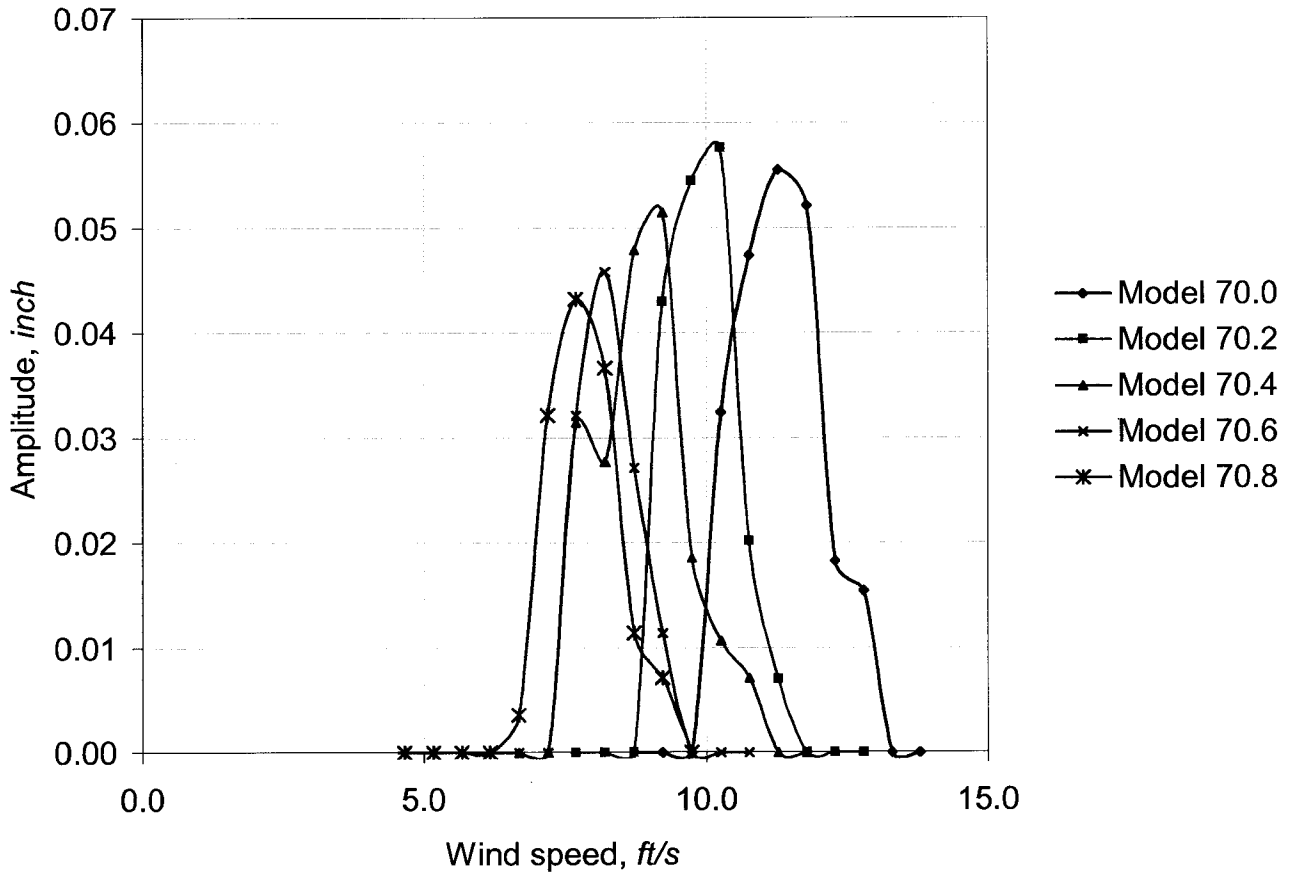

Figure 5.9. Amplitude vs. wind speed, $L/D = 7.0$

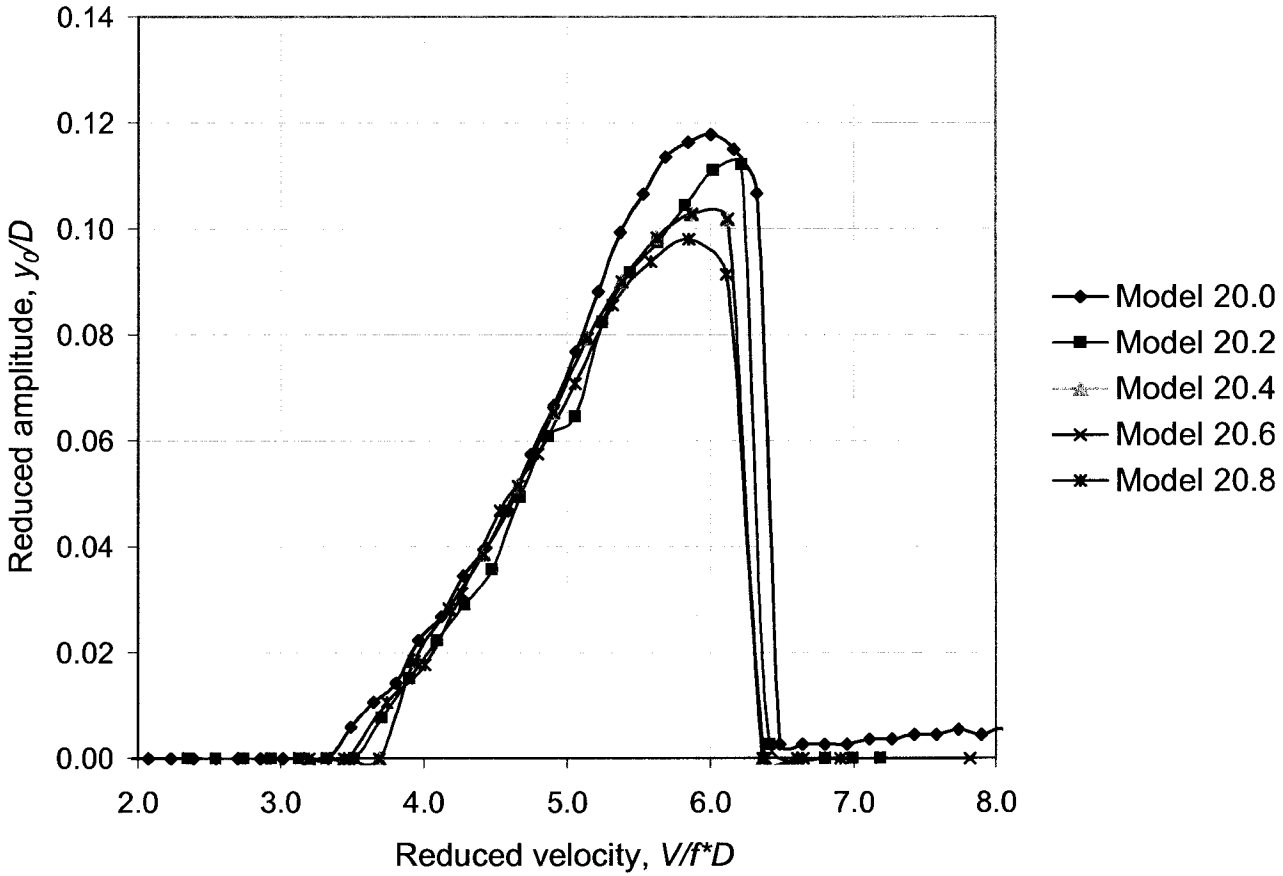

Figure 5.10. Reduced amplitude vs. reduced velocity, $L/D = 2.0$

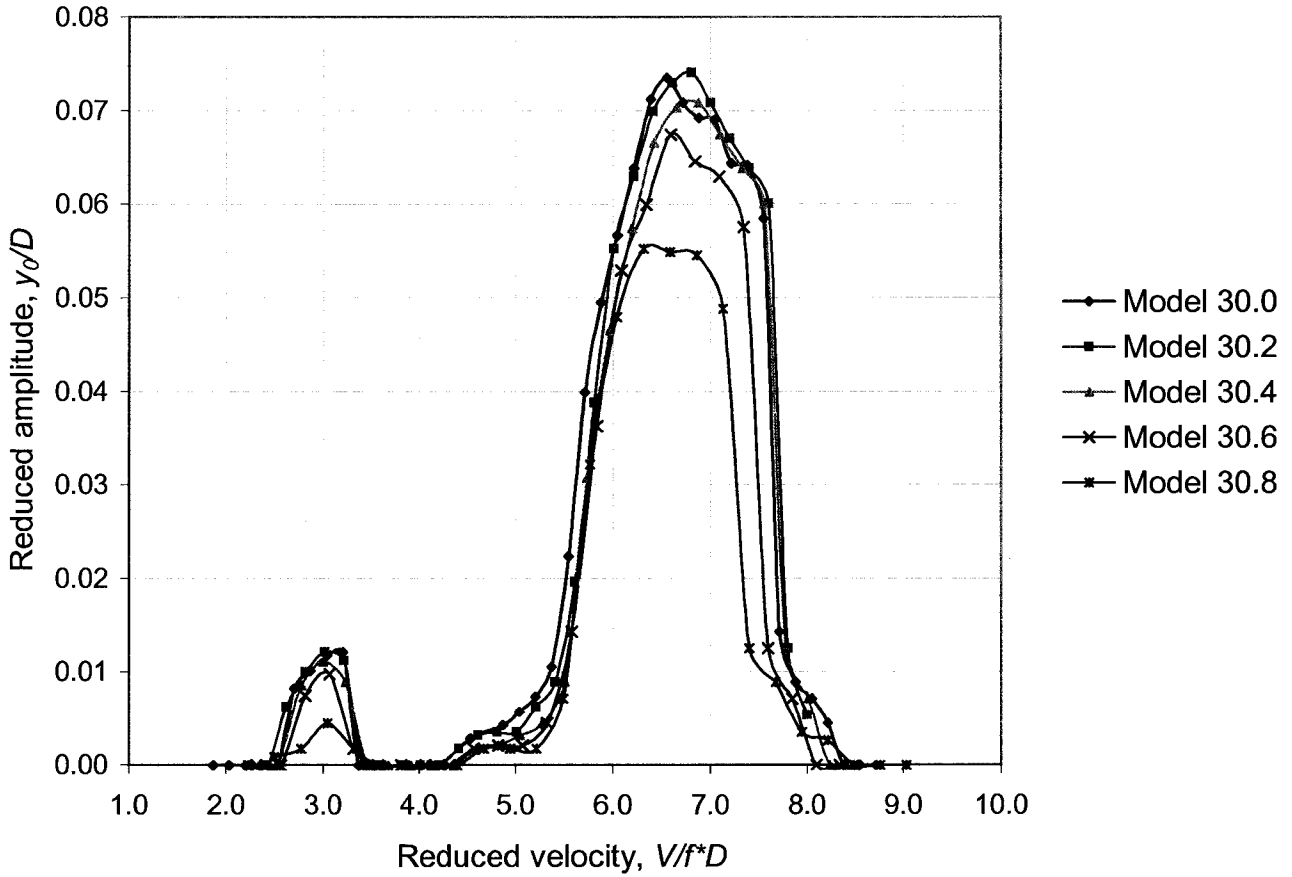

Figure 5.11. Reduced amplitude vs. reduced velocity, $L/D = 3.0$

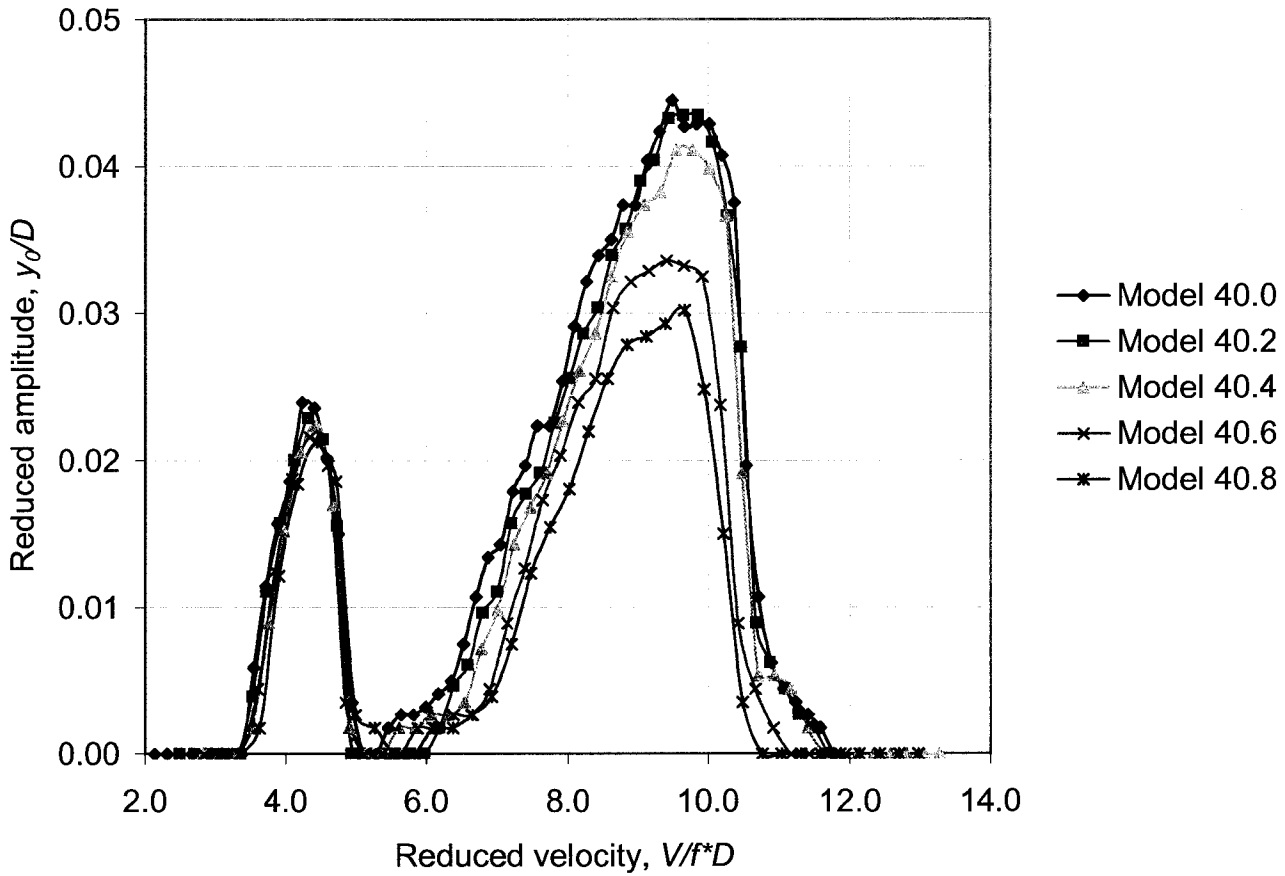

Figure 5.12. Reduced amplitude vs. reduced velocity, $L/D = 4.0$

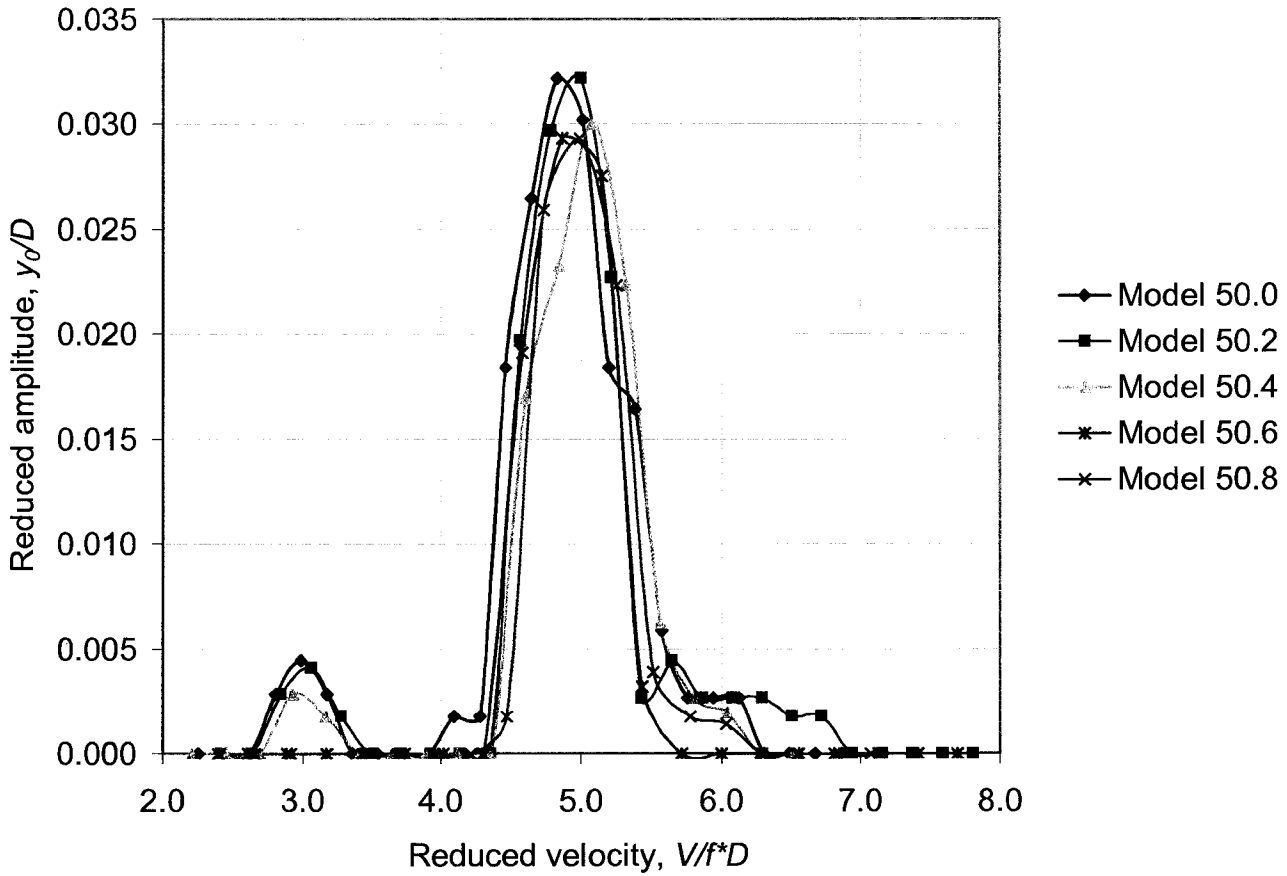

Figure 5.13. Reduced amplitude vs. reduced velocity, $L/D = 5.0$

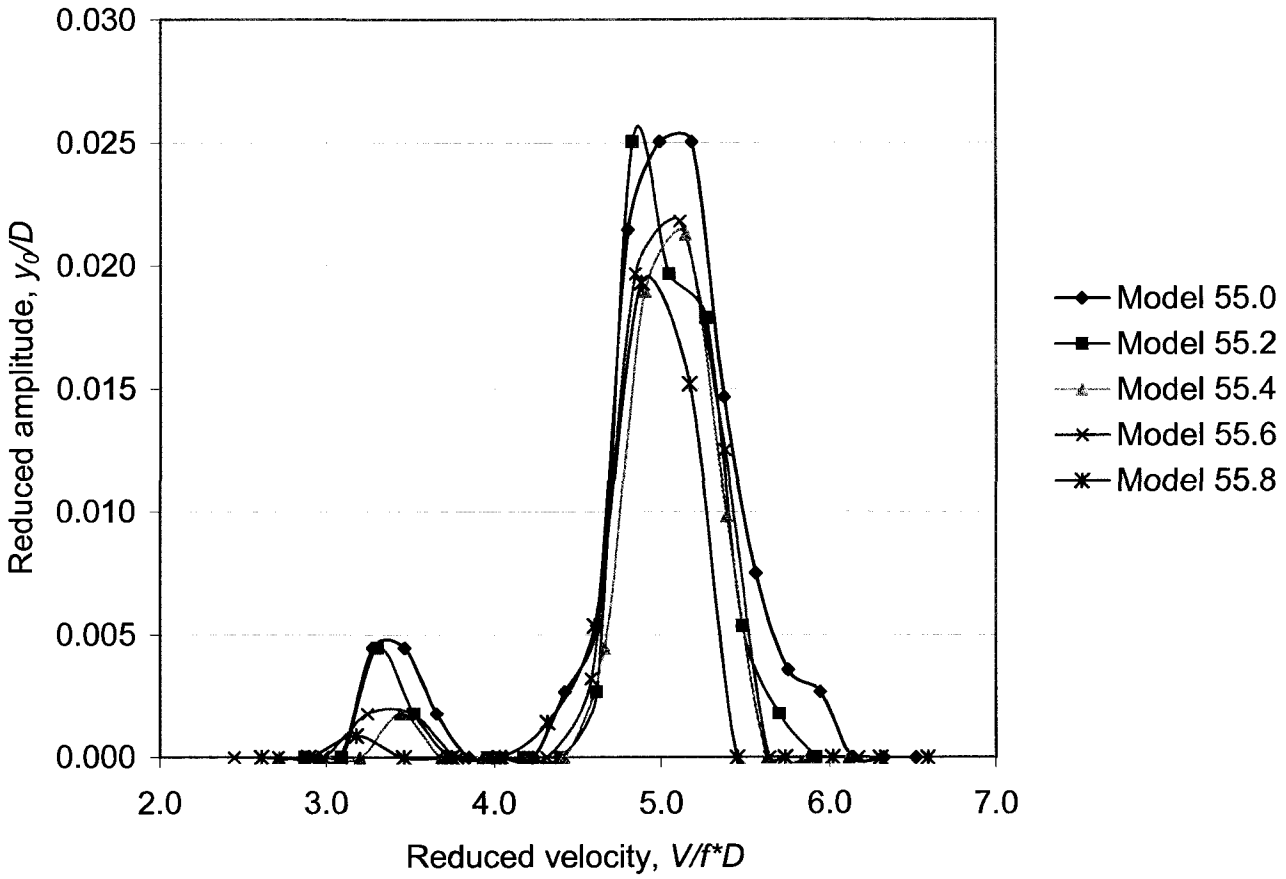

Figure 5.14. Reduced amplitude vs. reduced velocity, $L/D = 5.5$

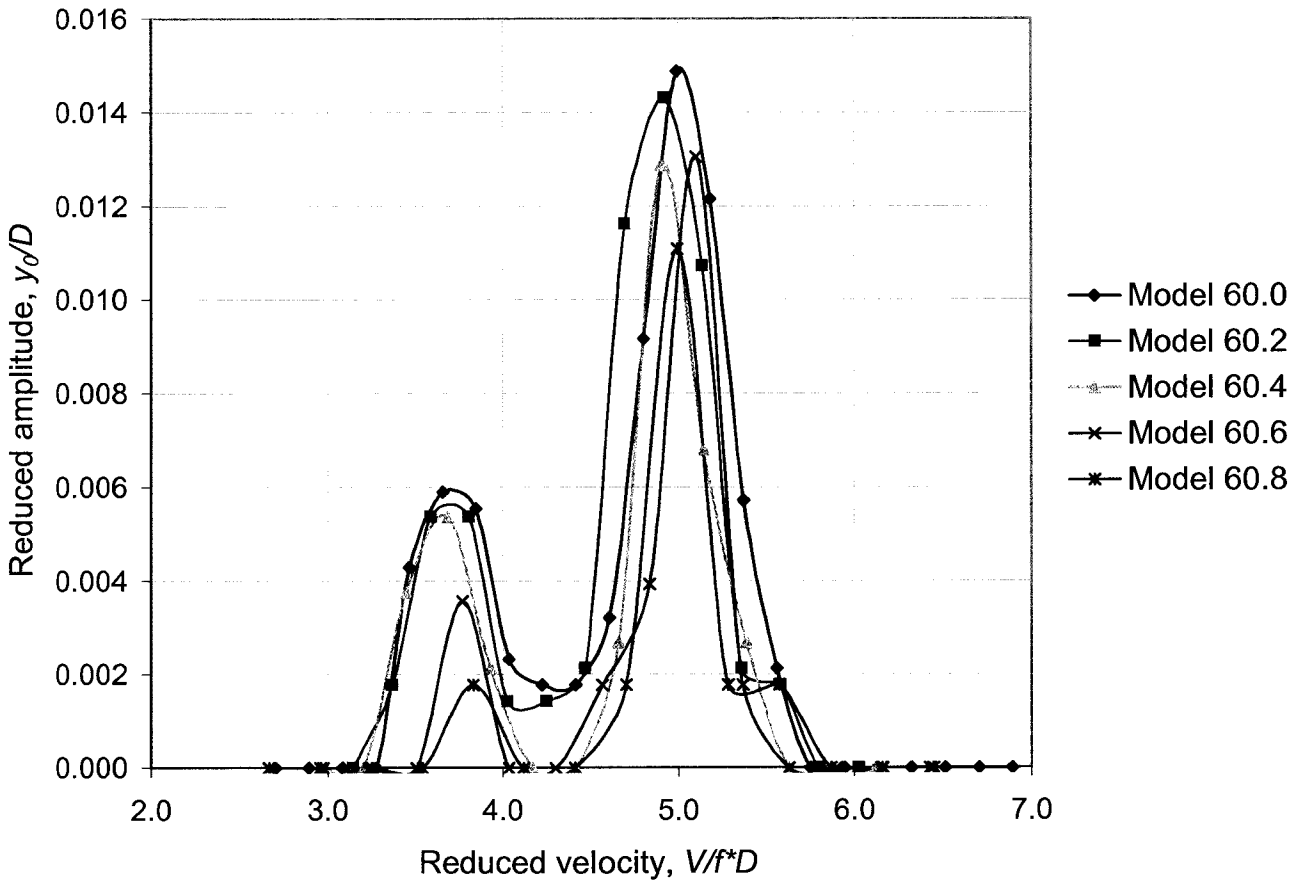

Figure 5.15. Reduced amplitude vs. reduced velocity, $L/D = 6.0$

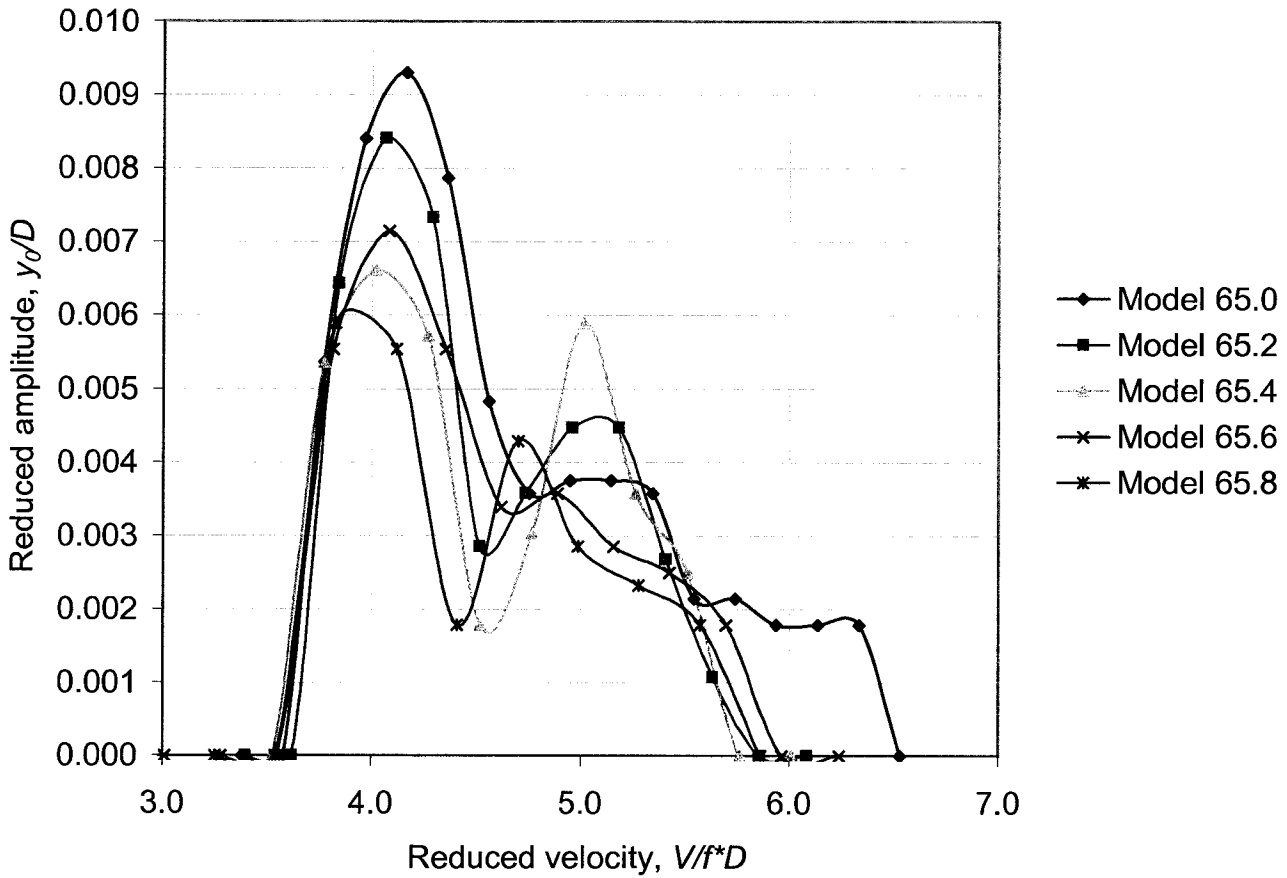

Figure 5.16. Reduced amplitude vs. reduced velocity, $L/D = 6.5$

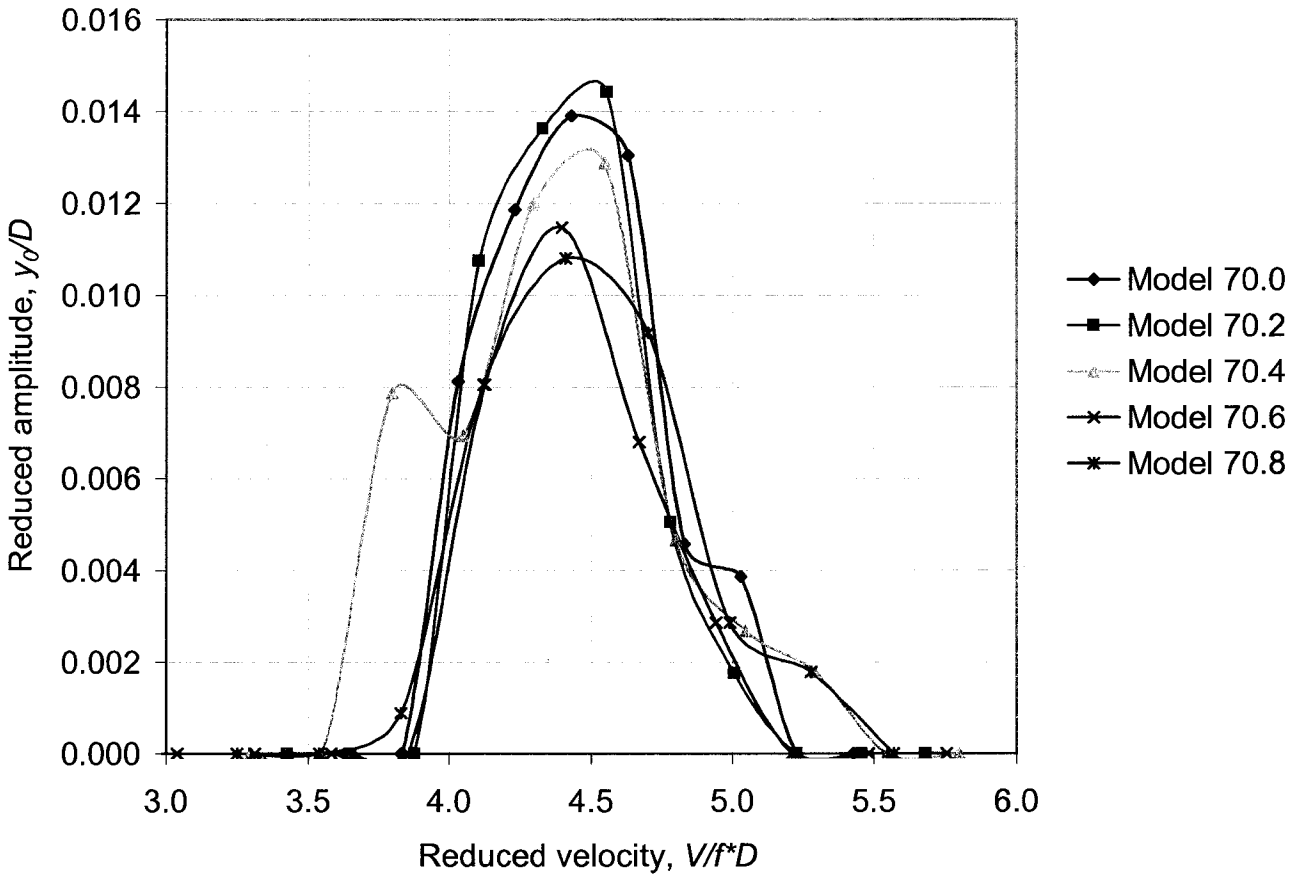

Figure 5.17. Reduced amplitude vs. reduced velocity, $L/D = 7.0$

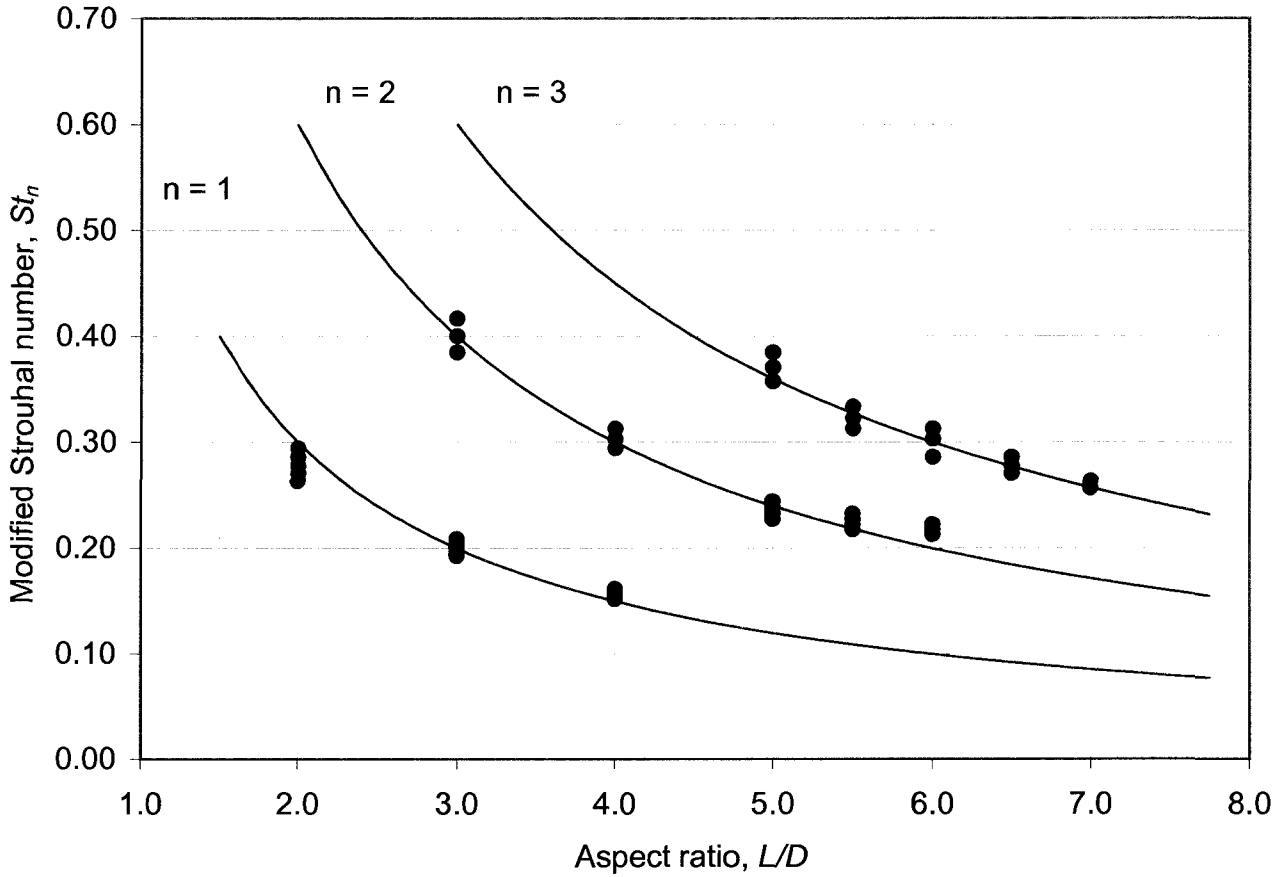

Figure 5.18. Modified Strouhal number vs. aspect ratio, *L/D*

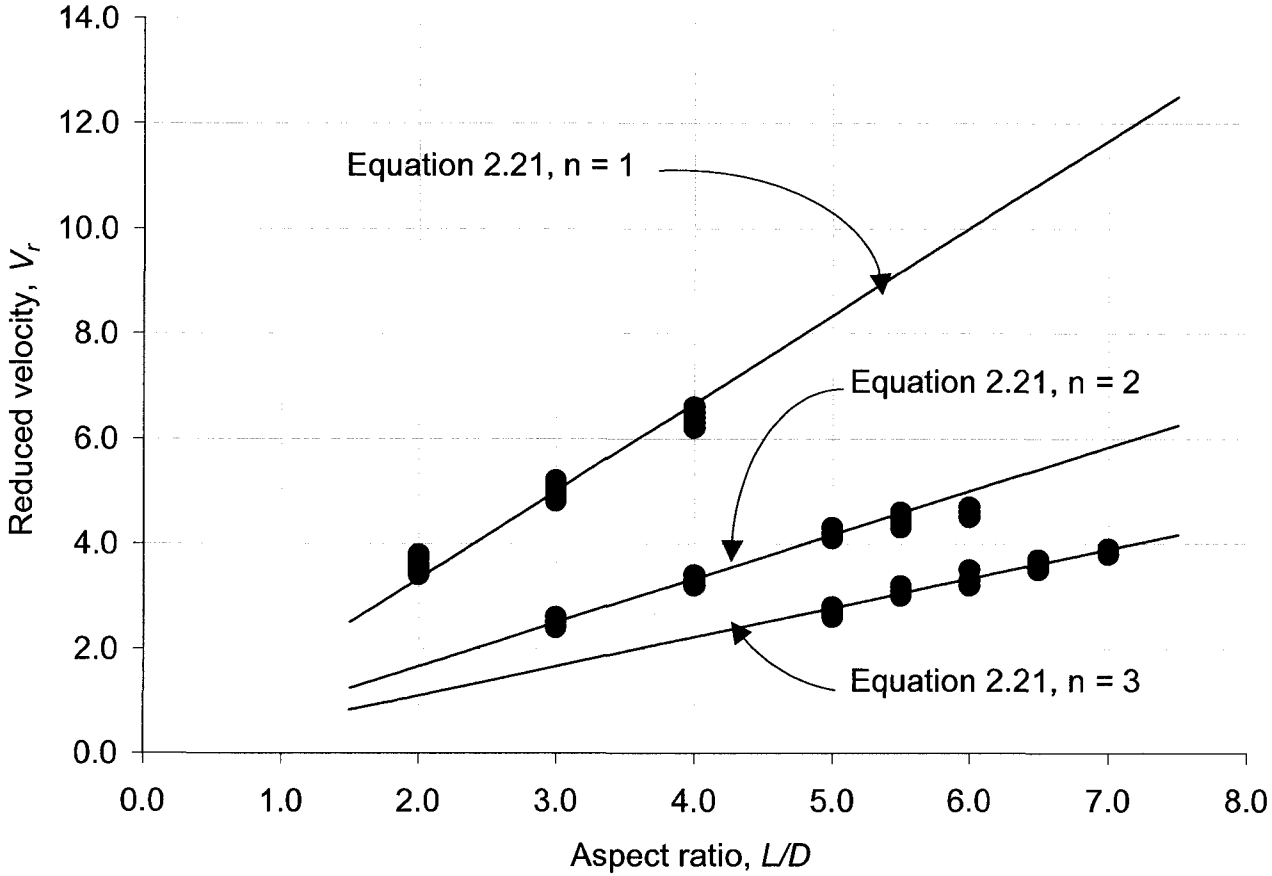

Figure 5.19. Reduced velocity vs. aspect ratio, *L/D*

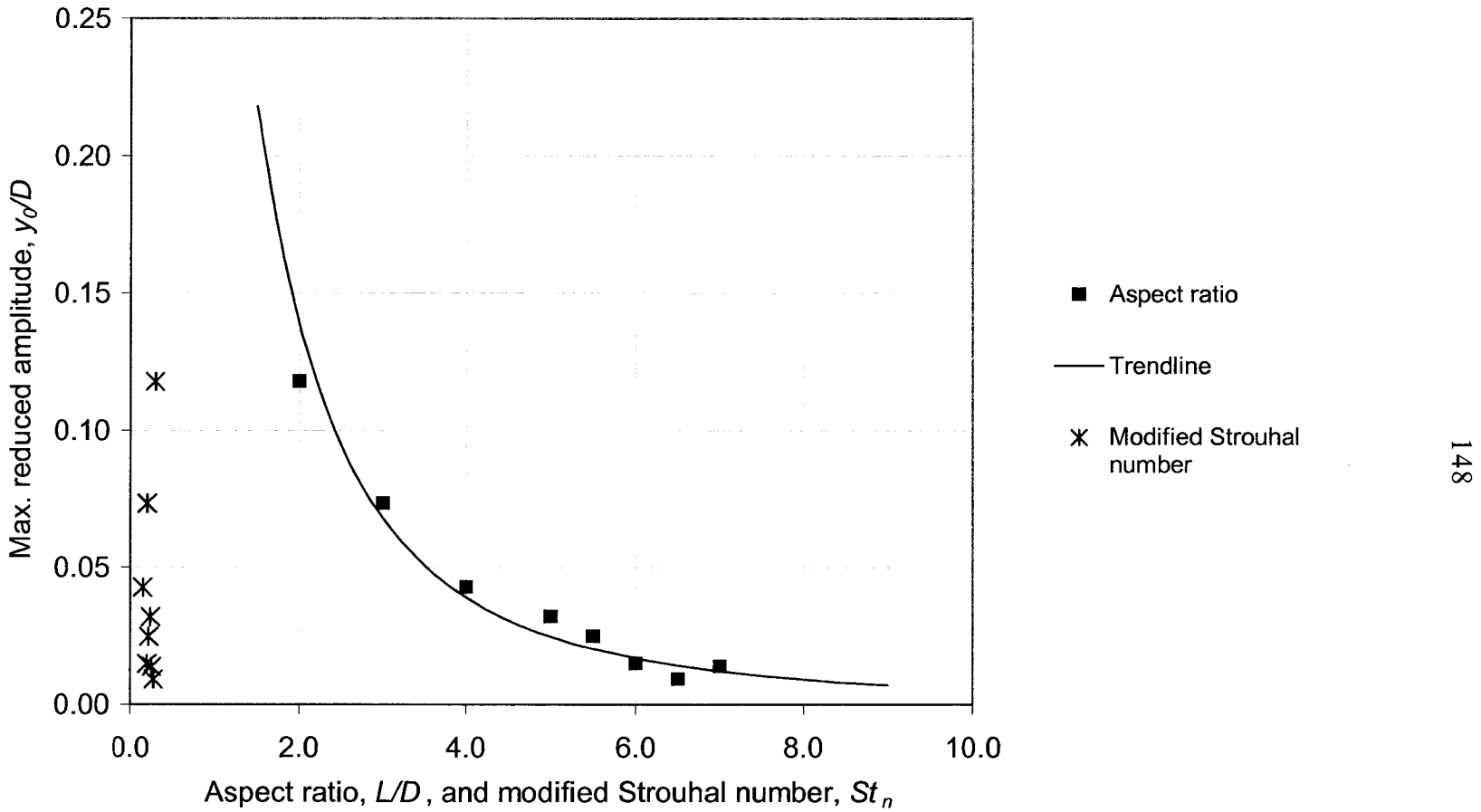

Figure 5.20. Maximum y_0/D vs. L/D and St_n

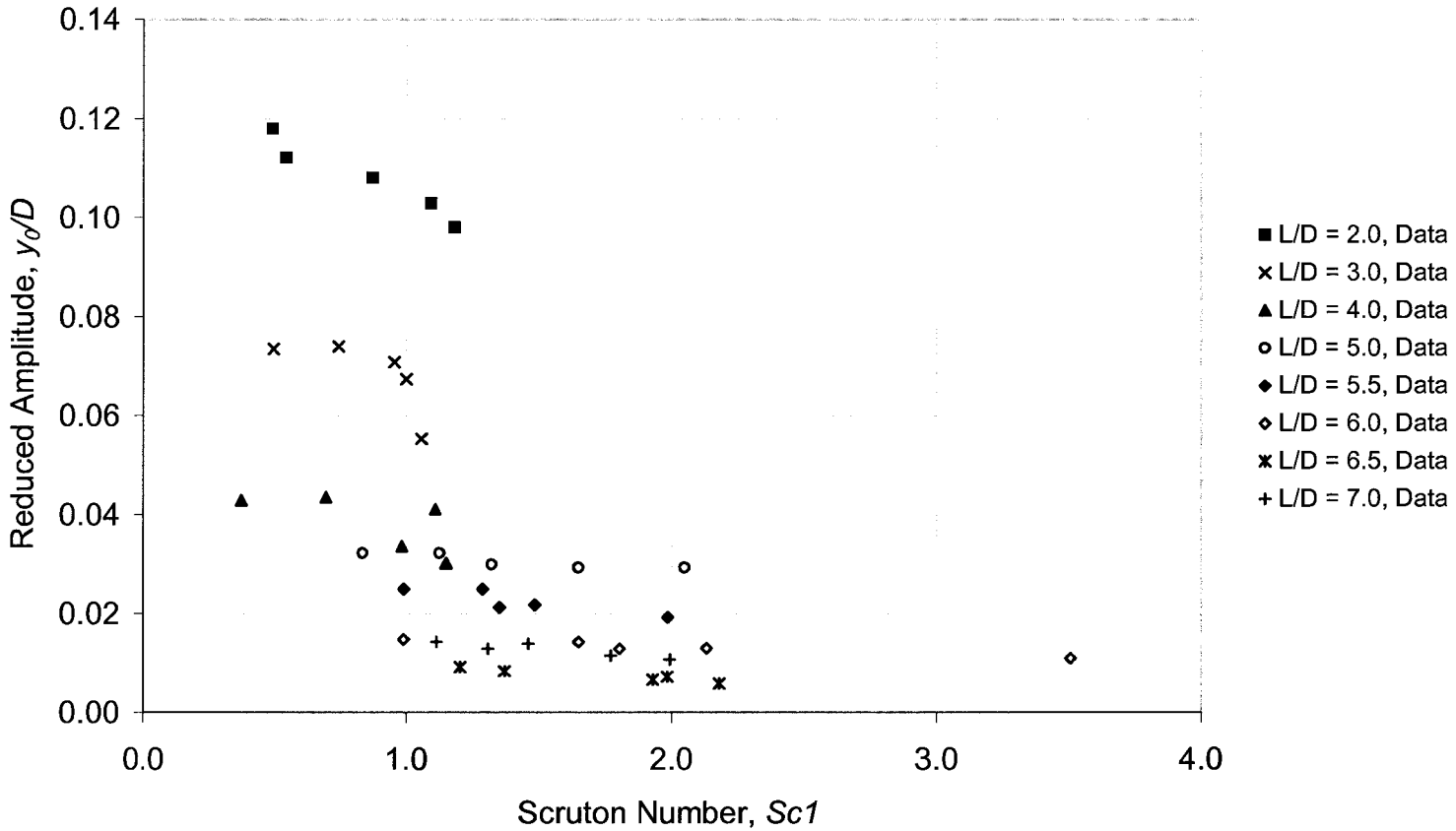

Figure 5.21. Reduced amplitude vs. *Sc1*

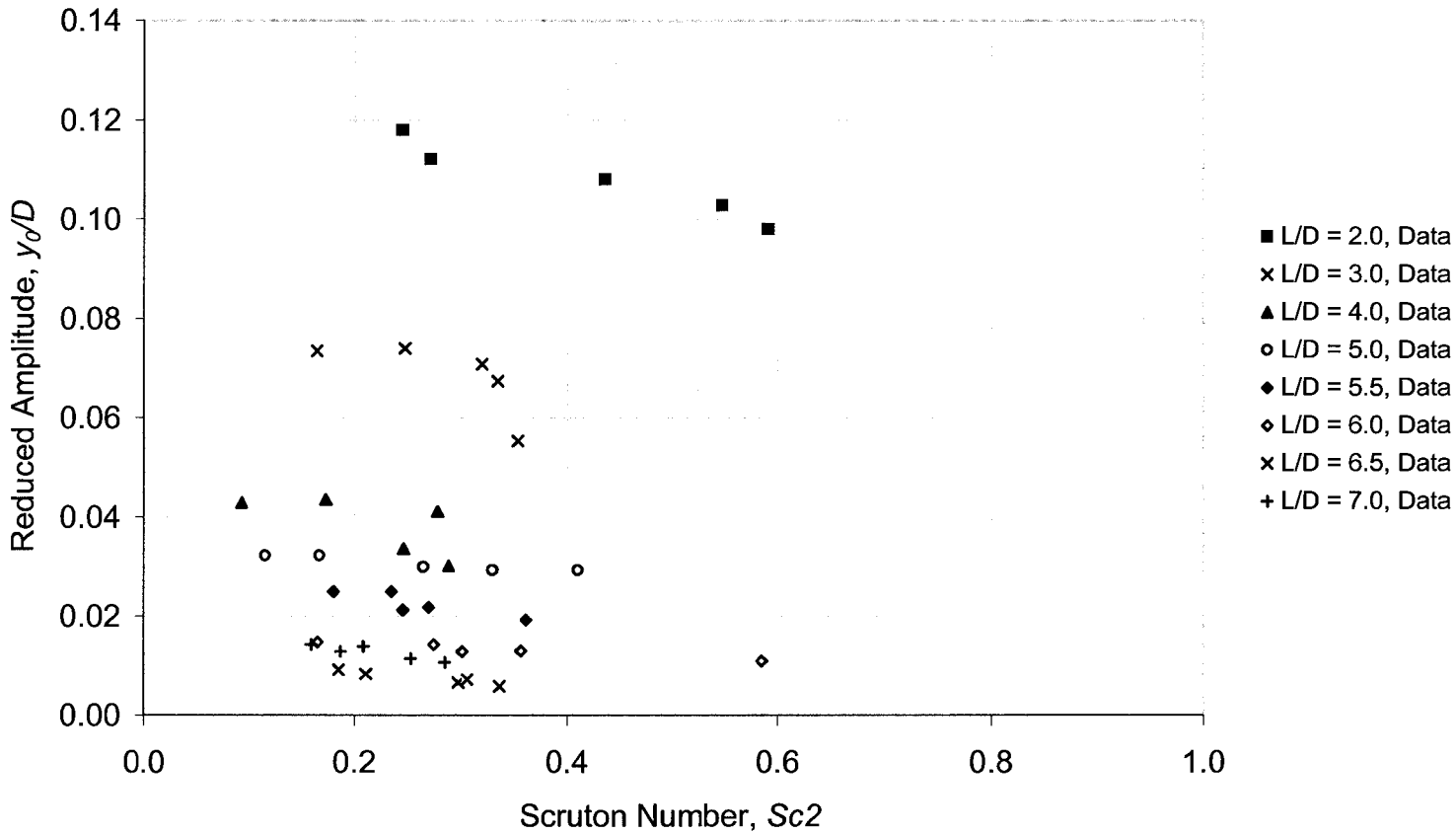

Figure 5.22. Reduced amplitude vs. *Sc2*

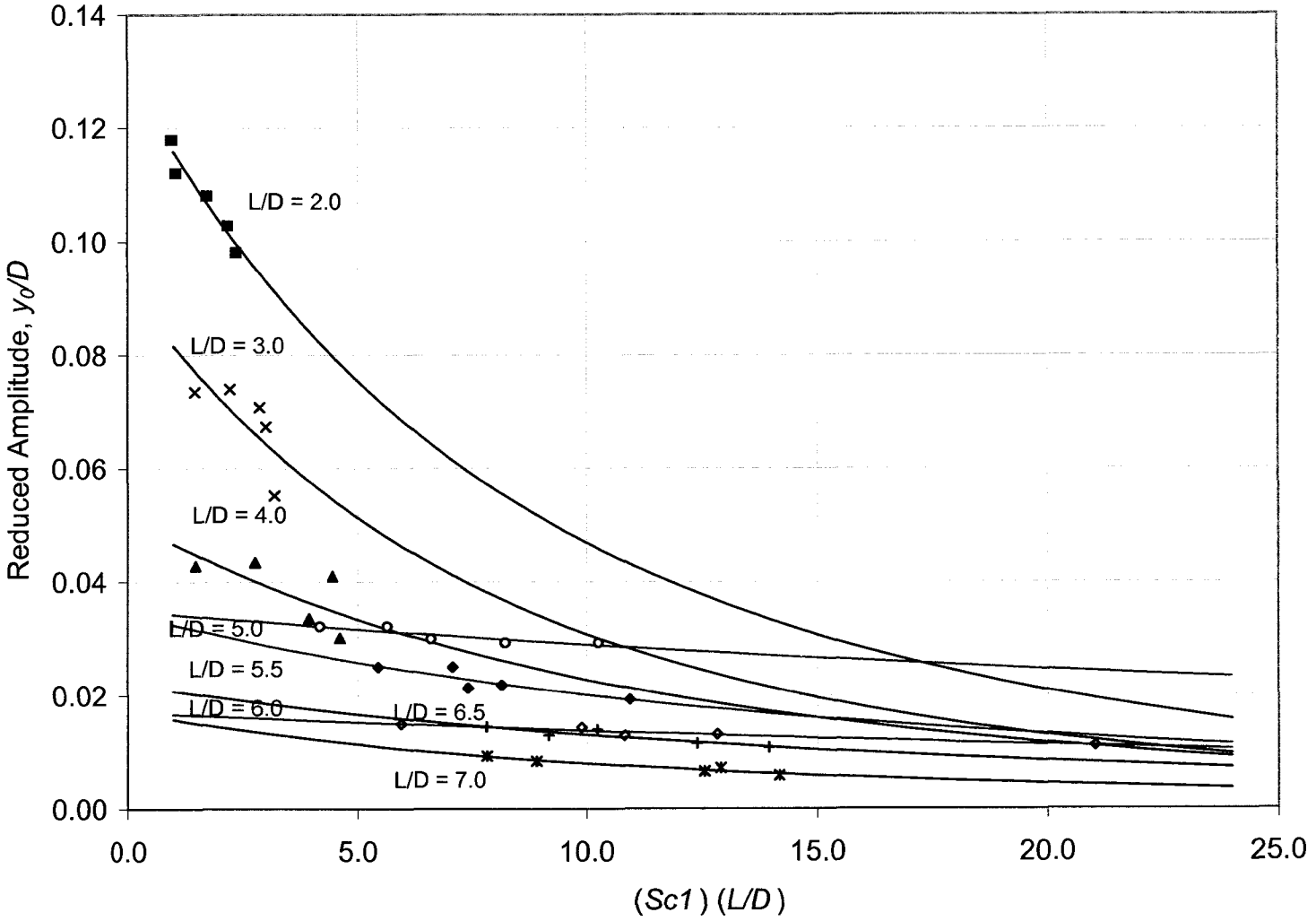

Figure 5.23. Reduced amplitude vs. *(Sc1)(L/D)*

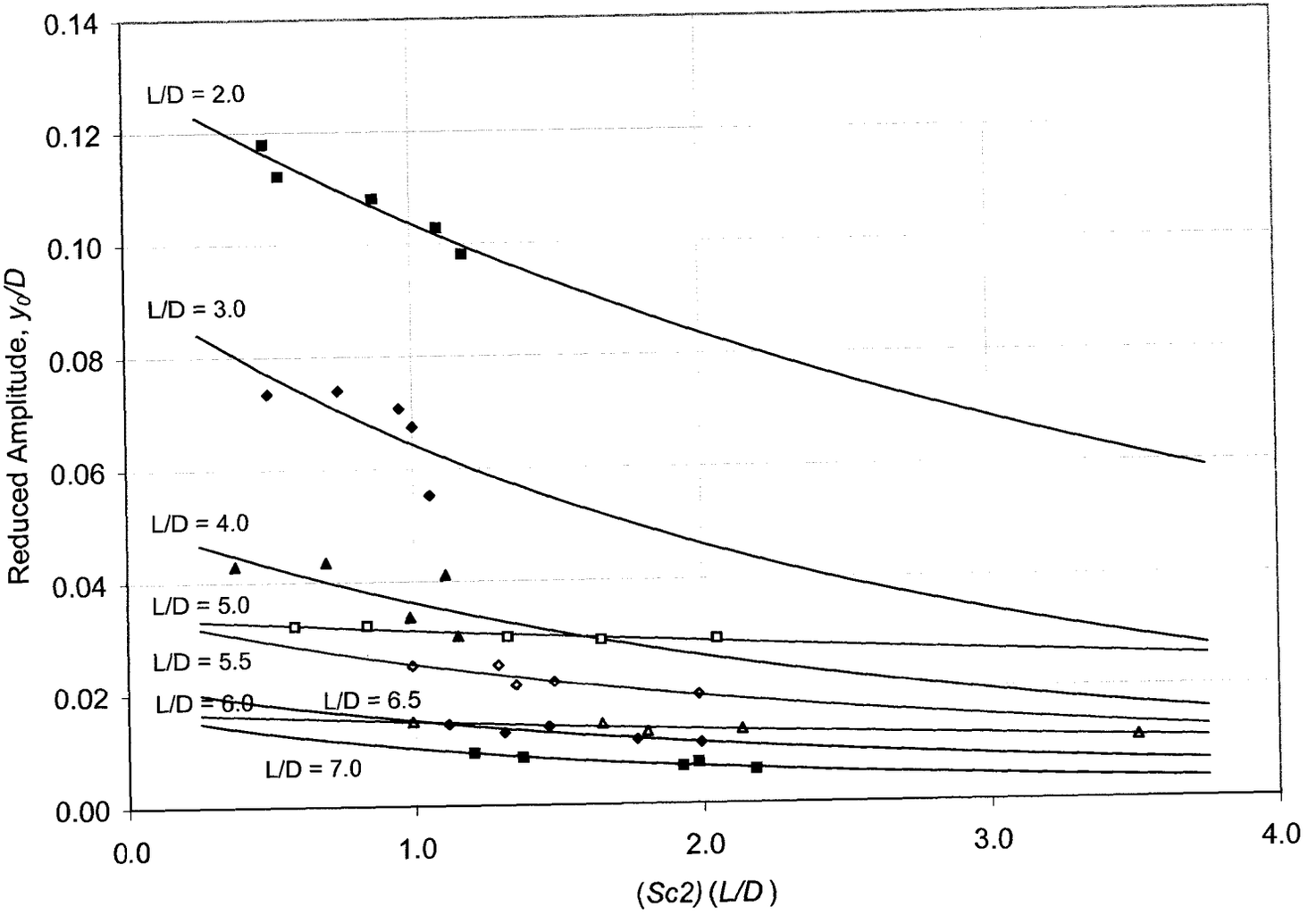

Figure 5.24. Reduced amplitude vs. *(Sc2)(L/D)*

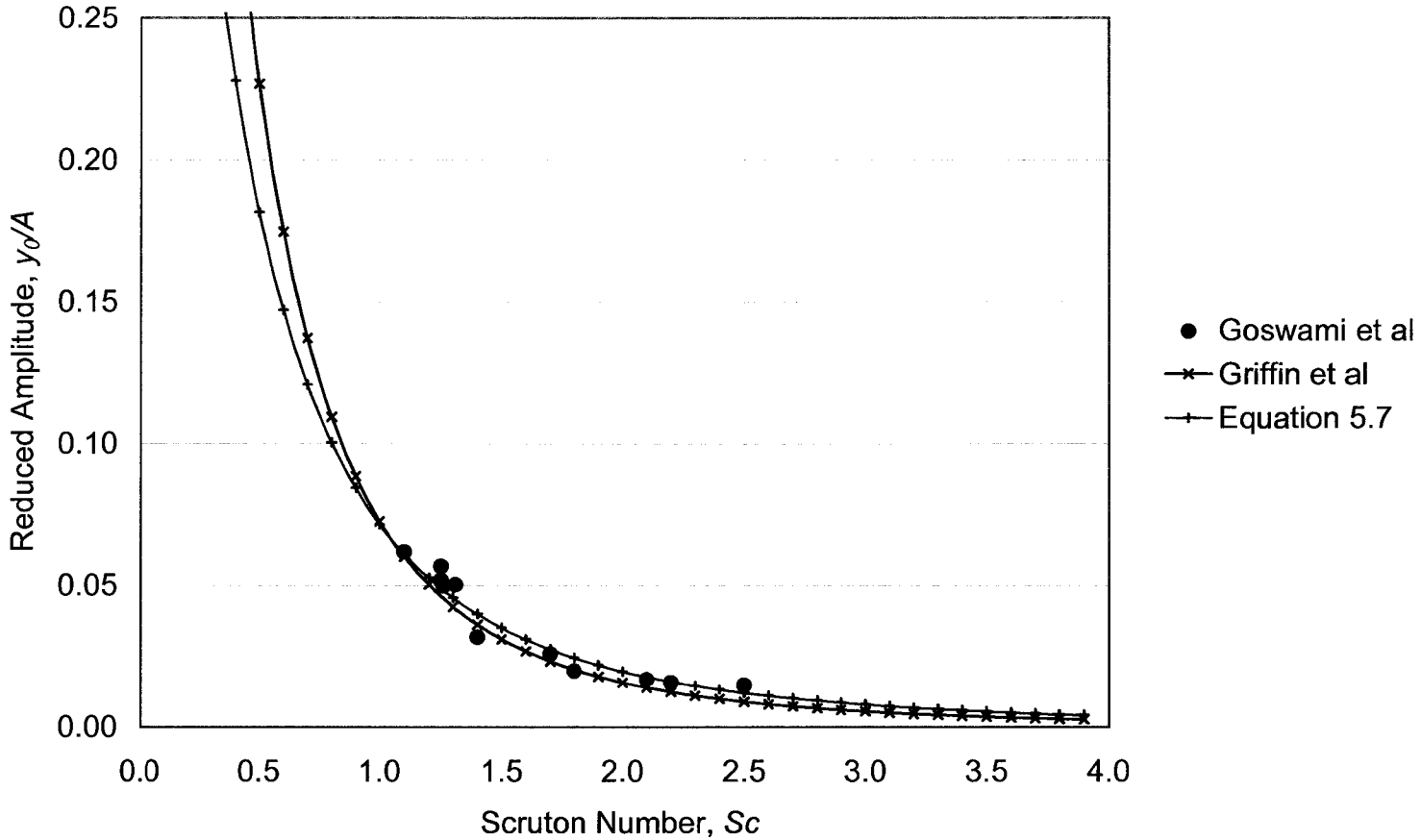

Figure 5.25. Reduced amplitude vs. *Sc*, circular cylinders

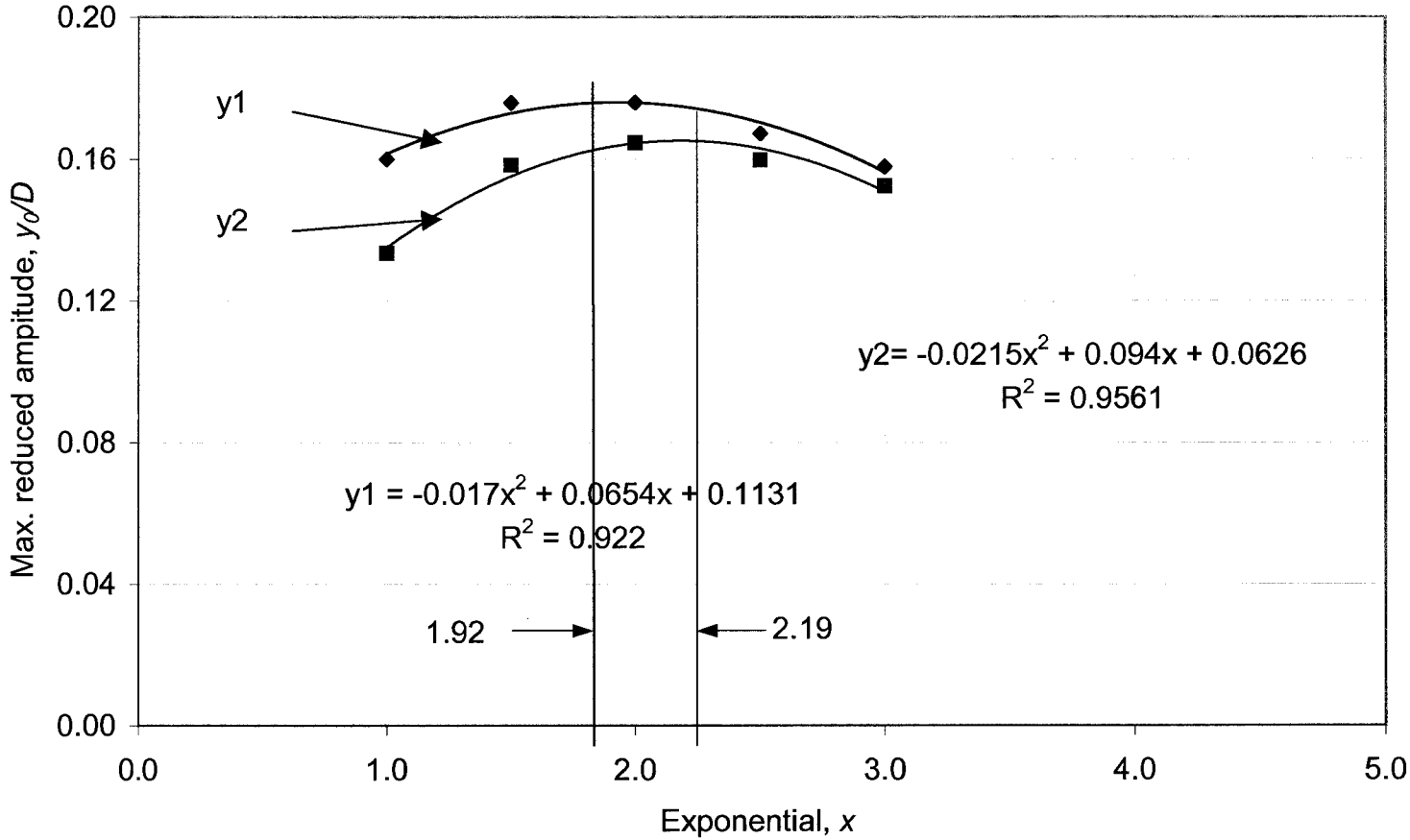

Figure 5.26. Maximum reduced amplitude vs. x for *Sc1*

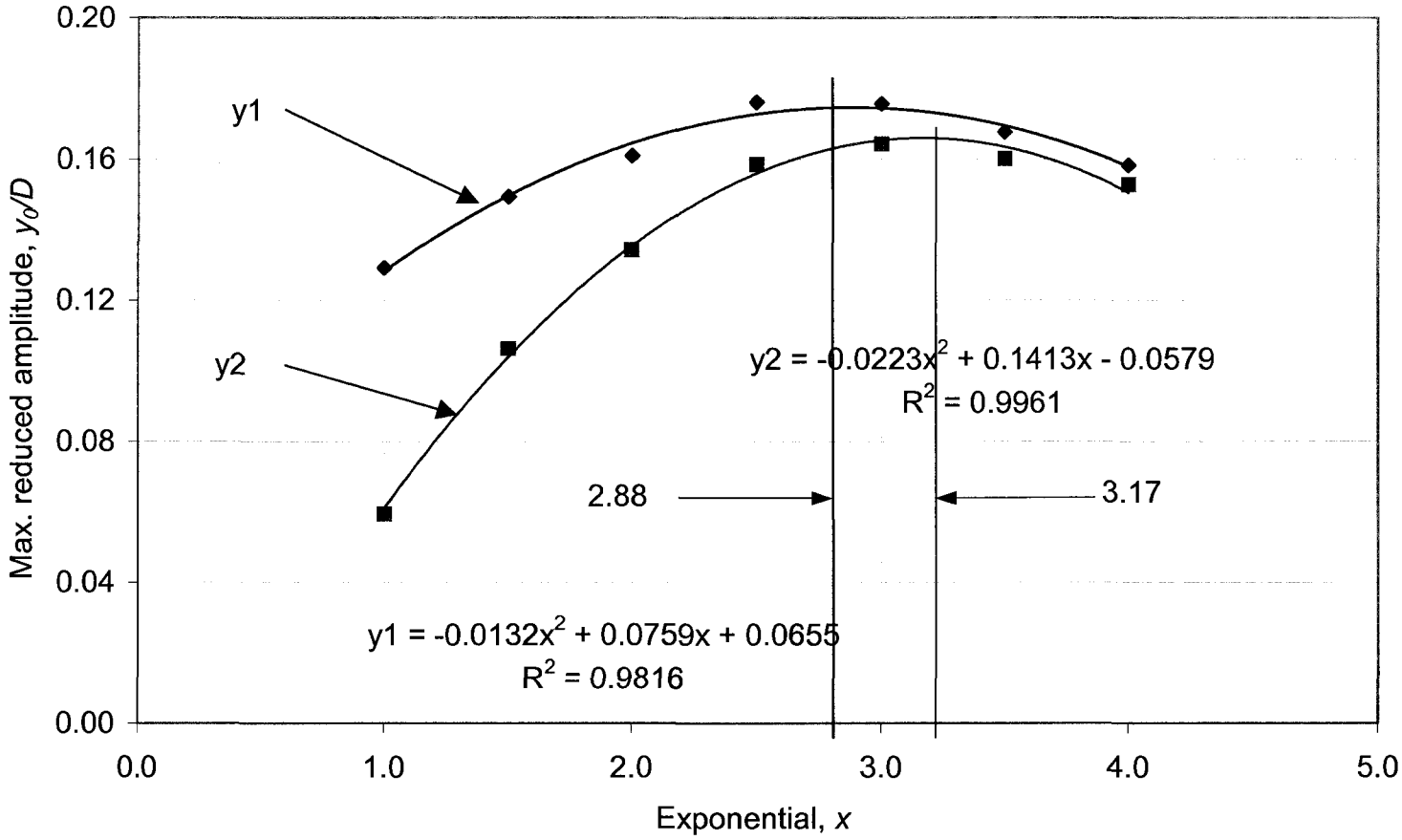

Figure 5.27. Maximum reduced amplitude vs. x for *Sc2*

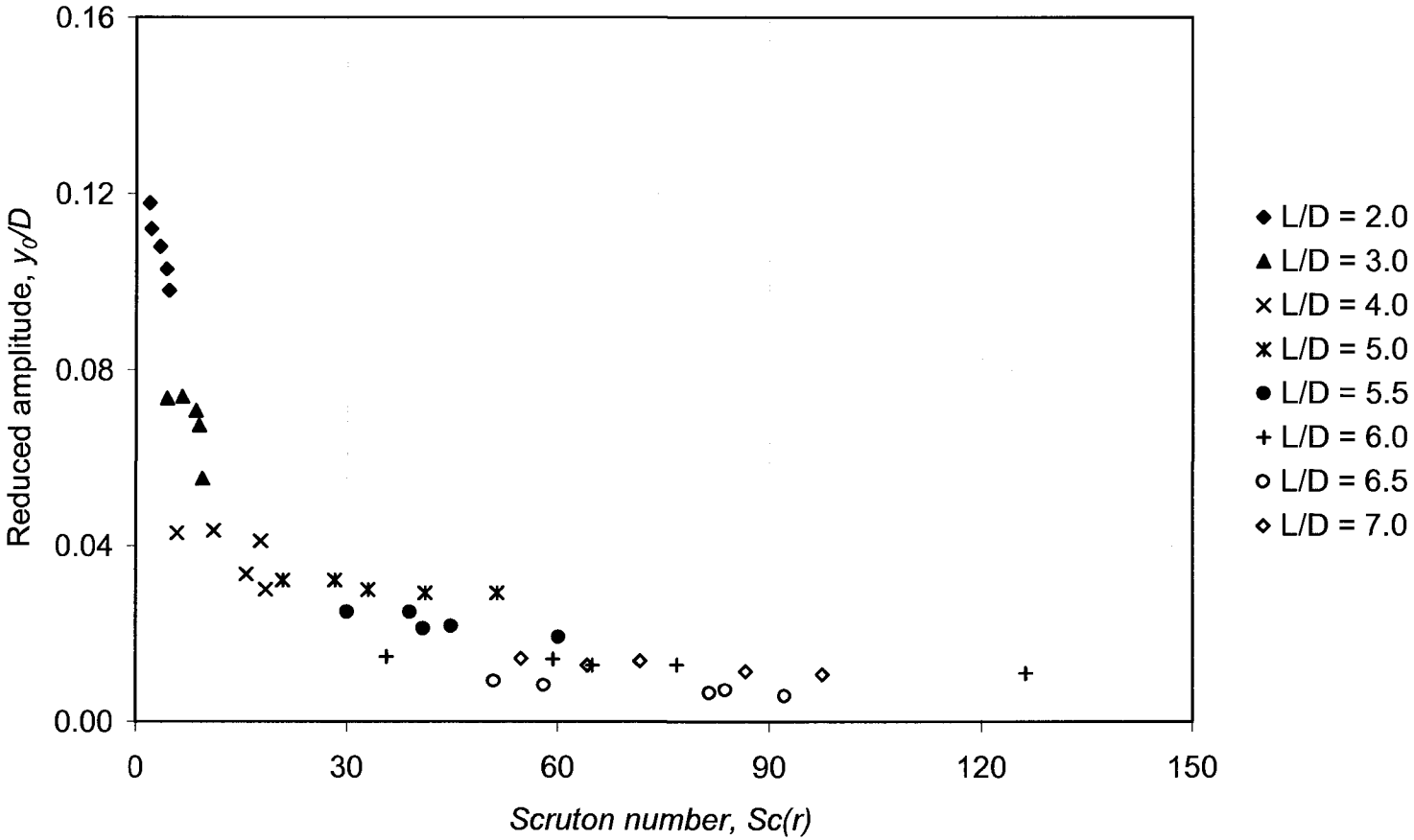

Figure 5.28. Reduced amplitude vs. *Sc(r)*, rectangular cylinders

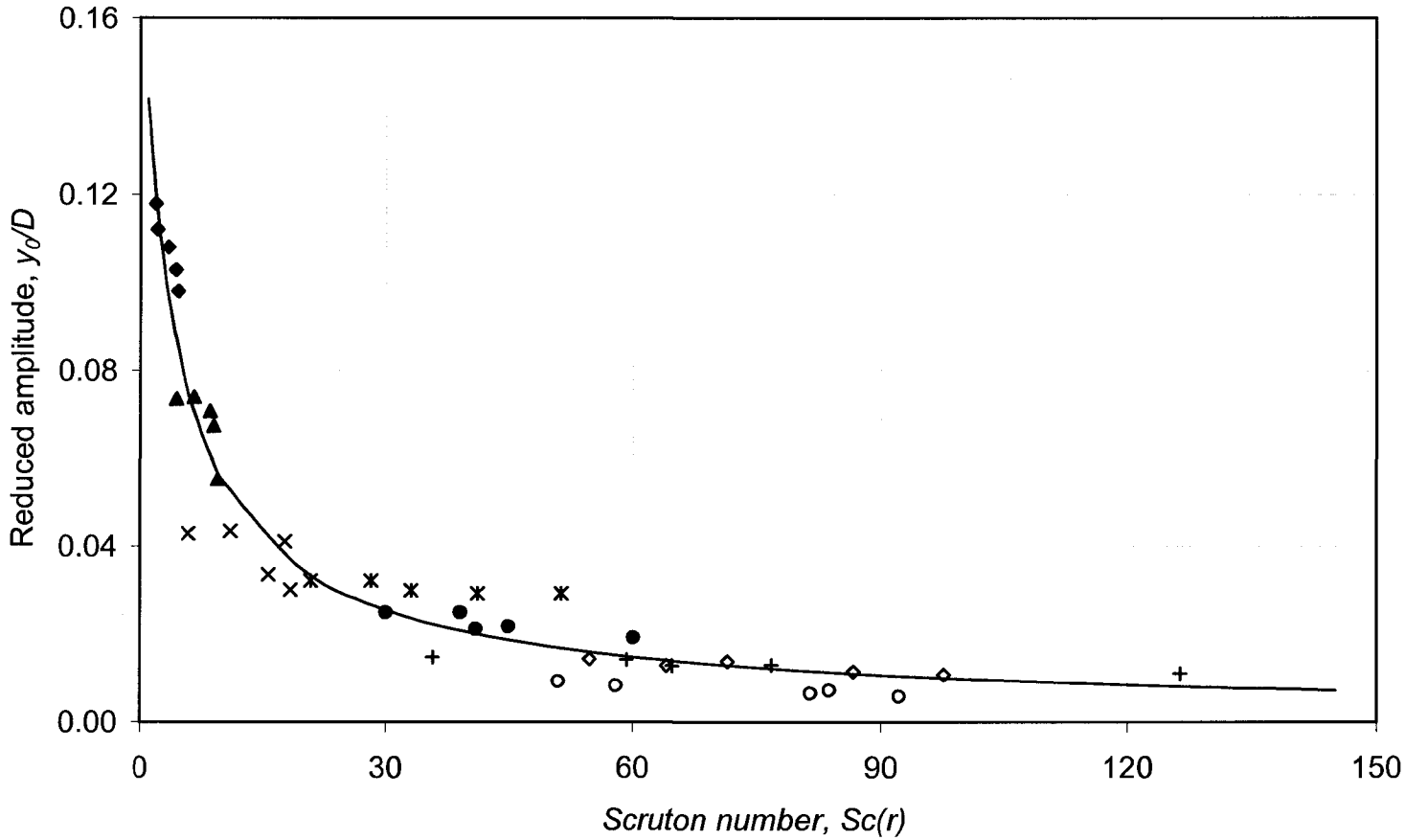

Figure 5.29. Response equation curve, rectangular cylinders

CHAPTER 6

SUMMARY & CONCLUSIONS

6.1. Introduction

Wind tunnel tests of forty elastically supported rectangular models were performed in a smooth air flow with angle of incidence equal to zero degrees. Eight models were tested with aspect ratios that varied from $2 \leq L/D \leq 7$. Each model was tested five times, each time with a different mass.

The tests were performed over a range of wind speeds that produced vortex-induced vibrations transverse to the direction of the wind in all test cases. All eight models exhibited lock-in during at least one wind speed regime, five models exhibited lock-in during two wind speed regimes.

Each model was suspended in a force balance system that allowed only vertical motion transverse to the air flow. The dynamic parameters of each model, including the mass, stiffness, natural frequency and system damping, were experimentally determined prior to the beginning of the wind tests. During each test the wind speed was increased incrementally. The wind speed at the onset of lock-in was recorded. During lock-in, the vibration amplitude and the velocity of the wind at each wind speed increment were recorded.

The collected data was used to create plots of the reduced amplitude vs. the reduced velocity for each aspect ratio. The results of the tests verified the use of the modified Strouhal number to predict the onset of lock-in. A mass/damping/ geometry parameter analogous to the Scruton number was derived from the data.

Finally, the data was used to derive a single vortex-induced vibration response equation for the range of aspect ratios tested given the mass/damping/geometry parameter.

6.2. Vortex-Induced Vibrations

Vortex-induced vibrations transverse to the direction of the wind were observed during each experiment over at least one wind regime. Five models were observed to exhibit vortex-induced vibrations during two wind regimes. The observed reduced velocity at the initiation of vortex-induced vibrations was taken as the onset of lock-in for each aspect ratio and agrees with previously published research data.

The models were principally excited by impinging leading edge vortex shedding rather then trailing edge vortex shedding known to excite circular cylinders. Because the impinging leading edge vortices result from separated flow from the leading edges, the Strouhal number and the modified Strouhal number are insensitive to the Reynolds number of the wind velocity.

For the range of Reynolds number tested, the experimental results, including the reduced amplitude vs. reduced velocity, compare favorably with the results reported in previously published research. Furthermore, the modified Strouhal number at the onset of lock-in for elastically supported rectangular cylinders agrees with previously published data.

Vortex-induced vibrations occurred over a discrete range or ranges of reduced velocities for each aspect ratio. The reduced amplitude of each model varied

depending on the aspect ratio, mass and damping and ranged from approximately 0.12 to less than 0.01. The amplitudes were observed to be self-limiting irrespective of the level of damping present in the system.

6.3. Modified Strouhal Number

The traditional Strouhal number, the nondimensional constant based on the cross-flow thickness of the body, relates the vortex shedding frequency at the trailing edge of a stationary circular cylinder to the velocity of the approaching air flow. This Strouhal number does not predict the wind speed at the onset of lock-in for elastically supported rectangular cylinders. Likewise, the Strouhal number that relates the vortex shedding frequency at the trailing edge of a stationary rectangular cylinder to the velocity of the approaching air flow and that is based on the along-flow length of the rectangular cylinder, does not predict the wind speed when lock-in will occur for elastically supported rectangular cylinders.

To accurately predict the reduced velocity at the onset of lock-in, the modified Strouhal number must be used to calculate the critical reduced velocity. The modified Strouhal number is a function of the inverse of the aspect ratio and is related to the wind velocity along the sides of the cylinder. Depending on the dynamic mass and system damping, several wind regimes may produce vortex-induced vibrations according to the equation for the modified Strouhal number, St_n, for n = 1, 2, or 3.

6.4. Scruton Number for Rectangular Cylinders

To account for the rectangular shape of the current test models, a mass/damping/geometry parameter for rectangular cylinders, *Sc(r)*, was derived as part of the current study (Equation 5.11). This parameter is analogous to the Scruton number developed for circular cylinders. Based on the current study results, the rectangular Scruton number was determined to be a function of the mass, system damping and a ratio of the along-wind length to the across-wind thickness.

6.5. Response Equation

A single vortex-induced response equation (Equation 5.12) was derived from the reduced amplitude vs. mass/damping/geometry parameter data (Figure 5.28). The response equation can be used to predict the maximum amplitude of vortex-induced vibrations of rectangular cylinders within the range of aspect ratios and Reynolds number used in the current experiments.

The response equation was derived assuming the form of equation would be similar to the equation previously derived to predict the vortex-induced response of circular cylinders. To account for the rectangular shape, a mass/damping/geometry parameter for rectangular cylinders, *Sc(r)*, analogous to the Scruton number for circular cylinders was derived as part of the current study.

As seen in the plot of Figure 5.29, Equation 5.12 accurately describes the maximum amplitude vortex-induced response of a rectangular cylinder during lock-in.

6.6. Future Work

To further verify the accuracy and useful range of the rectangular cylinder response equation and to verify the validity of the rectangular Scruton number, the following future work is recommended:

1. Conduct additional wind tunnel tests to confirm the reduced amplitude, y_0/D, vs. rectangular Scruton number, $Sc(r)$, relation observed during the current study using a similar range of aspect ratios. Recognizing how quickly the response curve converges towards zero with an increase in Scruton number, the aspect ratios to be tested should be heavily weighted towards the smaller end of the aspect ratio range; that is, L/D = 2.0, 3.0, and 4.0.
2. Conduct additional wind tunnel tests to extend the range of velocities using similar aspect ratios as used in the current study to ascertain if additional modes of the modified Strouhal number can be excited. In particular, extend the range of velocities for aspect ratios, L/D = 5.0, 5.5, and 6.0, to ascertain if the first mode of the modified Strouhal number can be excited. If the first mode of the modified Strouhal number can be excited, the reduced amplitude of vibration observed during this mode as compared to the reduced amplitudes recorded during the current study would be of paramount interest.
3. Similar to Item 2, conduct additional wind tunnel tests for aspect ratios, L/D = 6.6 and 7.0, to ascertain if the first and/or second modes of the modified Strouhal number can be excited. If these modes can be excited,

the reduced amplitude of vibration, compared to the reduced amplitudes recorded during the current study, would be of paramount interest.

4. Conduct additional wind tunnel tests to extend the range of rectangular Scruton number, *Sc(r)*, beyond the range tested during the current study by increasing the mass and/or damping of the models.
5. Conduct additional wind tunnel tests that include a visualization tool to ascertain the exact behavior of the impinging leading edge vortices along the side surfaces of the models. Of particular interest would be the interaction of the vortices traveling along the side surfaces of the models and the vortices that form at the trailing edge. The system mass/damping parameter that determines the system natural frequency, along with the free-stream velocity, may interact with the trailing edge vortex shedding frequency to dictate which mode of the modified Strouhal number is excited. It is possible that the largest vibration amplitudes occur when the modified Strouhal number coincides with the traditional Strouhal number for elastically supported rectangular cylinders.
6. Conduct additional wind tunnel tests that include various angles of incidence model surface roughness.
7. Conduct additional wind tunnel tests with varying sizes of end plates to study the effects of three-dimensional vortices forming at each end of the model.

APPENDIX A

FAN SPEED CALIBRATION

A.1. Calibration

The fan speed vs. wind speed calibration was completed by installing a pitot tube through the floor of the wind tunnel immediately ahead of the test section. The pitot tube was connected to a hand-held anemometer with digital readout. The fan speed was set at 1.5 *Hz* and increased incrementally until a fan speed of 15 *Hz* was reached. At each increment, the wind speed that was displayed on the anemometer was recorded. Because of a slight wandering of the values displayed by the anemometer, two and sometimes three wind speeds were recorded at each fan speed. This data is tabulated in Table A.1.

A linear regression of the data, including all multiple wind speed values at a particular fan speed, was performed using Microsoft *Excel*. The regression returned the following linear relationship of fan speed to wind speed,

$$y = 5.076x - 1.428 \quad \text{(Equation A.1)}$$

where y = wind speed in ft/s, and

x = fan speed in Hz.

Figure A.1 is a plot of the linear regression.

Table A.1. Fan speed vs. wind speed.

Fan Speed Hz	Wind speed ft/s.		
1.5	6.7	6.0	7.3
2.0	8.5	7.9	9.0
2.5	10.8	11.2	11.6
3.0	13.4	13.7	14.0
3.5	16.1	16.4	16.9
4.0	18.7	19.1	18.4
4.5	21.1	21.6	
5.0	3.9	23.7	
6.0	28.8	28.7	
7.0	33.7	33.8	33.6
8.0	39.5	40.0	40.4
9.0	44.6	44.2	
10.0	49.2	49.6	
11.0	54.1	54.4	
12.0	59.7	59.4	
13.0	64.1	64.4	
14.0	69.2	69.4	69.7
15.0	74.9	74.7	75.2

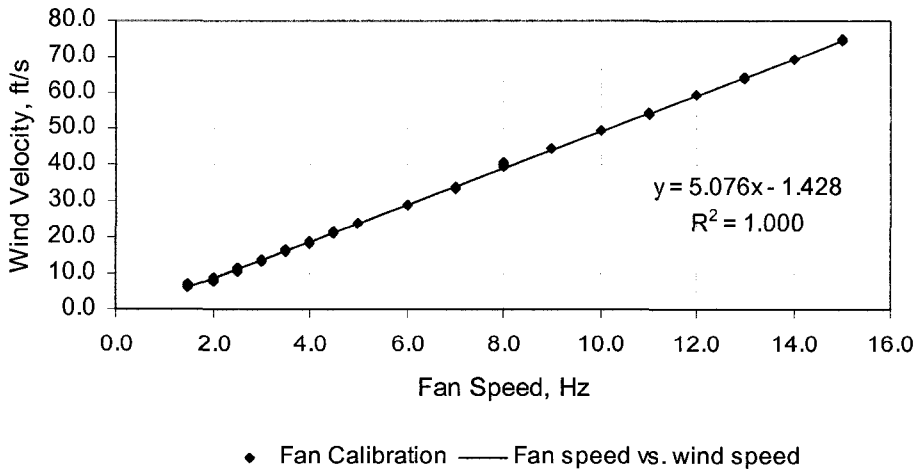

Figure A.1. Fan speed vs. wind speed calibration.

APPENDIX B

SYSTEM MASS, STIFFNESS & FREQUENCY

B.1. Background

The equation for the calculation of the system natural frequency can be written as,

$$\omega^2 = \frac{k}{m} \quad \text{.....(Equation B.1)}$$

where ω = the natural frequency of the system,

m = the system mass to be determined, and

k = the system stiffness to be determined.

Rearranging, Equation B.1 can be written as:

$$\frac{1}{\omega^2} = \frac{m}{k} \quad \text{.....(Equation B.2)}$$

Finally, the same equation can be written as the added mass equation:

$$\frac{1}{\omega_i^2} = \frac{1}{k}(m + M_i) \quad \text{.....(Equation B.3)}$$

where M_i = the known mass added to the system.

B.2. System Mass and Stiffness

While suspended by the force balance system in still air, each specimen was manually excited and allowed to vibrate freely. The natural frequency of the specimen, in *Hz*, was recorded from the frequency spectrum displayed by the electronic data acquisition system. A set of data for f_i, and consequently ω_i, was

experimentally obtained by adding mass, M_i, where $i = 0, 1,.., 5$, to each specimen in the form of iron weights. One pound was added at each increment. Therefore, the incremental added mass, M_i, was equal to 0.031 slugs; so that M_0 was equal to zero slugs, M_1 was equal to 0.031 slugs, etc.

Assuming the added mass equation maps as a straight line, a linear regression between the inverse of the natural frequency squared, $1/\omega^2$, and the added mass, M_i, was performed using the Microsoft *Excel* software. The regression returned the y intercept, the slope of the line, and the R^2 term, where R is approximately equal to a point estimate of the correlation coefficient (Ang and Tang, 1975). The system stiffness, k, is calculated as the inverse of the slope of the regressed line divided by the value of gravity, 32.2 *ft/s*; the system natural frequency, ω, is calculated as the square root of the inverse of the y intercept; and the system mass, m, is calculated by dividing the stiffness, k, by the square of the natural frequency, ω^2.

The natural frequencies observed for the forty models are given in Table B.1 through B.8. The values returned from the linear regression are listed in Table B.9 through B.16 with the calculated natural frequency, spring stiffness, dynamic mass, and apparent dynamic weight.

Table B.1. Recorded frequencies (*Hz & rad/s*), *L/D* = 2.0

	Added weight, *lb*											
Model	0		1		2		3		4		5	
20.0	9.625	60.476	8.375	52.622	7.500	47.124	6.750	42.412	6.250	39.270	6.875	36.914
20.2	7.875	49.480	7.125	44.768	6.500	40.840	6.125	38.485	5.750	36.128	5.375	33.772
20.4	6.875	43.197	6.375	40.055	6.000	37.700	5.625	35.343	5.250	32.987	5.000	31.416
20.6	6.250	39.270	5.875	36.914	5.500	34.558	5.250	32.987	5.000	31.416	4.750	29.845
20.8	5.750	36.128	5.500	34.558	5.125	32.201	4.875	30.631	4.750	29.845	4.500	28.274

Table B.2. Recorded frequencies (*Hz & rad/s*), *L/D* = 3.0

	Added weight, *lb*											
Model	0		1		2		3		4		5	
30.0	9.125	57.334	8.000	50.266	7.188	45.160	6.563	41.233	6.125	38.485	5.750	36.128
30.2	7.688	48.302	6.938	43.590	6.375	40.055	5.938	37.306	5.625	35.343	5.313	33.380
30.4	6.688	42.019	6.188	38.877	5.813	36.521	5.438	34.165	5.188	32.594	4.938	31.023
30.6	6.063	38.092	5.688	35.736	5.375	33.772	5.125	32.201	4.938	31.023	4.688	29.452
30.8	5.625	35.343	5.250	32.987	5.000	31.416	4.750	29.845	4.625	29.060	4.375	27.489

Table B.3. Recorded frequencies (*Hz & rad/s*), *L/D* = 4.0

	Added weight, *lb*											
Model	0		1		2		3		4		5	
40.0	8.625	54.193	7.750	48.695	7.000	43.982	6.375	40.055	6.000	37.699	5.625	35.343
40.2	7.375	46.339	6.875	43.197	6.250	39.270	5.875	36.914	5.500	34.558	5.250	32.987
40.4	6.500	40.841	6.125	38.485	5.750	36.128	5.375	33.772	5.125	32.201	4.875	30.631
40.6	6.000	37.699	5.625	35.343	5.375	33.772	5.000	31.416	4.750	29.845	4.625	29.060
40.8	5.500	34.558	5.250	32.987	5.000	31.416	4.750	29.845	4.500	28.274	4.375	27.489

Table B.4. Recorded frequencies (*Hz & rad/s*), *L/D* = 5.0

	Added weight, *lb*											
Model	0		1		2		3		4		5	
50.0	8.250	51.836	7.375	46.339	6.750	42.412	6.250	39.270	5.875	36.914	5.500	34.558
50.2	7.125	44.768	6.500	40.841	6.000	37.699	5.625	35.343	5.375	33.772	5.125	32.201
50.4	6.375	40.055	5.874	36.914	5.625	35.343	5.375	33.772	5.000	31.416	4.875	30.631
50.6	5.875	36.914	5.500	34.558	5.250	32.987	5.000	31.416	4.750	29.845	4.625	29.060
50.8	5.375	33.772	5.125	32.201	4.875	30.631	4.750	29.845	4.500	28.274	4.375	27.489

Table B.5. Recorded frequencies (*Hz & rad/s*), *L/D* = 5.5

	Added weight, *lb*											
Model	0		1		2		3		4		5	
55.0	8.000	50.266	7.250	45.553	6.625	41.626	6.125	38.485	5.750	36.128	5.500	34.558
55.2	7.000	43.982	6.500	40.841	6.000	37.699	5.625	35.343	5.375	33.772	5.125	32.201
55.4	6.250	39.270	5.875	36.914	5.500	34.558	5.250	32.987	5.000	31.416	4.750	29.845
55.6	5.750	36.128	5.375	33.772	5.125	32.201	4.875	30.631	4.750	29.845	4.500	28.274
55.8	5.375	33.772	5.125	32.201	4.875	30.631	4.625	29.060	4.500	28.274	4.375	27.489

Table B.6. Recorded frequencies (*Hz & rad/s*), *L/D* = 6.0

	Added weight, *lb*											
Model	0		1		2		3		4		5	
60.0	8.000	50.266	7.250	45.553	6.625	41.626	6.125	38.485	5.750	36.128	5.500	34.558
60.2	6.875	43.197	6.375	40.055	6.000	37.699	5.625	35.343	5.375	33.772	5.125	32.201
60.4	6.250	39.270	5.875	36.914	5.500	34.558	5.250	32.987	5.000	31.416	4.750	29.845
60.6	5.750	36.128	5.375	33.772	5.125	32.201	4.875	30.631	4.625	29.050	4.500	28.274
60.8	5.250	32.987	5.000	31.416	4.875	30.631	4.625	29.060	4.500	28.274	4.375	27.489

Table B.7. Recorded frequencies (*Hz & rad/s*), *L/D* = 6.5

	Added weight, *lb*											
Model	0		1		2		3		4		5	
6.5.0	7.750	48.695	7.000	43.982	6.500	40.841	6.000	37.699	5.625	35.343	5.375	33.772
6.5.2	6.750	42.412	6.375	40.055	5.875	36.914	5.500	34.558	5.250	32.987	5.000	31.416
6.5.4	6.125	38.485	5.750	36.128	5.500	34.558	5.125	32.201	5.000	31.416	4.750	29.845
6.5.6	5.625	35.343	5.375	33.772	5.125	32.201	4.875	30.631	4.625	29.060	4.500	28.274
6.5.8	5.250	32.987	5.000	31.416	4.750	29.845	4.625	29.060	4.500	28.274	4.250	26.704

Table B.8. Recorded frequencies (*Hz & rad/s*), *L/D* = 7.0

	Added weight, *lb*											
Model	0		1		2		3		4		5	
7.0.0	7.625	47.909	7.000	43.982	6.375	40.055	6.000	37.699	5.625	35.343	5.375	33.772
7.0.2	6.750	42.412	6.250	39.270	5.875	36.914	5.500	34.558	5.250	32.987	5.000	31.416
7.0.4	6.125	38.485	5.625	35.343	5.375	33.772	5.125	32.201	4.875	30.631	4.625	29.060
7.0.6	5.625	35.343	5.250	32.987	5.125	32.201	4.875	30.631	4.625	29.060	4.500	28.274
7.0.8	5.250	32.987	5.000	31.416	4.750	29.845	4.625	29.060	4.500	28.274	4.250	26.704

Table B.9. Statistical analysis, $L/D = 2.0$

Model	R^2	y intercept	Slope	Frequency *rad/s*	Frequency *Hz*	Stiffness *lb/ft*	Mass *slugs*	Weight *lb*
20.0	0.9992	2.7030×10^{-4}	9.3425×10^{-5}	60.824	9.681	332.417	0.090	2.893
20.2	0.9979	4.0760×10^{-4}	9.1964×10^{-5}	49.532	7.883	337.696	0.138	4.432
20.4	0.9962	5.2517×10^{-4}	9.6304×10^{-5}	43.636	6.945	322.477	0.169	5.453
20.6	0.9985	6.4405×10^{-4}	9.4021×10^{-5}	39.404	6.271	330.309	0.213	6.850
20.8	0.9914	7.5971×10^{-4}	9.6603×10^{-5}	36.281	5.774	321.481	.0.244	7.864

Table B.10. Statistical analysis, $L/D = 3.0$

Model	R^2	y intercept	Slope	Frequency *rad/s*	Frequency *Hz*	Stiffness *lb/ft*	Mass *slugs*	Weight *lb*
30.0	0.9998	3.0480×10^{-4}	9.2734×10^{-5}	57.278	9.116	334.893	0.102	3.287
30.2	0.9994	4.3276×10^{-4}	9.3215×10^{-5}	48.070	7.651	333.165	0.144	4.643
30.4	0.9994	5.6610×10^{-4}	9.4548×10^{-5}	42.0296	6.689	328.467	0.186	5.987
30.6	0.9978	6.9085×10^{-4}	9.0675×10^{-5}	38.0458	6.055	342.497	0.237	7.619
30.8	0.9934	8.0914×10^{-4}	1.0054×10^{-4}	35.155	5.595	308.879	0.250	8.048

Table B.11. Statistical analysis, $L/D = 4.0$

Model	R^2	y intercept	Slope	Frequency *rad/s*	Frequency *Hz*	Stiffness *lb/ft*	Mass *slugs*	Weight *lb*
40.0	0.9988	3.3547×10^{-4}	9.2922×10^{-5}	54.598	8.690	334.213	0.112	3.610
40.2	0.9975	4.5746×10^{-4}	9.3037×10^{-5}	46.754	7.441	333.802	0.153	4.917
40.4	0.9977	5.8823×10^{-4}	9.4564×10^{-5}	41.231	6.562	328.411	0.193	6.221
40.6	0.9916	6.9977×10^{-4}	1.0016×10^{-4}	37.803	6.017	310.066	0.217	6.987
40.8	0.9947	8.2524×10^{-4}	1.0100×10^{-4}	34.810	5.540	307.473	0.254	8.170

Table B.12. Statistical analysis, $L/D = 5.0$

Model	R^2	y intercept	Slope	Frequency *rad/s*	Frequency *Hz*	Stiffness *lb/ft*	Mass *slugs*	Weight *lb*
50.0	0.9995	$3.7204.\text{x}10^{-4}$	9.2086×10^{-5}	51.845	8.251	337.247	0.126	4.040
50.2	0.9971	5.0809×10^{-4}	9.3022×10^{-5}	44.364	7.061	333.857	0.170	5.462
50.4	0.9890	6.2889×10^{-4}	8.9343×10^{-5}	39.876	6.346	347.602	0.219	7.039
50.6	0.9963	7.3970×10^{-4}	9.1475×10^{-5}	36.768	5.852	339.503	0.251	8.086
50.8	0.9939	8.7570×10^{-4}	8.9982×10^{-5}	33.793	5.378	345.135	0.302	9.732

Table B.13. Statistical analysis, $L/D = 5.5$

Model	R^2	y intercept	Slope	Frequency *rad/s*	Frequency *Hz*	Stiffness *lb/ft*	Mass *slugs*	Weight *lb*
55.0	0.9981	3.9663×10^{-4}	9.0247×10^{-5}	50.212	7.990	344.121	0.136	4.395
55.2	0.9981	5.1750×10^{-4}	9.0453×10^{-5}	43.959	6.996	343.337	0.178	5.721
55.4	0.9985	6.4404×10^{-4}	9.4021×10^{-5}	39.404	6.271	330.309	0.213	6.850
55.6	0.9934	7.7472×10^{-4}	9.3226×10^{-5}	35.928	5.718	333.126	0.2581	8.310
55.8	0.9923	8.8156×10^{-4}	9.1739×10^{-5}	33.680	5.360	338.524	0.298	9.609

Table B.14. Statistical analysis, $L/D = 6.0$

Model	R^2	y intercept	Slope	Frequency *rad/s*	Frequency *Hz*	Stiffness *lb/ft*	Mass *slugs*	Weight *lb*
60.0	0.9981	3.9663×10^{-4}	9.0247×10^{-5}	50.212	7.991	344.121	0.137	4.395
60.2	0.9994	5.3648×10^{-4}	8.5708×10^{-5}	43.174	6.871	362.344	0.194	6.259
60.4	0.9985	6.4405×10^{-4}	9.4021×10^{-5}	39.404	6.271	330.309	0.213	6.850
60.6	0.9964	7.7179×10^{-4}	9.8497×10^{-5}	35.996	5.729	315.297	0.243	7.836
60.8	0.9929	9.2229×10^{-4}	8.1519×10^{-5}	32.928	5.241	380.965	0.351	11.314

Table B.15. Statistical analysis, $L/D = 6.5$

Model	R^2	y intercept	Slope	Frequency *rad/s*	Frequency *Hz*	Stiffness *lb/ft*	Mass *slugs*	Weight *lb*
65.0	0.9986	4.2247×10^{-4}	9.2289×10^{-5}	48.652	7.743	336.508	0.142	4.578
65.2	0.9969	5.4638×10^{-4}	9.3629×10^{-5}	42.781	6.809	331.690	0.181	5.836
65.4	0.9923	6.7466×10^{-4}	8.8733×10^{-5}	38.500	6.127	349.993	0.236	7.603
65.6	0.9949	7.8982×10^{-4}	9.3579×10^{-5}	35.582	5.663	331.868	0.2621	8.440
65.8	0.9841	9.2077×10^{-4}	9.1180×10^{-5}	32.955	5.245	340.601	0.314	10.098

Table B.16. Statistical analysis, $L/D = 7.0$

Model	R^2	y intercept	Slope	Frequency *rad/s*	Frequency *Hz*	Stiffness *lb/ft*	Mass *slugs*	Weight *lb*
70.0	0.9984	4.3543×10^{-4}	8.9619×10^{-5}	47.923	7.627	346.533	0.151	4.859
70.2	0.9994	5.5597×10^{-4}	9.1471×10^{-5}	42.411	6.750	339.516	0.189	6.078
70.4	0.9952	6.8294×10^{-4}	9.7954×10^{-5}	38.266	6.090	317.048	0.217	6.972
70.6	0.9896	8.0592×10^{-4}	8.9958×10^{-5}	35.225	5.606	345.227	0.278	8.959
70.8	0.9841	9.2077×10^{-4}	9.1180×10^{-5}	32.955	5.245	340.601	0.314	10.098

APPENDIX C

SYSTEM DAMPING

C.1. Background

For an under-damped mechanical system, the damping ratio can be determined from the diminishing dynamic response of the system; that is, the logarithmic decrement, δ,

$$\delta = \frac{1}{n} \ln \frac{x_0}{x_n} \quad \text{.....(Equation C.1)}$$

where δ = the logarithmic decrement,

x_0 = the initial vibration amplitude, and

x_n = the vibration amplitude after n cycles.

The logarithmic decrement can be shown as,

$$\delta = \frac{2\pi\zeta}{\sqrt{1-\zeta^2}} \quad \text{.....(Equation C.2)}$$

where ζ = the damping ratio.

After manipulation, the equation can be rewritten,

$$\zeta = \frac{\delta}{\sqrt{4\pi^2 + \delta^2}} \quad \text{.....(Equation C.3)}$$

For small values of δ ($\delta << 1.0$), the equation for the damping ratio can be written,

$$\zeta = \frac{\delta}{2\pi} \quad \text{.....(Equation C.4)}$$

C.2. System Damping

While suspended by the force balance system in still air, each specimen was manually given an initial displacement and allowed to vibrate freely. The amplitudes of vibration, in mV, were noted from the real-time history displayed by the signal analyzer for a specific number of vibration cycles. A data set of four amplitudes was obtained for each specimen. Using the amplitude values, the damping ratio, ζ, was calculated using Equation C.4.

The amplitudes, in mV, for the fourth, tenth, twentieth, and thirtieth cycles, along with the calculated damping ration, ζ, are listed in Table C.1 through C.8.

The maximum value of ζ was calculated as 0.33% corresponding to a δ of 0.020 using Equation C.4. Equation C.3 would have returned a value of ζ = 0.328% for this δ. Thus the use of the approximate Equation C.4 is justified.

Table C.1. Structural Damping, *L/D* = 2.0

Specimen	Amplitude after 4 cycles *mV*	Amplitude after 10 cycles *mV*	Amplitude after 20 cycles *mV*	Amplitude after 30 cycles *mV*	Damping *% of critical*
20.0	345	327	290	259	0.18
20.2	350	334	301	278	0.13
20.4	544	507	454	407	0.17
20.6	665	616	559	502	0.17
20.8	421	377	357	322	0.16

Table C.2. Structural Damping, *L/D* = 3.0

Specimen	Amplitude after 4 cycles *mV*	Amplitude after 10 cycles *mV*	Amplitude after 20 cycles *mV*	Amplitude after 30 cycles *mV*	Damping *% of critical*
30.0	300	287	263	238	0.16
30.2	519	469	424	382	0.17
30.4	482	425	377	338	0.17
30.6	384	360	322	295	0.14
30.8	388	367	346	317	0.14

Table C.3. Structural Damping, $L/D = 4.0$

Specimen	Amplitude after 4 cycles *mV*	Amplitude after 10 cycles *mV*	Amplitude after 20 cycles *mV*	Amplitude after 30 cycles *mV*	Damping *% of critical*
40.0	255	245	219	205	0.11
40.2	440	418	370	337	0.15
40.4	633	584	516	457	0.19
40.6	537	503	459	418	0.15
40.8	490	460	419	381	0.15

Table C.4. Structural Damping, $L/D = 5.0$

Specimen	Amplitude after 4 cycles *mV*	Amplitude after 10 cycles *mV*	Amplitude after 20 cycles *mV*	Amplitude after 30 cycles *mV*	Damping *% of critical*
50.0	495	441	381	331	0.22
50.2	482	425	365	317	0.22
50.4	338	319	275	243	0.20
50.6	539	480	408	345	0.27
50.8	431	399	361	323	0.18

Table C.5. Structural Damping, *L/D* = 5.5

Specimen	Amplitude after 4 cycles *mV*	Amplitude after 10 cycles *mV*	Amplitude after 20 cycles *mV*	Amplitude after 30 cycles *mV*	Damping *% of critical*
55.0	401	355	315	271	0.24
55.2	549	498	422	363	0.22
55.4	464	389	342	300	0.20
55.6	488	437	385	342	0.19
55.8	647	577	472	411	0.22

Table C.6. Structural Damping, *L/D* = 6.0

Specimen	Amplitude after 4 cycles *mV*	Amplitude after 10 cycles *mV*	Amplitude after 20 cycles *mV*	Amplitude after 30 cycles *mV*	Damping *% of critical*
60.0	348	313	267	229	0.24
60.2	535	484	399	334	0.28
60.4	409	366	301	253	0.28
60.6	640	535	444	371	0.29
60.8	658	575	466	379	0.33

Table C.7. Structural Damping, $L/D = 6.5$

Specimen	Amplitude after 4 cycles *mV*	Amplitude after 10 cycles *mV*	Amplitude after 20 cycles *mV*	Amplitude after 30 cycles *mV*	Damping *% of critical*
65.0	394	344	282	237	0.28
65.2	382	344	290	248	0.25
65.4	674	603	490	413	0.27
65.6	572	519	440	377	0.25
65.8	446	415	352	304	0.23

Table C.8. Structural Damping, $L/D = 7.0$

Specimen	Amplitude after 4 cycles *mV*	Amplitude after 10 cycles *mV*	Amplitude after 20 cycles *mV*	Amplitude after 30 cycles *mV*	Damping *% of critical*
70.0	785	669	525	429	0.32
70.2	604	529	465	390	0.28
70.4	383	352	316	279	0.20
70.6	347	310	284	249	0.21
70.8	622	566	486	426	0.21

APPENDIX D

SCRUTON NUMBER

D.1. Background

The Scruton number is defined as a non-dimensional parameter incorporating the ratio of structural mass and structural damping to fluid mass. The Scruton number, *Sc*, for a circular cylinder is determined from,

$$Sc = (4\pi)\frac{m_e \zeta}{\rho D^2} \quad \text{..... (Equation D.1)}$$

where m_e = the structure mass per unit length,

ζ = the structural damping as a percentage of critical,

ρ = the density of the fluid, and

D = the cross-wind body dimension.

Another definition of the Scruton number for a circular cylinder is,

$$Sc1 = \frac{m_e \zeta}{\rho D^2} \quad \text{..... (Equation D.2)}$$

This value will differ from the value returned from Equation D.1 by the factor of constant 4π.

D.2. Scruton Number

Two Scruton numbers were calculated for each rectangular specimen using the mass per unit length, the density of air, and the product of representative cross-section dimensions. First, the Scruton number was calculated for the rectangular

cylinders according to Equation D.2. The Scruton number for the rectangular cylinders was also calculated according to the following equation,

$$Sc2 = \frac{m_e \zeta}{\rho D L} \quad \text{..... (Equation D.3)}$$

The values returned from both equations are tabulated in Table D.1 through D.8.

Table D.1. Scruton number, $L/D = 2.0$

Model	Mass *slugs*	Damping *% critical*	*Sc* *Based on* D^2	*Sc* *Based on D*L*
20.0	0.0899	0.18	0.4893	0.2447
20.2	0.1376	0.13	0.5413	0.2707
20.4	0.1694	0.17	0.8710	0.4355
20.6	0.2127	0.17	1.0940	0.5470
20.8	0.2442	0.16	1.1821	0.5911

Table D.2. Scruton number, $L/D = 3.0$

Model	Mass *slugs*	Damping *% critical*	*Sc* *Based on* D^2	*Sc* *Based on D*L*
30.0	0.1021	0.16	0.4941	0.1647
30.2	0.1442	0.17	0.7415	0.2472
30.4	0.1859	0.17	0.9563	0.3188
30.6	0.2366	0.14	1.0021	0.3340
30.8	0.2499	0.14	1.0585	0.3528

Table D.3. Scruton number, $L/D = 4.0$

Model	Mass *slugs*	Damping *% critical*	*Sc* *Based on* D^2	*Sc* *Based on D*L*
40.0	0.1121	0.11	0.3731	0.0933
40.2	0.1527	0.15	0.6929	0.1732
40.4	0.1932	0.19	1.1104	0.2776
40.6	0.2170	0.15	0.9846	0.2461
40.8	0.2537	0.15	1.1514	0.2879

Table D.4. Scruton number, $L/D = 5.0$

Model	Mass *slugs*	Damping *% critical*	*Sc* *Based on* D^2	*Sc* *Based on D*L*
50.0	0.1255	0.22	0.8350	0.1670
50.2	0.1696	0.22	1.1289	0.2258
50.4	0.2186	0.20	1.3227	0.2645
50.6	0.2511	0.27	2.0513	0.4103
50.8	0.3022	0.18	1.6458	0.3292

Table D.5. Scruton number, $L/D = 5.5$

Model	Mass *slugs*	Damping *% critical*	*Sc* *Based on* D^2	*Sc* *Based on D*L*
55.0	0.1365	0.24	0.9910	0.1802
55.2	0.1777	0.24	1.2900	0.2345
55.4	0.2127	0.21	1.3515	0.2703
55.6	0.2581	0.19	1.4834	0.2697
55.8	0.2984	0.22	1.9862	0.3611

Table D.6. Scruton number, $L/D = 6.0$

Model	Mass *slugs*	Damping *% critical*	*Sc* *Based on* D^2	*Sc* *Based on D*L*
60.0	0.1365	0.24	0.9910	0.1652
60.2	0.1944	0.28	1.6466	0.2744
60.4	0.2127	0.28	1.8020	0.3003
60.6	0.2433	0.29	2.1349	0.3558
60.8	0.3514	0.33	3.5076	0.5846

Table D.7. Scruton number, $L/D = 6.5$

Model	Mass *slugs*	Damping *% critical*	*Sc* *Based on* D^2	*Sc* *Based on D*L*
65.0	0.1422	0.28	1.2042	0.1853
65.2	0.1813	0.25	1.3710	0.2109
65.4	0.2361	0.27	1.9287	0.2967
65.6	0.2621	0.25	1.9824	0.3050
65.8	0.3136	0.23	2.1821	0.3357

Table D.8. Scruton number, L/D = 7.0

Model	Mass *slugs*	Damping *% critical*	*Sc* *Based on* D^2	*Sc* *Based on D*L*
70.0	0.1509	0.32	1.4607	0.2087
70.2	0.1888	0.28	1.5717	0.2245
70.4	0.2165	0.20	1.3100	0.1871
70.6	0.2165	0.21	1.7675	0.2525
70.8	0.3136	0.21	1.9924	0.2846

APPENDIX E

WIND SPEED AND AMPLITUDE DATA

E.1. Wind speed and amplitude data.

The wind speed and amplitude data that were displayed by the signal analyzer and recorded are tabulated in Table E.1 through Table E.40 for each model tested. The data includes the fan speed in *Hz*, the wind speed in *ft/s*, the vibration amplitude in *mV*, the amplitude in *inches*, the reduced velocity, the reduced amplitude and the Reynolds number of the air flow.

Table E.1. Experimental data, Model 20.0.

Fan Speed *Hz*	Wiind velocity *ft/s*	Amplitude *mV*	Amplitude *inches*	Reduced velocity	Reduced amplitude	Reynolds number
1.50	6.19	0	0.000	1.92	0.0000	1.31E+04
1.60	6.69	0	0.000	2.07	0.0000	1.42E+04
1.70	7.20	0	0.000	2.23	0.0000	1.53E+04
1.80	7.71	0	0.000	2.39	0.0000	1.64E+04
1.90	8.22	0	0.000	2.55	0.0000	1.74E+04
2.00	8.73	0	0.000	2.70	0.0000	1.85E+04
2.10	9.23	0	0.000	2.86	0.0000	1.96E+04
2.20	9.74	0	0.000	3.02	0.0000	2.07E+04
2.30	10.25	0	0.000	3.18	0.0000	2.18E+04
2.40	10.76	0	0.000	3.33	0.0000	2.28E+04
2.50	11.26	33	0.024	3.49	0.0059	2.39E+04
2.60	11.77	60	0.043	3.65	0.0107	2.50E+04
2.70	12.28	80	0.057	3.81	0.0143	2.61E+04
2.80	12.79	125	0.089	3.96	0.0224	2.71E+04
2.90	13.29	150	0.107	4.12	0.0268	2.82E+04
3.00	13.80	193	0.138	4.28	0.0345	2.93E+04
3.10	14.31	223	0.160	4.43	0.0399	3.04E+04
3.20	14.82	262	0.187	4.59	0.0469	3.15E+04
3.30	15.32	321	0.230	4.75	0.0574	3.25E+04
3.40	15.83	373	0.267	4.91	0.0667	3.36E+04
3.50	16.34	430	0.308	5.06	0.0769	3.47E+04
3.60	16.85	493	0.353	5.22	0.0882	3.58E+04
3.70	17.35	556	0.398	5.38	0.0994	3.68E+04
3.80	17.86	596	0.426	5.54	0.1066	3.79E+04
3.90	18.37	635	0.454	5.69	0.1136	3.90E+04
4.00	18.88	651	0.466	5.85	0.1164	4.01E+04
4.10	19.38	659	0.471	6.01	0.1179	4.12E+04
4.20	19.89	643	0.460	6.16	0.1150	4.22E+04
4.30	20.40	597	0.427	6.32	0.1068	4.33E+04
4.40	20.91	15	0.011	6.48	0.0027	4.44E+04
4.50	21.41	15	0.011	6.64	0.0027	4.55E+04
4.60	21.92	15	0.011	6.79	0.0027	4.65E+04
4.70	22.43	15	0.011	6.95	0.0027	4.76E+04
4.80	22.94	20	0.014	7.11	0.0036	4.87E+04
4.90	23.44	20	0.014	7.27	0.0036	4.98E+04
5.00	23.95	25	0.018	7.42	0.0045	5.09E+04
5.10	24.46	25	0.018	7.58	0.0045	5.19E+04
5.20	24.97	30	0.021	7.74	0.0054	5.30E+04
5.30	25.48	25	0.018	7.89	0.0045	5.41E+04
5.40	25.98	30	0.021	8.05	0.0054	5.52E+04
5.50	26.49	0	0.000	8.21	0.0000	5.62E+04
5.60	27.00	0	0.000	8.37	0.0000	5.73E+04
5.70	27.51	0	0.000	8.52	0.0000	5.84E+04
5.80	28.01	0	0.000	8.68	0.0000	5.95E+04

Table E.1. Continued.

Fan Speed *Hz*	Wiind velocity *ft/s*	Amplitude *mV*	Amplitude *inches*	Reduced velocity	Reduced amplitude	Reynolds number
5.90	28.52	0	0.000	8.84	0.0000	6.06E+04
6.00	29.03	0	0.000	9.00	0.0000	6.16E+04
6.10	29.54	0	0.000	9.15	0.0000	6.27E+04
6.20	30.04	0	0.000	9.31	0.0000	6.38E+04
6.30	30.55	0	0.000	9.47	0.0000	6.49E+04
6.40	31.06	50	0.036	9.63	0.0089	6.59E+04
6.50	31.57	70	0.050	9.78	0.0125	6.70E+04
6.60	32.07	70	0.050	9.94	0.0125	6.81E+04
6.70	32.58	70	0.050	10.10	0.0125	6.92E+04
6.80	33.09	70	0.050	10.25	0.0125	7.03E+04
6.90	33.60	70	0.050	10.41	0.0125	7.13E+04
7.00	34.10	70	0.050	10.57	0.0125	7.24E+04
7.10	34.61	80	0.057	10.73	0.0143	7.35E+04
7.20	35.12	80	0.057	10.88	0.0143	7.46E+04
7.30	35.63	100	0.072	11.04	0.0179	7.56E+04
7.40	36.13	105	0.075	11.20	0.0188	7.67E+04
7.50	36.64	110	0.079	11.36	0.0197	7.78E+04
7.60	37.15	125	0.089	11.51	0.0224	7.89E+04
7.70	37.66	150	0.107	11.67	0.0268	8.00E+04
7.80	38.16	150	0.107	11.83	0.0268	8.10E+04
7.90	38.67	175	0.125	11.98	0.0313	8.21E+04
8.00	39.18	200	0.143	12.14	0.0358	8.32E+04
8.10	39.69	200	0.143	12.30	0.0358	8.43E+04
8.20	40.20	200	0.143	12.46	0.0358	8.53E+04
8.40	41.21	244	0.175	12.77	0.0436	8.75E+04
8.60	42.23	294	0.210	13.09	0.0526	8.97E+04
8.80	43.24	298	0.213	13.40	0.0533	9.18E+04
9.00	44.26	320	0.229	13.71	0.0572	9.40E+04
9.20	45.27	344	0.246	14.03	0.0615	9.61E+04
9.40	46.29	350	0.250	14.34	0.0626	9.83E+04
9.60	47.30	376	0.269	14.66	0.0673	1.00E+05
9.80	48.32	414	0.296	14.97	0.0740	1.03E+05
10.00	49.33	481	0.344	15.29	0.0860	1.05E+05
10.20	50.35	509	0.364	15.60	0.0910	1.07E+05
10.40	51.36	500	0.358	15.92	0.0894	1.09E+05
10.60	52.38	581	0.416	16.23	0.1039	1.11E+05
10.80	53.39	600	0.429	16.55	0.1073	1.13E+05
11.00	54.41	630	0.451	16.86	0.1127	1.16E+05
11.60	57.45	733	0.524	17.80	0.1311	1.22E+05
11.80	58.47	901	0.645	18.12	0.1612	1.24E+05
12.00	59.48	905	0.647	18.43	0.1619	1.26E+05

Table E.2. Experimental data, Model 20.2.

Fan Speed *Hz*	Wiind velocity *ft/s*	Amplitude *mV*	Amplitude *inches*	Reduced velocity	Reduced amplitude	Reynolds number
1.50	6.19	0.00	0.000	2.35	0.0000	1.31E+04
1.60	6.69	0.00	0.000	2.55	0.0000	1.42E+04
1.70	7.20	0.00	0.000	2.74	0.0000	1.53E+04
1.80	7.71	0.00	0.000	2.93	0.0000	1.64E+04
1.90	8.22	0.00	0.000	3.13	0.0000	1.74E+04
2.00	8.73	0.00	0.000	3.32	0.0000	1.85E+04
2.10	9.23	0.00	0.000	3.51	0.0000	1.96E+04
2.20	9.74	43.00	0.031	3.71	0.0077	2.07E+04
2.30	10.25	85.00	0.061	3.90	0.0152	2.18E+04
2.40	10.76	125.00	0.089	4.09	0.0224	2.28E+04
2.50	11.26	163.00	0.117	4.29	0.0292	2.39E+04
2.60	11.77	200.00	0.143	4.48	0.0358	2.50E+04
2.70	12.28	276.00	0.197	4.67	0.0494	2.61E+04
2.80	12.79	340.00	0.243	4.87	0.0608	2.71E+04
2.90	13.29	361.00	0.258	5.06	0.0646	2.82E+04
3.00	13.80	461.00	0.330	5.25	0.0825	2.93E+04
3.10	14.31	513.00	0.367	5.45	0.0918	3.04E+04
3.20	14.82	545.00	0.390	5.64	0.0975	3.15E+04
3.30	15.32	584.00	0.418	5.83	0.1045	3.25E+04
3.40	15.83	621.00	0.444	6.02	0.1111	3.36E+04
3.50	16.34	627.00	0.449	6.22	0.1121	3.47E+04
3.60	16.85	15.00	0.011	6.41	0.0027	3.58E+04
3.80	17.86	0.00	0.000	6.80	0.0000	3.79E+04
3.90	18.37	0.00	0.000	6.99	0.0000	3.90E+04
4.00	18.88	0.00	0.000	7.18	0.0000	4.01E+04
4.20	19.89	0.00	0.000	7.57	0.0000	4.22E+04
4.40	20.91	20.00	0.014	7.96	0.0036	4.44E+04
4.60	21.92	20.00	0.014	8.34	0.0036	4.65E+04
4.80	22.94	25.00	0.018	8.73	0.0045	4.87E+04
5.00	23.95	25.00	0.018	9.12	0.0045	5.09E+04
5.50	26.49	40.00	0.029	10.08	0.0072	5.62E+04
6.00	29.03	70.00	0.050	11.05	0.0125	6.16E+04
6.20	30.04	85.00	0.061	11.43	0.0152	6.38E+04
6.40	31.06	125.00	0.089	11.82	0.0224	6.59E+04
6.60	32.07	150.00	0.107	12.21	0.0268	6.81E+04
6.80	33.09	175.00	0.125	12.59	0.0313	7.03E+04
7.00	34.10	217.00	0.155	12.98	0.0388	7.24E+04
7.20	35.12	244.00	0.175	13.36	0.0436	7.46E+04
7.40	36.13	295.00	0.211	13.75	0.0528	7.67E+04
7.60	37.15	345.00	0.247	14.14	0.0617	7.89E+04
7.80	38.16	399.00	0.285	14.52	0.0714	8.10E+04
8.00	39.18	411.00	0.294	14.91	0.0735	8.32E+04
8.20	40.20	503.00	0.360	15.30	0.0900	8.53E+04
8.40	41.21	530.00	0.379	15.68	0.0948	8.75E+04

Table E.2. Continued.

Fan Speed *Hz*	Wiind velocity *ft/s*	Amplitude *mV*	Amplitude *inches*	Reduced velocity	Reduced amplitude	Reynolds number
8.60	42.23	597.00	0.427	16.07	0.1068	8.97E+04
8.80	43.24	617.00	0.441	16.46	0.1104	9.18E+04
9.00	44.26	633.00	0.453	16.84	0.1132	9.40E+04
9.20	45.27	690.00	0.494	17.23	0.1234	9.61E+04
9.40	46.29	691.00	0.494	17.61	0.1236	9.83E+04
9.60	47.30	717.00	0.513	18.00	0.1282	1.00E+05
9.80	48.32	809.00	0.579	18.39	0.1447	1.03E+05
10.00	49.33	867.00	0.620	18.77	0.1551	1.05E+05
10.50	51.87	900.00	0.644	19.74	0.1610	1.10E+05
11.00	54.41	1000.00	0.715	20.71	0.1789	1.16E+05
11.50	56.95	1170.00	0.837	21.67	0.2093	1.21E+05
12.00	59.48	1310.00	0.937	22.64	0.2343	1.26E+05

Table E.3. Experimental data, Model 20.4.

Fan Speed *Hz*	Wiind velocity *ft/s*	Amplitude *mV*	Amplitude *inches*	Reduced velocity	Reduced amplitude	Reynolds number
1.80	7.71	0.00	0.000	3.33	0.0000	1.64E+04
1.90	8.22	0.00	0.000	3.55	0.0000	1.74E+04
2.00	8.73	80.00	0.057	3.77	0.0143	1.85E+04
2.10	9.23	107.00	0.077	3.99	0.0191	1.96E+04
2.20	9.74	155.00	0.111	4.21	0.0277	2.07E+04
2.30	10.25	225.00	0.161	4.43	0.0402	2.18E+04
2.40	10.76	290.00	0.207	4.65	0.0519	2.28E+04
2.50	11.26	360.00	0.258	4.87	0.0644	2.39E+04
2.60	11.77	426.00	0.305	5.08	0.0762	2.50E+04
2.70	12.28	481.00	0.344	5.30	0.0860	2.61E+04
2.80	12.79	549.00	0.393	5.52	0.0982	2.71E+04
2.90	13.29	592.00	0.424	5.74	0.1059	2.82E+04
3.00	13.80	604.00	0.432	5.96	0.1080	2.93E+04
3.10	14.31	573.00	0.410	6.18	0.1025	3.04E+04
3.20	14.82	0.00	0.000	6.40	0.0000	3.15E+04
3.50	16.34	15.00	0.011	7.06	0.0027	3.47E+04
4.00	18.88	15.00	0.011	8.15	0.0027	4.01E+04
4.50	21.41	20.00	0.014	9.25	0.0036	4.55E+04
5.00	23.95	30.00	0.021	10.35	0.0054	5.09E+04
5.50	26.49	70.00	0.050	11.44	0.0125	5.62E+04
6.00	29.03	130.00	0.093	12.54	0.0233	6.16E+04
6.50	31.57	300.00	0.215	13.64	0.0537	6.70E+04
7.00	34.10	400.00	0.286	14.73	0.0715	7.24E+04
7.50	36.64	524.00	0.375	15.83	0.0937	7.78E+04
8.00	39.18	700.00	0.501	16.92	0.1252	8.32E+04
8.50	41.72	800.00	0.572	18.02	0.1431	8.86E+04
9.00	44.26	980.00	0.701	19.12	0.1753	9.40E+04
9.50	46.79	1100.00	0.787	20.21	0.1967	9.93E+04
10.00	49.33	1150.00	0.823	21.31	0.2057	1.05E+05

Table E.4. Experimental data, Model 20.6.

Fan Speed *Hz*	Wiind velocity *ft/s*	Amplitude *mV*	Amplitude *inches*	Reduced velocity	Reduced amplitude	Reynolds number
1.60	6.69	0.00	0.000	3.20	0.0000	1.42E+04
1.70	7.20	0.00	0.000	3.45	0.0000	1.53E+04
1.80	7.71	0.00	0.000	3.69	0.0000	1.64E+04
1.90	8.22	104.00	0.074	3.93	0.0186	1.74E+04
2.00	8.73	159.00	0.114	4.17	0.0284	1.85E+04
2.10	9.23	216.00	0.155	4.42	0.0386	1.96E+04
2.20	9.74	288.00	0.206	4.66	0.0515	2.07E+04
2.30	10.25	366.00	0.262	4.90	0.0655	2.18E+04
2.40	10.76	444.00	0.318	5.14	0.0794	2.28E+04
2.50	11.26	504.00	0.361	5.39	0.0901	2.39E+04
2.60	11.77	550.00	0.393	5.63	0.0984	2.50E+04
2.70	12.28	575.00	0.411	5.87	0.1028	2.61E+04
2.80	12.79	570.00	0.408	6.12	0.1020	2.71E+04
2.90	13.29	0.00	0.000	6.36	0.0000	2.82E+04
3.00	13.80	0.00	0.000	6.60	0.0000	2.93E+04
3.50	16.34	0.00	0.000	7.82	0.0000	3.47E+04
4.00	18.88	15.00	0.011	9.03	0.0027	4.01E+04
4.50	21.41	25.00	0.018	10.24	0.0045	4.55E+04
5.00	23.95	60.00	0.043	11.46	0.0107	5.09E+04
5.50	26.49	150.00	0.107	12.67	0.0268	5.62E+04
6.00	29.03	400.00	0.286	13.89	0.0715	6.16E+04
6.50	31.57	400.00	0.286	15.10	0.0715	6.70E+04
7.00	34.10	597.00	0.427	16.31	0.1068	7.24E+04
7.50	36.64	734.00	0.525	17.53	0.1313	7.78E+04
8.00	39.18	883.00	0.632	18.74	0.1579	8.32E+04
8.50	41.72	1040.00	0.744	19.96	0.1860	8.86E+04

Table E.5. Experimental data, Model 20.8.

Fan Speed *Hz*	Wiind velocity *ft/s*	Amplitude *mV*	Amplitude *inches*	Reduced velocity	Reduced amplitude	Reynolds number
1.60	6.69	0.00	0.000	3.48	0.0000	1.42E+04
1.70	7.20	60.00	0.043	3.74	0.0107	1.53E+04
1.80	7.71	100.00	0.072	4.01	0.0179	1.64E+04
1.90	8.22	175.00	0.125	4.27	0.0313	1.74E+04
2.00	8.73	262.00	0.187	4.53	0.0469	1.85E+04
2.10	9.23	322.00	0.230	4.80	0.0576	1.96E+04
2.20	9.74	396.00	0.283	5.06	0.0708	2.07E+04
2.30	10.25	479.00	0.343	5.32	0.0857	2.18E+04
2.40	10.76	525.00	0.376	5.59	0.0939	2.28E+04
2.50	11.26	548.00	0.392	5.85	0.0980	2.39E+04
2.60	11.77	511.00	0.366	6.12	0.0914	2.50E+04
2.70	12.28	0.00	0.000	6.38	0.0000	2.61E+04
2.80	12.79	0.00	0.000	6.64	0.0000	2.71E+04
2.90	13.29	0.00	0.000	6.91	0.0000	2.82E+04
3.00	13.80	10.00	0.007	7.17	0.0018	2.93E+04
3.50	16.34	15.00	0.011	8.49	0.0027	3.47E+04
4.00	18.88	30.00	0.021	9.81	0.0054	4.01E+04
4.50	21.41	70.00	0.050	11.13	0.0125	4.55E+04
5.00	23.95	125.00	0.089	12.44	0.0224	5.09E+04
5.50	26.49	300.00	0.215	13.76	0.0537	5.62E+04
6.00	29.03	400.00	0.286	15.08	0.0715	6.16E+04
6.50	31.57	632.00	0.452	16.40	0.1130	6.70E+04
7.00	34.10	800.00	0.572	17.72	0.1431	7.24E+04
7.50	36.64	940.00	0.673	19.04	0.1681	7.78E+04
8.00	39.18	1030.00	0.737	20.36	0.1842	8.32E+04
8.50	41.72	1080.00	0.773	21.67	0.1932	8.86E+04

Table E.6. Experimental data, Model 30.0.

Fan Speed *Hz*	Wiind velocity *ft/s*	Amplitude *mV*	Amplitude *inches*	Reduced velocity	Reduced amplitude	Reynolds number
1.40	5.68	0.00	0.000	1.87	0.0000	1.21E+04
1.50	6.19	0.00	0.000	2.04	0.0000	1.31E+04
1.60	6.69	0.00	0.000	2.20	0.0000	1.42E+04
1.70	7.20	0.00	0.000	2.37	0.0000	1.53E+04
1.80	7.71	0.00	0.000	2.54	0.0000	1.64E+04
1.90	8.22	46.00	0.033	2.70	0.0082	1.74E+04
2.00	8.73	57.00	0.041	2.87	0.0102	1.85E+04
2.10	9.23	66.00	0.047	3.04	0.0118	1.96E+04
2.20	9.74	68.00	0.049	3.21	0.0122	2.07E+04
2.30	10.25	0.00	0.000	3.37	0.0000	2.18E+04
2.40	10.76	0.00	0.000	3.54	0.0000	2.28E+04
2.60	11.77	0.00	0.000	3.87	0.0000	2.50E+04
2.80	12.79	0.00	0.000	4.21	0.0000	2.71E+04
3.00	13.80	16.00	0.011	4.54	0.0029	2.93E+04
3.20	14.82	24.00	0.017	4.88	0.0043	3.15E+04
3.30	15.32	32.00	0.023	5.04	0.0057	3.25E+04
3.40	15.83	41.00	0.029	5.21	0.0073	3.36E+04
3.50	16.34	59.00	0.042	5.38	0.0106	3.47E+04
3.60	16.85	125.00	0.089	5.54	0.0224	3.58E+04
3.70	17.35	223.00	0.160	5.71	0.0399	3.68E+04
3.80	17.86	277.00	0.198	5.88	0.0495	3.79E+04
3.90	18.37	317.00	0.227	6.05	0.0567	3.90E+04
4.00	18.88	357.00	0.255	6.21	0.0639	4.01E+04
4.10	19.38	398.00	0.285	6.38	0.0712	4.12E+04
4.20	19.89	411.00	0.294	6.55	0.0735	4.22E+04
4.30	20.40	396.00	0.283	6.71	0.0708	4.33E+04
4.40	20.91	387.00	0.277	6.88	0.0692	4.44E+04
4.50	21.41	386.00	0.276	7.05	0.0690	4.55E+04
4.60	21.92	360.00	0.258	7.21	0.0644	4.65E+04
4.70	22.43	359.00	0.257	7.38	0.0642	4.76E+04
4.80	22.94	327.00	0.234	7.55	0.0585	4.87E+04
4.90	23.44	80.00	0.057	7.72	0.0143	4.98E+04
5.00	23.95	50.00	0.036	7.88	0.0089	5.09E+04
5.10	24.46	40.00	0.029	8.05	0.0072	5.19E+04
5.20	24.97	25.00	0.018	8.22	0.0045	5.30E+04
5.30	25.48	0.00	0.000	8.38	0.0000	5.41E+04
5.40	25.98	0.00	0.000	8.55	0.0000	5.52E+04
5.50	26.49	0.00	0.000	8.72	0.0000	5.62E+04

Table E.7. Experimental data, Model 30.2.

Fan Speed *Hz*	Wiind velocity *ft/s*	Amplitude *mV*	Amplitude *inches*	Reduced velocity	Reduced amplitude	Reynolds number
1.40	5.68	0.00	0.000	2.23	0.0000	1.21E+04
1.50	6.19	0.00	0.000	2.43	0.0000	1.31E+04
1.60	6.69	35.00	0.025	2.63	0.0063	1.42E+04
1.70	7.20	56.00	0.040	2.82	0.0100	1.53E+04
1.80	7.71	68.00	0.049	3.02	0.0122	1.64E+04
1.90	8.22	63.00	0.045	3.22	0.0113	1.74E+04
2.00	8.73	0.00	0.000	3.42	0.0000	1.85E+04
2.10	9.23	0.00	0.000	3.62	0.0000	1.96E+04
2.20	9.74	0.00	0.000	3.82	0.0000	2.07E+04
2.30	10.25	0.00	0.000	4.02	0.0000	2.18E+04
2.40	10.76	0.00	0.000	4.22	0.0000	2.28E+04
2.50	11.26	10.00	0.007	4.42	0.0018	2.39E+04
2.60	11.77	18.00	0.013	4.62	0.0032	2.50E+04
2.70	12.28	20.00	0.014	4.81	0.0036	2.61E+04
2.80	12.79	20.00	0.014	5.01	0.0036	2.71E+04
2.90	13.29	35.00	0.025	5.21	0.0063	2.82E+04
3.00	13.80	50.00	0.036	5.41	0.0089	2.93E+04
3.10	14.31	110.00	0.079	5.61	0.0197	3.04E+04
3.20	14.82	217.00	0.155	5.81	0.0388	3.15E+04
3.30	15.32	309.00	0.221	6.01	0.0553	3.25E+04
3.40	15.83	352.00	0.252	6.21	0.0630	3.36E+04
3.50	16.34	391.00	0.280	6.41	0.0699	3.47E+04
3.60	16.85	408.00	0.292	6.61	0.0730	3.58E+04
3.70	17.35	414.00	0.296	6.80	0.0740	3.68E+04
3.80	17.86	396.00	0.283	7.00	0.0708	3.79E+04
3.90	18.37	375.00	0.268	7.20	0.0671	3.90E+04
4.00	18.88	357.00	0.255	7.40	0.0639	4.01E+04
4.10	19.38	336.00	0.240	7.60	0.0601	4.12E+04
4.20	19.89	70.00	0.050	7.80	0.0125	4.22E+04
4.30	20.40	30.00	0.021	8.00	0.0054	4.33E+04

Table E.8. Experimental data, Model 30.4.

Fan Speed *Hz*	Wiind velocity *ft/s*	Amplitude *mV*	Amplitude *inches*	Reduced velocity	Reduced amplitude	Reynolds number
1.40	5.68	0.00	0.000	2.55	0.0000	1.21E+04
1.50	6.19	48.00	0.034	2.77	0.0086	1.31E+04
1.60	6.69	62.00	0.044	3.00	0.0111	1.42E+04
1.70	7.20	50.00	0.036	3.23	0.0089	1.53E+04
1.80	7.71	0.00	0.000	3.46	0.0000	1.64E+04
1.90	8.22	0.00	0.000	3.69	0.0000	1.74E+04
2.00	8.73	0.00	0.000	3.91	0.0000	1.85E+04
2.10	9.23	0.00	0.000	4.14	0.0000	1.96E+04
2.20	9.74	0.00	0.000	4.37	0.0000	2.07E+04
2.30	10.25	10.00	0.007	4.60	0.0018	2.18E+04
2.40	10.76	12.00	0.009	4.82	0.0021	2.28E+04
2.50	11.26	18.00	0.013	5.05	0.0032	2.39E+04
2.60	11.77	25.00	0.018	5.28	0.0045	2.50E+04
2.70	12.28	50.00	0.036	5.51	0.0089	2.61E+04
2.80	12.79	172.00	0.123	5.73	0.0308	2.71E+04
2.90	13.29	260.00	0.186	5.96	0.0465	2.82E+04
3.00	13.80	321.00	0.230	6.19	0.0574	2.93E+04
3.10	14.31	372.00	0.266	6.42	0.0665	3.04E+04
3.20	14.82	393.00	0.281	6.64	0.0703	3.15E+04
3.30	15.32	396.00	0.283	6.87	0.0708	3.25E+04
3.40	15.83	377.00	0.270	7.10	0.0674	3.36E+04
3.50	16.34	357.00	0.255	7.33	0.0639	3.47E+04
3.60	16.85	336.00	0.240	7.56	0.0601	3.58E+04
3.70	17.35	70.00	0.050	7.78	0.0125	3.68E+04
3.80	17.86	40.00	0.029	8.01	0.0072	3.79E+04
3.90	18.37	0.00	0.000	8.24	0.0000	3.90E+04
4.00	18.88	0.00	0.000	8.47	0.0000	4.01E+04

Table E.9. Experimental data, Model 30.6.

Fan Speed *Hz*	Wiind velocity *ft/s*	Amplitude *mV*	Amplitude *inches*	Reduced velocity	Reduced amplitude	Reynolds number
1.20	4.66	0.00	0.000	2.31	0.0000	9.90E+03
1.30	5.17	0.00	0.000	2.56	0.0000	1.10E+04
1.40	5.68	42.00	0.030	2.81	0.0075	1.21E+04
1.50	6.19	55.00	0.039	3.07	0.0098	1.31E+04
1.60	6.69	10.00	0.007	3.32	0.0018	1.42E+04
1.70	7.20	0.00	0.000	3.57	0.0000	1.53E+04
1.80	7.71	0.00	0.000	3.82	0.0000	1.64E+04
1.90	8.22	0.00	0.000	4.07	0.0000	1.74E+04
2.00	8.73	0.00	0.000	4.32	0.0000	1.85E+04
2.10	9.23	10.00	0.007	4.57	0.0018	1.96E+04
2.20	9.74	12.00	0.009	4.83	0.0021	2.07E+04
2.30	10.25	12.00	0.009	5.08	0.0021	2.18E+04
2.40	10.76	25.00	0.018	5.33	0.0045	2.28E+04
2.50	11.26	80.00	0.057	5.58	0.0143	2.39E+04
2.60	11.77	203.00	0.145	5.83	0.0363	2.50E+04
2.70	12.28	296.00	0.212	6.08	0.0529	2.61E+04
2.80	12.79	335.00	0.240	6.33	0.0599	2.71E+04
2.90	13.29	377.00	0.270	6.59	0.0674	2.82E+04
3.00	13.80	361.00	0.258	6.84	0.0646	2.93E+04
3.10	14.31	352.00	0.252	7.09	0.0630	3.04E+04
3.20	14.82	322.00	0.230	7.34	0.0576	3.15E+04
3.30	15.32	70.00	0.050	7.59	0.0125	3.25E+04
3.40	15.83	40.00	0.029	7.84	0.0072	3.36E+04
3.50	16.34	0.00	0.000	8.09	0.0000	3.47E+04
3.60	16.85	0.00	0.000	8.35	0.0000	3.58E+04

Table E.10. Experimental data, Model 30.8.

Fan Speed *Hz*	Wiind velocity *ft/s*	Amplitude *mV*	Amplitude *inches*	Reduced velocity	Reduced amplitude	Reynolds number
1.20	4.66	5.00	0.004	2.50	0.0009	9.90E+03
1.30	5.17	10.00	0.007	2.77	0.0018	1.10E+04
1.40	5.68	25.00	0.018	3.05	0.0045	1.21E+04
1.50	6.19	10.00	0.007	3.32	0.0018	1.31E+04
1.60	6.69	0.00	0.000	3.59	0.0000	1.42E+04
1.70	7.20	0.00	0.000	3.86	0.0000	1.53E+04
1.80	7.71	0.00	0.000	4.13	0.0000	1.64E+04
1.90	8.22	0.00	0.000	4.41	0.0000	1.74E+04
2.00	8.73	10.00	0.007	4.68	0.0018	1.85E+04
2.10	9.23	10.00	0.007	4.95	0.0018	1.96E+04
2.20	9.74	10.00	0.007	5.22	0.0018	2.07E+04
2.30	10.25	40.00	0.029	5.49	0.0072	2.18E+04
2.40	10.76	180.00	0.129	5.77	0.0322	2.28E+04
2.50	11.26	268.00	0.192	6.04	0.0479	2.39E+04
2.60	11.77	309.00	0.221	6.31	0.0553	2.50E+04
2.70	12.28	307.00	0.220	6.58	0.0549	2.61E+04
2.80	12.79	305.00	0.218	6.86	0.0546	2.71E+04
2.90	13.29	273.00	0.195	7.13	0.0488	2.82E+04
3.00	13.80	70.00	0.050	7.40	0.0125	2.93E+04
3.10	14.31	50.00	0.036	7.67	0.0089	3.04E+04
3.20	14.82	20.00	0.014	7.94	0.0036	3.15E+04
3.30	15.32	15.00	0.011	8.22	0.0027	3.25E+04
3.40	15.83	0.00	0.000	8.49	0.0000	3.36E+04
3.50	16.34	0.00	0.000	8.76	0.0000	3.47E+04
3.60	16.85	0.00	0.000	9.03	0.0000	3.58E+04

Table E.11. Experimental data, Model 40.0.

Fan Speed *Hz*	Wiind velocity *ft/s*	Amplitude *mV*	Amplitude *inches*	Reduced velocity	Reduced amplitude	Reynolds number
1.50	6.19	0.00	0.000	2.14	0.0000	1.31E+04
1.60	6.69	0.00	0.000	2.31	0.0000	1.42E+04
1.70	7.20	0.00	0.000	2.49	0.0000	1.53E+04
1.80	7.71	0.00	0.000	2.66	0.0000	1.64E+04
1.90	8.22	0.00	0.000	2.84	0.0000	1.74E+04
2.00	8.73	0.00	0.000	3.01	0.0000	1.85E+04
2.10	9.23	0.00	0.000	3.19	0.0000	1.96E+04
2.20	9.74	0.00	0.000	3.36	0.0000	2.07E+04
2.30	10.25	33.00	0.024	3.54	0.0059	2.18E+04
2.40	10.76	64.00	0.046	3.71	0.0114	2.28E+04
2.50	11.26	88.00	0.063	3.89	0.0157	2.39E+04
2.60	11.77	104.00	0.074	4.06	0.0186	2.50E+04
2.70	12.28	134.00	0.096	4.24	0.0240	2.61E+04
2.80	12.79	132.00	0.094	4.41	0.0236	2.71E+04
2.90	13.29	113.00	0.081	4.59	0.0202	2.82E+04
3.00	13.80	84.00	0.060	4.76	0.0150	2.93E+04
3.10	14.31	20.00	0.014	4.94	0.0036	3.04E+04
3.20	14.82	0.00	0.000	5.12	0.0000	3.15E+04
3.30	15.32	0.00	0.000	5.29	0.0000	3.25E+04
3.40	15.83	10.00	0.007	5.47	0.0018	3.36E+04
3.50	16.34	15.00	0.011	5.64	0.0027	3.47E+04
3.60	16.85	15.00	0.011	5.82	0.0027	3.58E+04
3.70	17.35	18.00	0.013	5.99	0.0032	3.68E+04
3.80	17.86	23.00	0.016	6.17	0.0041	3.79E+04
3.90	18.37	28.00	0.020	6.34	0.0050	3.90E+04
4.00	18.88	42.00	0.030	6.52	0.0075	4.01E+04
4.10	19.38	60.00	0.043	6.69	0.0107	4.12E+04
4.20	19.89	75.00	0.054	6.87	0.0134	4.22E+04
4.30	20.40	80.00	0.057	7.04	0.0143	4.33E+04
4.40	20.91	100.00	0.072	7.22	0.0179	4.44E+04
4.50	21.41	110.00	0.079	7.39	0.0197	4.55E+04
4.60	21.92	125.00	0.089	7.57	0.0224	4.65E+04
4.70	22.43	125.00	0.089	7.74	0.0224	4.76E+04
4.80	22.94	142.00	0.102	7.92	0.0254	4.87E+04
4.90	23.44	163.00	0.117	8.09	0.0292	4.98E+04
5.00	23.95	180.00	0.129	8.27	0.0322	5.09E+04
5.10	24.46	190.00	0.136	8.44	0.0340	5.19E+04
5.20	24.97	196.00	0.140	8.62	0.0351	5.30E+04
5.30	25.48	209.00	0.150	8.80	0.0374	5.41E+04
5.40	25.98	209.00	0.150	8.97	0.0374	5.52E+04
5.50	26.49	226.00	0.162	9.15	0.0404	5.62E+04
5.60	27.00	237.00	0.170	9.32	0.0424	5.73E+04
5.70	27.51	249.00	0.178	9.50	0.0445	5.84E+04
5.80	28.01	239.00	0.171	9.67	0.0427	5.95E+04

Table E.11. Continued.

Fan Speed *Hz*	Wiind velocity *ft/s*	Amplitude *mV*	Amplitude *inches*	Reduced velocity	Reduced amplitude	Reynolds number
5.90	28.52	240.00	0.172	9.85	0.0429	6.06E+04
6.00	29.03	240.00	0.172	10.02	0.0429	6.16E+04
6.10	29.54	228.00	0.163	10.20	0.0408	6.27E+04
6.20	30.04	210.00	0.150	10.37	0.0376	6.38E+04
6.30	30.55	110.00	0.079	10.55	0.0197	6.49E+04
6.40	31.06	60.00	0.043	10.72	0.0107	6.59E+04
6.50	31.57	35.00	0.025	10.90	0.0063	6.70E+04
6.60	32.07	25.00	0.018	11.07	0.0045	6.81E+04
6.70	32.58	20.00	0.014	11.25	0.0036	6.92E+04
6.80	33.09	15.00	0.011	11.42	0.0027	7.03E+04
6.90	33.60	10.00	0.007	11.60	0.0018	7.13E+04
7.00	34.10	0.00	0.000	11.77	0.0000	7.24E+04

Table E.12. Experimental data, Model 40.2.

Fan Speed *Hz*	Wiind velocity *ft/s*	Amplitude *mV*	Amplitude *inches*	Reduced velocity	Reduced amplitude	Reynolds number
1.50	6.19	0.00	0.000	2.49	0.0000	1.31E+04
1.60	6.69	0.00	0.000	2.70	0.0000	1.42E+04
1.70	7.20	0.00	0.000	2.90	0.0000	1.53E+04
1.80	7.71	0.00	0.000	3.11	0.0000	1.64E+04
1.90	8.22	0.00	0.000	3.31	0.0000	1.74E+04
2.00	8.73	22.00	0.016	3.52	0.0039	1.85E+04
2.10	9.23	62.00	0.044	3.72	0.0111	1.96E+04
2.20	9.74	88.00	0.063	3.93	0.0157	2.07E+04
2.30	10.25	112.00	0.080	4.13	0.0200	2.18E+04
2.40	10.76	128.00	0.092	4.34	0.0229	2.28E+04
2.50	11.26	120.00	0.086	4.54	0.0215	2.39E+04
2.60	11.77	87.00	0.062	4.75	0.0156	2.50E+04
2.70	12.28	0.00	0.000	4.95	0.0000	2.61E+04
2.80	12.79	0.00	0.000	5.15	0.0000	2.71E+04
2.90	13.29	0.00	0.000	5.36	0.0000	2.82E+04
3.00	13.80	0.00	0.000	5.56	0.0000	2.93E+04
3.10	14.31	0.00	0.000	5.77	0.0000	3.04E+04
3.20	14.82	0.00	0.000	5.97	0.0000	3.15E+04
3.30	15.32	10.00	0.007	6.18	0.0018	3.25E+04
3.40	15.83	26.00	0.019	6.38	0.0047	3.36E+04
3.50	16.34	34.00	0.024	6.59	0.0061	3.47E+04
3.60	16.85	54.00	0.039	6.79	0.0097	3.58E+04
3.70	17.35	62.00	0.044	7.00	0.0111	3.68E+04
3.80	17.86	88.00	0.063	7.20	0.0157	3.79E+04
3.90	18.37	99.00	0.071	7.41	0.0177	3.90E+04
4.00	18.88	107.00	0.077	7.61	0.0191	4.01E+04
4.10	19.38	126.00	0.090	7.81	0.0225	4.12E+04
4.20	19.89	143.00	0.102	8.02	0.0256	4.22E+04
4.30	20.40	160.00	0.114	8.22	0.0286	4.33E+04
4.40	20.91	170.00	0.122	8.43	0.0304	4.44E+04
4.50	21.41	190.00	0.136	8.63	0.0340	4.55E+04
4.60	21.92	200.00	0.143	8.84	0.0358	4.65E+04
4.70	22.43	218.00	0.156	9.04	0.0390	4.76E+04
4.80	22.94	226.00	0.162	9.25	0.0404	4.87E+04
4.90	23.44	242.00	0.173	9.45	0.0433	4.98E+04
5.00	23.95	243.00	0.174	9.66	0.0435	5.09E+04
5.10	24.46	243.00	0.174	9.86	0.0435	5.19E+04
5.20	24.97	233.00	0.167	10.07	0.0417	5.30E+04
5.30	25.48	205.00	0.147	10.27	0.0367	5.41E+04
5.40	25.98	155.00	0.111	10.48	0.0277	5.52E+04
5.50	26.49	50.00	0.036	10.68	0.0089	5.62E+04
5.60	27.00	35.00	0.025	10.88	0.0063	5.73E+04
5.70	27.51	25.00	0.018	11.09	0.0045	5.84E+04
5.80	28.01	15.00	0.011	11.29	0.0027	5.95E+04

Table E.12. Continued.

Fan Speed *Hz*	Wiind velocity *ft/s*	Amplitude *mV*	Amplitude *inches*	Reduced velocity	Reduced amplitude	Reynolds number
5.90	28.52	10.00	0.007	11.50	0.0018	6.06E+04
6.00	29.03	0.00	0.000	11.70	0.0000	6.16E+04

Table E.13. Experimental data, Model 40.4.

Fan Speed *Hz*	Wiind velocity *ft/s*	Amplitude *mV*	Amplitude *inches*	Reduced velocity	Reduced amplitude	Reynolds number
1.50	6.19	0.00	0.000	2.83	0.0000	1.31E+04
1.60	6.69	0.00	0.000	3.06	0.0000	1.42E+04
1.70	7.20	0.00	0.000	3.29	0.0000	1.53E+04
1.80	7.71	10.00	0.007	3.52	0.0018	1.64E+04
1.90	8.22	50.00	0.036	3.76	0.0089	1.74E+04
2.00	8.73	85.00	0.061	3.99	0.0152	1.85E+04
2.10	9.23	115.00	0.082	4.22	0.0206	1.96E+04
2.20	9.74	125.00	0.089	4.45	0.0224	2.07E+04
2.30	10.25	95.00	0.068	4.69	0.0170	2.18E+04
2.40	10.76	10.00	0.007	4.92	0.0018	2.28E+04
2.50	11.26	0.00	0.000	5.15	0.0000	2.39E+04
2.60	11.77	0.00	0.000	5.38	0.0000	2.50E+04
2.70	12.28	10.00	0.007	5.61	0.0018	2.61E+04
2.80	12.79	10.00	0.007	5.85	0.0018	2.71E+04
2.90	13.29	15.00	0.011	6.08	0.0027	2.82E+04
3.00	13.80	15.00	0.011	6.31	0.0027	2.93E+04
3.10	14.31	20.00	0.014	6.54	0.0036	3.04E+04
3.20	14.82	40.00	0.029	6.77	0.0072	3.15E+04
3.30	15.32	55.00	0.039	7.01	0.0098	3.25E+04
3.40	15.83	80.00	0.057	7.24	0.0143	3.36E+04
3.50	16.34	94.00	0.067	7.47	0.0168	3.47E+04
3.60	16.85	107.00	0.077	7.70	0.0191	3.58E+04
3.70	17.35	127.00	0.091	7.93	0.0227	3.68E+04
3.80	17.86	146.00	0.104	8.17	0.0261	3.79E+04
3.90	18.37	160.00	0.114	8.40	0.0286	3.90E+04
4.00	18.88	182.00	0.130	8.63	0.0326	4.01E+04
4.10	19.38	199.00	0.142	8.86	0.0356	4.12E+04
4.20	19.89	209.00	0.150	9.09	0.0374	4.22E+04
4.30	20.40	214.00	0.153	9.33	0.0383	4.33E+04
4.40	20.91	230.00	0.165	9.56	0.0411	4.44E+04
4.50	21.41	230.00	0.165	9.79	0.0411	4.55E+04
4.60	21.92	223.00	0.160	10.02	0.0399	4.65E+04
4.70	22.43	205.00	0.147	10.25	0.0367	4.76E+04
4.80	22.94	107.00	0.077	10.49	0.0191	4.87E+04
4.90	23.44	30.00	0.021	10.72	0.0054	4.98E+04
5.00	23.95	30.00	0.021	10.95	0.0054	5.09E+04
5.10	24.46	25.00	0.018	11.18	0.0045	5.19E+04
5.20	24.97	10.00	0.007	11.41	0.0018	5.30E+04
5.30	25.48	0.00	0.000	11.65	0.0000	5.41E+04
5.40	25.98	0.00	0.000	11.88	0.0000	5.52E+04
5.50	26.49	0.00	0.000	12.11	0.0000	5.62E+04
5.60	27.00	0.00	0.000	12.34	0.0000	5.73E+04
5.70	27.51	0.00	0.000	12.57	0.0000	5.84E+04
5.80	28.01	0.00	0.000	12.81	0.0000	5.95E+04

Table E.13. Continued.

Fan Speed *Hz*	Wiind velocity *ft/s*	Amplitude *mV*	Amplitude *inches*	Reduced velocity	Reduced amplitude	Reynolds number
5.90	28.52	0.00	0.000	13.04	0.0000	6.06E+04
6.00	29.03	0.00	0.000	13.27	0.0000	6.16E+04

Table E.14. Experimental data, Model 40.6.

Fan Speed *Hz*	Wiind velocity *ft/s*	Amplitude *mV*	Amplitude *inches*	Reduced velocity	Reduced amplitude	Reynolds number
1.40	5.68	0.00	0.000	2.83	0.0000	1.21E+04
1.50	6.19	0.00	0.000	3.09	0.0000	1.31E+04
1.60	6.69	0.00	0.000	3.34	0.0000	1.42E+04
1.70	7.20	25.00	0.018	3.59	0.0045	1.53E+04
1.80	7.71	70.00	0.050	3.84	0.0125	1.64E+04
1.90	8.22	105.00	0.075	4.10	0.0188	1.74E+04
2.00	8.73	121.00	0.087	4.35	0.0216	1.85E+04
2.10	9.23	110.00	0.079	4.60	0.0197	1.96E+04
2.20	9.74	20.00	0.014	4.86	0.0036	2.07E+04
2.30	10.25	0.00	0.000	5.11	0.0000	2.18E+04
2.40	10.76	0.00	0.000	5.36	0.0000	2.28E+04
2.50	11.26	0.00	0.000	5.62	0.0000	2.39E+04
2.60	11.77	10.00	0.007	5.87	0.0018	2.50E+04
2.70	12.28	10.00	0.007	6.12	0.0018	2.61E+04
2.80	12.79	15.00	0.011	6.38	0.0027	2.71E+04
2.90	13.29	15.00	0.011	6.63	0.0027	2.82E+04
3.00	13.80	25.00	0.018	6.88	0.0045	2.93E+04
3.10	14.31	50.00	0.036	7.13	0.0089	3.04E+04
3.20	14.82	71.00	0.051	7.39	0.0127	3.15E+04
3.30	15.32	97.00	0.069	7.64	0.0173	3.25E+04
3.40	15.83	114.00	0.082	7.89	0.0204	3.36E+04
3.50	16.34	134.00	0.096	8.15	0.0240	3.47E+04
3.60	16.85	143.00	0.102	8.40	0.0256	3.58E+04
3.70	17.35	170.00	0.122	8.65	0.0304	3.68E+04
3.80	17.86	180.00	0.129	8.91	0.0322	3.79E+04
3.90	18.37	184.00	0.132	9.16	0.0329	3.90E+04
4.00	18.88	188.00	0.135	9.41	0.0336	4.01E+04
4.10	19.38	186.00	0.133	9.67	0.0333	4.12E+04
4.20	19.89	182.00	0.130	9.92	0.0326	4.22E+04
4.30	20.40	133.00	0.095	10.17	0.0238	4.33E+04
4.40	20.91	50.00	0.036	10.42	0.0089	4.44E+04
4.50	21.41	25.00	0.018	10.68	0.0045	4.55E+04
4.60	21.92	10.00	0.007	10.93	0.0018	4.65E+04
4.70	22.43	0.00	0.000	11.18	0.0000	4.76E+04
4.80	22.94	0.00	0.000	11.44	0.0000	4.87E+04
4.90	23.44	0.00	0.000	11.69	0.0000	4.98E+04
5.00	23.95	0.00	0.000	11.94	0.0000	5.09E+04

Table E.15. Experimental data, Model 40.8.

Fan Speed *Hz*	Wiind velocity *ft/s*	Amplitude *mV*	Amplitude *inches*	Reduced velocity	Reduced amplitude	Reynolds number
1.40	5.68	0.00	0.000	3.08	0.0000	1.21E+04
1.50	6.19	0.00	0.000	3.35	0.0000	1.31E+04
1.60	6.69	10.00	0.007	3.63	0.0018	1.42E+04
1.70	7.20	68.00	0.049	3.90	0.0122	1.53E+04
1.80	7.71	103.00	0.074	4.17	0.0184	1.64E+04
1.90	8.22	119.00	0.085	4.45	0.0213	1.74E+04
2.00	8.73	104.00	0.074	4.72	0.0186	1.85E+04
2.10	9.23	15.00	0.011	5.00	0.0027	1.96E+04
2.20	9.74	10.00	0.007	5.27	0.0018	2.07E+04
2.30	10.25	0.00	0.000	5.55	0.0000	2.18E+04
2.40	10.76	0.00	0.000	5.82	0.0000	2.28E+04
2.50	11.26	10.00	0.007	6.10	0.0018	2.39E+04
2.60	11.77	10.00	0.007	6.37	0.0018	2.50E+04
2.70	12.28	15.00	0.011	6.65	0.0027	2.61E+04
2.80	12.79	22.00	0.016	6.92	0.0039	2.71E+04
2.90	13.29	42.00	0.030	7.20	0.0075	2.82E+04
3.00	13.80	69.00	0.049	7.47	0.0123	2.93E+04
3.10	14.31	86.50	0.062	7.75	0.0155	3.04E+04
3.20	14.82	101.00	0.072	8.02	0.0181	3.15E+04
3.30	15.32	123.00	0.088	8.30	0.0220	3.25E+04
3.40	15.83	143.00	0.102	8.57	0.0256	3.36E+04
3.50	16.34	156.00	0.112	8.85	0.0279	3.47E+04
3.60	16.85	159.00	0.114	9.12	0.0284	3.58E+04
3.70	17.35	164.00	0.117	9.40	0.0293	3.68E+04
3.80	17.86	169.00	0.121	9.67	0.0302	3.79E+04
3.90	18.37	139.00	0.099	9.95	0.0249	3.90E+04
4.00	18.88	84.00	0.060	10.22	0.0150	4.01E+04
4.10	19.38	20.00	0.014	10.50	0.0036	4.12E+04
4.20	19.89	0.00	0.000	10.77	0.0000	4.22E+04
4.30	20.40	0.00	0.000	11.05	0.0000	4.33E+04
4.40	20.91	0.00	0.000	11.32	0.0000	4.44E+04
4.50	21.41	0.00	0.000	11.60	0.0000	4.55E+04
4.60	21.92	0.00	0.000	11.87	0.0000	4.65E+04
4.70	22.43	0.00	0.000	12.15	0.0000	4.76E+04
4.80	22.94	0.00	0.000	12.42	0.0000	4.87E+04
4.90	23.44	0.00	0.000	12.70	0.0000	4.98E+04
5.00	23.95	0.00	0.000	12.97	0.0000	5.09E+04

Table E.16. Experimental data, Model 50.0.

Fan Speed *Hz*	Wiind velocity *ft/s*	Amplitude *mV*	Amplitude *inches*	Reduced velocity	Reduced amplitude	Reynolds number
1.50	6.19	0.00	0.000	2.25	0.0000	1.31E+04
1.60	6.69	0.00	0.000	2.43	0.0000	1.42E+04
1.70	7.20	0.00	0.000	2.62	0.0000	1.53E+04
1.80	7.71	16.00	0.011	2.80	0.0029	1.64E+04
1.90	8.22	25.00	0.018	2.99	0.0045	1.74E+04
2.00	8.73	16.00	0.011	3.17	0.0029	1.85E+04
2.10	9.23	0.00	0.000	3.36	0.0000	1.96E+04
2.20	9.74	0.00	0.000	3.54	0.0000	2.07E+04
2.30	10.25	0.00	0.000	3.73	0.0000	2.18E+04
2.40	10.76	0.00	0.000	3.91	0.0000	2.28E+04
2.50	11.26	10.00	0.007	4.09	0.0018	2.39E+04
2.60	11.77	10.00	0.007	4.28	0.0018	2.50E+04
2.70	12.28	103.00	0.074	4.46	0.0184	2.61E+04
2.80	12.79	148.00	0.106	4.65	0.0265	2.71E+04
2.90	13.29	180.00	0.129	4.83	0.0322	2.82E+04
3.00	13.80	169.00	0.121	5.02	0.0302	2.93E+04
3.10	14.31	103.00	0.074	5.20	0.0184	3.04E+04
3.20	14.82	92.00	0.066	5.39	0.0165	3.15E+04
3.30	15.32	33.00	0.024	5.57	0.0059	3.25E+04
3.40	15.83	15.00	0.011	5.76	0.0027	3.36E+04
3.50	16.34	15.00	0.011	5.94	0.0027	3.47E+04
3.60	16.85	15.00	0.011	6.12	0.0027	3.58E+04
3.70	17.35	0.00	0.000	6.31	0.0000	3.68E+04
3.80	17.86	0.00	0.000	6.49	0.0000	3.79E+04
3.90	18.37	0.00	0.000	6.68	0.0000	3.90E+04
4.00	18.88	0.00	0.000	6.86	0.0000	4.01E+04

Table E.17. Experimental data, Model 50.2.

Fan Speed *Hz*	Wiind velocity *ft/s*	Amplitude *mV*	Amplitude *inches*	Reduced velocity	Reduced amplitude	Reynolds number
1.40	5.68	0.00	0.000	2.41	0.0000	1.21E+04
1.50	6.19	0.00	0.000	2.63	0.0000	1.31E+04
1.60	6.69	16.00	0.011	2.84	0.0029	1.42E+04
1.70	7.20	23.00	0.016	3.06	0.0041	1.53E+04
1.80	7.71	10.00	0.007	3.28	0.0018	1.64E+04
1.90	8.22	0.00	0.000	3.49	0.0000	1.74E+04
2.00	8.73	0.00	0.000	3.71	0.0000	1.85E+04
2.10	9.23	0.00	0.000	3.92	0.0000	1.96E+04
2.20	9.74	0.00	0.000	4.14	0.0000	2.07E+04
2.30	10.25	0.00	0.000	4.35	0.0000	2.18E+04
2.40	10.76	110.00	0.079	4.57	0.0197	2.28E+04
2.50	11.26	166.00	0.119	4.79	0.0297	2.39E+04
2.60	11.77	180.00	0.129	5.00	0.0322	2.50E+04
2.70	12.28	127.00	0.091	5.22	0.0227	2.61E+04
2.80	12.79	15.00	0.011	5.43	0.0027	2.71E+04
2.90	13.29	25.00	0.018	5.65	0.0045	2.82E+04
3.00	13.80	15.00	0.011	5.86	0.0027	2.93E+04
3.10	14.31	15.00	0.011	6.08	0.0027	3.04E+04
3.20	14.82	15.00	0.011	6.30	0.0027	3.15E+04
3.30	15.32	10.00	0.007	6.51	0.0018	3.25E+04
3.40	15.83	10.00	0.007	6.73	0.0018	3.36E+04
3.50	16.34	0.00	0.000	6.94	0.0000	3.47E+04
3.60	16.85	0.00	0.000	7.16	0.0000	3.58E+04
3.70	17.35	0.00	0.000	7.37	0.0000	3.68E+04
3.80	17.86	0.00	0.000	7.59	0.0000	3.79E+04
3.90	18.37	0.00	0.000	7.80	0.0000	3.90E+04

Table E.18. Experimental data, Model 50.4.

Fan Speed *Hz*	Wiind velocity *ft/s*	Amplitude *mV*	Amplitude *inches*	Reduced velocity	Reduced amplitude	Reynolds number
1.20	4.66	0.00	0.000	2.20	0.0000	9.90E+03
1.30	5.17	0.00	0.000	2.44	0.0000	1.10E+04
1.40	5.68	0.00	0.000	2.68	0.0000	1.21E+04
1.50	6.19	16.00	0.011	2.92	0.0029	1.31E+04
1.60	6.69	10.00	0.007	3.16	0.0018	1.42E+04
1.70	7.20	0.00	0.000	3.40	0.0000	1.53E+04
1.80	7.71	0.00	0.000	3.64	0.0000	1.64E+04
1.90	8.22	0.00	0.000	3.88	0.0000	1.74E+04
2.00	8.73	0.00	0.000	4.12	0.0000	1.85E+04
2.10	9.23	0.00	0.000	4.36	0.0000	1.96E+04
2.20	9.74	95.00	0.068	4.60	0.0170	2.07E+04
2.30	10.25	130.00	0.093	4.84	0.0233	2.18E+04
2.40	10.76	168.00	0.120	5.08	0.0300	2.28E+04
2.50	11.26	125.00	0.089	5.32	0.0224	2.39E+04
2.60	11.77	35.00	0.025	5.56	0.0063	2.50E+04
2.70	12.28	15.00	0.011	5.80	0.0027	2.61E+04
2.80	12.79	11.00	0.008	6.04	0.0020	2.71E+04
2.90	13.29	0.00	0.000	6.28	0.0000	2.82E+04
3.00	13.80	0.00	0.000	6.52	0.0000	2.93E+04

Table E.19. Experimental data, Model 50.6.

Fan Speed *Hz*	Wiind velocity *ft/s*	Amplitude *mV*	Amplitude *inches*	Reduced velocity	Reduced amplitude	Reynolds number
1.20	4.66	0.00	0.000	2.39	0.0000	9.90E+03
1.30	5.17	0.00	0.000	2.65	0.0000	1.10E+04
1.40	5.68	0.00	0.000	2.91	0.0000	1.21E+04
1.50	6.19	0.00	0.000	3.17	0.0000	1.31E+04
1.60	6.69	0.00	0.000	3.43	0.0000	1.42E+04
1.70	7.20	0.00	0.000	3.69	0.0000	1.53E+04
1.80	7.71	0.00	0.000	3.95	0.0000	1.64E+04
1.90	8.22	0.00	0.000	4.21	0.0000	1.74E+04
2.00	8.73	10.00	0.007	4.47	0.0018	1.85E+04
2.10	9.23	145.00	0.104	4.73	0.0259	1.96E+04
2.20	9.74	164.00	0.117	4.99	0.0293	2.07E+04
2.30	10.25	125.00	0.089	5.25	0.0224	2.18E+04
2.40	10.76	22.00	0.016	5.51	0.0039	2.28E+04
2.50	11.26	10.00	0.007	5.77	0.0018	2.39E+04
2.60	11.77	8.00	0.006	6.03	0.0014	2.50E+04
2.70	12.28	0.00	0.000	6.29	0.0000	2.61E+04
2.80	12.79	0.00	0.000	6.55	0.0000	2.71E+04
2.90	13.29	0.00	0.000	6.81	0.0000	2.82E+04
3.00	13.80	0.00	0.000	7.08	0.0000	2.93E+04

Table E.20. Experimental data, Model 50.8.

Fan Speed *Hz*	Wiind velocity *ft/s*	Amplitude *mV*	Amplitude *inches*	Reduced velocity	Reduced amplitude	Reynolds number
1.20	4.66	0.00	0.000	2.60	0.0000	9.90E+03
1.30	5.17	0.00	0.000	2.88	0.0000	1.10E+04
1.40	5.68	0.00	0.000	3.17	0.0000	1.21E+04
1.50	6.19	0.00	0.000	3.45	0.0000	1.31E+04
1.60	6.69	0.00	0.000	3.73	0.0000	1.42E+04
1.70	7.20	0.00	0.000	4.02	0.0000	1.53E+04
1.80	7.71	0.00	0.000	4.30	0.0000	1.64E+04
1.90	8.22	107.00	0.077	4.58	0.0191	1.74E+04
2.00	8.73	164.00	0.117	4.87	0.0293	1.85E+04
2.10	9.23	154.00	0.110	5.15	0.0275	1.96E+04
2.20	9.74	18.00	0.013	5.43	0.0032	2.07E+04
2.30	10.25	0.00	0.000	5.72	0.0000	2.18E+04
2.40	10.76	0.00	0.000	6.00	0.0000	2.28E+04
2.50	11.26	0.00	0.000	6.28	0.0000	2.39E+04
2.60	11.77	0.00	0.000	6.57	0.0000	2.50E+04
2.70	12.28	0.00	0.000	6.85	0.0000	2.61E+04
2.80	12.79	0.00	0.000	7.13	0.0000	2.71E+04
2.90	13.29	0.00	0.000	7.41	0.0000	2.82E+04
3.00	13.80	0.00	0.000	7.70	0.0000	2.93E+04

Table E.21. Experimental data, Model 55.0.

Fan Speed *Hz*	Wiind velocity *ft/s*	Amplitude *mV*	Amplitude *inches*	Reduced velocity	Reduced amplitude	Reynolds number
1.80	7.71	0.00	0.000	2.89	0.0000	1.64E+04
1.90	8.22	0.00	0.000	3.08	0.0000	1.74E+04
2.00	8.73	25.00	0.018	3.28	0.0045	1.85E+04
2.10	9.23	25.00	0.018	3.47	0.0045	1.96E+04
2.20	9.74	10.00	0.007	3.66	0.0018	2.07E+04
2.30	10.25	0.00	0.000	3.85	0.0000	2.18E+04
2.40	10.76	0.00	0.000	4.04	0.0000	2.28E+04
2.50	11.26	0.00	0.000	4.23	0.0000	2.39E+04
2.60	11.77	15.00	0.011	4.42	0.0027	2.50E+04
2.70	12.28	30.00	0.021	4.61	0.0054	2.61E+04
2.80	12.79	120.00	0.086	4.80	0.0215	2.71E+04
2.90	13.29	140.00	0.100	4.99	0.0250	2.82E+04
3.00	13.80	140.00	0.100	5.18	0.0250	2.93E+04
3.10	14.31	82.00	0.059	5.37	0.0147	3.04E+04
3.20	14.82	42.00	0.030	5.56	0.0075	3.15E+04
3.30	15.32	20.00	0.014	5.75	0.0036	3.25E+04
3.40	15.83	15.00	0.011	5.94	0.0027	3.36E+04
3.50	16.34	0.00	0.000	6.13	0.0000	3.47E+04
3.60	16.85	0.00	0.000	6.32	0.0000	3.58E+04
3.70	17.35	0.00	0.000	6.51	0.0000	3.68E+04
3.80	17.86	0.00	0.000	6.71	0.0000	3.79E+04

Table E.22. Experimental data, Model 55.2.

Fan Speed *Hz*	Wiind velocity *ft/s*	Amplitude *mV*	Amplitude *inches*	Reduced velocity	Reduced amplitude	Reynolds number
1.60	6.69	0.00	0.000	2.87	0.0000	1.42E+04
1.70	7.20	0.00	0.000	3.09	0.0000	1.53E+04
1.80	7.71	25.00	0.018	3.31	0.0045	1.64E+04
1.90	8.22	10.00	0.007	3.52	0.0018	1.74E+04
2.00	8.73	0.00	0.000	3.74	0.0000	1.85E+04
2.10	9.23	0.00	0.000	3.96	0.0000	1.96E+04
2.20	9.74	0.00	0.000	4.18	0.0000	2.07E+04
2.30	10.25	0.00	0.000	4.39	0.0000	2.18E+04
2.40	10.76	15.00	0.011	4.61	0.0027	2.28E+04
2.50	11.26	140.00	0.100	4.83	0.0250	2.39E+04
2.60	11.77	110.00	0.079	5.05	0.0197	2.50E+04
2.70	12.28	100.00	0.072	5.26	0.0179	2.61E+04
2.80	12.79	30.00	0.021	5.48	0.0054	2.71E+04
2.90	13.29	10.00	0.007	5.70	0.0018	2.82E+04
3.00	13.80	0.00	0.000	5.92	0.0000	2.93E+04

Table E.23. Experimental data, Model 55.4.

Fan Speed *Hz*	Wiind velocity *ft/s*	Amplitude *mV*	Amplitude *inches*	Reduced velocity	Reduced amplitude	Reynolds number
1.40	5.68	0.00	0.000	2.72	0.0000	1.21E+04
1.50	6.19	0.00	0.000	2.96	0.0000	1.31E+04
1.60	6.69	0.00	0.000	3.20	0.0000	1.42E+04
1.70	7.20	10.00	0.007	3.45	0.0018	1.53E+04
1.80	7.71	0.00	0.000	3.69	0.0000	1.64E+04
1.90	8.22	0.00	0.000	3.93	0.0000	1.74E+04
2.00	8.73	0.00	0.000	4.17	0.0000	1.85E+04
2.10	9.23	0.00	0.000	4.42	0.0000	1.96E+04
2.20	9.74	25.00	0.018	4.66	0.0045	2.07E+04
2.30	10.25	106.00	0.076	4.90	0.0190	2.18E+04
2.40	10.76	119.00	0.085	5.14	0.0213	2.28E+04
2.50	11.26	55.00	0.039	5.39	0.0098	2.39E+04
2.60	11.77	0.00	0.000	5.63	0.0000	2.50E+04
2.70	12.28	0.00	0.000	5.87	0.0000	2.61E+04
2.80	12.79	0.00	0.000	6.12	0.0000	2.71E+04

Table E.24. Experimental data, Model 55.6.

Fan Speed *Hz*	Wiind velocity *ft/s*	Amplitude *mV*	Amplitude *inches*	Reduced velocity	Reduced amplitude	Reynolds number
1.20	4.66	0.00	0.000	2.45	0.0000	9.90E+03
1.30	5.17	0.00	0.000	2.71	0.0000	1.10E+04
1.40	5.68	0.00	0.000	2.98	0.0000	1.21E+04
1.50	6.19	10.00	0.007	3.25	0.0018	1.31E+04
1.60	6.69	10.00	0.007	3.51	0.0018	1.42E+04
1.70	7.20	0.00	0.000	3.78	0.0000	1.53E+04
1.80	7.71	0.00	0.000	4.05	0.0000	1.64E+04
1.90	8.22	0.00	0.000	4.31	0.0000	1.74E+04
2.00	8.73	18.00	0.013	4.58	0.0032	1.85E+04
2.10	9.23	110.00	0.079	4.84	0.0197	1.96E+04
2.20	9.74	122.00	0.087	5.11	0.0218	2.07E+04
2.30	10.25	70.00	0.050	5.38	0.0125	2.18E+04
2.40	10.76	0.00	0.000	5.64	0.0000	2.28E+04
2.50	11.26	0.00	0.000	5.91	0.0000	2.39E+04
2.60	11.77	0.00	0.000	6.18	0.0000	2.50E+04

Table E.25. Experimental data, Model 55.8.

Fan Speed *Hz*	Wiind velocity *ft/s*	Amplitude *mV*	Amplitude *inches*	Reduced velocity	Reduced amplitude	Reynolds number
1.20	4.66	0.00	0.000	2.61	0.0000	9.90E+03
1.30	5.17	0.00	0.000	2.89	0.0000	1.10E+04
1.40	5.68	5.00	0.004	3.18	0.0009	1.21E+04
1.50	6.19	0.00	0.000	3.46	0.0000	1.31E+04
1.60	6.69	0.00	0.000	3.75	0.0000	1.42E+04
1.70	7.20	0.00	0.000	4.03	0.0000	1.53E+04
1.80	7.71	8.00	0.006	4.31	0.0014	1.64E+04
1.90	8.22	30.00	0.021	4.60	0.0054	1.74E+04
2.00	8.73	108.00	0.077	4.88	0.0193	1.85E+04
2.10	9.23	85.00	0.061	5.17	0.0152	1.96E+04
2.20	9.74	0.00	0.000	5.45	0.0000	2.07E+04
2.30	10.25	0.00	0.000	5.74	0.0000	2.18E+04
2.40	10.76	0.00	0.000	6.02	0.0000	2.28E+04
2.50	11.26	0.00	0.000	6.30	0.0000	2.39E+04
2.60	11.77	0.00	0.000	6.59	0.0000	2.50E+04

Table E.26. Experimental data, Model 60.0.

Fan Speed *Hz*	Wiind velocity *ft/s*	Amplitude *mV*	Amplitude *inches*	Reduced velocity	Reduced amplitude	Reynolds number
1.70	7.20	0.00	0.000	2.70	0.0000	1.53E+04
1.80	7.71	0.00	0.000	2.89	0.0000	1.64E+04
1.90	8.22	0.00	0.000	3.08	0.0000	1.74E+04
2.00	8.73	0.00	0.000	3.28	0.0000	1.85E+04
2.10	9.23	24.00	0.017	3.47	0.0043	1.96E+04
2.20	9.74	33.00	0.024	3.66	0.0059	2.07E+04
2.30	10.25	31.00	0.022	3.85	0.0055	2.18E+04
2.40	10.76	13.00	0.009	4.04	0.0023	2.28E+04
2.50	11.26	10.00	0.007	4.23	0.0018	2.39E+04
2.60	11.77	10.00	0.007	4.42	0.0018	2.50E+04
2.70	12.28	18.00	0.013	4.61	0.0032	2.61E+04
2.80	12.79	51.30	0.037	4.80	0.0092	2.71E+04
2.90	13.29	83.20	0.060	4.99	0.0149	2.82E+04
3.00	13.80	68.00	0.049	5.18	0.0122	2.93E+04
3.10	14.31	32.00	0.023	5.37	0.0057	3.04E+04
3.20	14.82	12.00	0.009	5.56	0.0021	3.15E+04
3.30	15.32	0.00	0.000	5.75	0.0000	3.25E+04
3.40	15.83	0.00	0.000	5.94	0.0000	3.36E+04
3.50	16.34	0.00	0.000	6.13	0.0000	3.47E+04
3.60	16.85	0.00	0.000	6.32	0.0000	3.58E+04
3.70	17.35	0.00	0.000	6.51	0.0000	3.68E+04
3.80	17.86	0.00	0.000	6.71	0.0000	3.79E+04
3.90	18.37	0.00	0.000	6.90	0.0000	3.90E+04
4.00	18.88	0.00	0.000	7.09	0.0000	4.01E+04
4.20	19.89	0.00	0.000	7.47	0.0000	4.22E+04
4.40	20.91	0.00	0.000	7.85	0.0000	4.44E+04
4.60	21.92	0.00	0.000	8.23	0.0000	4.65E+04
4.80	22.94	0.00	0.000	8.61	0.0000	4.87E+04
5.00	23.95	0.00	0.000	8.99	0.0000	5.09E+04
5.20	24.97	0.00	0.000	9.37	0.0000	5.30E+04
5.40	25.98	0.00	0.000	9.75	0.0000	5.52E+04
5.60	27.00	0.00	0.000	10.14	0.0000	5.73E+04
5.80	28.01	0.00	0.000	10.52	0.0000	5.95E+04
6.00	29.03	0.00	0.000	10.90	0.0000	6.16E+04
6.20	30.04	0.00	0.000	11.28	0.0000	6.38E+04
6.40	31.06	0.00	0.000	11.66	0.0000	6.59E+04
6.60	32.07	0.00	0.000	12.04	0.0000	6.81E+04
6.80	33.09	0.00	0.000	12.42	0.0000	7.03E+04
7.00	34.10	0.00	0.000	12.80	0.0000	7.24E+04
7.20	35.12	0.00	0.000	13.18	0.0000	7.46E+04
7.40	36.13	0.00	0.000	13.56	0.0000	7.67E+04
7.60	37.15	0.00	0.000	13.95	0.0000	7.89E+04
7.80	38.16	0.00	0.000	14.33	0.0000	8.10E+04
8.00	39.18	0.00	0.000	14.71	0.0000	8.32E+04

Table E.26. Continued.

Fan Speed *Hz*	Wiind velocity *ft/s*	Amplitude *mV*	Amplitude *inches*	Reduced velocity	Reduced amplitude	Reynolds number
8.20	40.20	0.00	0.000	15.09	0.0000	8.53E+04
8.40	41.21	0.00	0.000	15.47	0.0000	8.75E+04
8.60	42.23	0.00	0.000	15.85	0.0000	8.97E+04
8.80	43.24	0.00	0.000	16.23	0.0000	9.18E+04
9.00	44.26	0.00	0.000	16.61	0.0000	9.40E+04
9.20	45.27	0.00	0.000	16.99	0.0000	9.61E+04
9.40	46.29	0.00	0.000	17.38	0.0000	9.83E+04
9.60	47.30	0.00	0.000	17.76	0.0000	1.00E+05
9.80	48.32	0.00	0.000	18.14	0.0000	1.03E+05
10.00	49.33	0.00	0.000	18.52	0.0000	1.05E+05

Table E.27. Experimental data, Model 60.2.

Fan Speed *Hz*	Wiind velocity *ft/s*	Amplitude *mV*	Amplitude *inches*	Reduced velocity	Reduced amplitude	Reynolds number
1.70	7.20	0.00	0.000	3.14	0.0000	1.53E+04
1.80	7.71	10.00	0.007	3.37	0.0018	1.64E+04
1.90	8.22	30.00	0.021	3.59	0.0054	1.74E+04
2.00	8.73	30.00	0.021	3.81	0.0054	1.85E+04
2.10	9.23	8.00	0.006	4.03	0.0014	1.96E+04
2.20	9.74	8.00	0.006	4.25	0.0014	2.07E+04
2.30	10.25	12.00	0.009	4.47	0.0021	2.18E+04
2.40	10.76	65.00	0.047	4.70	0.0116	2.28E+04
2.50	11.26	80.00	0.057	4.92	0.0143	2.39E+04
2.60	11.77	60.00	0.043	5.14	0.0107	2.50E+04
2.70	12.28	12.00	0.009	5.36	0.0021	2.61E+04
2.80	12.79	10.00	0.007	5.58	0.0018	2.71E+04
2.90	13.29	0.00	0.000	5.80	0.0000	2.82E+04
3.00	13.80	0.00	0.000	6.03	0.0000	2.93E+04

Table E.28. Experimental data, Model 60.4

Fan Speed *Hz*	Wiind velocity *ft/s*	Amplitude *mV*	Amplitude *inches*	Reduced velocity	Reduced amplitude	Reynolds number
1.50	6.19	0.00	0.000	2.96	0.0000	1.31E+04
1.60	6.69	0.00	0.000	3.20	0.0000	1.42E+04
1.70	7.20	21.00	0.015	3.45	0.0038	1.53E+04
1.80	7.71	30.00	0.021	3.69	0.0054	1.64E+04
1.90	8.22	12.00	0.009	3.93	0.0021	1.74E+04
2.00	8.73	0.00	0.000	4.17	0.0000	1.85E+04
2.10	9.23	0.00	0.000	4.42	0.0000	1.96E+04
2.20	9.74	15.00	0.011	4.66	0.0027	2.07E+04
2.30	10.25	72.00	0.052	4.90	0.0129	2.18E+04
2.40	10.76	38.00	0.027	5.14	0.0068	2.28E+04
2.50	11.26	15.00	0.011	5.39	0.0027	2.39E+04
2.60	11.77	0.00	0.000	5.63	0.0000	2.50E+04
2.70	12.28	0.00	0.000	5.87	0.0000	2.61E+04
2.80	12.79	0.00	0.000	6.12	0.0000	2.71E+04

Table E.29. Experimental data, Model 60.6.

Fan Speed *Hz*	Wiind velocity *ft/s*	Amplitude *mV*	Amplitude *inches*	Reduced velocity	Reduced amplitude	Reynolds number
1.40	5.68	0.00	0.000	2.97	0.0000	1.21E+04
1.50	6.19	0.00	0.000	3.24	0.0000	1.31E+04
1.60	6.69	0.00	0.000	3.51	0.0000	1.42E+04
1.70	7.20	20.00	0.014	3.77	0.0036	1.53E+04
1.80	7.71	0.00	0.000	4.04	0.0000	1.64E+04
1.90	8.22	0.00	0.000	4.30	0.0000	1.74E+04
2.00	8.73	10.00	0.007	4.57	0.0018	1.85E+04
2.10	9.23	22.00	0.016	4.83	0.0039	1.96E+04
2.20	9.74	73.00	0.052	5.10	0.0131	2.07E+04
2.30	10.25	10.00	0.007	5.37	0.0018	2.18E+04
2.40	10.76	0.00	0.000	5.63	0.0000	2.28E+04
2.50	11.26	0.00	0.000	5.90	0.0000	2.39E+04
2.60	11.77	0.00	0.000	6.16	0.0000	2.50E+04
2.70	12.28	0.00	0.000	6.43	0.0000	2.61E+04

Table E.30. Experimental data, Model 60.8.

Fan Speed *Hz*	Wiind velocity *ft/s*	Amplitude *mV*	Amplitude *inches*	Reduced velocity	Reduced amplitude	Reynolds number
1.20	4.66	0.00	0.000	2.67	0.0000	9.90E+03
1.30	5.17	0.00	0.000	2.96	0.0000	1.10E+04
1.40	5.68	0.00	0.000	3.25	0.0000	1.21E+04
1.50	6.19	0.00	0.000	3.54	0.0000	1.31E+04
1.60	6.69	10.00	0.007	3.83	0.0018	1.42E+04
1.70	7.20	0.00	0.000	4.12	0.0000	1.53E+04
1.80	7.71	0.00	0.000	4.41	0.0000	1.64E+04
1.90	8.22	10.00	0.007	4.70	0.0018	1.74E+04
2.00	8.73	62.00	0.044	4.99	0.0111	1.85E+04
2.10	9.23	10.00	0.007	5.29	0.0018	1.96E+04
2.20	9.74	10.00	0.007	5.58	0.0018	2.07E+04
2.30	10.25	0.00	0.000	5.87	0.0000	2.18E+04
2.40	10.76	0.00	0.000	6.16	0.0000	2.28E+04
2.50	11.26	0.00	0.000	6.45	0.0000	2.39E+04

Table E.31. Experimental data, Model 65.0.

Fan Speed *Hz*	Wiind velocity *ft/s*	Amplitude *mV*	Amplitude *inches*	Reduced velocity	Reduced amplitude	Reynolds number
2.00	8.73	0.00	0.000	3.38	0.0000	1.85E+04
2.10	9.23	0.00	0.000	3.58	0.0000	1.96E+04
2.20	9.74	30.00	0.021	3.77	0.0054	2.07E+04
2.30	10.25	47.00	0.034	3.97	0.0084	2.18E+04
2.40	10.76	52.00	0.037	4.17	0.0093	2.28E+04
2.50	11.26	44.00	0.031	4.36	0.0079	2.39E+04
2.60	11.77	27.00	0.019	4.56	0.0048	2.50E+04
2.70	12.28	20.00	0.014	4.76	0.0036	2.61E+04
2.80	12.79	21.00	0.015	4.95	0.0038	2.71E+04
2.90	13.29	21.00	0.015	5.15	0.0038	2.82E+04
3.00	13.80	20.00	0.014	5.35	0.0036	2.93E+04
3.10	14.31	12.00	0.009	5.54	0.0021	3.04E+04
3.20	14.82	12.00	0.009	5.74	0.0021	3.15E+04
3.30	15.32	10.00	0.007	5.94	0.0018	3.25E+04
3.40	15.83	10.00	0.007	6.13	0.0018	3.36E+04
3.50	16.34	10.00	0.007	6.33	0.0018	3.47E+04
3.60	16.85	0.00	0.000	6.53	0.0000	3.58E+04
3.70	17.35	0.00	0.000	6.72	0.0000	3.68E+04

Table E.32. Experimental data, Model 65.2.

Fan Speed *Hz*	Wiind velocity *ft/s*	Amplitude *mV*	Amplitude *inches*	Reduced velocity	Reduced amplitude	Reynolds number
1.80	7.71	0.00	0.000	3.40	0.0000	1.64E+04
1.90	8.22	0.00	0.000	3.62	0.0000	1.74E+04
2.00	8.73	36.00	0.026	3.84	0.0064	1.85E+04
2.10	9.23	47.00	0.034	4.07	0.0084	1.96E+04
2.20	9.74	41.00	0.029	4.29	0.0073	2.07E+04
2.30	10.25	16.00	0.011	4.52	0.0029	2.18E+04
2.40	10.76	20.00	0.014	4.74	0.0036	2.28E+04
2.50	11.26	25.00	0.018	4.96	0.0045	2.39E+04
2.60	11.77	25.00	0.018	5.19	0.0045	2.50E+04
2.70	12.28	15.00	0.011	5.41	0.0027	2.61E+04
2.80	12.79	6.00	0.004	5.63	0.0011	2.71E+04
2.90	13.29	0.00	0.000	5.86	0.0000	2.82E+04
3.00	13.80	0.00	0.000	6.08	0.0000	2.93E+04

Table E.33. Experimental data, Model 65.4.

Fan Speed *Hz*	Wiind velocity *ft/s*	Amplitude *mV*	Amplitude *inches*	Reduced velocity	Reduced amplitude	Reynolds number
1.60	6.69	0.00	0.000	3.28	0.0000	1.42E+04
1.70	7.20	0.00	0.000	3.53	0.0000	1.53E+04
1.80	7.71	30.00	0.021	3.77	0.0054	1.64E+04
1.90	8.22	37.00	0.026	4.02	0.0066	1.74E+04
2.00	8.73	32.00	0.023	4.27	0.0057	1.85E+04
2.10	9.23	10.00	0.007	4.52	0.0018	1.96E+04
2.20	9.74	17.00	0.012	4.77	0.0030	2.07E+04
2.30	10.25	33.00	0.024	5.02	0.0059	2.18E+04
2.40	10.76	20.00	0.014	5.27	0.0036	2.28E+04
2.50	11.26	14.00	0.010	5.51	0.0025	2.39E+04
2.60	11.77	0.00	0.000	5.76	0.0000	2.50E+04
2.70	12.28	0.00	0.000	6.01	0.0000	2.61E+04

Table E.34. Experimental data, Model 65.6.

Fan Speed *Hz*	Wiind velocity *ft/s*	Amplitude *mV*	Amplitude *inches*	Reduced velocity	Reduced amplitude	Reynolds number
1.40	5.68	0.00	0.000	3.01	0.0000	1.21E+04
1.50	6.19	0.00	0.000	3.28	0.0000	1.31E+04
1.60	6.69	0.00	0.000	3.55	0.0000	1.42E+04
1.70	7.20	31.00	0.022	3.82	0.0055	1.53E+04
1.80	7.71	40.00	0.029	4.08	0.0072	1.64E+04
1.90	8.22	31.00	0.022	4.35	0.0055	1.74E+04
2.00	8.73	19.00	0.014	4.62	0.0034	1.85E+04
2.10	9.23	20.00	0.014	4.89	0.0036	1.96E+04
2.20	9.74	16.00	0.011	5.16	0.0029	2.07E+04
2.30	10.25	14.00	0.010	5.43	0.0025	2.18E+04
2.40	10.76	10.00	0.007	5.70	0.0018	2.28E+04
2.50	11.26	0.00	0.000	5.97	0.0000	2.39E+04
2.60	11.77	0.00	0.000	6.24	0.0000	2.50E+04

Table E.35. Experimental data, Model 65.8.

Fan Speed *Hz*	Wiind velocity *ft/s*	Amplitude *mV*	Amplitude *inches*	Reduced velocity	Reduced amplitude	Reynolds number
1.30	5.17	0.00	0.000	2.96	0.0000	1.10E+04
1.40	5.68	0.00	0.000	3.25	0.0000	1.21E+04
1.50	6.19	0.00	0.000	3.54	0.0000	1.31E+04
1.60	6.69	33.00	0.024	3.83	0.0059	1.42E+04
1.70	7.20	31.00	0.022	4.12	0.0055	1.53E+04
1.80	7.71	10.00	0.007	4.41	0.0018	1.64E+04
1.90	8.22	24.00	0.017	4.70	0.0043	1.74E+04
2.00	8.73	16.00	0.011	4.99	0.0029	1.85E+04
2.10	9.23	13.00	0.009	5.28	0.0023	1.96E+04
2.20	9.74	10.00	0.007	5.57	0.0018	2.07E+04
2.30	10.25	0.00	0.000	5.86	0.0000	2.18E+04

Table E.36. Experimental data, Model 70.0.

Fan Speed *Hz*	Wiind velocity *ft/s*	Amplitude *mV*	Amplitude *inches*	Reduced velocity	Reduced amplitude	Reynolds number
2.00	8.73	0.00	0.000	3.43	0.0000	1.85E+04
2.10	9.23	0.00	0.000	3.63	0.0000	1.96E+04
2.20	9.74	0.00	0.000	3.83	0.0000	2.07E+04
2.30	10.25	45.40	0.032	4.03	0.0081	2.18E+04
2.40	10.76	66.30	0.047	4.23	0.0119	2.28E+04
2.50	11.26	77.70	0.056	4.43	0.0139	2.39E+04
2.60	11.77	72.90	0.052	4.63	0.0130	2.50E+04
2.70	12.28	25.60	0.018	4.83	0.0046	2.61E+04
2.80	12.79	21.60	0.015	5.03	0.0039	2.71E+04
2.90	13.29	0.00	0.000	5.23	0.0000	2.82E+04
3.00	13.80	0.00	0.000	5.43	0.0000	2.93E+04

Table E.37. Experimental data, Model 70.2.

Fan Speed *Hz*	Wiind velocity *ft/s*	Amplitude *mV*	Amplitude *inches*	Reduced velocity	Reduced amplitude	Reynolds number
1.80	7.71	0.00	0.000	3.43	0.0000	1.64E+04
1.90	8.22	0.00	0.000	3.65	0.0000	1.74E+04
2.00	8.73	0.00	0.000	3.88	0.0000	1.85E+04
2.10	9.23	60.10	0.043	4.10	0.0107	1.96E+04
2.20	9.74	76.20	0.055	4.33	0.0136	2.07E+04
2.30	10.25	80.60	0.058	4.55	0.0144	2.18E+04
2.40	10.76	28.20	0.020	4.78	0.0050	2.28E+04
2.50	11.26	9.89	0.007	5.01	0.0018	2.39E+04
2.60	11.77	0.00	0.000	5.23	0.0000	2.50E+04
2.70	12.28	0.00	0.000	5.46	0.0000	2.61E+04
2.80	12.79	0.00	0.000	5.68	0.0000	2.71E+04

Table E.38. Experimental data, Model 70.4.

Fan Speed *Hz*	Wiind velocity *ft/s*	Amplitude *mV*	Amplitude *inches*	Reduced velocity	Reduced amplitude	Reynolds number
1.60	6.69	0.00	0.000	3.30	0.0000	1.42E+04
1.70	7.20	0.00	0.000	3.55	0.0000	1.53E+04
1.80	7.71	44.00	0.031	3.80	0.0079	1.64E+04
1.90	8.22	38.80	0.028	4.05	0.0069	1.74E+04
2.00	8.73	67.00	0.048	4.30	0.0120	1.85E+04
2.10	9.23	72.00	0.052	4.55	0.0129	1.96E+04
2.20	9.74	26.00	0.019	4.80	0.0047	2.07E+04
2.30	10.25	15.00	0.011	5.05	0.0027	2.18E+04
2.40	10.76	10.00	0.007	5.30	0.0018	2.28E+04
2.50	11.26	0.00	0.000	5.55	0.0000	2.39E+04
2.60	11.77	0.00	0.000	5.80	0.0000	2.50E+04

Table E.39. Experimental data, Model 70.6.

Fan Speed *Hz*	Wiind velocity *ft/s*	Amplitude *mV*	Amplitude *inches*	Reduced velocity	Reduced amplitude	Reynolds number
1.40	5.68	0.00	0.000	3.04	0.0000	1.21E+04
1.50	6.19	0.00	0.000	3.31	0.0000	1.31E+04
1.60	6.69	0.00	0.000	3.58	0.0000	1.42E+04
1.70	7.20	0.00	0.000	3.85	0.0000	1.53E+04
1.80	7.71	45.00	0.032	4.13	0.0080	1.64E+04
1.90	8.22	64.10	0.046	4.40	0.0115	1.74E+04
2.00	8.73	38.00	0.027	4.67	0.0068	1.85E+04
2.10	9.23	16.00	0.011	4.94	0.0029	1.96E+04
2.20	9.74	0.00	0.000	5.21	0.0000	2.07E+04
2.30	10.25	0.00	0.000	5.48	0.0000	2.18E+04
2.40	10.76	0.00	0.000	5.76	0.0000	2.28E+04

Table E.40. Experimental data, Model 70.8

Fan Speed *Hz*	Wiind velocity *ft/s*	Amplitude *mV*	Amplitude *inches*	Reduced velocity	Reduced amplitude	Reynolds number
1.20	4.66	0.00	0.000	2.67	0.0000	9.90E+03
1.30	5.17	0.00	0.000	2.96	0.0000	1.10E+04
1.40	5.68	0.00	0.000	3.25	0.0000	1.21E+04
1.50	6.19	0.00	0.000	3.54	0.0000	1.31E+04
1.60	6.69	5.00	0.004	3.83	0.0009	1.42E+04
1.70	7.20	45.00	0.032	4.12	0.0080	1.53E+04
1.80	7.71	60.40	0.043	4.41	0.0108	1.64E+04
1.90	8.22	51.30	0.037	4.70	0.0092	1.74E+04
2.00	8.73	16.00	0.011	4.99	0.0029	1.85E+04
2.10	9.23	10.00	0.007	5.28	0.0018	1.96E+04
2.20	9.74	0.00	0.000	5.57	0.0000	2.07E+04

APPENDIX F

ELECTRONIC DATA

F.1. Wind speed and amplitude data.

The electronic files recorded by the data acquisition system are tabulated in Table F.1. The information listed in the table includes the file name, the aspect ratio, the number of clamps, the fan speed, the sampling rate, and the length of record.

Table F.1. Electronic Data, Model 20.0.

File name	Aspect ratio *L/D*	# of clamps	Fan speed *Hz*	Sampling rate *Hz*	Record length *seconds*
20_0_02_5	2.0	0	2.5	500	30
20_0_02_6	2.0	0	2.6	500	30
20_0_02_7	2.0	0	2.7	500	30
20_0_02_8	2.0	0	2.8	500	30
20_0_02_9	2.0	0	2.9	500	30
20_0_03_0	2.0	0	3.0	500	30
20_0_03_1	2.0	0	3.1	500	30
20_0_03_2	2.0	0	3.2	500	30
20_0_03_3	2.0	0	3.3	500	30
20_0_03_4	2.0	0	3.4	500	30
20_0_03_5	2.0	0	3.5	500	30
20_0_03_6	2.0	0	3.6	500	30
20_0_03_7	2.0	0	3.7	500	30
20_0_03_8	2.0	0	3.8	500	30
20_0_03_9	2.0	0	3.9	500	30
20_0_04_0	2.0	0	4.0	500	30
20_0_04_1	2.0	0	4.1	500	30
20_0_04_2	2.0	0	4.2	500	30
20_0_04_3	2.0	0	4.3	500	30
20_0_04_4	2.0	0	4.4	500	30
20_0_04_5	2.0	0	4.5	500	30
20_0_04_6	2.0	0	4.6	500	30
20_0_04_7	2.0	0	4.7	500	30
20_0_04_8	2.0	0	4.8	500	30
20_0_04_9	2.0	0	4.9	500	30
20_0_05_0	2.0	0	5.0	500	30
20_0_05_1	2.0	0	5.1	500	30
20_0_05_2	2.0	0	5.2	500	30
20_0_05_3	2.0	0	5.3	500	30
20_0_05_4	2.0	0	5.4	500	30
20_0_05_5	2.0	0	5.5	500	30
20_0_05_6	2.0	0	5.6	500	30
20_0_05_7	2.0	0	5.7	500	30
20_0_05_8	2.0	0	5.8	500	30
20_0_05_9	2.0	0	5.9	500	30
20_0_06_0	2.0	0	6.0	500	30
20_0_06_1	2.0	0	6.1	500	30
20_0_06_2	2.0	0	6.2	500	30
20_0_06_3	2.0	0	6.3	500	30
20_0_06_4	2.0	0	6.4	500	30
20_0_06_5	2.0	0	6.5	500	30
20_0_06_6	2.0	0	6.6	500	30
20_0_06_7	2.0	0	6.7	500	30
20_0_06_8	2.0	0	6.8	500	30

Table F.1. Continued.

File name	Aspect ratio *L/D*	# of clamps	Fan speed *Hz*	Sampling rate *Hz*	Record length *seconds*
20_0_06_9	2.0	0	6.9	500	30
20_0_07_0	2.0	0	7.0	500	30
20_0_07_1	2.0	0	7.1	500	30
20_0_07_2	2.0	0	7.2	500	30
20_0_07_3	2.0	0	7.3	500	30
20_0_07_4	2.0	0	7.4	500	30
20_0_07_5	2.0	0	7.5	500	30
20_0_07_6	2.0	0	7.6	500	30
20_0_07_7	2.0	0	7.7	500	30
20_0_07_8	2.0	0	7.8	500	30
20_0_07_9	2.0	0	7.9	500	30
20_0_08_0	2.0	0	8.0	500	30
20_0_08_1	2.0	0	8.1	500	30
20_0_08_2	2.0	0	8.2	500	30
20_0_08_4	2.0	0	8.4	500	30
20_0_08_6	2.0	0	8.6	500	30
20_0_08_8	2.0	0	8.8	500	30
20_0_09_0	2.0	0	9.0	500	30
20_0_09_2	2.0	0	9.2	500	30
20_0_09_4	2.0	0	9.4	500	30
20_0_09_6	2.0	0	9.6	500	30
20_0_09_8	2.0	0	9.8	500	30
20_0_10_0	2.0	0	10.0	500	30
20_0_10_2	2.0	0	10.2	500	30
20_0_10_4	2.0	0	10.4	500	30
20_0_10_6	2.0	0	10.6	500	30
20_0_10_8	2.0	0	10.8	500	30
20_0_11_0	2.0	0	11.0	500	30
20_0_11_2	2.0	0	11.2	500	30
20_0_11_4	2.0	0	11.4	500	30
20_0_11_6	2.0	0	11.6	500	30
20_0_11_8	2.0	0	11.8	500	30
20_0_12_0	2.0	0	12.0	500	30

Table F.2. Electronic data, Model 20.2.

File name	Aspect ratio *L/D*	# of clamps	Fan speed *Hz*	Sampling rate *Hz*	Record length *seconds*
20_2_02_2	2.0	2	2.2	500	30
20_2_02_3	2.0	2	2.3	500	30
20_2_02_4	2.0	2	2.4	500	30
20_2_02_5	2.0	2	2.5	500	30
20_2_02_6	2.0	2	2.6	500	30
20_2_02_7	2.0	2	2.7	500	30
20_2_02_8	2.0	2	2.8	500	30
20_2_02_9	2.0	2	2.9	500	30
20_2_03_0	2.0	2	3.0	500	30
20_2_03_1	2.0	2	3.1	500	30
20_2_03_2	2.0	2	3.2	500	30
20_2_03_3	2.0	2	3.3	500	30
20_2_03_4	2.0	2	3.4	500	30
20_2_03_5	2.0	2	3.5	500	30
20_2_03_6	2.0	2	3.6	500	30
20_2_03_7	2.0	2	3.7	500	30
20_2_03_8	2.0	2	3.8	500	30
20_2_06_0	2.0	2	6.0	500	30
20_2_06_2	2.0	2	6.2	500	30
20_2_06_4	2.0	2	6.4	500	30
20_2_06_6	2.0	2	6.6	500	30
20_2_06_8	2.0	2	6.8	500	30
20_2_07_0	2.0	2	7.0	500	30
20_2_07_2	2.0	2	7.2	500	30
20_2_07_4	2.0	2	7.4	500	30
20_2_07_6	2.0	2	7.6	500	30
20_2_07_8	2.0	2	7.8	500	30
20_2_08_0	2.0	2	8.0	500	30
20_2_08_2	2.0	2	8.2	500	30
20_2_08_4	2.0	2	8.4	500	10
20_2_08_6	2.0	2	8.6	500	10
20_2_08_8	2.0	2	8.8	500	10
20_2_09_0	2.0	2	9.0	500	10
20_2_09_2	2.0	2	9.2	500	10
20_2_09_4	2.0	2	9.4	500	10
20_2_09_6	2.0	2	9.6	500	10
20_2_09_8	2.0	2	9.8	500	10
20_2_10_0	2.0	2	10.0	500	10
20_2_10_5	2.0	2	10.5	500	10
20_2_11_0	2.0	2	11.0	500	10
20_2_11_5	2.0	2	11.5	500	10
20_2_12_0	2.0	2	12.0	500	10

Table F.3. Electronic data, Model 20.4.

File name	Aspect ratio *L/D*	# of clamps	Fan speed *Hz*	Sampling rate *Hz*	Record length *seconds*
20_4_02_0	2.0	4	2.0	500	30
20_4_02_1	2.0	4	2.1	500	30
20_4_02_2	2.0	4	2.2	500	30
20_4_02_3	2.0	4	2.3	500	30
20_4_02_4	2.0	4	2.4	500	30
20_4_02_5	2.0	4	2.5	500	30
20_4_02_6	2.0	4	2.6	500	30
20_4_02_7	2.0	4	2.7	500	30
20_4_02_8	2.0	4	2.8	500	30
20_4_02_9	2.0	4	2.9	500	30
20_4_03_0	2.0	4	3.0	500	30
20_4_03_1	2.0	4	3.1	500	30
20_4_03_2	2.0	4	3.2	500	30
20_4_03_5	2.0	4	3.5	500	10
20_4_04_0	2.0	4	4.0	500	10
20_4_04_5	2.0	4	4.5	500	10
20_4_05_0	2.0	4	5.0	500	10
20_4_05_5	2.0	4	5.5	500	10
20_4_06_0	2.0	4	6.0	500	10
20_4_06_5	2.0	4	6.5	500	10
20_4_07_0	2.0	4	7.0	500	10
20_4_07_5	2.0	4	7.5	500	10
20_4_08_0	2.0	4	8.0	500	10
20_4_08_5	2.0	4	8.5	500	10
20_4_09_0	2.0	4	9.0	500	10
20_4_09_5	2.0	4	9.5	500	10
20_4_10_0	2.0	4	10.0	500	10

Table F.4. Electronic data, Model 20.6.

File name	Aspect ratio *L/D*	# of clamps	Fan speed *Hz*	Sampling rate *Hz*	Record length *seconds*
20_6_01_9A	2.0	6	1.9	500	30
20_6_01_9B	2.0	6	1.9	500	30
20_6_02_0	2.0	6	2.0	500	30
20_6_02_1	2.0	6	2.1	500	30
20_6_02_2	2.0	6	2.2	500	30
20_6_02_3	2.0	6	2.3	500	30
20_6_02_4	2.0	6	2.4	500	30
20_6_02_5	2.0	6	2.5	500	30
20_6_02_6	2.0	6	2.6	500	30
20_6_02_7	2.0	6	2.7	500	30
20_6_02_8	2.0	6	2.8	500	30
20_6_02_9	2.0	6	2.9	500	30
20_6_03_0	2.0	6	3.0	500	30
20_6_03_5	2.0	6	3.5	500	10
20_6_04_0	2.0	6	4.0	500	10
20_6_04_5	2.0	6	4.5	500	10
20_6_05_0	2.0	6	5.0	500	10
20_6_05_5	2.0	6	5.5	500	10
20_6_06_0	2.0	6	6.0	500	10
20_6_06_5	2.0	6	6.5	500	10
20_6_07_0	2.0	6	7.0	500	10
20_6_07_5	2.0	6	7.5	500	10
20_6_08_0	2.0	6	8.0	500	10
20_6_08_5	2.0	6	8.5	500	10

Table F.5. Electronic data, Model 20.8.

File name	Aspect ratio *L/D*	# of clamps	Fan speed *Hz*	Sampling rate *Hz*	Record length *seconds*
20_8_01_7	2.0	8	1.7	500	30
20_8_01_8	2.0	8	1.8	500	30
20_8_01_9	2.0	8	1.9	500	30
20_8_02_0	2.0	8	2.0	500	30
20_8_02_1	2.0	8	2.1	500	30
20_8_02_2	2.0	8	2.2	500	30
20_8_02_3	2.0	8	2.3	500	30
20_8_02_4	2.0	8	2.4	500	30
20_8_02_5	2.0	8	2.5	500	30
20_8_02_6	2.0	8	2.6	500	30
20_8_02_7	2.0	8	2.7	500	30
20_8_03_0	2.0	8	3.0	500	30
20_8_03_5	2.0	8	3.5	500	10
20_8_04_0	2.0	8	4.0	500	10
20_8_04_5	2.0	8	4.5	500	10
20_8_05_0	2.0	8	5.0	500	10
20_8_05_5	2.0	8	5.5	500	10
20_8_06_0	2.0	8	6.0	500	10
20_8_06_5	2.0	8	6.5	500	10
20_8_07_0	2.0	8	7.0	500	10
20_8_07_5	2.0	8	7.5	500	10
20_8_08_0	2.0	8	8.0	500	10
20_8_08_5	2.0	8	8.5	500	10

Table F.6. Electronic data, Model 30.0.

File name	Aspect ratio *L/D*	# of clamps	Fan speed *Hz*	Sampling rate *Hz*	Record length *seconds*
30_0_01_8	3.0	0	1.8	500	30
30_0_01_9	3.0	0	1.9	500	30
30_0_02_0	3.0	0	2.0	500	30
30_0_02_1	3.0	0	2.1	500	30
30_0_02_2	3.0	0	2.2	500	30
30_0_02_3	3.0	0	2.3	500	30
30_0_03_2	3.0	0	3.2	500	30
30_0_03_3	3.0	0	3.3	500	30
30_0_03_4	3.0	0	3.4	500	30
30_0_03_5	3.0	0	3.5	500	30
30_0_03_6	3.0	0	3.6	500	30
30_0_03_7	3.0	0	3.7	500	30
30_0_03_8	3.0	0	3.8	500	30
30_0_03_9	3.0	0	3.9	500	30
30_0_04_0	3.0	0	4.0	500	30
30_0_04_1	3.0	0	4.1	500	30
30_0_04_2	3.0	0	4.2	500	30
30_0_04_3	3.0	0	4.3	500	30
30_0_04_4	3.0	0	4.4	500	30
30_0_04_5	3.0	0	4.5	500	30
30_0_04_6	3.0	0	4.6	500	30
30_0_04_7	3.0	0	4.7	500	30
30_0_04_8	3.0	0	4.8	500	30
30_0_04_9	3.0	0	4.9	500	30
30_0_05_0	3.0	0	5.0	500	30
30_0_05_1	3.0	0	5.1	500	30
30_0_RunUp	3.0	0	4.2	500	60

Table F.7. Electronic data, Model 30.2.

File name	Aspect ratio *L/D*	# of clamps	Fan speed *Hz*	Sampling rate *Hz*	Record length *seconds*
30_2_01_6	3.0	2	1.6	500	30
30_2_01_7	3.0	2	1.7	500	30
30_2_01_8	3.0	2	1.8	500	30
30_2_01_9	3.0	2	1.9	500	30
30_2_02_0	3.0	2	2.0	500	30
30_2_02_6	3.0	2	2.6	500	30
30_2_02_7	3.0	2	2.7	500	30
30_2_02_8	3.0	2	2.8	500	30
30_2_02_9	3.0	2	2.9	500	30
30_2_03_0	3.0	2	3.0	500	30
30_2_03_1	3.0	2	3.1	500	30
30_2_03_2	3.0	2	3.2	500	30
30_2_03_3	3.0	2	3.3	500	30
30_2_03_4	3.0	2	3.4	500	30
30_2_03_5	3.0	2	3.5	500	30
30_2_03_6	3.0	2	3.6	500	30
30_2_03_7	3.0	2	3.7	500	30
30_2_03_8	3.0	2	3.8	500	30
30_2_03_9	3.0	2	3.9	500	30
30_2_04_0	3.0	2	4.0	500	30
30_2_04_1	3.0	2	4.1	500	30
30_2_04_2	3.0	2	4.2	500	30
30_2_04_3	3.0	2	4.3	500	30
30_2_RunUp	3.0	2	3.7	500	30

Table F.8. Electronic data, Model 30.4.

File name	Aspect ratio *L/D*	# of clamps	Fan speed *Hz*	Sampling rate *Hz*	Record length *seconds*
30_4_01_5	3.0	4	1.5	500	30
30_4_01_6	3.0	4	1.6	500	30
30_4_01_7	3.0	4	1.7	500	30
30_4_01_8	3.0	4	1.8	500	30
30_4_02_3	3.0	4	2.3	500	30
30_4_02_4	3.0	4	2.4	500	30
30_4_02_5	3.0	4	2.5	500	30
30_4_02_6	3.0	4	2.6	500	30
30_4_02_7	3.0	4	2.7	500	30
30_4_02_8	3.0	4	2.8	500	30
30_4_02_9	3.0	4	2.9	500	30
30_4_03_0	3.0	4	3.0	500	30
30_4_03_1	3.0	4	3.1	500	30
30_4_03_2	3.0	4	3.2	500	30
30_4_03_3	3.0	4	3.3	500	30
30_4_03_4	3.0	4	3.4	500	30
30_4_03_5	3.0	4	3.5	500	30
30_4_03_6	3.0	4	3.6	500	30
30_4_03_7	3.0	4	3.7	500	30
30_4_03_8	3.0	4	3.8	500	30
30_4_RunUp	3.0	4	3.3	500	30

Table F.9. Electronic data, Model 30.6.

File name	Aspect ratio *L/D*	# of clamps	Fan speed *Hz*	Sampling rate *Hz*	Record length *seconds*
30_6_01_4	3.0	6	1.4	500	30
30_6_01_5	3.0	6	1.5	500	30
30_6_01_6	3.0	6	1.6	500	30
30_6_02_3	3.0	6	2.3	500	30
30_6_02_4	3.0	6	2.4	500	30
30_6_02_5	3.0	6	2.5	500	30
30_6_02_6	3.0	6	2.6	500	30
30_6_02_7	3.0	6	2.7	500	30
30_6_02_8	3.0	6	2.8	500	30
30_6_02_9	3.0	6	2.9	500	30
30_6_03_0	3.0	6	3.0	500	30
30_6_03_1	3.0	6	3.1	500	30
30_6_03_2	3.0	6	3.2	500	30
30_6_03_3	3.0	6	3.3	500	30
30_6_03_4	3.0	6	3.4	500	30
30_6_03_5	3.0	6	3.5	500	30
30_6_RunUp	3.0	6	2.9	500	30

Table F.10. Electronic data, Model 30.8.

File name	Aspect ratio *L/D*	# of clamps	Fan speed *Hz*	Sampling rate *Hz*	Record length *seconds*
30_8_01_4	3.0	8	1.4	500	30
30_8_01_5	3.0	8	1.5	500	30
30_8_02_2	3.0	8	2.2	500	30
30_8_02_3	3.0	8	2.3	500	30
30_8_02_4	3.0	8	2.4	500	30
30_8_02_5	3.0	8	2.5	500	30
30_8_02_6	3.0	8	2.6	500	30
30_8_02_7	3.0	8	2.7	500	30
30_8_02_8	3.0	8	2.8	500	30
30_8_02_9	3.0	8	2.9	500	30
30_8_03_0A	3.0	8	3.0	500	30
30_8_03_0B	3.0	8	3.0	500	30
30_8_03_1	3.0	8	3.1	500	30
30_8_03_2	3.0	8	3.2	500	30
30_8_03_3	3.0	8	3.3	500	30
30_8_RunUp	3.0	8	2.6	500	30

Table F.11. Electronic data, Model 40.0.

File name	Aspect ratio *L/D*	# of clamps	Fan speed *Hz*	Sampling rate *Hz*	Record length *seconds*
40_0_02_3A	4.0	0	2.3	500	30
40_0_02_3B	4.0	0	2.3	500	30
40_0_02_4A	4.0	0	2.4	500	30
40_0_02_4B	4.0	0	2.4	500	30
40_0_02_5A	4.0	0	2.5	500	30
40_0_02_5B	4.0	0	2.5	500	30
40_0_02_6A	4.0	0	2.6	500	30
40_0_02_6B	4.0	0	2.6	500	30
40_0_02_7A	4.0	0	2.6	500	30
40_0_02_7B	4.0	0	2.6	500	30
40_0_02_8A	4.0	0	2.6	500	30
40_0_02_8B	4.0	0	2.6	500	30
40_0_02_9A	4.0	0	2.6	500	30
40_0_02_9B	4.0	0	2.6	500	30
40_0_03_0A	4.0	0	2.6	500	30
40_0_03_0B	4.0	0	2.6	500	30
40_0_03_1A	4.0	0	2.6	500	30
40_0_03_1B	4.0	0	2.6	500	30
40_0_03_6A	4.0	0	3.6	500	30
40_0_03_6B	4.0	0	3.6	500	30
40_0_03_7A	4.0	0	3.7	500	30
40_0_03_7B	4.0	0	3.7	500	30
40_0_03_8A	4.0	0	3.8	500	30
40_0_03_8B	4.0	0	3.8	500	30
40_0_03_9A	4.0	0	3.9	500	30
40_0_03_9B	4.0	0	3.9	500	30
40_0_04_0A	4.0	0	4.0	500	30
40_0_04_0B	4.0	0	4.0	500	30
40_0_04_1A	4.0	0	4.1	500	30
40_0_04_1B	4.0	0	4.1	500	30
40_0_04_2A	4.0	0	4.2	500	30
40_0_04_2B	4.0	0	4.2	500	30
40_0_04_3A	4.0	0	4.3	500	30
40_0_04_3B	4.0	0	4.3	500	30
40_0_04_4A	4.0	0	4.4	500	30
40_0_04_4B	4.0	0	4.4	500	30
40_0_04_5A	4.0	0	4.5	500	30
40_0_04_5B	4.0	0	4.5	500	30
40_0_04_6A	4.0	0	4.6	500	30
40_0_04_6B	4.0	0	4.6	500	30
40_0_04_7A	4.0	0	4.7	500	30
40_0_04_7B	4.0	0	4.7	500	30
40_0_04_8A	4.0	0	4.8	500	30
40_0_04_8B	4.0	0	4.8	500	30

Table F.11. Continued.

File name	Aspect ratio *L/D*	# of clamps	Fan speed *Hz*	Sampling rate *Hz*	Record length *seconds*
40_0_04_9A	4.0	0	4.9	500	30
40_0_04_9B	4.0	0	4.9	500	30
40_0_05_0A	4.0	0	5.0	500	30
40_0_05_0B	4.0	0	5.0	500	30
40_0_05_1A	4.0	0	5.1	500	30
40_0_05_1B	4.0	0	5.1	500	30
40_0_05_2A	4.0	0	5.2	500	30
40_0_05_2B	4.0	0	5.2	500	30
40_0_05_3A	4.0	0	5.3	500	30
40_0_05_3B	4.0	0	5.3	500	30
40_0_05_4A	4.0	0	5.4	500	30
40_0_05_4B	4.0	0	5.4	500	30
40_0_05_5A	4.0	0	5.5	500	30
40_0_05_5B	4.0	0	5.5	500	30
40_0_05_6A	4.0	0	5.6	500	30
40_0_05_6B	4.0	0	5.6	500	30
40_0_05_7A	4.0	0	5.7	500	30
40_0_05_7B	4.0	0	5.7	500	30
40_0_05_8A	4.0	0	5.8	500	30
40_0_05_8B	4.0	0	5.8	500	30
40_0_05_9A	4.0	0	5.9	500	30
40_0_05_9B	4.0	0	5.9	500	30
40_0_06_0A	4.0	0	6.0	500	30
40_0_06_0B	4.0	0	6.0	500	30
40_0_06_1A	4.0	0	6.1	500	30
40_0_06_1B	4.0	0	6.1	500	30
40_0_06_2A	4.0	0	6.2	500	30
40_0_06_2B	4.0	0	6.2	500	30
40_0_06_3A	4.0	0	6.3	500	30
40_0_06_3B	4.0	0	6.3	500	30
40_0_06_4A	4.0	0	6.4	500	30
40_0_06_4B	4.0	0	6.4	500	30
40_0_06_5A	4.0	0	6.5	500	30
40_0_06_5B	4.0	0	6.5	500	30
40_0_06_6A	4.0	0	6.6	500	30
40_0_06_6B	4.0	0	6.6	500	30
40_0_06_7A	4.0	0	6.7	500	10
40_0_06_7B	4.0	0	6.7	500	10
40_0_06_8A	4.0	0	6.8	500	10
40_0_06_8B	4.0	0	6.8	500	10
40_0_RunUp	4.0	0	5.7	500	30

Table F.12. Electronic data, Model 40.2.

File name	Aspect ratio *L/D*	# of clamps	Fan speed *Hz*	Sampling rate *Hz*	Record length *seconds*
40_2_02_0A	4.0	2	2.0	500	10
40_2_02_0B	4.0	2	2.0	500	10
40_2_02_1A	4.0	2	2.1	500	10
40_2_02_1B	4.0	2	2.1	500	10
40_2_02_2A	4.0	2	2.2	500	10
40_2_02_2B	4.0	2	2.2	500	10
40_2_02_3A	4.0	2	2.3	500	10
40_2_02_3B	4.0	2	2.3	500	10
40_2_02_4A	4.0	2	2.4	500	10
40_2_02_4B	4.0	2	2.4	500	10
40_2_02_5A	4.0	2	2.5	500	10
40_2_02_5B	4.0	2	2.5	500	10
40_2_02_6A	4.0	2	2.6	500	10
40_2_02_6B	4.0	2	2.6	500	10
40_2_02_6C	4.0	2	2.6	500	30
40_2_03_3A	4.0	2	3.3	500	10
40_2_03_3B	4.0	2	3.3	500	10
40_2_03_4A	4.0	2	3.4	500	10
40_2_03_4B	4.0	2	3.4	500	10
40_2_03_5A	4.0	2	3.5	500	10
40_2_03_5B	4.0	2	3.5	500	10
40_2_03_6A	4.0	2	3.6	500	10
40_2_03_6B	4.0	2	3.6	500	10
40_2_03_7A	4.0	2	3.7	500	10
40_2_03_7B	4.0	2	3.7	500	10
40_2_03_8A	4.0	2	3.8	500	10
40_2_03_8B	4.0	2	3.8	500	10
40_2_03_9A	4.0	2	3.9	500	10
40_2_03_9B	4.0	2	3.9	500	10
40_2_04_0A	4.0	2	4.0	500	10
40_2_04_0B	4.0	2	4.0	500	10
40_2_04_1A	4.0	2	4.1	500	10
40_2_04_1B	4.0	2	4.1	500	10
40_2_04_2A	4.0	2	4.2	500	10
40_2_04_2B	4.0	2	4.2	500	10
40_2_04_3A	4.0	2	4.3	500	10
40_2_04_3B	4.0	2	4.3	500	10
40_2_04_4A	4.0	2	4.4	500	10
40_2_04_4B	4.0	2	4.4	500	10
40_2_04_5A	4.0	2	4.5	500	10
40_2_04_5B	4.0	2	4.5	500	10
40_2_04_6A	4.0	2	4.6	500	10
40_2_04_6B	4.0	2	4.6	500	10
40_2_04_7A	4.0	2	4.7	500	10

Table F.12. Continued.

File name	Aspect ratio *L/D*	# of clamps	Fan speed *Hz*	Sampling rate *Hz*	Record length *seconds*
40_2_04_7B	4.0	2	4.7	500	10
40_2_04_8A	4.0	2	4.8	500	10
40_2_04_8B	4.0	2	4.8	500	10
40_2_04_9A	4.0	2	4.9	500	10
40_2_04_9B	4.0	2	4.9	500	10
40_2_05_0A	4.0	2	5.0	500	10
40_2_05_0B	4.0	2	5.0	500	10
40_2_05_1A	4.0	2	5.1	500	10
40_2_05_1B	4.0	2	5.1	500	10
40_2_05_2A	4.0	2	5.2	500	10
40_2_05_2B	4.0	2	5.2	500	10
40_2_05_3A	4.0	2	5.3	500	10
40_2_05_3B	4.0	2	5.3	500	10
40_2_05_4A	4.0	2	5.4	500	10
40_2_05_4B	4.0	2	5.4	500	10
40_2_05_5A	4.0	2	5.5	500	10
40_2_05_5B	4.0	2	5.5	500	10
40_2_05_6A	4.0	2	5.6	500	10
40_2_05_6B	4.0	2	5.6	500	10
40_2_05_7A	4.0	2	5.7	500	10
40_2_05_7B	4.0	2	5.7	500	10
40_2_RunUp	4.0	2	5.0	500	30

Table F.13. Electronic data, Model 40.4.

File name	Aspect ratio *L/D*	# of clamps	Fan speed *Hz*	Sampling rate *Hz*	Record length *seconds*
40_4_01_9A	4.0	4	1.9	500	10
40_4_01_9B	4.0	4	1.9	500	10
40_4_02_0A	4.0	4	2.0	500	10
40_4_02_0B	4.0	4	2.0	500	10
40_4_02_1A	4.0	4	2.1	500	10
40_4_02_1B	4.0	4	2.1	500	10
40_4_02_2A	4.0	4	2.2	500	10
40_4_02_2B	4.0	4	2.2	500	10
40_4_02_3A	4.0	4	2.3	500	10
40_4_02_3B	4.0	4	2.3	500	10
40_4_02_4A	4.0	4	2.4	500	10
40_4_02_4B	4.0	4	2.4	500	10
40_4_02_9A	4.0	4	2.9	500	10
40_4_02_9B	4.0	4	2.9	500	10
40_4_03_0A	4.0	4	3.0	500	30
40_4_03_0B	4.0	4	3.0	500	10
40_4_03_1A	4.0	4	3.1	500	10
40_4_03_1B	4.0	4	3.1	500	30
40_4_03_2A	4.0	4	3.2	500	10
40_4_03_2B	4.0	4	3.2	500	30
40_4_03_3A	4.0	4	3.3	500	10
40_4_03_3B	4.0	4	3.3	500	30
40_4_03_4A	4.0	4	3.4	500	10
40_4_03_4B	4.0	4	3.4	500	30
40_4_03_5A	4.0	4	3.5	500	10
40_4_03_5B	4.0	4	3.5	500	30
40_4_03_6A	4.0	4	3.6	500	10
40_4_03_6B	4.0	4	3.6	500	30
40_4_03_7A	4.0	4	3.7	500	10
40_4_03_7B	4.0	4	3.7	500	30
40_4_03_8A	4.0	4	3.8	500	10
40_4_03_8B	4.0	4	3.8	500	30
40_4_03_9A	4.0	4	3.9	500	10
40_4_03_9B	4.0	4	3.9	500	30
40_4_04_0A	4.0	4	4.0	500	10
40_4_04_0B	4.0	4	4.0	500	30
40_4_04_1A	4.0	4	4.1	500	10
40_4_04_1B	4.0	4	4.1	500	30
40_4_04_2A	4.0	4	4.2	500	10
40_4_04_2B	4.0	4	4.2	500	30
40_4_04_3A	4.0	4	4.3	500	10
40_4_04_3B	4.0	4	4.3	500	30
40_4_04_4A	4.0	4	4.4	500	10
40_4_04_4B	4.0	4	4.4	500	30

Table F.13. Continued.

File name	Aspect ratio *L/D*	# of clamps	Fan speed *Hz*	Sampling rate *Hz*	Record length *seconds*
40_4_04_5A	4.0	4	4.5	500	10
40_4_04_5B	4.0	4	4.5	500	30
40_4_04_6A	4.0	4	4.6	500	10
40_4_04_6B	4.0	4	4.6	500	30
40_4_04_7A	4.0	4	4.7	500	10
40_4_04_7B	4.0	4	4.7	500	30
40_4_04_8A	4.0	4	4.8	500	10
40_4_04_8B	4.0	4	4.8	500	30
40_4_04_9A	4.0	4	4.9	500	10
40_4_04_9B	4.0	4	4.9	500	30
40_4_05_0A	4.0	4	5.0	500	10
40_4_05_0B	4.0	4	5.0	500	30
40_4_05_1A	4.0	4	5.1	500	10
40_4_05_1B	4.0	4	5.1	500	30
40_4_RunUp	4.0	4	4.4	500	30

Table F.14. Electronic data, Model 40.6.

File name	Aspect ratio *L/D*	# of clamps	Fan speed *Hz*	Sampling rate *Hz*	Record length *seconds*
40_6_01_8A	4.0	6	1.8	500	10
40_6_01_8B	4.0	6	1.8	500	30
40_6_01_9A	4.0	6	1.9	500	10
40_6_01_9B	4.0	6	1.9	500	30
40_6_02_0	4.0	6	2.0	500	30
40_6_02_1	4.0	6	2.1	500	30
40_6_02_2	4.0	6	2.2	500	30
40_6_02_8	4.0	6	2.8	500	30
40_6_02_9	4.0	6	2.9	500	30
40_6_03_0	4.0	6	3.0	500	30
40_6_03_1	4.0	6	3.1	500	30
40_6_03_2	4.0	6	3.2	500	30
40_6_03_3	4.0	6	3.3	500	30
40_6_03_4	4.0	6	3.4	500	30
40_6_03_5	4.0	6	3.5	500	30
40_6_03_6	4.0	6	3.6	500	30
40_6_03_7	4.0	6	3.7	500	30
40_6_03_8	4.0	6	3.8	500	30
40_6_03_9	4.0	6	3.9	500	30
40_6_04_0	4.0	6	4.0	500	30
40_6_04_1	4.0	6	4.1	500	30
40_6_04_2	4.0	6	4.2	500	30
40_6_04_3	4.0	6	4.3	500	30
40_6_04_4	4.0	6	4.4	500	30
40_6_04_5	4.0	6	4.5	500	30
40_6_04_6	4.0	6	4.6	500	30
40_6_RunUp	4.0	6	4.0	500	60

Table F.15. Electronic data, Model 40.8.

File name	Aspect ratio *L/D*	# of clamps	Fan speed *Hz*	Sampling rate *Hz*	Record length *seconds*
40_8_01_8	4.0	8	1.8	500	30
40_8_01_9	4.0	8	1.9	500	30
40_8_02_0	4.0	8	2.0	500	30
40_8_02_1	4.0	8	2.1	500	30
40_8_02_2	4.0	8	2.2	500	30
40_8_02_7	4.0	8	2.7	500	30
40_8_02_8	4.0	8	2.8	500	30
40_8_02_9	4.0	8	2.9	500	30
40_8_03_0	4.0	8	3.0	500	30
40_8_03_1	4.0	8	3.1	500	30
40_8_03_2	4.0	8	3.2	500	30
40_8_03_3	4.0	8	3.3	500	30
40_8_03_4	4.0	8	3.4	500	30
40_8_03_5	4.0	8	3.5	500	30
40_8_03_6	4.0	8	3.6	500	30
40_8_03_7	4.0	8	3.7	500	30
40_8_03_8	4.0	8	3.8	500	30
40_8_03_9	4.0	8	3.9	500	30
40_8_04_0	4.0	8	4.0	500	30
40_8_04_1	4.0	8	4.1	500	30
40_8_04_2	4.0	8	4.2	500	30
40_8_RunUp	4.0	8	3.8	500	180

Table F.16. Electronic data, Model 50.0.

File name	Aspect ratio *L/D*	# of clamps	Fan speed *Hz*	Sampling rate *Hz*	Record length *seconds*
50_0_01_8A	5.0	0	1.8	500	10
50_0_01_8B	5.0	0	1.8	500	10
50_0_01_9A	5.0	0	1.9	500	10
50_0_01_9B	5.0	0	1.9	500	10
50_0_02_0A	5.0	0	2.0	500	10
50_0_02_0B	5.0	0	2.0	500	10
50_0_02_7A	5.0	0	2.7	500	10
50_0_02_7B	5.0	0	2.7	500	10
50_0_02_8A	5.0	0	2.8	500	10
50_0_02_8B	5.0	0	2.8	500	10
50_0_02_9A	5.0	0	2.9	500	10
50_0_02_9B	5.0	0	2.9	500	10
50_0_03_0A	5.0	0	3.0	500	10
50_0_03_0B	5.0	0	3.0	500	10
50_0_03_1A	5.0	0	3.1	500	10
50_0_03_1B	5.0	0	3.1	500	10
50_0_03_2A	5.0	0	3.2	500	10
50_0_03_2B	5.0	0	3.2	500	10
50_0_03_3A	5.0	0	3.3	500	10
50_0_03_3B	5.0	0	3.3	500	10
50_0_03_4A	5.0	0	3.4	500	10
50_0_03_4B	5.0	0	3.4	500	10
50_0_RunUp	5.0	0	2.0	500	30

Table F.17. Electronic data, Model 50.2.

File name	Aspect ratio *L/D*	# of clamps	Fan speed *Hz*	Sampling rate *Hz*	Record length *seconds*
50_2_01_6A	5.0	2	1.6	500	10
50_2_01_6B	5.0	2	1.6	500	10
50_2_01_7A	5.0	2	1.7	500	10
50_2_01_7B	5.0	2	1.7	500	10
50_2_01_8A	5.0	2	1.8	500	10
50_2_01_8B	5.0	2	1.8	500	10
50_2_02_4A	5.0	2	2.4	500	10
50_2_02_4B	5.0	2	2.4	500	10
50_2_02_5A	5.0	2	2.5	500	10
50_2_02_5B	5.0	2	2.5	500	10
50_2_02_6A	5.0	2	2.6	500	10
50_2_02_6B	5.0	2	2.6	500	10
50_2_02_7A	5.0	2	2.7	500	10
50_2_02_7B	5.0	2	2.7	500	10
50_2_02_8A	5.0	2	2.8	500	30
50_2_02_8B	5.0	2	2.8	500	30
50_2_02_9A	5.0	2	2.9	500	30
50_2_02_9B	5.0	2	2.9	500	30
50_2_03_0A	5.0	2	3.0	500	30
50_2_03_0B	5.0	2	3.0	500	30
50_2_RunUp	5.0	2	2.6	500	30

Table F.18. Electronic data, Model 50.4.

File name	Aspect ratio *L/D*	# of clamps	Fan speed *Hz*	Sampling rate *Hz*	Record length *seconds*
50_4_01_5A	5.0	4	1.5	500	10
50_4_01_5B	5.0	4	1.5	500	10
50_4_01_6A	5.0	4	1.6	500	10
50_4_01_6B	5.0	4	1.6	500	10
50_4_02_2A	5.0	4	2.2	500	30
50_4_02_2B	5.0	4	2.2	500	30
50_4_02_3A	5.0	4	2.3	500	10
50_4_02_3B	5.0	4	2.3	500	10
50_4_02_4A	5.0	4	2.4	500	10
50_4_02_4B	5.0	4	2.4	500	10
50_4_02_5A	5.0	4	2.5	500	10
50_4_02_5B	5.0	4	2.5	500	10
50_4_02_6A	5.0	4	2.6	500	30
50_4_02_6B	5.0	4	2.6	500	30
50_4_02_7A	5.0	4	2.7	500	10
50_4_02_7B	5.0	4	2.7	500	10
50_4_RunUp	5.0	4	2.4	500	30

Table F.19. Electronic data, Model 50.6.

File name	Aspect ratio *L/D*	# of clamps	Fan speed *Hz*	Sampling rate *Hz*	Record length *seconds*
50_6_02_0A	5.0	6	2.0	500	10
50_6_02_0B	5.0	6	2.0	500	10
50_6_02_1A	5.0	6	2.1	500	10
50_6_02_1B	5.0	6	2.1	500	10
50_6_02_2A	5.0	6	2.2	500	10
50_6_02_2B	5.0	6	2.2	500	10
50_6_02_3A	5.0	6	2.3	500	10
50_6_02_3B	5.0	6	2.3	500	10
50_6_02_4A	5.0	6	2.4	500	10
50_6_02_4B	5.0	6	2.4	500	10
50_6_RunUp	5.0	6	2.2	500	30

Table F.20. Electronic data, Model 50.8.

File name	Aspect ratio *L/D*	# of clamps	Fan speed *Hz*	Sampling rate *Hz*	Record length *seconds*
50_8_01_9A	5.0	8	1.9	500	10
50_8_01_9B	5.0	8	1.9	500	10
50_8_02_0A	5.0	8	2.0	500	10
50_8_02_0B	5.0	8	2.0	500	10
50_8_02_1A	5.0	8	2.1	500	10
50_8_02_1B	5.0	8	2.1	500	10
50_8_02_2A	5.0	8	2.2	500	10
50_8_02_2B	5.0	8	2.2	500	10
50_8_RunUp	5.0	8	2.0	500	30

Table F.21. Electronic data, Model 55.0.

File name	Aspect ratio *L/D*	# of clamps	Fan speed *Hz*	Sampling rate *Hz*	Record length *seconds*
50_0_01_8A	5.5	0	1.8	500	10
50_0_01_8B	5.5	0	1.8	500	10
50_0_01_9A	5.5	0	1.9	500	10
50_0_01_9B	5.5	0	1.9	500	10
55_0_02_0A	5.5	0	2.0	500	10
55_0_02_0B	5.5	0	2.0	500	10
55_0_02_1A	5.5	0	2.1	500	10
55_0_02_1B	5.5	0	2.1	500	10
55_0_02_7A	5.5	0	2.7	500	10
50_0_02_7B	5.5	0	2.7	500	10
55_0_02_8A	5.5	0	2.8	500	10
55_0_02_8B	5.5	0	2.8	500	10
55_0_02_9A	5.5	0	2.9	500	10
55_0_02_9B	5.5	0	2.9	500	10
55_0_03_0A	5.5	0	3.0	500	10
55_0_03_0B	5.5	0	3.0	500	10
55_0_03_1A	5.5	0	3.1	500	10
55_0_03_1B	5.5	0	3.1	500	10
55_0_03_2A	5.5	0	3.2	500	10
55_0_03_2B	5.5	0	3.2	500	10
55_0_03_2C	5.5	0	3.2	500	10
55_0_03_3A	5.5	0	3.3	500	10
55_0_03_3B	5.5	0	3.3	500	10
55_0_03_4A	5.5	0	3.4	500	10
55_0_03_4B	5.5	0	3.4	500	10
55_0_RunUp	5.5	0	2.8	500	30

Table F.22. Electronic data, Model 55.2.

File name	Aspect ratio *L/D*	# of clamps	Fan speed *Hz*	Sampling rate *Hz*	Record length *seconds*
55_2_01_8A	5.5	2	1.8	500	10
55_2_01_8B	5.5	2	1.8	500	10
55_2_01_9A	5.5	2	1.9	500	10
55_2_01_9B	5.5	2	1.9	500	10
55_2_02_4A	5.5	2	2.4	500	10
55_2_02_4B	5.5	2	2.4	500	10
55_2_02_5A	5.5	2	2..5	500	10
55_2_02_5B	5.5	2	2.5	500	10
55_2_02_6A	5.5	2	2.6	500	10
55_2_02_6B	5.5	2	2.6	500	10
55_2_02_7A	5.5	2	2.7	500	10
55_2_02_7B	5.5	2	2.7	500	10
55_2_02_8A	5.5	2	2.8	500	10
55_2_02_8B	5.5	2	2.8	500	10
55_2_02_9A	5.5	2	2.9	500	10
55_2_02_9B	5.5	2	2.9	500	10
55_2_RunUp	5.5	2	2.6	500	30

Table F.23. Electronic data, Model 55.4.

File name	Aspect ratio *L/D*	# of clamps	Fan speed *Hz*	Sampling rate *Hz*	Record length *seconds*
55_4_02_2A	5.5	4	2.2	500	10
55_4_02_2B	5.5	4	2.2	500	10
55_4_02_3A	5.5	4	2.3	500	10
55_4_02_3B	5.5	4	2.3	500	10
55_4_02_4A	5.5	4	2.4	500	10
55_4_02_4B	5.5	4	2.4	500	10
55_4_02_5A	5.5	4	2.5	500	10
55_4_02_5B	5.5	4	2.5	500	10
55_4_RunUp	5.5	4	2.4	500	30

Table F.24. Electronic data, Model 55.6.

File name	Aspect ratio *L/D*	# of clamps	Fan speed *Hz*	Sampling rate *Hz*	Record length *seconds*
55_6_02_0A	5.5	6	2.0	500	10
55_6_02_0B	5.5	6	2.0	500	10
55_6_02_1A	5.5	6	2.1	500	10
55_6_02_1B	5.5	6	2.1	500	10
55_6_02_2A	5.5	6	2.2	500	10
55_6_02_2B	5.5	6	2.2	500	10
55_6_02_3A	5.5	6	2.3	500	10
55_6_02_3B	5.5	6	2.3	500	10
55_6_RunUp	5.5	6	2.2	500	30

Table F.25. Electronic data, Model 55.8.

File name	Aspect ratio *L/D*	# of clamps	Fan speed *Hz*	Sampling rate *Hz*	Record length *seconds*
55_8_01_9A	5.5	8	1.9	500	30
55_8_01_9B	5.5	8	1.9	500	30
55_8_02_0A	5.5	8	2.0	500	10
55_8_02_0B	5.5	8	2.0	500	10
55_8_02_1A	5.5	8	2.1	500	30
55_8_02_1B	5.5	8	2.1	500	30
55_8_RunUp	5.5	8	2.0	500	30

Table F.26. Electronic data, Model 60.0.

File name	Aspect ratio *L/D*	# of clamps	Fan speed *Hz*	Sampling rate *Hz*	Record length *seconds*
60_0_02_1A	6.0	0	2.1	500	10
60_0_02_1B	6.0	0	2.1	500	10
60_0_02_2A	6.0	0	2.2	500	10
60_0_02_2B	6.0	0	2.2	500	10
60_0_02_3A	6.0	0	2.3	500	10
60_0_02_3B	6.0	0	2.3	500	10
60_0_02_4A	6.0	0	2.4	500	10
60_0_02_4B	6.0	0	2.4	500	10
60_0_02_5A	6.0	0	2.5	500	10
60_0_02_5B	6.0	0	2.5	500	10
60_0_02_6A	6.0	0	2.6	500	10
60_0_02_6B	6.0	0	2.6	500	10
60_0_02_7A	6.0	0	2.7	500	10
60_0_02_7B	6.0	0	2.7	500	10
60_0_02_8A	6.0	0	2.8	500	10
60_0_02_8B	6.0	0	2.8	500	10
60_0_02_9A	6.0	0	2.9	500	10
60_0_02_9B	6.0	0	2.9	500	10
60_0_03_0A	6.0	0	3.0	500	10
60_0_03_0B	6.0	0	3.0	500	10
60_0_03_1A	6.0	0	3.1	500	10
60_0_03_1B	6.0	0	3.1	500	10
60_0_03_2A	6.0	0	3.2	500	10
60_0_03_2B	6.0	0	3.2	500	10
60_0_09_0A	6.0	0	9.0	500	10
60_0_09_0B	6.0	0	9.0	500	10
60_0_09_2A	6.0	0	9.2	500	10
60_0_09_2B	6.0	0	9.2	500	10
60_0_09_4A	6.0	0	9.4	500	10
60_0_09_4B	6.0	0	9.4	500	10
60_0_RunUp	6.0	0	2.2	500	30

Table F.27. Electronic data, Model 60.2.

File name	Aspect ratio *L/D*	# of clamps	Fan speed *Hz*	Sampling rate *Hz*	Record length *seconds*
60_2_01_8A	6.0	2	1.8	500	10
60_2_01_8B	6.0	2	1.8	500	10
60_2_01_9A	6.0	2	1.9	500	10
60_2_01_9B	6.0	2	1.9	500	10
60_2_02_0A	6.0	2	2.0	500	10
60_2_02_0B	6.0	2	2.0	500	10
60_2_02_1A	6.0	2	2.1	500	10
60_2_02_1B	6.0	2	2.1	500	10
60_2_02_3B	6.0	2	2.3	500	10
60_2_02_3B	6.0	2	2.3	500	10
60_2_02_4A	6.0	2	2.4	500	10
60_2_02_4B	6.0	2	2.4	500	10
60_2_02_5A	6.0	2	2.5	500	10
60_2_02_5B	6.0	2	2.5	500	10
60_2_02_6A	6.0	2	2.6	500	10
60_2_02_6B	6.0	2	2.6	500	10
60_2_02_7A	6.0	2	2.7	500	10
60_2_02_7B	6.0	2	2.7	500	10
60_2_02_8A	6.0	2	2.8	500	10
60_2_02_8B	6.0	2	2.8	500	10
60_2_RunUp	6.0	2	2.6	500	30

Table F.28. Electronic data, Model 60.4.

File name	Aspect ratio *L/D*	# of clamps	Fan speed *Hz*	Sampling rate *Hz*	Record length *seconds*
60_4_01_7A	6.0	4	1.7	500	10
60_4_01_7B	6.0	4	1.7	500	10
60_4_01_8A	6.0	4	1.8	500	10
60_4_01_8B	6.0	4	1.8	500	10
60_4_01_9A	6.0	4	1.9	500	10
60_4_01_9B	6.0	4	1.9	500	10
60_4_02_0A	6.0	4	2.0	500	10
60_4_02_0B	6.0	4	2.0	500	10
60_4_02_1A	6.0	4	2.1	500	10
60_4_02_1B	6.0	4	2.1	500	10
60_4_02_2A	6.0	4	2.2	500	10
60_4_02_2B	6.0	4	2.2	500	10
60_4_02_3A	6.0	4	2.3	500	10
60_4_02_3B	6.0	4	2.3	500	10
60_4_02_4A	6.0	4	2.4	500	10
60_4_02_4B	6.0	4	2.4	500	10
60_4_02_5A	6.0	4	2.5	500	10
60_4_02_5B	6.0	4	2.5	500	10
60_4_RunUp	6.0	4	2.4	500	30

Table F.29. Electronic data, Model 60.6.

File name	Aspect ratio *L/D*	# of clamps	Fan speed *Hz*	Sampling rate *Hz*	Record length *seconds*
60_6_01_7A	6.0	6	1.7	500	10
60_6_01_7B	6.0	6	1.7	500	10
60_6_02_1A	6.0	6	2.1	500	10
60_6_02_1B	6.0	6	2.1	500	10
60_6_02_2A	6.0	6	2.2	500	10
60_6_02_2B	6.0	6	2.2	500	10
60_6_RunUp	6.0	6	2.1	500	30

Table F.30. Electronic data, Model 60.8.

File name	Aspect ratio *L/D*	# of clamps	Fan speed *Hz*	Sampling rate *Hz*	Record length *seconds*
60_8_01_9A	6.0	8	1.9	500	10
60_8_01_9B	6.0	8	1.9	500	10
60_8_02_0A	6.0	8	2.0	500	10
60_8_02_0B	6.0	8	2.0	500	10
60_8_02_1A	6.0	8	2.1	500	10
60_8_02_1B	6.0	8	2.1	500	10
60_8_RunUp	6.0	8	2.0	500	30

Table F.31. Electronic data, Model 65.0.

File name	Aspect ratio *L/D*	# of clamps	Fan speed *Hz*	Sampling rate *Hz*	Record length *seconds*
65_0_02_2A	6.5	0	2.2	500	10
65_0_02_2B	6.5	0	2.2	500	10
65_0_02_3A	6.5	0	2.3	500	10
65_0_02_3B	6.5	0	2.3	500	10
65_0_02_4A	6.5	0	2.4	500	10
65_0_02_4B	6.5	0	2.4	500	10
65_0_02_5A	6.5	0	2.5	500	10
65_0_02_5B	6.5	0	2.5	500	10
65_0_02_6A	6.5	0	2.6	500	10
65_0_02_6B	6.5	0	2.6	500	10
65_0_02_7A	6.5	0	2.7	500	10
65_0_02_7B	6.5	0	2.7	500	10
65_0_02_8A	6.5	0	2.8	500	10
65_0_02_8B	6.5	0	2.8	500	10
65_0_02_9A	6.5	0	2.9	500	10
65_0_02_9B	6.5	0	2.9	500	10
65_0_03_0A	6.5	0	3.0	500	10
65_0_03_0B	6.5	0	3.0	500	10
65_0_RunUp	6.5	0	2.4	500	30

Table F.32. Electronic data, Model 65.2.

File name	Aspect ratio *L/D*	# of clamps	Fan speed *Hz*	Sampling rate *Hz*	Record length *seconds*
65_2_01_9A	6.5	2	1.9	500	10
65_2_01_9B	6.5	2	1.9	500	10
65_2_02_0A	6.5	2	2.0	500	10
65_2_02_0B	6.5	2	2.0	500	10
65_2_02_1A	6.5	2	2.1	500	10
65_2_02_1B	6.5	2	2.1	500	10
65_2_02_2B	6.5	2	2.2	500	10
65_2_02_2B	6.5	2	2.2	500	10
65_2_02_3B	6.5	2	2.3	500	10
65_2_02_3B	6.5	2	2.3	500	10
65_2_02_4A	6.5	2	2.4	500	10
65_2_02_4B	6.5	2	2.4	500	10
65_2_02_5A	6.5	2	2..5	500	10
65_2_02_5B	6.5	2	2.5	500	10
65_2_02_6A	6.5	2	2.6	500	10
65_2_02_6B	6.5	2	2.6	500	10
65_2_02_7A	6.5	2	2.7	500	10
65_2_02_7B	6.5	2	2.7	500	10
65_2_02_8A	6.5	2	2.8	500	10
65_2_02_8B	6.5	2	2.8	500	10
65_2_RunUp	6.5	2	2.1	500	30

Table F.33. Electronic data, Model 65.4.

File name	Aspect ratio *L/D*	# of clamps	Fan speed *Hz*	Sampling rate *Hz*	Record length *seconds*
65_4_01_7A	6.5	4	1.7	500	10
65_4_01_7B	6.5	4	1.7	500	10
65_4_01_8A	6.5	4	1.8	500	10
65_4_01_8B	6.5	4	1.8	500	10
65_4_01_9A	6.5	4	1.9	500	10
65_4_01_9B	6.5	4	1.9	500	10
65_4_02_0A	6.5	4	2.0	500	10
65_4_02_0B	6.5	4	2.0	500	10
65_4_02_1A	6.5	4	2.1	500	10
65_4_02_1B	6.5	4	2.1	500	10
65_4_02_2A	6.5	4	2.2	500	10
65_4_02_2B	6.5	4	2.2	500	10
65_4_02_3A	6.5	4	2.3	500	10
65_4_02_3B	6.5	4	2.3	500	10
65_4_02_4A	6.5	4	2.4	500	10
65_4_02_4B	6.5	4	2.4	500	10
65_4_02_5A	6.5	4	2.5	500	10
65_4_02_5B	6.5	4	2.5	500	10
65_4_02_6B	6.5	4	2.5	500	10
65_4_02_6B	6.5	4	2.5	500	10

Table F.34. Electronic data, Model 65.6.

File name	Aspect ratio *L/D*	# of clamps	Fan speed *Hz*	Sampling rate *Hz*	Record length *seconds*
65_6_01_7A	6.5	6	1.7	500	10
65_6_01_7B	6.5	6	1.7	500	10
65_6_01_8A	6.5	6	1.8	500	10
65_6_01_8B	6.5	6	1.8	500	10
65_6_01_9A	6.5	6	1.9	500	10
65_6_01_9B	6.5	6	1.9	500	10
65_6_02_0A	6.5	6	2.0	500	10
65_6_02_0B	6.5	6	2.0	500	10
65_6_02_1A	6.5	6	2.1	500	10
65_6_02_1B	6.5	6	2.1	500	10
65_6_02_2A	6.5	6	2.2	500	10
65_6_02_2B	6.5	6	2.2	500	10
65_6_02_3A	6.5	6	2.2	500	10
65_6_02_3B	6.5	6	2.2	500	10

Table F.35. Electronic data, Model 65.8.

File name	Aspect ratio *L/D*	# of clamps	Fan speed *Hz*	Sampling rate *Hz*	Record length *seconds*
65_8_01_5A	6.5	8	1.5	500	10
65_8_01_5B	6.5	8	1.5	500	10
65_8_01_6A	6.5	8	1.6	500	10
65_8_01_6B	6.5	8	1.6	500	10
65_8_01_7A	6.5	8	1.7	500	10
65_8_01_7B	6.5	8	1.7	500	10
65_8_01_8A	6.5	8	1.8	500	10
65_8_01_8B	6.5	8	1.8	500	10
65_8_01_9A	6.5	8	1.9	500	10
65_8_01_9B	6.5	8	1.9	500	10
65_8_02_0A	6.5	8	2.0	500	10
65_8_02_0B	6.5	8	2.0	500	10
65_8_02_1A	6.5	8	2.1	500	10
65_8_02_1B	6.5	8	2.1	500	10

Table F.36. Electronic data, Model 70.0.

File name	Aspect ratio *L/D*	# of clamps	Fan speed *Hz*	Sampling rate *Hz*	Record length *seconds*
70_0_02_3A	7.0	0	2.3	500	10
70_0_02_3B	7.0	0	2.3	500	10
70_0_02_4A	7.0	0	2.4	500	10
70_0_02_4B	7.0	0	2.4	500	10
70_0_02_5A	7.0	0	2.5	500	10
70_0_02_5B	7.0	0	2.5	500	10
70_0_02_6A	7.0	0	2.6	500	10
70_0_02_6B	7.0	0	2.6	500	10
70_0_02_7A	7.0	0	2.7	500	10
70_0_02_7B	7.0	0	2.7	500	10
70_0_02_8A	7.0	0	2.8	500	10
70_0_02_8B	7.0	0	2.8	500	10
70_0_RunUp	7.0	0	2.5	500	30

Table F.37. Electronic data, Model 70.2.

File name	Aspect ratio *L/D*	# of clamps	Fan speed *Hz*	Sampling rate *Hz*	Record length *seconds*
70_2_02_0A	7.0	2	2.0	500	10
70_2_02_0B	7.0	2	2.0	500	10
70_2_02_1A	7.0	2	2.1	500	10
70_2_02_1B	7.0	2	2.1	500	10
70_2_02_2B	7.0	2	2.2	500	10
70_2_02_2B	7.0	2	2.2	500	10
70_2_02_3B	7.0	2	2.3	500	10
70_2_02_3B	7.0	2	2.3	500	10
70_2_02_4A	7.0	2	2.4	500	10
70_2_02_4B	7.0	2	2.4	500	10
70_2_02_5A	7.0	2	2..5	500	10
70_2_02_5B	7.0	2	2.5	500	10
70_2_RunUp	7.0	2	2.3	500	30

Table F.38. Electronic data, Model 70.4.

File name	Aspect ratio *L/D*	# of clamps	Fan speed *Hz*	Sampling rate *Hz*	Record length *seconds*
70_4_01_8A	7.0	4	1.8	500	10
70_4_01_8B	7.0	4	1.8	500	10
70_4_01_9A	7.0	4	1.9	500	10
70_4_01_9B	7.0	4	1.9	500	10
70_4_02_0A	7.0	4	2.0	500	10
70_4_02_0B	7.0	4	2.0	500	10
70_4_02_1A	7.0	4	2.1	500	10
70_4_02_1B	7.0	4	2.1	500	10
70_4_02_2A	7.0	4	2.2	500	10
70_4_02_2B	7.0	4	2.2	500	10
70_4_02_3A	7.0	4	2.3	500	10
70_4_02_3B	7.0	4	2.3	500	10
70_4_RunUp	7.0	4	2.1	500	10

Table F.39. Electronic data, Model 70.6.

File name	Aspect ratio *L/D*	# of clamps	Fan speed *Hz*	Sampling rate *Hz*	Record length *seconds*
70_6_01_7A	7.0	6	1.7	500	10
70_6_01_7B	7.0	6	1.7	500	10
70_6_01_8A	7.0	6	1.8	500	10
70_6_01_8B	7.0	6	1.8	500	10
70_6_01_9A	7.0	6	1.9	500	10
70_6_01_9B	7.0	6	1.9	500	10
70_6_02_0A	7.0	6	2.0	500	10
70_6_02_0B	7.0	6	2.0	500	10
70_6_02_1A	7.0	6	2.1	500	10
70_6_02_1B	7.0	6	2.1	500	10
70_6_02_2A	7.0	6	2.2	500	10
70_6_02_2B	7.0	6	2.2	500	10
70_6_RunUp	7.0	6	1.9	500	30

Table F.40. Electronic data, Model 70.8.

File name	Aspect ratio *L/D*	# of clamps	Fan speed *Hz*	Sampling rate *Hz*	Record length *seconds*
70_8_01_6A	7.0	8	1.6	500	10
70_8_01_6B	7.0	8	1.6	500	10
70_8_01_7A	7.0	8	1.7	500	10
70_8_01_7B	7.0	8	1.7	500	10
70_8_01_8A	7.0	8	1.8	500	10
70_8_01_8B	7.0	8	1.8	500	10
70_8_01_9A	7.0	8	1.9	500	10
70_8_01_9B	7.0	8	1.9	500	10
70_8_02_0A	7.0	8	2.0	500	10
70_8_02_0B	7.0	8	2.0	500	10
70_8_RunUp	7.0	8	1.8	500	30

REFERENCES

Anderson, J.D., Jr., 2001. *Fundamentals of Aerodynamics*, 3rd ed., McGraw-Hill, New York, NY.

Ang, A. H-S. & Tang, W.H., 1975. *Probability Concepts in Engineering Planning and Design Volume I: Basic Principles*, John Wiley & Sons, New York, NY.

Basu, R.I., 1985. "Aerodynamic forces on structures of circular cross-section. Part 1." *Journal of Wind Engineering and Industrial Aerodynamics*, **21**, 273-294.

Basu, R.I., 1986. "Aerodynamic forces on structures of circular cross-section. Part 2." *Journal of Wind Engineering and Industrial Aerodynamics*, **24**, 33-59.

Bearman, P.W., 1969. "On vortex shedding from a circular cylinder in the critical Reynolds number regime." *Journal of Fluid Mechanics*, **3**, 577-585.

Bearman, P.W., Gartshore, I.S., Maull, & D.J., Parkinson, G.V., 1987. "Experiments on flow-induced vibration of a square-section cylinder," *Journal of Fluids and Structures*, **1**, 19-34.

Blevins, R.D., 1992. *Applied Fluid Dynamics Handbook*, Krieger Publishing Company, Malabar, Florida.

Blevins, R.D., 1994. *Flow-Induced Vibration*, 2nd ed., Krieger Publishing Company, Malabar, FL.

Collins, J.A., 1993. *Failure of Materials in Mechanical Design: Analysis, Prediction, Prevention*, 2nd ed., John Wiley & Sons, New York, NY.

Corless, R.M. & Parkinson, G.V., 1988. "A model of the combined effects of vortex-induced oscillation and galloping." *Journal of Fluids and Structures*, **2**, 203-220.

Deniz, S. & Staubli, T., 1997. "Oscillating rectangular and octagonal profiles: Interaction of leading- and trailing-edge vortex formation." *Journal of Fluids and Structures*, **11**, 3-31.

Dieter, G.E., 1986. *Mechanical Metallurgy*, 3rd ed., McGraw-Hill, New York, NY.

Dowell, E.H., Crawley, E.F., Curtiss, H.C., Peters, D.A., Scanlan, R.H., & Sisto, F., 1995. *A Modern Course in Aeroelasticity*, 3rd ed., Kluwer Academic Publishers, Dordrecht, The Netherlands.

Goswami, I., Scanlan, R.H., & Jones, N.P., 1993. "Vortex-induced vibration of circular cylinders. I: Experimental Data." *Journal of Engineering Mechanics*, **11**, 2270-2287.

Dyrbye, C. & Hansen, S.O., 1997. *Wind Loads on Structures*, John Wiley & Sons, Chichester, England.

Fuchs, H.O. & Stephens, R.I., 1980. *Metal Fatigue in Engineering*, John Wiley & Sons, New York, NY.

Holmes, J.D., 2001. *Wind Loading of Structures*, Spon Press, London, England.

Khalak, A. & Williamson, C.H.K., 1999. "Motions, forces and mode transitions in vortex-induced vibrations at low mass-damping." *Journal of Fluids and Structures*, **13**, 813-851.

King, R., 1977. "A Review of Vortex Shedding Research and its Applications," *Ocean Engineering*, **4**, 141-171.

Knisely, C.W., 1990. "Strouhal numbers of rectangular cylinders at incidence: A review and new data." *Journal of Fluids and Structures*, **4**, 371-393.

Kobayashi, H., Kawatani, M., & Kim, H., 1992. "Effects of turbulence characteristics on vortex-induced oscillation of rectangular cylinders." *Journal of Wind Engineering and Industrial Aerodynamics*, **41-44**, 775-785.

Komatsu, S., & Kobayashi, H., 1980. "Vortex-induced oscillation of bluff cylinders." *Journal of Wind Engineering and Industrial Aerodynamics*, **6**, 335-362.

Laneville & Yong, 1983. "Mean flow patterns around two-dimensional rectangular cylinders and their interpretation," *Journal of Wind Engineering and Industrial Aerodynamics*, **14**, 387-398.

Liu, Henry, 1991. *Wind Engineering: A Handbook for Structural Engineers*, Prentice-Hall, Englewood Cliffs, NJ.

Matsumoto, M., 1999. "Vortex shedding of bluff bodies: A review," *Journal of Fluids and Structures*, **13**, 791-811.

Melchers, R.E., 1999. *Structural Reliability Analysis and Prediction*, 2nd ed., John Wiley & Sons, Chichester, England.

Nakamura, Y. & Nakashima, M., 1986. "Vortex excitation of prisms with elongated rectangular, H and T cross-sections," *Journal of Fluid Mechanics*, **163**, 149-169.

Nakamura, Y., Ohya, Y., & Tsuruta, H., 1991. "Experiments on vortex shedding from flat plates with square leading and trailing edges," *Journal of Fluid Mechanics*, **222**, 437-447.

Naudascher, E. & Rockwell, D., 1994. *Flow-Induced Vibrations, An Engineering Guide*, A.A. Balkema Publisher, Rotterdam, The Netherlands.

Naudascher, E. & Wang, Y., 1993. "Flow-induced vibrations of prismatic bodies and grids of prisms," *Journal of Fluids and Structures*, 7, 341-373.

Newland, D.E., 1993. *An Introduction to Random Vibrations, Spectral & Wavelet Analysis*, 3rd ed., Longman Group Limited, Essex, England.

Nguyen, T.D. & Naudascher, E., 1991. "Vibration of beams and trashracks in parallel and inclined flow," *Journal of Hydraulic Engineering*, **8**, 1056-1076.

Okajima, A., 1982. "Strouhal numbers of rectangular cylinders," *Journal of Fluid Mechanics*, **123**, 379-398.

Parkinson, G., 1989. "Phenomena and modelling of flow-induced vibrations of bluff bodies," *Prog. Aerospace Science*, **26**, 169-224.

Rolfe, S.T. & Barsom, J.M., 1977. *Fracture and Fatigue Control in Structures: Applications of Fracture Mechanics*, Prentice-Hall, Englewood Cliffs, NJ.

Sarpkaya, T. 1979. "Vortex-induced oscillations, a selective review," *Journal of Applied Mechanics*, **46**, 241-258.

Simiu, E. & Scanlan, R.H., 1996. *Wind Effects on Structures, Fundamentals and Applications to Design*, 3rd ed., John Wiley & Sons, New York, NY.

Skop, R.A. & Griffin, O.M., 1975. "On a theory for the vortex-excited oscillations of flexible cylindrical structures." *Journal of Sound and Vibration*, **41**(3), 263-274.

Sobczyk, K. & Spencer, B.F., Jr., 1992. *Random Fatigue: From Data to Theory*, Academic Press, San Diego, CA.

Sólnes, Júlíus, 1997. *Stochastic Processes and Random Vibrations*, John Wiley & Sons, Chichester, England.

Washizu, K., Ohya, A., Otsuki, Y., & Fujii, K., 1978. "Aeroelastic instability of rectangular cylinders in a heaving mode." *Journal of Sound and Vibration*, **59**, 195-210.

Wirsching, P.H., Paez, T.L., & Ortiz, K., 1995. *Random Vibrations: Theory and Practice*, John Wiley & Sons, New York, NY.

Zdravkovich, M.M., 1982. "Modification of Vortex Shedding in the Synchronization Range," *Journal of Fluids Engineering*, **104**, 513-517.